Universidade de São Paulo
Instituto de Física

Estrutura eletrônica e excitações magnéticas de supercondutores magnéticos

Marli dos Reis Cantarino

Orientador: Prof. Dr. Fernando Assis Garcia
Coorientador: Prof. Dr. Tulio Costa Rizuti da Rocha

Tese de doutorado apresentada ao Instituto de Física da Universidade de São Paulo, como requisito parcial para a obtenção do título de Doutora em Ciências.

Banca Examinadora:
Prof. Dr. Fernando Assis Garcia - Orientador (IFUSP)
Prof. Dr. Sergio Luiz Morelhão (IFUSP)
Profa. Dra. Thereza Cristina de Lacerda Paiva (UFRJ)
Prof. Dr. Luís Henrique de Lima (UFABC)
Prof. Dr. Victor Luiz Quito (IFSC - USP)

São Paulo
2023

FICHA CATALOGRÁFICA
Preparada pelo Serviço de Biblioteca e Informação
do Instituto de Física da Universidade de São Paulo

Cantarino, Marli dos Reis

Estrutura eletrônica e excitações magnéticas de supercondutores magnéticos /Electronic structure and magnetic excitations of magnetic superconductors. São Paulo, 2023.

Tese (Doutorado) - Universidade de São Paulo. Instituto de Física. Depto. de Física Aplicada.

Orientador: Prof. Dr. Fernando Assis Garcia

Área de Concentração: Física do Estado Sólido

Unitermos: 1. Radiação sincrotron; 2. Espectroscopia de raios-x; 3. Supercondutores baseados em ferro; 4. Estrutura eletrônica.

USP/IF/SBI-027/2023

University of São Paulo
Physics Institute

Electronic structure and magnetic excitations of magnetic superconductors

Marli dos Reis Cantarino

Supervisor: Prof. Dr. Fernando Assis Garcia
Co-supervisor: Prof. Dr. Tulio Costa Rizuti da Rocha

Thesis submitted to the Physics Institute of the University of São Paulo in partial fulfillment of the requirements for the degree of Doctor of Science.

Examining Committee:
Prof. Dr. Fernando Assis Garcia - Supervisor (IFUSP)
Prof. Dr. Sergio Luiz Morelhão (IFUSP)
Profa. Dra. Thereza Cristina de Lacerda Paiva (UFRJ)
Prof. Dr. Luís Henrique de Lima (UFABC)
Prof. Dr. Victor Luiz Quito (IFSC - USP)

São Paulo
2023

Agradecimentos

Pelo financiamento do meu doutorado e do estágio de pesquisa no exterior, processos nº 2019/05150-7 e nº 2020/13701-0, agradeço à Fundação de Amparo à Pesquisa do Estado de São Paulo (FAPESP). O presente trabalho foi realizado com apoio da Coordenação de Aperfeiçoamento de Pessoal de Nível Superior – Brasil (CAPES) – Processo: 88887.340921/2019-00, durante 3 meses iniciais.

Agradeço aos membros da banca por lerem a primeira versão deste trabalho e darem contribuições importantes para melhoria do texto.

Sou muito grata ao meu orientador, Fernando Garcia, pelos ensinamentos, paciência e disponibilidade ao longo do período do meu doutorado, e antes dele. Também gostaria de agradecer ao meu coorientador, Tulio Rocha, por me receber nas linhas PGM e IPE do Laboratório Nacional de Luz Síncrotron (LNLS) e me ensinar do zero sobre a instrumentação do espectrômetro e muitas outras coisas. Sua presença e disposição foram fundamentais para o sucesso desse trabalho.

Não poderia deixar de agradecer aos meus colegas durante esse período, que estiveram junto comigo em momentos de trabalho e descontração: Alvaro, Lauro, Rodrigo, Pedro, Juliana, Wagner, Hanna e Carlos. Agradeço também aos professores e funcionários do IFUSP que me auxiliaram nesse caminho de alguma forma, em especial ao Eric Andrade pelas conversas elucidativas sobre teoria. E ainda aos funcionários e amigos do LNLS, Thiago, Flávio, Wendell, Luiz, Natália, Matheus e Adriana, pela companhia e apoio.

Gostaria de agradecer ao Claude Monney por me receber em seu grupo na Universidade de Fribourg, pelo profissionalismo, disponibilidade e acolhimento. Também agradeço aos meus colegas Geoffroy, Christopher, Maxime, Björn, Fred, Aki, Elina, Roxana e Subhrangsu pelos ensinamentos, colaborações e tempo juntos.

Meus agradecimentos ao laboratório Max IV por tempo de linha na estação experimental Bloch, na proposta 20200293, e o suporte da Gerardina Carbone e do Craig Polley. Agradeço ao Aniruddha e à Khadiza pelo suporte indispensável no nosso tempo de linha no midsommar. Também agradeço ao pessoal da estação experimental ADRESS, do *Swiss Light Source*, pelo suporte e companhia nos tempos de linha que participei, ao Thorsten Schmitt, Wenliang Zhang, Yuan Wei, Teguh Asmara e à prof. Dr. Ana Akrap e o David Santos-Cottin por me cederem um pouco de seu tempo de linha para minhas amostras. E agradeço à Damaris pelo suporte e acolhimento.

Agradeço ao Ke-Jin Zhou e a todo pessoal da linha I21 do *Diamond Light Source* no Reino Unido pelo tempo de linha relativo à proposta MM33194. Em especial sou grata à Mirian Garcia-Fernandez, pelo apoio, companhia e incentivo, que foram além de todo aspecto experimental de RIXS.

Sou muito grata à prof. Cris Adriano, ao Kevin, ao Gabriel e ao prof. Pascoal Pagliuso do Grupo de Propriedades Ópticas e Magnéticas dos Sólidos pela parceria e pelas amostras usadas nesse trabalho. Agradeço também ao Abner por me receber em seu laboratório e pelas conversas.

Por fim, mas certamente não menos importante, quero agradecer à minha família e amigos pelo apoio incondicional e compreensão durante esta jornada desafiadora de um doutorado. Agradeço a Joaquim, Maria, Marisa, Miriam, Marlete, Josi, Rafael, Ana, Bartira, Luisa, Luane, Letícia, Luiz, Henrique, Zé, Sérgio, Mari, Kae, Jean, Hiro, Leo, Luísa, Letty, Wallace, Leila e Diego. Agradeço à Barbara por impedir tantas vezes que eu surtasse.

Sou eternamente grata ao Silvio pelo amor, companheirismo e apoio inigualáveis, que tornaram essa jornada ainda mais significativa e gratificante.

Abstract

The manipulation of electron counting and orbital occupation via chemical doping, chemical pressure, applied hydrostatic pressure, or strain can tune the ground state of a material. Iron-based superconductors (FeSC) are a class of materials in which high-temperature superconductivity (SC) can emerge using these strategies. This transition occurs in the presence of strong magnetic fluctuations, suggesting a low sensitivity to magnetic impurities. Surprisingly, when it comes to transition metal substitution, electron dopants can cause SC to emerge, while hole dopants do not.

This study employs Angle-Resolved Photoemission Spectroscopy (ARPES) to investigate the effect of hole doping in the Fe site of $Ba(Fe_{1-x}M_x)_2As_2$ (M = Mn, Cr) samples, probing the electronic band structure and its dependency on composition and temperature. The presented results show that for the case of Mn-substituted samples (MnBFA), electron and hole pockets remain nested, with Mn introduction mainly increasing the incoherence of the electronic bands and electronic correlations. These findings suggest that Mn tunes the material to a region between the correlated metal phase in $BaFe_2As_2$ and the Mott insulating phase in $BaMn_2As_2$, where disordered electronic phases can emerge. In the case of Cr substituted samples (CrBFA), hole doping was shown to take place, detuning the nesting condition between hole and electron states, and the electronic correlations increase with Cr content. However, no evidence of Mott phase behavior is observed in the ARPES experiments of a Cr-doped sample near the half-filling condition.

Moreover, Resonant Inelastic x-ray Scattering (RIXS) was applied to probe the Fe-derived magnetic excitations in these materials. The RIXS experiments of CrBFA suggest a scenario that is slightly different from that for MnBFA samples but also shows strong magnetic scattering between Fe and Cr-derived excitations.

This study explains the absence of SC in MnBFA as a combination of magnetic pair-breaking, disorder, and electronic correlations, while in CrBFA this absence is understood to be caused mainly because of magnetic pair-breaking and suppression of the itinerant spin fluctuations which promote the SC. These results shed light on the complex interplay between doping, magnetism, and electronic correlations in FeSC and correlated electron systems in general.

Keywords: iron arsenide, ARPES, RIXS, electronic correlation, disordered electronic phase

Resumo

A manipulação da contagem de elétrons e da ocupação orbital por meio de dopagem química, pressão química, pressão hidrostática ou deformação uniaxial pode ajustar o estado fundamental de um material. Os supercondutores baseados em ferro (FeSC) são uma classe de materiais em que a supercondutividade de alta temperatura (SC) pode surgir usando essas estratégias. Essa transição ocorre na presença de fortes flutuações magnéticas, sugerindo uma baixa sensibilidade a impurezas magnéticas. Surpreendentemente, quando se trata de substituição de metais de transição, dopantes eletrônicos podem fazer a SC surgir, enquanto dopantes de buracos não.

Empregando a Espectroscopia de Fotoemissão com Resolução Angular (ARPES) para investigar o efeito da dopagem com buracos no sítio de Fe em amostras de $Ba(Fe_{1-x}M_x)_2As_2$ (M = Mn, Cr), esta tese investiga a estrutura de bandas eletrônicas e sua dependência na composição e temperatura. Os resultados apresentados mostram que, no caso das amostras substituídas por Mn (MnBFA), os bolsões de elétrons e buracos permanecem aninhados, com a introdução de Mn aumentando principalmente a incoerência das bandas eletrônicas e as correlações eletrônicas. Essas descobertas sugerem que o Mn ajusta o material para uma região entre a fase metálica correlacionada em $BaFe_2As_2$ e a fase isolante de Mott em $BaMn_2As_2$, onde fases eletrônicas desordenadas podem emergir. No caso das amostras substituídas por Cr (CrBFA), a dopagem com buracos ocorre efetivamente, desajustando a condição de aninhamento entre estados de elétrons e buracos, e as correlações eletrônicas aumentam com o conteúdo de Cr. No entanto, nenhuma evidência de comportamento de fase de Mott é observada nos experimentos ARPES de para a amostra dopada com Cr próxima à condição de meio-preenchimento.

Além disso, a Espalhamento Inelástico de Raios X Ressonante (RIXS) foi aplicada para sondar as excitações magnéticas derivadas do Fe nesses materiais. Os experimentos de RIXS nos CrBFA sugerem um cenário ligeiramente diferente daquele para amostras de MnBFA, mas também mostram forte espalhamento magnético entre excitações derivadas do Fe e do Cr.

Este estudo explica a ausência de SC nas MnBFA como uma combinação de quebra de par magnético, desordem e correlações eletrônicas, enquanto nas CrBFA essa ausência é entendida como causada por quebra de pares magnéticos e supressão das flutuações de spin itinerante que promovem a SC. Esses resultados lançam luz sobre a complexa interação entre doping, magnetismo e correlações eletrônicas em FeSC e sistemas eletrônicos correlacionados em geral.

Palavras-chave: arseneto de ferro, RIXS, ARPES, correlação eletrônica, fases eletrônicas desordenadas

Contents

List of Figures

List of Tables

Chapter 1

Introduction

For strongly correlated materials, the interplay of spin, charge, lattice, and orbital degrees of freedom is known to be an important ingredient for the formation of quantum phenomena and different ground states. These degrees of freedom are described in terms of the concept of quasi-particles, which invoke particle-like properties of the low-lying energy excitations associated with the mentioned degrees of freedom. The resulting quasi-particles may interact among themselves. For instance, one speaks in terms of spin excitations and about how electrons, the charge degrees of freedom, interact with spin excitations. Another major coupling is the electron-phonon coupling, describing the coupling between electrons and the lattice degrees of freedom.

In the case of unconventional high-temperature superconductivity (HTSC) that appears for cuprates, iron-pnictides, nickelates, and heavy fermions, important ingredients that are believed to have a part in the Cooper-pair formation are [1, 2]: i) balance between localization and itinerancy of d (or f) electrons; ii) proximity to an antiferromagnetic (AF) order and magnetic fluctuations; iii) Fermi surface properties, nesting and topology; iv) bonding properties, including Hund's interaction, resulting spins, and bonding height and lengths.

To experimentally probe excitations and properties related to some of these ingredients, many techniques have been used over the years. In this work, the focus is to use a combination of Angle-Resolved Photoemission Spectroscopy (ARPES) and Resonant Inelastic x-ray Scattering (RIXS) to study transition metal substituted $BaFe_2As_2$, a prominent parent compound for Iron-based superconductivity (FeSC) [3].

The main features of FeSC are related to their multiband aspects. For instance, the most accepted order parameter symmetry of the superconducting state of most FeSC materials is the fully gapped s^{+-} gap symmetry. This is only possible for at least a two-band system wherein in each band the s-wave gap develops with an opposite phase sign than the other.

Additionally, Hund's interaction arises from the orbital-filling configuration, and it is believed to play a role in the different ground states in the FeSC phase diagram. In this regard, the electron-electron interaction, or electronic correlations, is believed to play a less prominent role when compared with Hund's interaction [4]. This is in contrast with the cuprates, where

the on-site Hubbard repulsion is the most important interaction, and for heavy-fermion materials, for which the Kondo coupling of the localized and itinerant electrons is the most important interaction.

The purpose of this work is to explore the non-superconducting sector of the phase diagrams in chemically substituted $BaFe_2As_2$. We focus on Mn and Cr substituted $BaFe_2As_2$, intending to investigate what impairs the formation of superconductivity in these materials and to contribute to the discussion about the HTSC mechanism.

In this regard, previous optical conductivity experiments explored the differences between these two substitutions and Co-doped $BaFe_2As_2$ [5], revealing the drastic decrease of Drude coherent peaks for both Mn and Cr substitution and larger impurity derived peak response for the Mn case. ARPES experiments were performed for the low Mn substitution range before [6] but with low resolution in momentum and energy. No trend of the electronic structure was discussed as a function of Mn. RIXS results for low Mn content were also reported, evidencing the anisotropic damping of magnetic excitations with Mn introduction [7]. $BaCr_2As_2$ was investigated by ARPES, revealing very sharp spectral weight lines associated with the energy bands, and a Fermi surface structure different from the one for $BaFe_2As_2$, with no electron pockets.

Nevertheless, no study so far has combined ARPES and RIXS for probing different doping levels of either Mn or Cr phase diagrams. Based on theoretical predictions, the results here presented can shed light on some proposed explanations for the absence of superconductivity in these materials. Consequently, is possible to elucidate the main ingredients that are relevant for the HTSC formation.

R. M. Fernandes et al. [8, 9] explain the absence of a superconducting ground state by a combination of Néel fluctuations and magnetic pair-breaking impurity scattering for the case of Mn substituted system. The Néel fluctuations have a (π, π) symmetry and would compete with the Fe-Fe spin fluctuations of $(\pi, 0)$ symmetry, that supposedly allow the formation of the s^{+-} state. M. N. Gastiasoro et al. [10, 11] explain the absence of superconductivity for the Mn-substituted system due to a cooperative behavior of the magnetic impurities through the RKKY interaction mediated by conduction electrons. This interaction, in the presence of electronic correlations, would result in the drastic reduction of superconductivity transition temperature T_c and would explain the formation of cluster order of the Mn impurities. Therefore, a combination of disorder, magnetic impurities, and electronic correlations would suppress the HTSC. This picture highlights the importance of impurity effects and their interaction with conduction electrons, more than just acting as magnetic scatterers.

D. S. Inosov et al. [12] suggested the existence of a Griffiths-type phase for the Mn substituted samples, consisting in the formation of antiferromagnetic rare regions without orthorhombic distortion, starting from the 12% Mn samples. In this phase, there would be a coexistence of paramagnetic regions and locally ordered clusters, resulting in the observed glassy behavior of the Mn local spins. The formation of a spin glass would be expected when putting together interacting magnetic impurities that are randomly localized, however, the Griffiths-type phase

is not the only explanation for this behavior, and the investigation of a quantum critical point in the phase diagram would be necessary to benchmark the existence of this phase.

The results here presented point in the direction that, although Mn and Cr substitutions would act as hole dopants, the effective doping is different for both cases. The ARPES results show this difference in effective hole dope and also in band coherence for these two materials, with evidence of cluster order only for the Mn case. The absence of SC in MnBFA is explained as a combination of magnetic pair-breaking, disorder, and electronic correlations, following what is predicted by the Gastiasoro picture, while in CrBFA this absence is understood to be caused mainly because of magnetic pair-breaking and suppression of the itinerant spin fluctuations which promote the SC, agreeing with Fernandes picture. These results help to understand the complex interplay between doping, magnetism, and electronic correlations in iron arsenides.

In Chapter 2 a review of the materials properties and phase diagrams is presented, with an explanation for different achievable phases and the characterized properties of the samples used in this study. In Chapter 3 the ARPES technique is explained in the theoretical and experimental aspects, along with the ARPES experimental methods for the results presented afterward. In Chapter 4 the ARPES results for the Mn substituted samples are presented, with analysis of Mn introduction and temperature effects, and spectral analysis. The results are discussed in context with a previous RIXS experiment. In Chapter 5 the results for the slightly Cr-substituted samples are presented, with the respective spectral analysis. In Chapter 6 the ARPES results for $BaCr_2As_2$ and $Ba(Fe_{0.515}Cr_{0.485})_2As_2$ are presented. For the former, a complete spectral analysis was performed for all the bands, which are very well resolved, while for the latter RIXS results are presented and discussed. Finally, in Chapter 7, all the main results are discussed together with the final remarks, conclusions, and outlook.

Additionally, there is an Appendix A with an explanation of theoretical and experimental aspects of the RIXS technique along with the optical study and simulation for the design and operation of the RIXS spectrometer of IPE beamline, the first Brazilian RIXS beamline.

Chapter 2

$BaFe_2As_2$ properties and phase diagrams

High-temperature superconductivity is a broad and somewhat recent field of study. Its origin dates back to 1986, with a paper entitled "*Possible high T_c superconductivity in the Ba-La-Cu-O system*" [13]. In this work, the observed transition temperature to the superconducting state was 30 K. This was enough to create a research area since the mechanisms known at the time for the formation of a superconducting state dictate that it would happen at a much lower temperature. Besides, superconductivity in the Ba-La-Cu-O system was quite unexpected, because this type of material is an oxide and was known to be an insulator.

Since then, many compounds based on the presence of Cu in which high-temperature superconductivity (HTSC) appears were synthesized and characterized [14], even though complete theoretical descriptions to explain such behavior were still lacking. This class of materials is called cuprates or CuSC and a long list of literature has been published in the past years concerning experimental results, different techniques, density functional theory calculation, theoretical descriptions, etc for this family of materials [15–18]. The highest transition temperature T_c achieved for the CuSC so far is 164 K, reported in 1994 for the mercury-based compound $HgBa_2Ca_2Cu_3O_{8+\delta}$ under high pressure of 45 GPa [19].

Many attempts to reproduce high-temperature superconductivity in compounds based on other transition metals were made, but the transition temperatures were never as high as the ones from the cuprates.

Nevertheless, in the year 2008, a paper was published with the title *Iron-Based Layered Superconductor $La[O_{1-x}F_x]FeAs$ ($x = 0.05 - 0.12$) with $T_c = 26$ K* [20], where high-temperature superconductivity was firstly reported in iron-based materials, 22 years after the cuprates. It was expected that this new class of superconductors would help understand the behavior and origin of superconductivity in cuprates, however, it turned out to have its own different physics and mechanisms [21], which raised many more questions.

This class of materials is known as iron-based superconductors (FeSC), in which superconductivity appears upon chemical substitution or applied pressure. There are several parent compounds, with different unit cells and overall structure, but they all share in common a layer of Fe coordinated by a pnictogen (As, P) or a chalcogen (Se, Te). Such a configuration can be

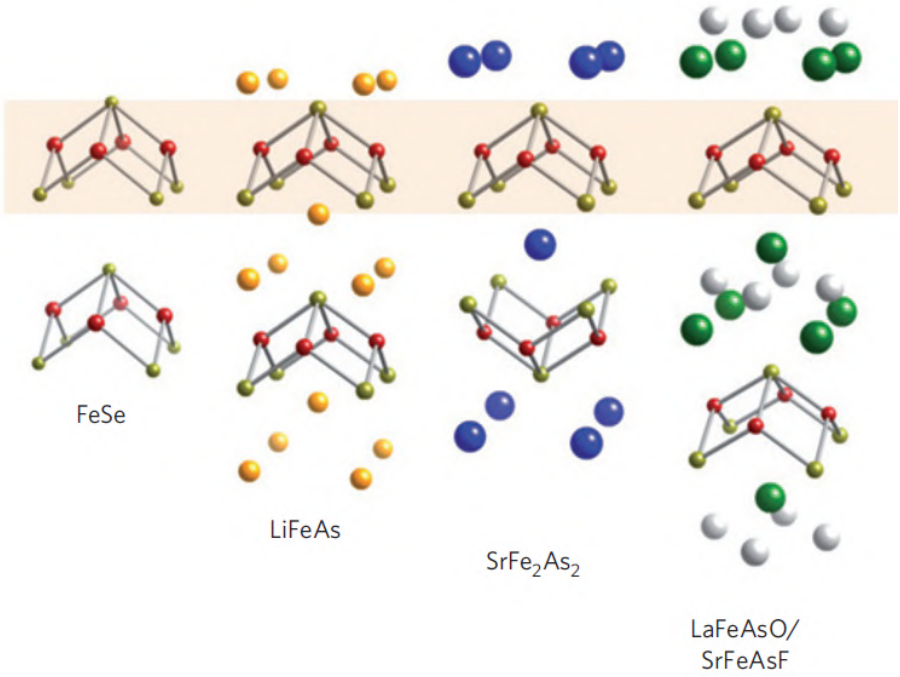

Figure 2.1: Structure for different types of parent compounds in the FeSC family of materials. From left to right: 11, 111, 122, and 1111 structure types. They all share in common a layer of Fe forming a square lattice that appears twice in the unit cell. From Ref. [22].

thought of as a corrugated plane, so this structure is basically 2D, as in the case of CuSC. This is illustrated in Figure 2.1. The FeSC are all classified by their stoichiometry and structure, for example, the RFeAsO, with R = rare earth is called 1111 materials, the EFe$_2$As$_2$, with E = alkaline metal or alkaline earth metal, are called 122 materials, the AFeAs with A = alkali metal are called 111 materials, etc. In this work, the focus is on the 122 family, with the parent compound BaFe$_2$As$_2$. More specifically, in the transition metal substituted samples, with putative hole doping and no superconducting dome. In the next sections, I'll further explain the properties of this parent compound, its phase diagrams, the different types of orders, and the expected effects on the electronic structure.

2.1 Phase diagrams for Ba(Fe$_{1-x}M_x$)$_2$As$_2$, M= Cr, Mn

The parent compound BaFe$_2$As$_2$ undergoes a spin density wave (SDW) phase transition at about 140 K [23]. This transition is followed by a structural transition from tetragonal to orthorhombic geometry, with a small orthorhombic distortion of about 0.5% [24]. The state in between is characterized as a nematic order.

In simple terms, the spin density wave (SDW) state is a magnetically ordered state that forms a spatial modulation of the spin density in metallic materials. It is fundamentally different from localized magnetically ordered states, such as ferromagnetism (FM) and antiferromagnetism (AFM), both in terms of its coupling mechanism and the importance of electronic states at

the Fermi surface (FS). In FM and AFM states, the exchange interaction between neighboring spins causes the spins to align in a preferred direction upon cooling, for a more energetically favorable configuration. In contrast, for SDW states (and charge density waves, which are analogous but involve charge instead of spin), the relevant interaction can arise from the nesting of the Fermi surface, with a characteristic interaction vector coupling different parts of the FS. The modulation of the spin density in the SDW state has a characteristic order vector defined by the new periodicity.

The nematic ordered state, by its turn, is a type of ordered phase that can occur in certain materials, particularly in liquid crystals. In a nematic ordered state, the long-range orientation is not fixed, but instead, there is some degree of directional order, with a preferred direction or axis of alignment. The nematic ordering does not involve a periodic arrangement of the atoms in the material. Instead, the ordering is typically more fluid and flexible, allowing the material to exhibit a range of interesting properties. In the case of FeSC, electronic nematicity refers to the spontaneous breaking of the rotational symmetry of the electronic states in the material. This means that the electronic states become preferentially aligned along one or more directions, forming a nematic order that is analogous to the nematic order observed in liquid crystals. The nematic order is speculated to be driven by a coupling between the electronic degrees of freedom and the lattice degrees of freedom. This coupling can give rise to a distortion of the lattice that breaks the rotational symmetry of the electronic states and leads to the observed nematic order.

In the $BaFe_2As_2$ phase diagram, the superconducting state can be achieved by multiple partial chemical substitution strategies [25–36]. A general phase diagram for the family of $BaFe_2As_2$ is shown in Figure 2.2. The substitution of Ba by K is called hole doping since it substitutes an atom for one with fewer electrons in the valence state. It results in the appearance of a superconducting transition for x up to $x = 1$, which means total substitution. On the other hand, the electron doping replacing Fe by Co presents superconductivity up to just about $x \sim 0.12$. That means that electron doping and hole doping are not equivalent when it comes to the formation of the superconducting pair in these materials.

SDW phase transition not only creates a magnetic periodic superstructure modulation in the material but is also accompanied by an orthorhombic structural distortion at a temperature slightly above the magnetic transition. This distortion is very small in a way that the lattice parameters can be approximated to the tetragonal phase ones. However, the whole crystal structure and magnetic lattices have rotational symmetry broken from C_4 to C_2. FeSC phase diagrams usually show a suppression of the SDW phase and it was believed that the instability of the SDW phase would be an ingredient to the unconventional superconductivity (SC), making the SDW fluctuations part of the pairing mechanism [38].

At the SDW phase, the smaller orthorhombic direction becomes ferromagnetic (FM) while the greater direction becomes antiferromagnetic (AFM), resulting in a stripe order as shown in Figure 2.3(a). This order also breaks the translational symmetry in the AFM direction, doubling the periodicity, which corresponds to folding in the reciprocal space illustrated in figure 2.3(b).

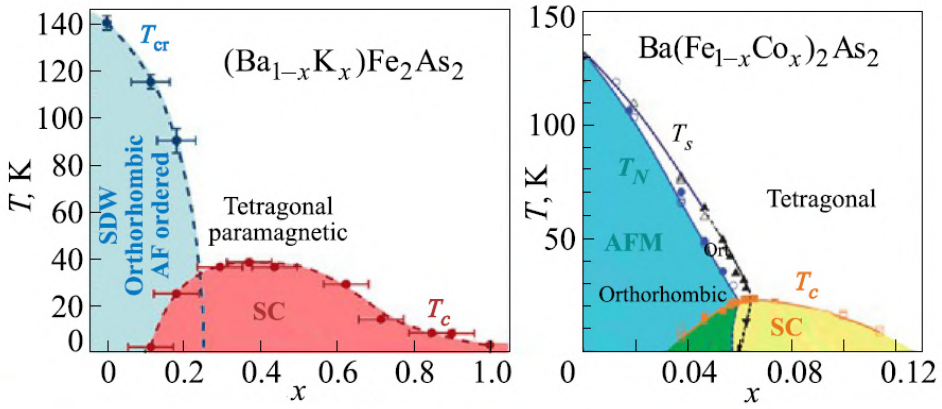

Figure 2.2: Phase diagram for the $Ba_{1-x}K_xFe_2As_2$ and $Ba(Fe_{1-x}Co_x)_2As_2$ samples as a function of x. The superconducting dome occurs in both hole (K) or electron (Co) substitution, but not in a symmetrical way. From Ref. [37].

Between the structural phase transition and the SDW phase transition, there exists a phase called nematic order [41]. Similarly to the SDW phase, the nematic order breaks the rotational symmetry. It is complicated to describe the order parameter for this phase since it is accompanied by other transitions. One of these transitions is the mentioned orthorhombic distortion, which is of structural/phonon origin, breaking the rotational C_4 symmetry down to C_2 without breaking the translational symmetry [40]. A second one is an orbital transition, presenting a break of degeneracy between d_{xz} and d_{yz} orbitals occupations, which is of electronic origin and implies an energy shift of both bands in opposite directions [42]. The third is the break of C_4 rotational symmetry for the static spin susceptibility $\chi(\mathbf{q})$, which becomes different for q_x and q_y directions even before the appearance of SDW divergence in the susceptibility. R. M. Fernandes et al. has described this problem as an "egg and chicken" problem [41] since all these transitions are intrinsically related to one another. They have argued that the nematic phase is electronic-driven using a Ginzburg-Landau free energy argument and with experimental evidence. The coupling to lattice degrees of freedom perturbs the idealized pure nematic transition, raising its expected critical temperature [2]. Even the electronic origin of the nematic transition, however, is still up for debate. It can be argued that the orbital degrees of freedom are responsible for the transition, with their interaction spontaneously lifting the degeneracy between d_{xz} and d_{yz} orbitals [43] and distorting the Fermi Surface. On the other hand, it can also be argued that the proximity to an antiferromagnetic instability, with stripe-like symmetry, beaks the rotational symmetry before the order takes place [44].

It is very challenging to separate both SDW and nematic influence on the band structure since their transition temperatures T_{nem} and T_{SDW} are very close and the structural, electronic, and magnetic properties are very similar in this small temperature range. Therefore, it is important to note that even with the SDW phase having some similar broken orders to the nematic phase, both phases are different mainly by the break of translational symmetry and the divergence in spin susceptibility $\chi(\mathbf{q})$ in the SDW phase.

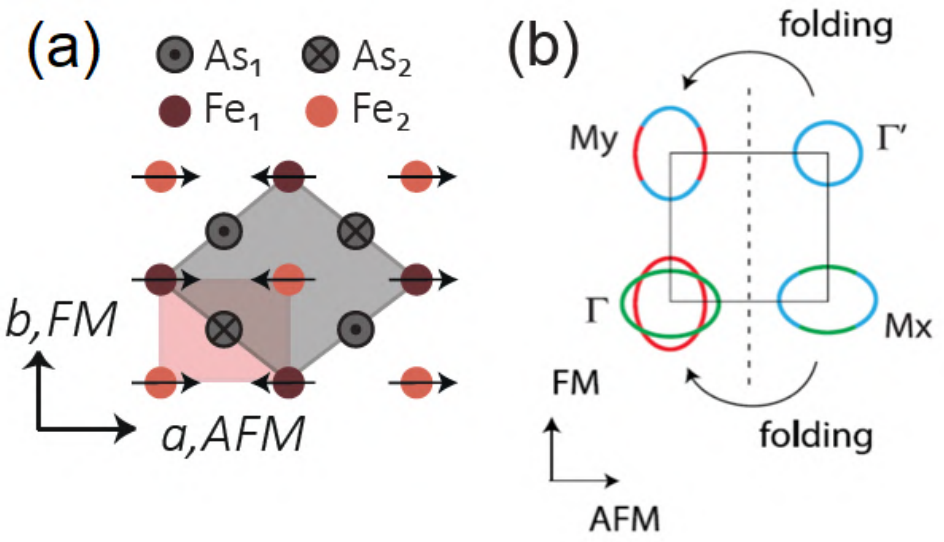

Figure 2.3: (a) Illustration of 2D Fe sublattice after the nematic transition and SDW transition. The red lattice corresponds to 1 Fe unit cell while the gray one corresponds to 2 Fe unit cell with As alternating between above and below Fe plane, from ref [39]. (b) Illustration of SDW band folding in the 1 Fe cell Fermi surface. The d_{xy}, d_{xz}, and d_{yz} orbitals are represented by the colors blue, red, and green respectively. Adapted from refs [39, 40].

With these considerations about the parent compound in mind, the attention can be turned to the phase diagrams of interest for this work. Among the possible strategies to achieve superconductivity, one that was largely explored was transition metal substitution [45, 35]. Systems with electron doping, such as Co, Ni, Cu, Rh, Pd, Pt, Au, Rh [26–29, 31–33], or isoelectronic substitution, such as Ru [34], present superconductivity. However SC is not observed in the cases of nominal hole doping with Cr [46, 47], Mn [6, 48–51, 5] or V [52]. Intriguing it is that for other substitutions, such as K, Rb, or Cs at the Ba site, superconductivity can be observed with hole doping [53–56]. This calls for speculation about the absence of SC in Mn and Cr substituted phase diagrams, which is the main purpose of this work.

The phase diagrams for the Mn and Cr substituted samples are shown in Figures 2.4, 2.5, and 2.6. In Figure 2.4, from Ref. [5], the differences between Mn substituted (MnBFA) and Cr substituted (Cr) samples are illustrated. For MnBFA the suppression of the SDW transition temperature T_{SDW}, forming the antiferromagnetic orthorhombic (AFO) phase, is almost linear up to 10% substitution. After, the orthorhombic distortion no longer takes place, making a crossover region of the phase diagram. For the CrBFA the T_{SDW} suppression seems to drop more rapidly for lower Cr concentrations and the orthorhombic distortion prevails for higher substitution levels.

To better understand the CrBFA phase diagram, the neutron diffraction study made by K. Marty et al. [46] can be inspected, which includes samples with x up to 0.47. Their phase diagram is illustrated in Figure 2.5 along with the ordered moment measured as a function of Cr concentration. The rapid drop of T_{SDW} for low Cr content is more evident here. For $x \gtrsim 0.3$, the average momentum drops to zero, indicating a G-type localized antiferromagnetic order.

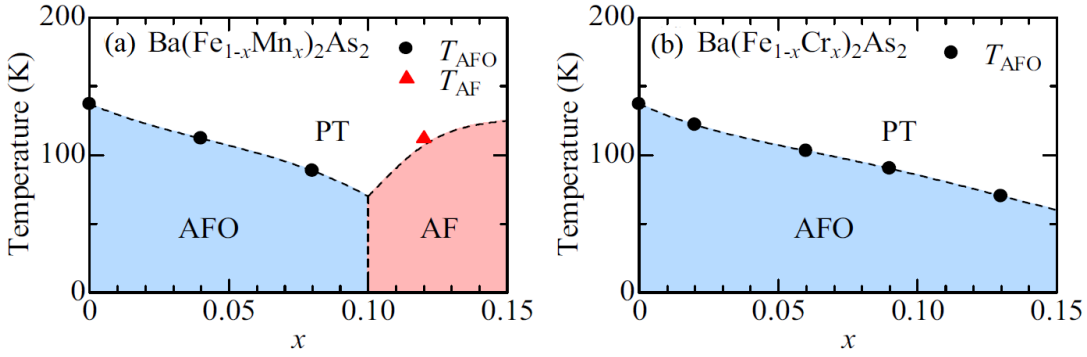

Figure 2.4: Phase diagram for the $Ba(Fe_{1-x}TM_x)_2As_2$ (*TM* = Cr, Mn) samples as a function of x. From Ref. [5], with data from Refs. [48, 46].

This is also the ground state for $BaCr_2As_2$ samples [57–60], indicating that after the crossover region of $x \sim 0.3$, the ground state must be the same for the rest of the phase diagram. Indeed, for $BaFeCrAs_2$ the ground state was found to have a G-type order and transition temperature of $T_N = 265$ K, while $T_N = 580$ K for $BaCr_2As_2$ [58].

It was speculated that $BaCr_2As_2$ could be analogous to $BaFe_2As_2$, due to the proximity of the Fe $3d^6$ and Cr $3d^4$ electronic configuration to half-filling [60]. Not only the transition temperature and degree of electronic correlation and localization are remarkably different, but also it is believed that the spins will be aligned along the c-axis for $BaCr_2As_2$, as is the case of $EuCr_2As_2$ [61]. For $BaFe_2As_2$ the SDW order is on the ab plane, with a strong influence of antiferromagnetic second neighbors super-exchange interaction [62], which is believed to play a role in the Cooper pair formation [2].

$BaMn_2As_2$, by its turn, has a localized antiferromagnetic order with $T_N = 625$ K [63–65] and it is believed that Mn substitution would continuously tune the system to the Mott insulator $BaMn_2As_2$ [66, 67]. A negligible band renormalization is expected for $BaMn_2As_2$ [65] and a DFT+DMFT study shows the importance of the Hund's exchange coupling J_H to achieve the insulating ground state [68].

In this sense, considering that Mn with a $2+$ oxidation state has five d electrons, a half-filling configuration would take place. Such configuration favors localization and it can be speculated that BaFeCrAs will also have, on average, five d electrons per Fe/Cr atom. Naively speaking, and disregarding random occupancy and disorder effects, the $x = 0.5$ CrBFA would be electronically equivalent to the Mott insulator $BaMn_2As_2$. An x-ray emission and absorption spectroscopy study have shown evidence of this increasing localization, pushing the system to a putative Mott insulator for x up to 0.47 [69].

However, such simplification can not be fully trusted. For the MnBFA samples, the theoretical scenario nowadays is more complex. The debate about this topic revolves around the relative relevance attributed to disorder, magnetic and impurity scattering, and the evolution of electronic band structure caused by Mn substitution. In this regard, it was theoretically predicted that a combination of disorder, magnetic impurities, and electronic correlations, sup-

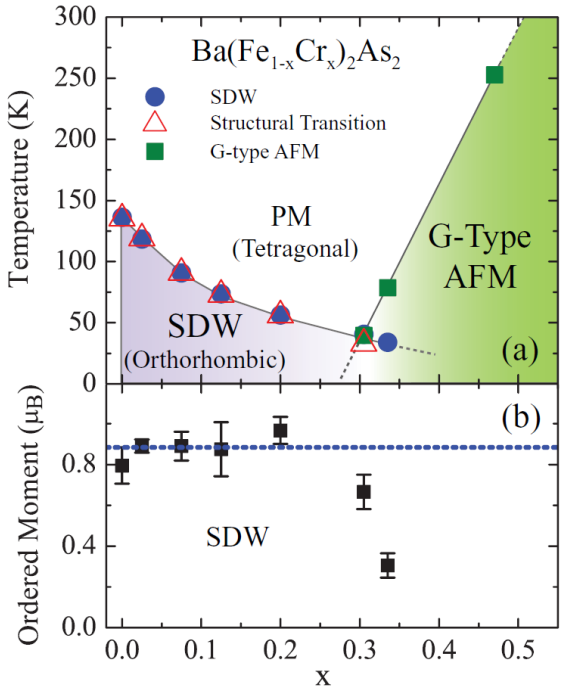

Figure 2.5: Phase diagram for the $Ba(Fe_{1-x}Cr_x)_2As_2$ samples as a function of x. The lower panel shows the average ordered Fe/Cr moment as a function of x in the ordered state obtained using the neutron diffraction technique. From Ref. [46].

presses HTSC [10, 11]. Although, the role of magnetic excitations promoted by the newly introduced spins and their symmetries can also explain the absence of SC [8, 70] and the detuning of the SDW nesting conditions can also be speculated to destroy an important interaction for the electron pair formation.

One of the main differences between the Mn and Cr phase diagrams, beyond the different substitution concentrations needed to fully suppress the SDW phase and the hindering of the orthorhombic transition, is the effective hole doping for these two systems. Some studies suggest that Mn does not introduce holes into the electronic structure [6, 51], while it was confirmed by Hall coefficient analysis extracted from resistivity measurements that holes are indeed introduced by Cr substitution [71].

For MnBFA substitution levels close to the mentioned crossover region, it was suggested the existence of a Griffiths-type phase [12], consisting in the formation of antiferromagnetic rare regions starting from the 12% Mn samples even above the T_{SDW} of the parent compound. In this phase, there would be a coexistence of paramagnetic regions and locally ordered clusters, resulting in a glassy behavior of the Mn local spins. The formation of a spin glass would be expected when putting together interacting magnetic impurities that are randomly localized. This is illustrated in Figure 2.6.

Considering all these differences and predictions, ARPES results will help to elucidate the doping mechanisms and degree of localization and correlation as a function of Mn and Cr content, as we shall see.

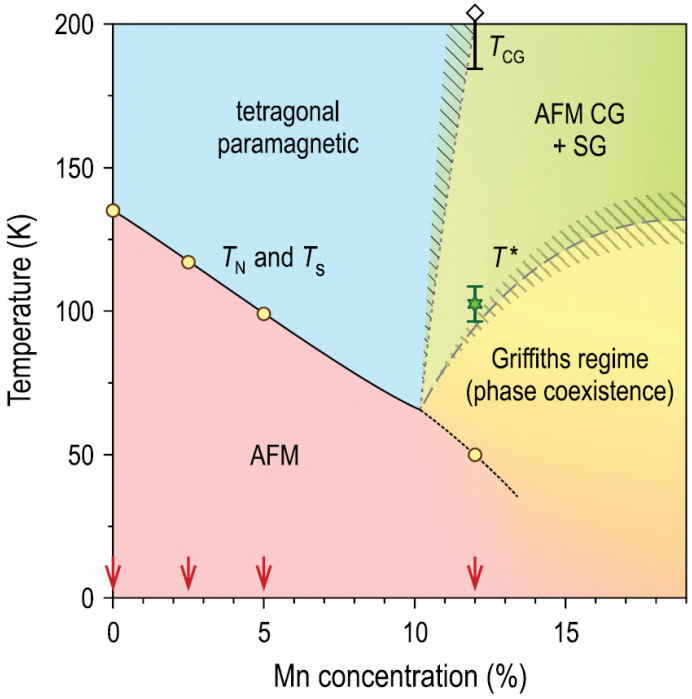

Figure 2.6: Phase diagram for the $Ba(Fe_{1-x}Mn_x)_2As_2$ samples as a function of x. The green-shaded region denotes the existence of spin glass (SG) fluctuation and cluster glass (CG) formation above the transition temperature. From Ref. [12].

2.2 $BaFe_2As_2$ crystal structure, reciprocal space and high symmetry points

$BaFe_2As_2$ (BFA) at room temperature has a body-centered tetragonal (bct) crystal structure with the symmetry of its base belonging to the $I4/mmm$ space group [72]. This is shown in Figure 2.7. However, since the electronic structure near the Fermi level is mainly composed by Fe derived contributions, it is also usual to interpret experimental data and to perform theoretical modeling based on the Fe unit cell, with a primitive tetragonal (pt) crystal structure rotated by $\pi/4$ from the BFA unit cell and lattice parameters multiplied by a factor of $\sqrt{2}/2$ in the directions $\mathbf{a}$ and $\mathbf{b}$ and by a factor of $1/2$ in the direction $\mathbf{c}$.

The reciprocal space primitive unit cell, known as Brillouin Zone (BZ), of both bct and pt lattices, are represented in Figure 2.8. As expected, the smaller lattice in real space will result in a larger BZ at the reciprocal space, as observed for the Fe pt lattice. It is important to notice that, at the reciprocal space for equally oriented tetragonal lattices, the M point in the pt BZ is at the same position as the X point in the bct BZ [72], this is the point where the electron pocket is located for BFA. As mentioned, the Fe pt lattice vectors are rotated by $\pi/4$ from the bct lattice. So their Γ-X and Γ-M directions will coincide as Figure 2.8 suggests, where only the pt lattice high-symmetry points are depicted.

All magnetism and most of the electronic structure for $BaFe_2As_2$ is originating from Fe atoms. The models based on Fe atoms are usually approximated by 2D square lattices since

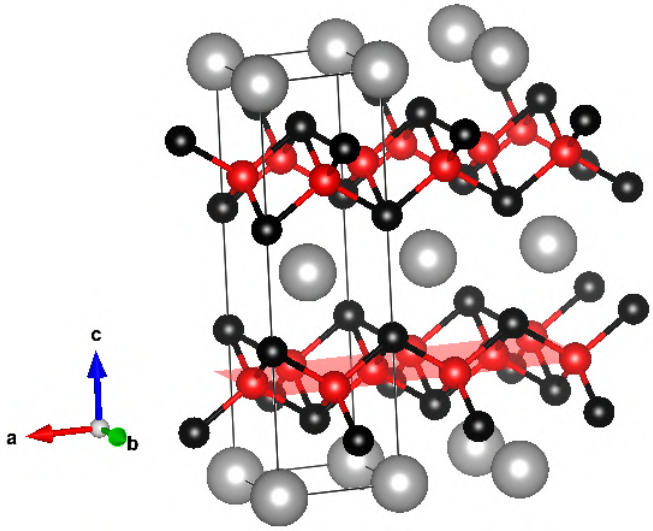

Figure 2.7: $BaFe_2As_2$ crystal structure at room temperature consisting of a body-centered tetragonal lattice with symmetry $I4/mmm$. The gray atoms represent Ba, while black is As and red is Fe. The iron plane is indicated by a red rectangle.

the inter-plane magnetic coupling is weak and the out-of-plane dispersion on the electronic structure can be neglected in some models.

The 2D square lattice has a square BZ with point X at (1,0) and M at (1,1) in units of π/a, as shown in Figure 2.9. The 1-Fe square unit cell will be rotated by $\pi/4$ from the bct unit cell, having the Γ-X and Γ-M directions coinciding with the 3D tetragonal lattice notation.

However, the high-symmetry point notation can become a little more complicated when we think in terms of the magnetic phase superstructure. Since the orthorhombic distortion is very small, it can be neglected in the SWD phase, which can be modeled in terms of the 2-Fe square lattice with the same basis vectors as the bct lattice. The reciprocal space of the 2-Fe square lattice will have half the area of the 1-Fe square lattice. This is understood in terms of folding in the reciprocal space. The point X at the 1-Fe square lattice will become the point M at the 2-Fe square lattice. This is shown with more details in Figure 2.9 and summarized in Table 2.1.

The 2-Fe square lattice is also referred to as folded. As mentioned, this is because the BZ for 2-Fe can be obtained by folding the corners of the 1-Fe BZ square to the Γ point. This can also be interpreted as translation symmetry operations that can unfold the 2-Fe to a 1-Fe Brillouin zone.

The reciprocal space folding occurs because the new lattice has 2-Fe atoms and has its periodicity multiplied by a factor of $\sqrt{2}$ due to the magnetic modulation. As a result, the reciprocal space will be reduced to half for the 2-Fe square lattice.

Also, when considering the alternating As atoms above and below the Fe plane, the full electronic orbital structure contributions from both Fe $3d$ orbitals and As $2p$ orbitals will be included only in the 2-Fe unit cell.

Table 2.1 was used to orient the experimental alignment for ARPES results in the next chapters. Since the sample is naturally oriented in its growth process by the **a** and **b** directions of the

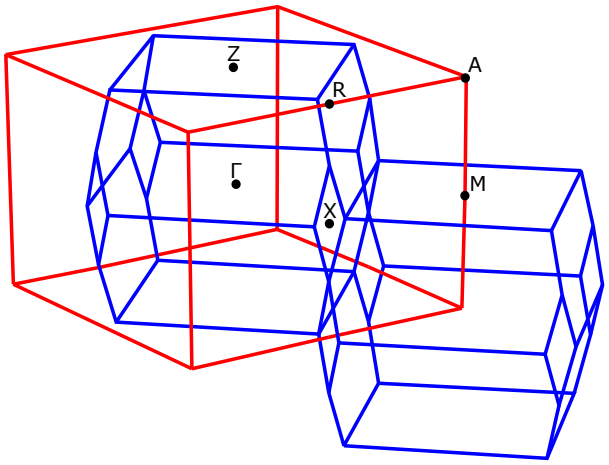

Figure 2.8: Body-centered tetragonal (blue) and primitive tetragonal (red) Brillouin zones. The primitive tetragonal unit cell corresponds to the Fe pt lattice, while the body-centered tetragonal unit cell corresponds to the BFA bct lattice. From ref. [73].

Dimension	3D		2D	
Lattice geometry	BFA (bct)	Fe (pt)	2-Fe (square)	1-Fe (square)
a (Å)	3.96	2.80	3.96	2.80
c (Å)	13.04	6.52	-	-
Basis Vector orientation	0	45°	0	45°
Sample aligned at 0°	Γ-M	Γ-M	Γ-X	Γ-M
Sample aligned at 45°	Γ-X	Γ-X	Γ-M	Γ-X

Table 2.1: The lattice parameters and lattice orientations for different types of 2D e 3D lattices used on literature to model the reciprocal space of FeSC. The basis vectors' orientation is in relation to the body-centered tetragonal (bct) basis vectors which also define the sample growth and sample orientation. The used lattice parameters are for the $BaFe_2As_2$ material.

bct unit cell, the sample positioned experimentally with the azimuthal angle equal to $0°$ (sample x-axis coinciding with the detector slit), and measured for its band structure horizontally, will be probed along the Γ-X direction for the 2-Fe lattice, which is equivalent to Γ-M in the other lattices as shown in 2.1. Similarly, a sample positioned experimentally with the azimuthal angle equal to $45°$, and measured for its band structure horizontally, will be probed along the Γ-M for the 2-Fe lattice, which is equivalent to Γ-X for the other lattices symmetry points notation.

In this work, the adopted notation is the bct structure, once the c-axis dispersion of the electronic structure will also be probed. In this notation, the BFA Fermi surface electron pockets will be at the X/Y points [72]. Since the sample properties are notation independent, is it important to stress that the electron pockets are always probed for the diagonal (sample aligned at $45°$) direction of the sample growth.

The samples studied in this work are $Ba(Fe_{1-x}M_x)_2As_2$, M =Mn, Cr. They were grown by the In-flux method as described in [74], by the Group of Optical and Magnetic Properties of Solids (*Grupo de Propriedades Ópticas e Magnéticas de Sólidos* - GPOMS) at the University of Campinas. This technique can be used to grow samples with different transition metal substitu-

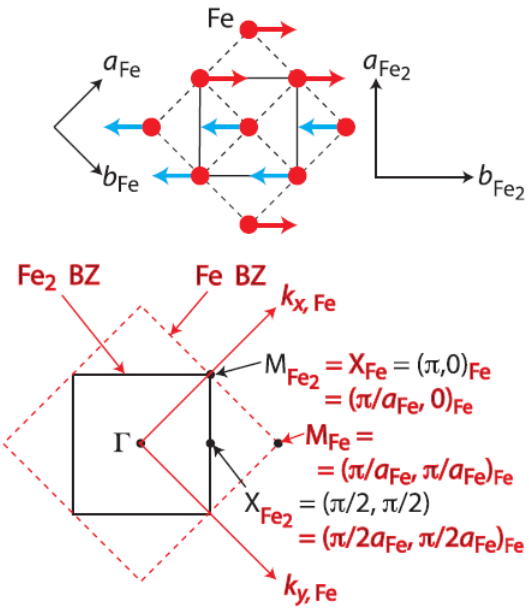

Figure 2.9: Real and reciprocal square lattices for 1 Fe unit cell and 2 Fe unit cell. The dashed lattice and red symmetry points refer to unfolded BZ. The solid line and black points refer to folded BZ. From ref. [72].

Batch	Dopant	x	Short name	a (Å)	c (Å)	T_{SDW} (K)	T_{AF} (K)
PGJ009	-	0	BFA	3.9587	13.035	134	-
PGJ589	Cr	0.03	Cr3%	3.95247	13.04303	109	-
PGJ761	Cr	0.085	Cr8.5%	3.97124	13.21435	79	-
PGJ762	Cr	0.485	BFCA	4.01449	13.34905	-	265 [58]
PGJ763	Cr	1	BCA	3.95228	13.63006	-	580 [58]
PGJ808	Mn	0.035	Mn3.5%	3.969215	13.13315	99	-
PGJ807	Mn	0.075	Mn7.5%	3.9402	13.0201	80	-

Table 2.2: Characterization table of the Mn and Cr substituted $BaFe_2As_2$ samples.

tions, by adjusting the heat treatment for each substitution to maximize the metal incorporation. The resulting crystals have the form of shiny platelets with dimensions of about $2.0 \times 2.0 \times 0.05$ mm^3.

With the use of several characterization techniques, such as Electron Spin Resonance (ESR), x-ray powder diffraction, electrical resistivity, and magnetic susceptibility, the quality of the samples was verified. The results showed no sign of bulk In incorporation, a lower concentration of defects, and the general high quality of the samples. The characterization performed by GPOMS is summarized in Table 2.2 for the x range. The transition metal proportion x for the samples of interest is presented in the notation $Ba(Fe_{1-x}M_x)_2As_2$.

Compared with other common methods such as self-flux and Sn-flux, the In-flux samples have shown a comparable or higher quality. The Sn-flux method has shown Sn incorporation, which is a disadvantage, despite the larger crystals resulting from this method. On the other hand, self-flux samples can present stoichiometric variations from 122 due to the excess of

FeAs.

2.3 Normal state and SDW phase band structure for $BaFe_2As_2$

The Fermi Surface (FS) of most of the iron pnictides, as is the case for $BaFe_2As_2$, consists of electron pockets at the X/Y points of the BZ and concentric hole pockets at the center of the BZ, at point Γ. The SDW order vector is $\mathbf{Q}_{\text{SDW}} = (\pi, 0, \pi)$ or $(0, \pi, \pi)$ and it is believed that this type of fluctuation is the origin for s^{+-} SC state [75].

Theoretically, for all iron arsenides, the Fe-As layers can be used to model the band structure in simple phenomenological models, such as tight-binding. Also, density functional theory can be used to calculate the band structure from first principles within some approximations. It was found theoretically, employing Hartree-Fock calculations, that the interaction between two electron pockets of the Néel type, $\mathbf{Q}_{\text{SDW}} = (\pi, \pi, 0)$ compete with $\mathbf{Q}$ and can be stabilized, but it has higher energy than the SDW ground state [76, 77].

It calls for speculation, once the $BaMn_2As_2$ has an insulating antiferromagnetic state, where Néel interaction is present along the Mn substituted BFA (MnBFA) phase diagram. Therefore, one can expect that Néel fluctuations would become energetically favorable, and that localization will play a role to suppress the metallicity.

It was predicted and experimentally confirmed that the tetrahedral crystal field in which Fe atoms are located inside $BaFe_2As_2$ structure makes the Fe t_{2g} orbitals (d_{xy}, d_{xz} and d_{yz}) slightly above the e_g orbitals (d_{z^2} and $d_{x^2-y^2}$). The electronic band structure at the Fermi level will be mostly dominated by the t_{2g} orbitals [39]. In the simplest model, the FeSC electronic bands derive from Fe $3d$-states that are subjected to the effects of the As ligands, which break the Fe $3d$-states degeneracy and instill a strong orbital character to the electronic bands [3, 2].

The three hole pockets at Γ and two electron pockets at X/Y are mainly composed of Fe d_{xz}/d_{yz} orbitals, hybridized from the four-fold rotational symmetry of the crystal lattice, and also from d_{xy} orbital. This is shown in Figure 2.10, which is based on a five orbitals model for LaFeAsO compound and is qualitatively the same as the one for $BaFe_2As_2$ [3].

A Spin Density Wave (SDW) is a low-energy ordered state that appears in solids. It appears in low temperatures of low-dimensional materials and consists of the formation of a superstructure with a periodic modulation of the density of spins. This superstructure has a periodicity $\boldsymbol{q}$, which can be observed with the use of the neutron diffraction technique or extracted from susceptibility measurements. If the periodicity $\boldsymbol{q}$ is a multiple or a rational fraction of the lattice constants, the SDW is termed commensurate. If it is an irrational multiple or fraction, it is called incommensurate.

However, when we think about the nematic splitting of electronic bands and SDW folding, the effects on the resulting electronic bands in the ordered state are a little complicated. On top of that, there is also the SDW gap opening which is highly orbital-dependent and difficult to observe experimentally, due to the multi-band aspect of the electronic band.

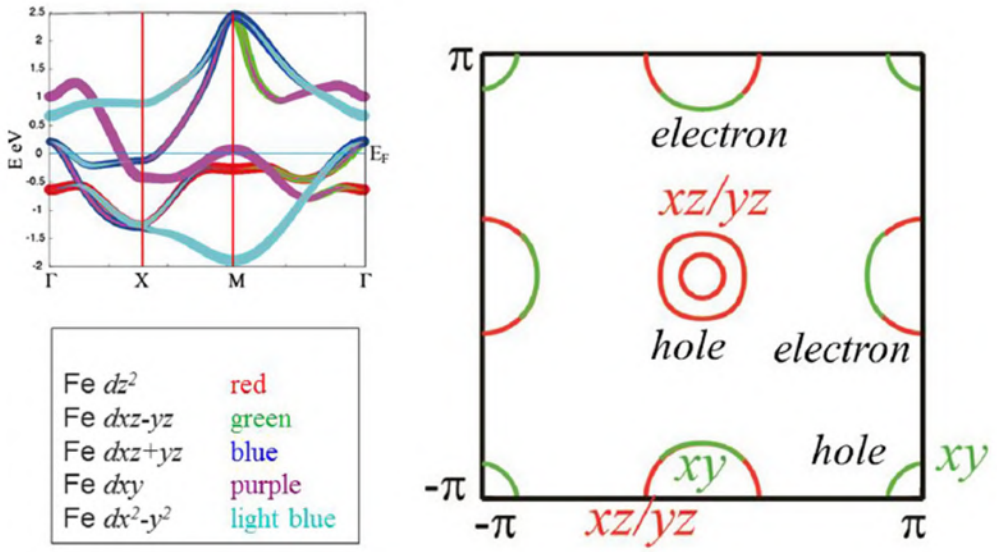

Figure 2.10: Orbital contribution to the hole pockets at Γ and electron pockets at X/Y for FeSC in the 1 Fe (unfolded) BZ. The C_4 rotational symmetry is present by considering d_{xz} equivalent to d_{yz}. From [3].

In Figure 2.11 it is possible to observe a tight-binding model describing $BaFe_2As_2$ electronic bands and their orbital composition at the normal state. As expected, there are three hole pockets at Γ and two electron pockets at X/Y with a symmetry between the Fe-derived $3d$ orbitals d_{xz} (red) and d_{yz} (green).

The nematic state, as discussed before, presents a symmetry break between d_{xz} and d_{yz} orbitals, with energy splitting shifting both orbitals in different energy directions. The arrows at the middle panel in Figure 2.11 illustrate such a shift, with the original bands as dotted lines and the shifted bands as full lines. The effect in the hole pocket at Γ is small, with one of the bands being pushed at the Fermi energy level. The effect is more pronounced in the electron pockets, with one of the electron pockets shifted up out of FS for the XZ and ΓY directions. The resulting FS has one less contribution in the horizontal direction to the electron pockets and an enlargement of the ZY electron pocket in the vertical direction.

As explained in the previous sections, the Brillouin Zone can be folded to change between different representations and periodicity of the crystal structure. However, such a folding can also be employed to model the increasing periodicity of a magnetically ordered state. Therefore, the SDW ordered state can also imply a folding, achieved by folding XZ and ΓY in half into themselves and folding YZ into ΓX, as shown in figure 2.3(b). The resulting electronic bands are shown in the lower panel of Figure 2.11 with the ticker lines corresponding to the original shifted bands of the nematic phase and the thinner lines showing the folded bands. From this, we can see that the experimental observation of those electronic bands can be extremely challenging. Even with enough instrumental resolution to separate the bands' contributions, the band assignment is quite tricky. Heike Pfau et al. [42] have done it in their work with the parent compound $BaFe_2As_2$ for the paramagnetic and SDW states. The comparison between

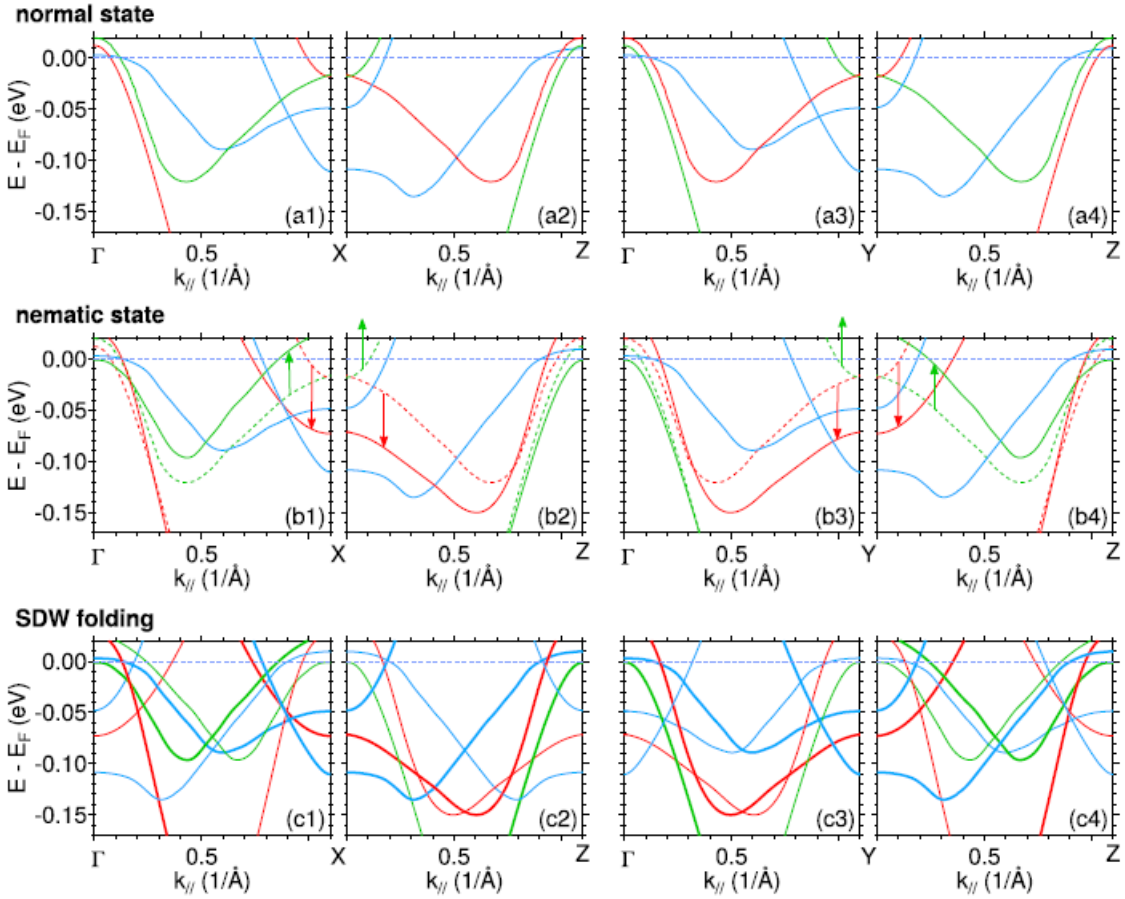

Figure 2.11: Resulting electronic bands for $BaFe_2As_2$ calculated from a tight-binding model for the 1 Fe unit cell in the normal state and manipulated to depict the nematic and SDW states. The X, Y, and Z points here correspond to the M_y, M_x and Γ' in figure 2.3(b) and the color codes for orbitals are the same with the d_{xy}, d_{xz} and d_{yz} orbitals being represented by the colors blue, red and green respectively. The nematic phase is achieved by the shift in opposite directions of bands d_{xz} and d_{yz}. The SDW folding is achieved by folding XZ and ΓY in half into themselves and folding YZ into ΓX. No SDW gap effect is considered here. From ref [42].

both states permitted them to perform a band assignment. However, it showed some differences with the model because the gap opening was disregarded.

Ming Yi et al. have shown in their review paper [40], that the SDW gap opening is orbital dependent and can be quite large for $BaFe_2As_2$. The largest one occurs for the d_{xy} orbital at the Y point and is larger than 50 meV. This gap results in the total absence of a d_{xy} contribution in the Y electron pocket since the electronic contribution does not cross the Fermi level. The same does not occur for the X electron pocket. The second-largest gap opening occurs for the d_{yz} orbital at the X point in the vertical direction of the BZ. This gap is of the size of about 30 meV and it is not large enough to push the electron and hole pockets out of FS.

As a result of SDW band folding and isotropic orbital dependent gap opening, the Fermi Surface topology at the ordered state not only will have the symmetry between d_{xz} and d_{yz} orbitals broken but also the d_{xy} contribution can appear at one electron pocket and not at the other, changing the orbital weight beyond the polarization selection rules, as it will be explained

in Section 3.1.4.

This will be further discussed when interpreting the orbital contribution to the Fermi surface of the MnBFA and CrBFA samples, with an electronic structure much closer to the parent compound BFA. The effects of Mn and Cr introduction were explored mainly with the use of ARPES, as will be explained in the following chapter.

Chapter 3

Angle Resolved PhotoEmission Spectroscopy (ARPES)

Immediately after the discovery of Iron-based superconductors (FeSC), there was a high number of theoretical and experimental research groups investigating the electronic structure and Fermi Surface (FS) of some compounds of this family employing Angle-Resolved PhotoEmission Spectroscopy (ARPES) [78–80, 6].

ARPES is a technique that permits direct access to the energy-momentum relationship of electrons in a material, which is known as its electronic band structure, exploring the photoelectric effect. A soft-energy X-ray beam hits the sample, and then an electron analyzer detects the number of emitted electrons as a function of energy and angle, making it a photon-in electron-out technique. The angular degree of freedom and its resolution in the experiment permits to access a wide range of the Brillouin Zone in the momentum space.

By analyzing the energy and momentum of the ejected electrons, ARPES can reveal the shape and dispersion of the energy bands, as well as the locations of band gaps and Fermi surfaces. This information can provide insight into the fundamental physical properties of a material, such as its electronic conductivity, magnetic behavior, and optical properties. The measured energy bands permit to perform analysis of band renormalization and effective mass relation by resolving the bands, and the lineshape allows the extraction of the single-particle self-energy related to each band.

ARPES is widely used in materials science and condensed matter physics and has applications in the development of new materials for electronic and optoelectronic devices. It is also used in the study of surface chemistry, where it can be used to investigate the interaction of molecules with surfaces and the electronic structure of thin films and interfaces, for example.

In the case of superconducting materials, it is possible to extract the superconducting energy gap from the Energy Distribution Curves (EDCs). One of the most important results in this aspect is the symmetry of the gap at the reciprocal space, which is reminiscent of the symmetry of the energetic favorable Cooper pairing. Indeed, the experimental study of the SC gap can support or discard a theoretical scenario for the SC mechanism.

Among the most important ARPES results for the FeSC materials in the first years of their discovery, we can list [81]:

- the multi-band aspect of the band structure, consisting of different contributions of the $3d$ orbitals from Fe;
- the presence of several electron and hole pockets in the FS;
- a more prominent 3D aspect to the electronic structure than in the case of cuprates;
- the symmetry of the order parameter is in general isotropic, characterized with s^{+-} symmetry.

In this regard, light polarization can be used to separate different orbital contributions to the band distribution [40]. Through the matrix elements formed by the initial and final states of the photoemission process, we can observe which orbital contribution will appear for each polarization, as we shall see.

In this chapter, I will cover the basic theoretical and experimental concepts behind the realization and analysis of an ARPES experiment. The results for the 122 $Ba(Fe_{1-x}Mn_x)_2As_2$ $Ba(Fe_{1-x}Cr_x)_2As_2$ samples will be presented along with self-energy and band character analysis in the following chapters.

3.1 Fundamentals

In an ARPES experiment, electrons are detected by an electron analyzer, a device that can focus an incoming beam of electrons to a slit and then deflect it in a semi-circle, using the potential lens effect, and make it hit the detector with different positions as a function of kinetic energies. The concept so far is the same as Photoemission spectroscopy (PES), with which we can measure the binding energies of electrons in the material by photoelectric effect intensity.

The Angle-Resolved part comes from having an analyzer with angular acceptance in the slit and an area detector. It permits the formation of an image of detected electrons intensity as a function of both energy and angle. This angle is related to the electron pre-emission momentum. To do so, however, the sample must be a single crystal with its alignment previously known by other methods. As we shall see, the detected intensity can be associated with the electronic band structure of the material and the Fermi surface (FS) can be reconstructed by those measurements.

As a consequence of photoemission, a hole is created in the solid. Theoretically, the creation of this photohole and its relation to ARPES can be described by the spectral function, also called the one-electron removal function.

However, simply measuring the electronic band structure and Fermi surface using ARPES may not be enough to understand the origin and mechanisms responsible for different ground

states in quantum materials, where strong electron correlations, electron-phonon coupling, and different phenomena can be present. For this, theoretical models and calculations can be helpful to utilize ARPES results' full potential.

3.1.1 Photoemission process

ARPES is a photon-in electron-out technique since it is based on the photoelectric effect. The monochromized light incident on the sample, with energy $h\nu$ in the region of soft x-rays, is absorbed by an electron. When the energy is greater than a characteristic work function ϕ, the electron is emitted with kinetic energy following equation 3.1, a well-known equation for the photoelectric effect.

$$E_k = h\nu - \phi \tag{3.1}$$

A more evolved theoretical description of the ARPES process includes the sample's many-body effects which are complex to describe. However, a complete approach can be achieved using quantum-mechanical perturbation theory to describe the transition rate. To do so, let us consider a Hamiltonian describing the electron on the solid plus the photon field as a weak time-dependent perturbation

$$\hat{H} = \hat{H}_0 + V_{\text{int}} e^{-i\omega t}, \tag{3.2}$$

where H_0 is the unperturbed Hamiltonian with known eigenstates and eigenvalues, and V_{int} is the photon field factor, given by:

$$V_{\text{int}} = -\frac{e}{mc}\mathbf{A} \cdot \mathbf{p}, \tag{3.3}$$

with $\mathbf{A}$ being the magnetic vector potential and $\mathbf{p} = \mathrm{i}\hbar\nabla$ the momentum operator. The expression for the photon field is deduced by considering a weak radiation field such that the two-photon process term proportional to $\mathbf{A}^2$ can be discarded, and adopting a choice of gauge to eliminate the scalar potential φ: $\nabla \cdot \mathbf{A} = 0$.

The transition rate from the initial state with N electrons to a final state with N electrons can be evaluated using Fermi's Golden Rule for a first-order perturbation as shown in equation 3.4 [82], where Ψ_i^N is the initial and Ψ_f^N is the final N electron states. The first term represents the transition matrix elements from the initial to the final state. The last term represents the energy conservation, where the final state energy E_f^N is equal to the initial state energy E_i^N summed with the absorbed photon energy.

$$w_{i\to f} = \frac{2\pi}{\hbar}\left|\left\langle \Psi_f^N \right| V_{\text{int}} \left|\Psi_i^N\right\rangle\right|^2 \delta\left(E_f^N - E_i^N - h\nu\right) \tag{3.4}$$

However, to include surface properties, which are fundamentally different from the bulk

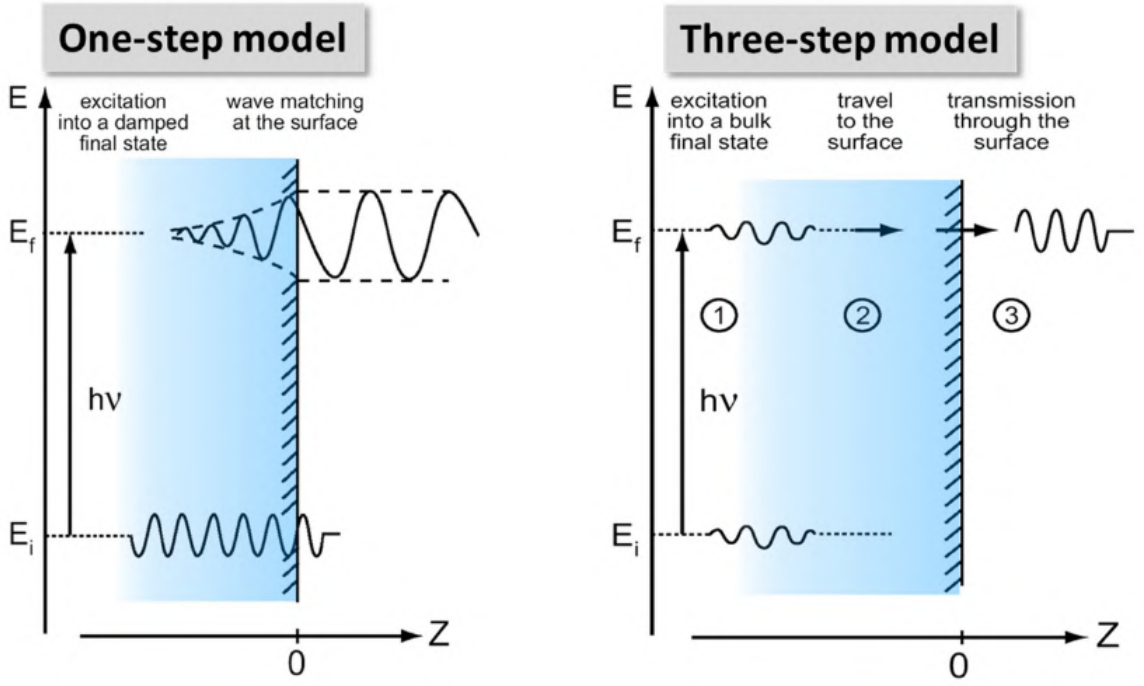

Figure 3.1: A comparison between one-step and three-step models for the photoemission process. Adapted from ref [84].

ones, the crystal Hamiltonian H_0 can become greatly complicated. Thinking of the photoemission process in this way is known as *one-step model*. One phenomenological model often used to describe this same process is the *three-step model* developed by Berglund and Spicer [83]. This model consists of breaking the photoemission process into three separate and independent processes: the bulk electron excitation by absorbing the photon energy, the transport of the electron from bulk to the surface, and the electron release into the vacuum. The comparison between one-step and three-step models is depicted in figure 3.1. The photoemission intensity will be defined by the product of the three processes probabilities. The second term can be described in a phenomenological way by the mean free path of the electron based on the internal scattering. It will be related to the penetration depth of the ARPES technique since bulk electrons deeper than the mean free path will hardly reach the sample surface. The third term can be described by the material surface energy barrier known as inner potential V_0, composed by work function ϕ and potential difference E_0 between the kinetic energy of an electron inside the crystal and at the vacuum. Therefore, all information regarding the electronic structure will be present in the first term.

Focusing on the first step, the ARPES intensity can be described by the transition rate from an initial to a final state both with N electrons. However, the creation of the photohole will imply different Hamiltonians and eigenstates in the final state. To avoid such complications, the *sudden approximation* is used. It consists of considering that the electron leaves the surface immediately after the excitation, not giving any time window to the relaxation process to interfere with the electron wavefunction. Therefore, instead of having a N electrons final state at the end

of the first step, the final state will have $N-1$ electrons and a free electron with wavefunction with momentum $\mathbf{k}$. The approximation is represented by equations 3.5.

$$\begin{aligned} \left|\Psi_f^N\right\rangle &\approx \phi_f^{\mathbf{k}} \left|\Psi_m^{N-1}\right\rangle \\ \left|\Psi_i^N\right\rangle &\approx \phi_i^{\mathbf{k}} \left|\Psi_i^{N-1}\right\rangle \end{aligned} \tag{3.5}$$

The final $N-1$ electrons state can be excited to different eigenfunctions $\left|\Psi_m^{N-1}\right\rangle$, where m is a set of quantum numbers containing all possible excitations of the final state [85], after the electron removal and before the decay. Therefore the total transmission probability will be given by the sum over m of all possible excited states.

The initial state fits into the sudden approximation if we consider it to be within the Hartree-Fock approximation, meaning that the total wave function can be written as a product of each electron wave function. Therefore, before the electron absorbs the photon energy, its state can be factorized from the total wave function.

With this, the transition matrix elements can be written as

$$\begin{aligned} \left\langle \Psi_f^N \right| V_{\text{int}} \left|\Psi_i^N\right\rangle &= \sum_m \left\langle \phi_f^{\mathbf{k}} \Psi_m^{N-1} \right| V_{\text{int}} \left|\phi_i^{\mathbf{k}} \Psi_i^{N-1}\right\rangle \\ &= \sum_m \left\langle \phi_f^{\mathbf{k}} \right| V_{\text{int}} \left|\phi_i^{\mathbf{k}}\right\rangle \left\langle \Psi_m^{N-1} \middle| \Psi_i^{N-1} \right\rangle \\ &\equiv \sum_m M_{i,f}^{\mathbf{k}} C_{m,i} \end{aligned} \tag{3.6}$$

where $M_{i,f}^{\mathbf{k}}$ is the one-electron transition matrix element and $C_{m,i}$ is the $N-1$ electrons state overlap integral. To calculate the total ARPES intensity, we need to integrate $w_{i\to f}$ for all i, j and it will be a function of the detected kinetic energy and momentum according to equation 3.7:

$$I(\mathbf{k}, E_k) = \frac{2\pi}{\hbar} \sum_m \sum_{i,f} \left|M_{i,f}^{\mathbf{k}}\right|^2 |C_{m,i}|^2 \, \delta\left(E_k + E_m^{N-1} - E_i^N - h\nu\right) \tag{3.7}$$

From this, we expect that if the electrons do not interact with each other, the removal of one electron would not affect the initial state, making $C_{m,i}$ coefficient equal to 1 for $m = i$ and zero otherwise. With electron interaction, the $C_{m,i}$ coefficient will represent a spectrum of weights for the photoemission intensity. Therefore, the *one-electron spectral function* can be defined as in equation 3.8. All the information regarding the sample electronic structure, which is the first step of the three-step model, will be included in this term.

$$A(\mathbf{k}, E_k) = \sum_m |C_{m,i}|^2 \, \delta\left(E_k + E_m^{N-1} - E_i^N - \hbar\nu\right) \tag{3.8}$$

However, temperature effects are not included in equation 3.7 for the ARPES intensity. A simplified way to account for such effects is to multiply the intensity by a Fermi-Dirac distribution function $f(E,T) = \left(e^{\frac{E}{k_B T}} + 1\right)^{-1}$, resulting in the most common expression for the ARPES intensity:

$$I(\mathbf{k}, E) = I_0(\mathbf{k}, \mathbf{A}) A(\mathbf{k}, E) f(E, T), \tag{3.9}$$

with E as the electron energy with respect to the Fermi level E_f and $I_0(\mathbf{k}, \mathbf{A}) \propto \sum_{i,f} \left|M_{i,f}^{\mathbf{k}}\right|^2$ as the transition matrix elements, which can be considered constant for a given geometry, but is also affected by the polarization and orbital spatial dependency, as we shall see in section 3.1.4.

It is important to remark that the equation 3.9 for the ARPES intensity does not account for experimental effects such as finite energy and momentum resolution. This model based on the three-step model and sudden approximation of Fermi's golden rule for the transition probability is somewhat limited due to the simplifications, but it permits us to understand the meaning of the resulting ARPES spectra. For quantitative analysis, other than phenomenological models, calculations based on the one-step model can be required to correctly compare theory and experiments.

3.1.2 One-particle spectral function and self-energy

From the equation 3.8 for the spectral function, the non-interacting picture ($C_{m,i} = 1$ for $m = i$ and 0 otherwise) would result in ARPES bands with no width whatsoever, that is, a delta function. Nevertheless, the electrons do interact, and the resulting ARPES spectra will always present a characteristic broadening of the lines. Following our formalism and within our approximation, the best way to approach this enlargement of band lines is by the use of Green's function [84].

The spectral function defined in equation 3.8 is connected to the single-particle Green's function by:

$$A(\mathbf{k}, E) = -\frac{1}{\pi} \operatorname{Im}(G(\mathbf{k}, E)). \tag{3.10}$$

Mathematically, a Green's function is defined as a solution to an inhomogeneous linear differential equation that results in a δ-type function. Physically, it is used to describe the time retarded response, or propagation, of an operator. The Green's function can always be expressed by an expansion of the operator eigenvalues. In the case of photoemission, the related Green's function will be defined by the one-electron removal operator from the N electrons system previously discussed, from which is possible to derive the spectral function by another method.

Additionally, to account for electron correlation effects, Green's function can be written in terms of the electron *self-energy* $\Sigma(\mathbf{k}, E)$:

$$G(\mathbf{k}, E) = \frac{1}{E - \epsilon_{\mathbf{k}} - \Sigma(\mathbf{k}, E)}, \tag{3.11}$$

where $\Sigma(\mathbf{k}, E)$ is defined as having a real part $\Sigma'(\mathbf{k}, E)$, related to energy renormalization when compared with a non-interacting system, and an imaginary part $\Sigma''(\mathbf{k}, E)$, related to the photoemission lifetime [82]. $\epsilon_{\mathbf{k}}$ is the electron band energy at a given $\mathbf{k}$. From this, the spectral function can be written as:

$$A(\mathbf{k}, E) = -\frac{1}{\pi} \frac{\Sigma''}{(E - \epsilon_{\mathbf{k}} - \Sigma')^2 - \Sigma''^2}. \tag{3.12}$$

By the conservation of energy, a detected photoelectron will have energy equal to its band energy summed with a self-energy factor when electron correlations are accounted for. Also, if the self-energy components are constant, the spectral function will have the form of a Lorentzian distribution with its full width at half maximum (FWHM) related to $2\Sigma''$ and center at $\epsilon_{\mathbf{k}} + \Sigma'$.

Since the self-energy components are complex to derive analytically, under some experimental conditions they could be estimated experimentally. However, in this case, the energy and momentum resolutions, neglected so far, become most important, because the resolution capacity to the line width is limited by the experimental resolution.

To account for these factors and the temperature effects, we need to multiply the spectral function by the Fermi-Dirac distribution as in eq. 3.7, and convoluted it by a 2D Gaussian with widths associated with energy and momentum resolution. Experimentally, it is usual to get the scattering rate Γ, associated with the imaginary part of the self energy Σ'' by a renormalization factor Z [86, 87]:

$$\Gamma = -2Z\Sigma''. \tag{3.13}$$

With this, the spectral function can be rewritten in terms of Γ, which is directly associated with experimental FWHM:

$$A(E, \mathbf{k}) = \frac{1}{\pi} Z(E, \mathbf{k}) \frac{\Gamma(E, \mathbf{k})/2}{(E - \epsilon^*_{\mathbf{k}})^2 + (\Gamma(E, \mathbf{k})/2)^2}, \tag{3.14}$$

where $\epsilon^*_{\mathbf{k}}$ is the renormalized particle dispersion. However, the experimental scattering rate may include terms that are not of a single particle, such as electron-phonon interactions and elastic scattering [87]. The elastic scattering by defects can be accounted as a constant background [88], in a semiclassical approximation. Otherwise, the elastic term dependency on E can be estimated as it relates to the band velocity as $\Gamma_{\text{el}}(E) = \Gamma(0)v(E)/v(0)$, where $E = 0$ refers to the Fermi energy.

For a simple Fermi liquid regime, we would expect that the renormalization function $Z = m/m^*$ is just a multiplicative constant, where m^* is the renormalized electron mass, and that the scattering rate would follow a quadratic behavior. However, for materials for which HTSC is present, the electronic behavior cannot be put into a simple framework. To explain the linear

in T resistivity for the cuprate superconductors it was proposed a marginal Fermi liquid (MFL) theory [89], where quantum critical fluctuations are related both to HTSC and to the linear in T resistivity [90], and the scattering of fermions in the presence of such fluctuations would result in a MFL.

In the MFL regime, the normalization function is energy dependent following the relation

$$Z_{\text{MF}}(E) = \frac{C_{\text{int}}}{1 + \lambda_{\text{MF}} \ln\left(\frac{E_c}{x}\right)}, \tag{3.15}$$

where $x = \max(|E|, k_B T) \approx [E^2 + (\frac{\pi}{2} k_B T)]^{\frac{1}{2}}$ and E_c is a cuttoff energy, C_{int} is an intensity multiplicative factor and λ_{MF} is a coupling constant that should be $\lambda = 1$ in a Planckian limit [91]. When $E >> k_B T$, x is linear in energy. For the MFL, the self-energy is given by

$$\Sigma_{\text{MF}}(E) = \lambda_{\text{MF}} \left[E \ln\left(\frac{E_c}{x}\right) + i\frac{\pi}{2} x \right]. \tag{3.16}$$

Therefore, for $E >> k_B T$, $\text{Im}\Sigma_{\text{MF}}$ is linear in energy for a MFL. From this equation, as every term is real and $\Sigma'' = \pi x/2$, we can express the Marginal Fermi Liquid Scattering rate Γ_{MF} in the case that Z_{MF} is not linear as:

$$\Gamma_{\text{MF}}(E) = -2 Z_{\text{MF}} \lambda_{\text{MF}} \frac{\pi}{2} x = \frac{\pi \lambda_{\text{MF}} x}{1 + \lambda_{\text{MF}} \ln\left(\frac{E_c}{x}\right)}. \tag{3.17}$$

The MFL model will be used in our self-energy analysis as a possible scenario for the electronic behavior for the 122 $Ba(Fe_{1-x}Mn_x)_2As_2$ and $Ba(Fe_{1-x}Cr_x)_2As_2$ materials. As we shall see, the Fermi Liquid response is not observed in our materials, justifying this approach.

3.1.3 Angle-resolved and momentum dependency of photoemission process

The ARPES spectrum is the intensity map as a function of momentum and binding energy for a given sample orientation. The binding energy is defined as a shift of the detected kinetic energy so that the Fermi energy E_F occurs when the binding energy E_B is equal to zero, as shown in equation 3.18. In this context, we can think of E_F as the minimum energy necessary to extract an electron from the material.

$$E_k = h\nu - \phi - |E_b| \tag{3.18}$$

The momentum dependency is associated with the angle of detection. The momentum parallel to the surface of the sample is conserved and this allows mapping the photoemission intensity as a function of parallel momentum and binding energy of the photoelectron. However, due to the media discontinuity in the perpendicular direction, the momentum will not be conserved.

This is illustrated in Figure 3.2.

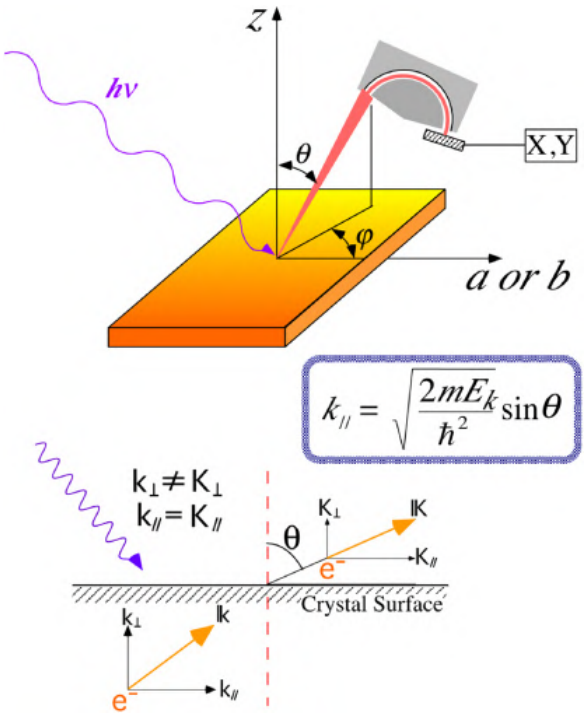

Figure 3.2: A schematic representation of an ARPES experiment with incident light of energy $h\nu$. The detector is positioned at a polar angle θ and azimuthal angle φ. The parallel to the sample surface projection of the detected momentum is shown in the blue box. $\mathbf{k}$ is the momentum inside the material, while $\mathbf{K}$ is the momentum at vacuum. From ref. [81]

$$E_K = \frac{\hbar^2 K^2}{2m} \tag{3.19}$$

The momentum of an electron inside the sample can be decomposed into parallel and perpendicular contributions $\mathbf{k} = \mathbf{k}_\perp + \mathbf{k}_\parallel$, where $\mathbf{k}_\perp = \mathbf{k}_z$ and $\mathbf{k}_\parallel = \mathbf{k}_x + \mathbf{k}_y$. Using the electronic dispersion for a free electron (eq. 3.19), which associates the kinetic energy to the momentum in the vacuum, it is possible to decompose also the electron momentum in vacuum $\mathbf{K}$ as stated by equations 3.20, where $K = |\mathbf{K}|$.

$$\begin{aligned} K_x = k_x &= \frac{\sqrt{2mE_k}}{\hbar}\sin\theta\cos\varphi \\ K_y = k_y &= \frac{\sqrt{2mE_k}}{\hbar}\sin\theta\sin\varphi \\ K_z &= \frac{\sqrt{2mE_k}}{\hbar}\cos\theta \end{aligned} \tag{3.20}$$

Here, θ is the polar angle and φ is the azimuthal angle, as shown in Figure 3.2. The analyzer slit takes a θ interval, so when $\varphi = 0$, the k_y value will be fixed and the measurement will be along k_x. The in-plane components are conserved, but the perpendicular, out-of-plane component is not. The k_z component can be deduced from the energy conservation, as shown

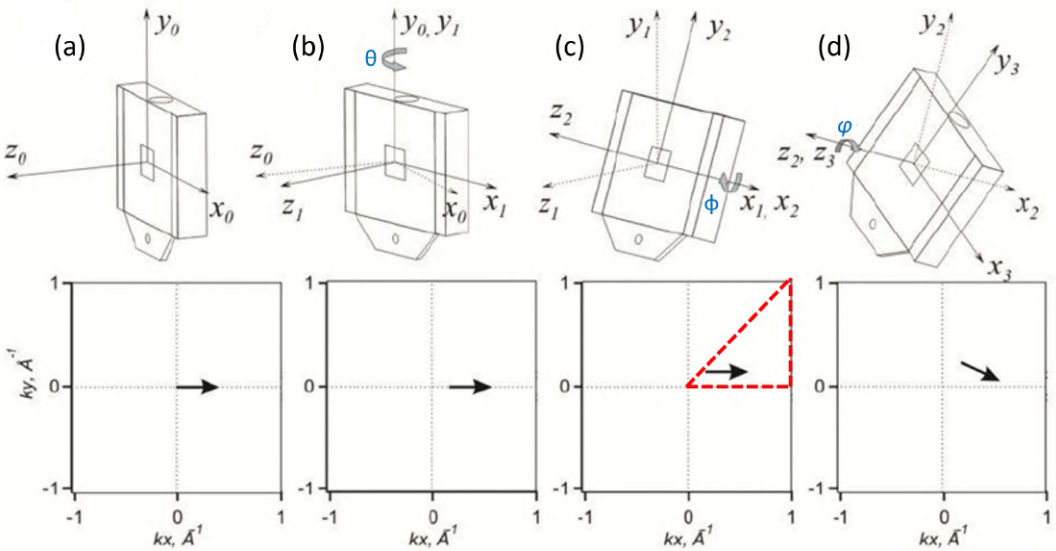

Figure 3.3: The rotational degrees of freedom for an ARPES experiment. The dashed red line marks a high-symmetry path $\Gamma X M \Gamma$. (a) At normal incidence, the momentum probed will be centered at the center of the BZ (Γ) and along the slit direction. (b) Rotating the polar angle θ changes the momentum center, without changing the high-symmetry direction. (c) Rotating the tilt angle ϕ changes the k_y probed value. (d) Rotating the azimuthal angle φ changes the sample direction being probed along the slit. Adapted from [92].

in equation 3.21: the inner potential V_0 has to be accounted for the electron leaving the material and be detected.

$$\begin{aligned} E_k + V_0 &= \frac{\hbar^2}{2m}(k_\perp^2 + k_\parallel^2) \\ k_\perp^2 &= (E_k + V_0)\frac{2m}{\hbar^2} - \frac{2m}{\hbar^2}E_k \sin^2\theta \\ k_\perp &= \frac{\sqrt{2m(E_k \cos^2\theta + V_0)}}{\hbar} \end{aligned} \tag{3.21}$$

Therefore, to characterize the full 3D Brillouin zone, one has to perform an ARPES experiment scanning for different angles to access different k_x and k_y values, as shown in equation 3.20 and illustrated in Figure 3.3. By changing the tilt angle ϕ it is possible to probe a k_x range for $k_y \neq 0$.

To perform the measurements along some different high-symmetry directions, the azimuthal angle φ is changed. In the case of a sample with 4-fold rotational symmetry, every $90°$ rotation will theoretically make no difference. So the other high-symmetry rotation different than $0°$ would be $45°$.

Additionally, it can be necessary to perform scans changing the incoming energy $h\nu$ to estimate the V_0 value necessary to identify the k_z high-symmetry points at the reciprocal space.

Nevertheless, some materials' electronic structure changes very little as a function of k_z. These are considered 2D materials when it comes to the Fermi surface, as is the case of the

cuprates. In the case of FeSC, although slightly, there is still some k_z dispersion.

3.1.4 Matrix elements and light-polarization effect on ARPES intensity

As shown previously, the ARPES intensity depends on the transition matrix elements, as the term $I_0(\mathbf{k}, \mathbf{A})$ is proportional to $\left|M_{i,f}^{\mathbf{k}}\right|^2$. Those matrix elements were defined in equation 3.6 as $M_{i,f}^{\mathbf{k}} = \left\langle \phi_f^{\mathbf{k}} \right| V_{\text{int}} \left| \phi_i^{\mathbf{k}} \right\rangle$, where $V_{\text{int}} \propto \mathbf{A} \cdot \mathbf{p}$ as defined in equation 3.3. This integral can be zero if the resulting integrand is an odd function with relation to the mirror plane, defined by the incoming light and the sample normal directions, as shown in Figure 3.4. It would result in no ARPES signal. So, to properly probe the electronic bands, the resulting integrand must be an even function with respect to the mirror plane. The incidence plane is defined by the incident light and detection direction, as shown as a transparent plane in Figure 3.4. The detector slit is positioned along the mirror plane.

The final state $\left|\phi_f^{\mathbf{k}}\right\rangle$ can be assumed to be a plane wave, which is always even. From this, the ARPES intensity will be non-zero if both the potential term V_{int} and the initial state $\left|\phi_i^{\mathbf{k}}\right\rangle$ are either odd or even simultaneously.

To analyze the parity of the potential term, we can write $\mathbf{A}$ as $A\hat{\varepsilon}$, with $\hat{\varepsilon}$ a unitary vector with the light polarization direction, supposing it is linearly polarized. Also, based on canonical commutation relations, $\mathbf{p}$ can be transformed into position $\mathbf{r}$. So the parity will be defined by the light polarization projection in the position space, meaning that we only need to look for the $\hat{\varepsilon}$ symmetry with respect to the mirror plane. If the polarization is parallel to the mirror plane, it is therefore even with respect to the mirror plane. This is defined as p or π light polarization. If the light polarization is perpendicular to the mirror plane, it will be odd with respect to the mirror plane. This is defined as s or σ polarization, as shown in Figure 3.4 [40, 42].

For the initial state parity, things are not so simple. Since the initial state is about the electron state at the material, it is basically about the orbital the electron is in. To illustrate, let us think about the d orbitals, most important for transition metals, such as Cu and Fe. If the sample is positioned with its x axis along the mirror plane direction (azimuthal angle $\varphi = 0$), the orbitals xy and yz will be odd whit respect to the x axis, while the orbitals z^2, $x^2 - y^2$ and xz will be even. From this, we can expect that the orbitals xy and yz will be detected only with σ light polarization while the orbitals z^2, $x^2 - y^2$ and xz will be detected only with π light polarization. Of course, if the sample has a four-fold rotational symmetry, the xz, and yz orbitals will be equivalent, resulting in a hybridization of the orbital weights to the ARPES intensity [93].

However, as we shall see, positioning the sample with azimuthal angle $\varphi = 45°$ permits to probe of a high-symmetry direction for square or tetragonal lattices. With this, the parity of the light polarization does not change, but the parity of the orbitals does. Now, the orbitals xy and z^2 are even with respect to the mirror plane, while the orbital $x^2 - y^2$ is odd. The orbitals xz and yz are neither even nor odd, so they will contribute to ARPES intensity for both linear light polarization, which will be termed as "mixed parity" here. These rules are illustrated in Table

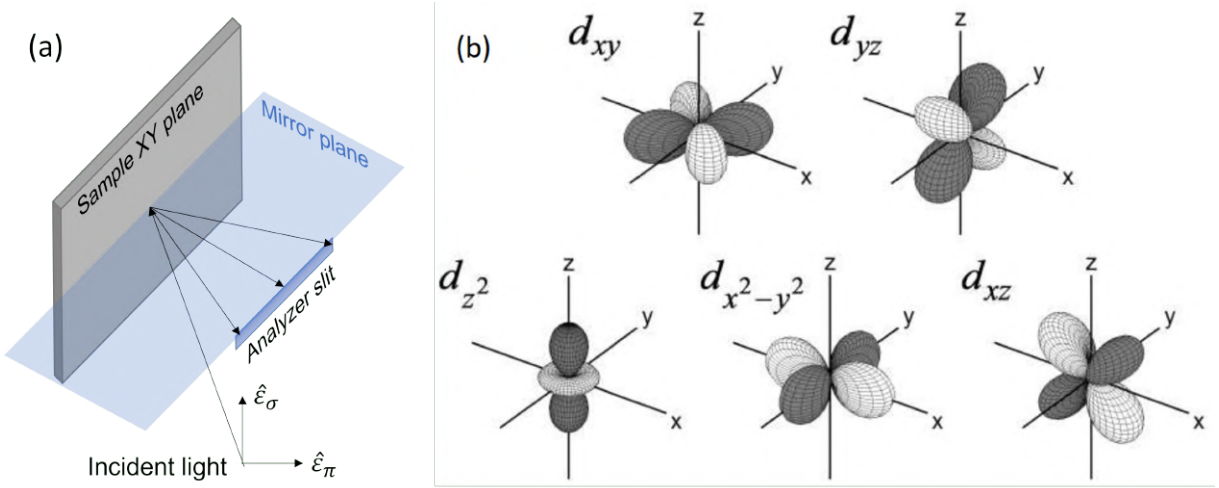

Figure 3.4: Illustration of orbital dependent ARPES intensity based on the transition matrix elements. (a) The mirror plane is defined by the incoming light and the sample's normal directions. (b) A representation of the d orbitals, which are relevant to the electronic and magnetic structure of the transition metals. The light and dark areas represent different phases for the orbital wave function.

3.1 for the $BaFe_2As_2$ derived materials. Several works have already presented this discussion [40, 42, 93–96], and they are the basis for the definitions considered here.

Pol.	Direction	$d_{x^2-y^2}$	d_{z^2}	d_{xz}	d_{yz}	d_{xy}
	Γ-X	x	x	x		
π-pol	Γ-M		x	m	m	x
	Γ-Y	x	x		x	
	Γ-X				x	x
σ-pol	Γ-M	x		m	m	
	Γ-Y			x		x

Table 3.1: Polarization and direction dependency of $3d$ orbitals contribution to the hole pockets at the Fermi Surface. The high symmetry directions are from the body-centered tetragonal structure of $BaFe_2As_2$. Yellow "m" represents mixed parity, while green "x" represents matching parity with polarization.

Nevertheless, these rules apply to the center of the Brillouin Zone and to a mirror plane defined as crossing this center. For these samples, due to the inequivalence of the As coordination, the mirror plane can be defined differently [95]. This will result in different polarization selection rules for the electron pockets. This is illustrated in Table 3.2. The polarization selection rules will be further discussed in terms of the ARPES results for the specific samples in the next chapters.

Pol.	e pocket direction	d_{xz}	d_{yz}	d_{xy}
π-pol	X-Γ	x		
	X-Y	m	m	m
	X-Z	x		x
σ-pol	X-Γ		x	x
	X-Y	m	m	m
	X-Z		x	

Table 3.2: Polarization and direction dependency of $3d$ orbitals contribution to the electron pockets at the Fermi Surface. The high symmetry directions are from the body-centered tetragonal structure of $BaFe_2As_2$. Yellow "m" represents mixed parity, while green "x" represents matching parity with polarization.

3.2 Instrumentation

The instrumentation for performing ARPES includes the x-ray source, the sample environment in ultra-high vacuum, and the electron analyzer, as will be discussed. Apart from the environment, the sample holder must have position and angular degrees of freedom to align it with the photon beam and to scan different k-space points.

The X-ray source doesn't need to be a synchrotron, usually, it is a helium lamp or a laser with emitted energy of a few eVs. However, the use of a synchrotron enables one to perform measurements in particular conditions that are inaccessible at the usual table-top ARPES setup. The synchrotron properties and components are explained in Appendix A.

The energy tunability provided by a synchrotron source permits access to different values of k_z at the measured spectra, which gives information on out-of-plane dispersion of the electronic structure as explained in section 3.1.3. This is important when the Fermi surface is not exactly 2D. Also, some tuning is required to find with precision the high-symmetry points at the reciprocal space.

Additionally, the use of higher energies is needed to reach further points in the reciprocal space, once the absolute value of $\mathbf{k}$ is proportional to the square root of the photoelectron kinetic energy.

One further advantage of using a synchrotron facility is that their high photon allows for performing ARPES experiments with different incident light polarization, which is needed when aiming to perform orbital-dependent studies of the electronic band structure, as discussed in Section 3.1.4.

To change the polarization, the most natural way to think is to change the electron analyzer position to rotate the entire incidence plane. Given the experimental setup, however, this is impracticable. Therefore, to change the light polarization, the vertical polarization is selected after leaving the undulator, defining a σ polarization with relation to the fixed incidence plane, which normally has lower photon counting than the incident π light polarization.

3.2.1 Vacuum and cryogenics

For soft X-rays, all elements should be in ultra-high vacuum (UHV), since the presence of air would absorb and scatter the photons with low energy. Therefore, in an ARPES setup, all the optical components, sample, and detection environments should be at pressure with a vacuum better than 10^{-10} torr.

To manipulate the sample inside the vacuum chamber, the sample holder is positioned inside a cryomanipulator, used to rotate and adjust the position of the sample inside the cooling ambient. To perform measurements at low temperatures, most beamlines count with liquid helium cryogenic systems. Liquid nitrogen can also be used to achieve temperatures that are not so low.

The photoemission process is surface sensitive, due to its low penetration depth of a few angstroms. Therefore, to perform a good quality measurement, the sample must be cleaved inside the vacuum chamber, to avoid oxidation and pollution to the measured surface.

The cleaving can be done by different methods. For example, for some Van der Waals materials, a scotch tape can be enough to beak the out-of-plane bonds and remove an entire layer of the sample, exposing a fresh surface inside the UHV environment. Some other samples require stronger gluing methods due to stronger bonds. This is the case of FeSC, which need to be glued to the sample holder using silver epoxy, and a metal pin is glued on top of the sample. Once inside the vacuum, the metal pin is removed with the help of a wobble stick, exposing a clean surface for photoemission. This process can be a little tricky and even prohibited for some specific samples, so the experience with the material of interest will direct the better method to have a clean surface.

Another possibility is to have the crystal growing inside a preparation vacuum chamber from the beginning, using evaporation or sputtering techniques, and having the sample transferred to the measuring chamber afterward through a UHV transfer line, with separated components with their vacuum pumps and transfer "doors". Not all facilities or setups support this process but it is possible in the most modern synchrotron beamlines.

It is important to maintain all vacuum components clean and free of contaminants, so the ARPES setup maintenance is very critical to attaining a good operating condition.

3.2.2 Electron analyzer

The electron analyzer, or spectrometer, consists of a hemispherical device able to deflect incoming electrons, in a curved trajectory, for different detection positions as a function of their kinetic energies. This deflection is based on the potential lens effect, where the beam of electrons can be focused by an electronic potential similarly as a photon beam can be affected by an optical lens system.

The electron analyzer functioning can be separated in a few steps: first, an electrostatic lens system decelerates and focuses the electron beam on the analyzer entrance slit; second, elec-

trons that pass through the entrance slit are deflected in the electric field between two spherical hemispheres; third, the electrons pass the exit slit and are detected.

The spectrometer components must be contained within an Ultra High Vacuum (UHV) environment to avoid scattering and absorption from air particles, besides the already mentioned sample surface oxidation. Also, the potential lens system is susceptible to magnetic field effects on electron trajectories. Therefore, the ARPES environment must ideally be far from magnetic field influence.

After the photoelectrons leave the sample, they are emitted in a wide range of directions. The slit width at the entrance of the electrostatic lens system and its distance from the sample defines the acceptance angle for the spectrometer. This angle is related to the maximum $\mathbf{k}$ range for the measured spectra. The electron lens system will focus the electron beam at the detector entrance, resolving the electrons by their angle around a certain θ about the sample normal. The electrostatic lens also will accelerate and decelerate the electrons, making all their kinetic energy around a certain value called Pass Energy (E_p), which will be ultimately related to the energy resolution.

Additionally, between the potential lens, some slits are placed to avoid vertical angular dispersion, assuring that the angular dispersion is along the entrance slit direction (horizontal) and that all electrons will enter the hemispherical analyzer at about the same vertical position, to be later separated by energy in this direction.

The hemispherical analyzer itself consists of two half-spheres with radius R_1 and R_2, kept at a potential difference V. When the beam of electrons enters the space between both half-spheres, it is deflected in a way that electrons with lower kinetic energy are more affected by the potential, being more deflected. This way, electrons with greater kinetic energy will describe a trajectory with a larger radius and hit the exit slit closer to the outer sphere, while the slower electron will hit the exit slit closer to the inner sphere. Therefore, the energy dispersion is created, as illustrated in Figure 3.5(a). For the electron detection to be resolved both in angle and energy, electrons with different angles and the same kinetic energy must travel along a plane perpendicular to the one resolving energy. This is shown in Figure 3.5(b).

After the exit slit, electrons will have their position determined by their respective kinetic energy and hit a set of microchannel plates (MCP), where each one of them works as an electron multiplier through secondary emission processes triggered by an electric field. Then, the electrons hit a florescent phosphor screen, generating an equivalent photon beam to be detected by a charge-coupled device (CCD).

The electrons are linearly dispersed in energy around the pass energy E_p, therefore, with higher E_P, the final intensities will be higher while the energy resolution will be lower. Such relation is summarized in equation 3.22, where w is the entrance slit width, $R_0 = (R_1 + R_2)/2$ is the mean radius between both spheres, and α is the acceptance angle.

$$\Delta E = E_p \left(\frac{w}{R_0} + \frac{\alpha^2}{4} \right) \tag{3.22}$$

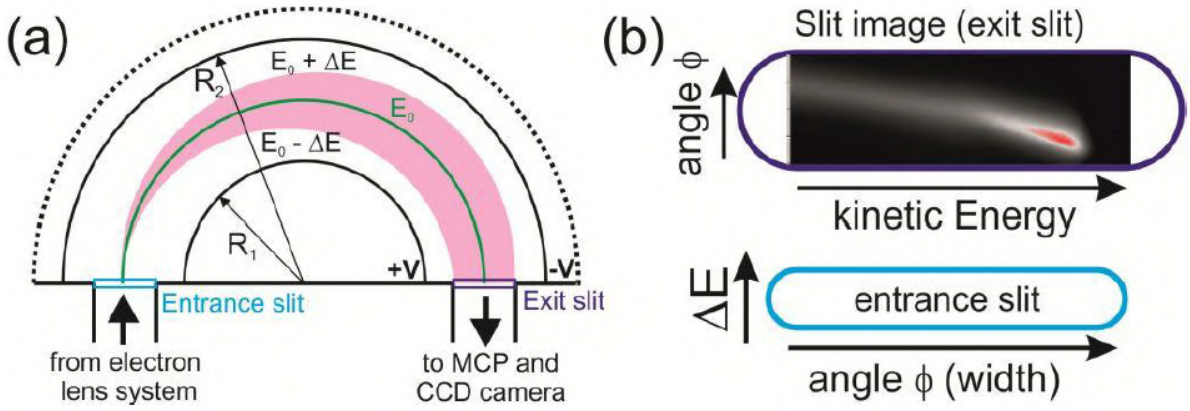

Figure 3.5: (a) A schematic representation of a spherical electron analyzer with internal radius R_1 and external radius R_2. (b) An example of spectral function measured at the exit slit for graphene as a function of angle and energy is shown in the entrance slit image. From ref [92]

The momentum resolution, in its turn, is related to the number of angle channels at the MCP and to the acceptance angle. Lower acceptance angles and a large number of channels will delivery better angle resolution at the final spectra, the former at the cost of intensity.

Therefore, technical advances in the field of electron analyzers are required to improve the ARPES experiment resolution, intensity, and feasibility altogether. In that sense, one important characteristic of an electron analyzer is its intrinsic work function. Achieving a lower analyzer work function enables probing ARPES spectra for lower binding energies and to work more efficiently with laser sources, with energies typically in the ultraviolet range.

At the Bloch beamline, the electron analyzer is the DA30 manufactured by Scienta Omicron. This type of analyzer has the advantage of using deflecting lens to acquire electrons in an area perpendicular to the slit direction. It allows probing Fermi surface maps without moving the sample at all, avoiding longer collection times, intensity inhomogeneities, and alignment problems. However, the probed Fermi Surface will have a circular shape, instead of a square typically measured when acquiring maps by moving the tilt angle. Therefore, some features for higher momentum points can be missed.

The DA30 has only discrete options of pass energy $E_p = 1, 2, 5, 10, 20, 50, 100, 200$ eV, making the tuning of energy resolution, electron counting, and binding energy range more limited. However, it is one of the available analyzers with greater resolution, and with a manipulator designed by Scienta Omicron, it can achieve small steps and good reproducibility in the sample position.

3.3 ARPES methods

The results presented here were performed at the Bloch beamline of the Max IV synchrotron in Lund, Sweden. The detection was made using the Scienta DA30 photoelectron analyzer. The

total energy resolution was set at about 8 to 10 meV for incident photon energies between 60 and 81 eV, and angular resolution of $0.1°$. The samples were glued on a Mo sample holder using silver epoxy and were cleaved using Al posts inside the main preparation chamber (vacuum of 3×10^{-10} mbar) and then transferred to the analyzer chamber (vacuum of 2×10^{-11} mbar) for the experiments.

For all samples, measurements were performed at 150 K and 20 K, corresponding to above and below T_{SDW}, respectively. The cooling was performed through a 6-axis cryo manipulator using a closed-cycle liquid Helium system.

The choice of energy was intended to probe the 2D electronic structure around the Γ and Z points of the material's Brillouin zone (BZ). The k_z position for $BaFe_2As_2$ was calculated by considering an inner potential V_0 of 14 eV and work function W of 4.4 eV [97], following the equation 3.21 divided by a factor of $2\pi/c$. With it, k_z will be in multiples of $2\pi/c$, resulting even integer for Γ point, and an odd integer for a Z point.

The experiments were carried out along the high symmetry directions Γ X and Γ M for both Γ and Z k_z levels, with the high symmetry points following the body-centered crystal structure. Linear horizontal (π) and vertical (σ) polarized X-rays were used to probe different Fe-$3d$ orbital contributions to the ARPES signal.

Chapter 4

ARPES results of Mn substituted $BaFe_2As_2$

In this chapter, the ARPES experimental results for the Mn-substituted samples (MnBFA) $Ba(Fe_{1-x}Mn_x)_2As_2$ are presented. The probed samples have $x = 0, 0.035, 0.075$, which will be referred to as BFA, Mn3.5%, and Mn7.5%, respectively, as defined in Table 2.2.

To describe the experimental ARPES results and its analysis, the crystal body-centered tetragonal geometry was adopted to label the Brillouin zone (BZ) high-symmetry points, as indicated in Table 2.1. As explained in chapter 2, for this notation the electron pockets are in the ΓX direction. The tetragonal paramagnetic (PM) state results, measured with $T = 150$ K for these samples, will also be termed as high-temperature (HT) results, whereas the orthorhombic spin density wave (SDW) state results, measured at 20 K, will be termed as low-temperature (LT) results.

The methods for the ARPES measurements are described in Section 3.3, and the results here presented will be briefly discussed and put in context with previous RIXS results [7] in Section 4.3.

4.1 High-temperature results

As explained in Section 3.3, a very complete set of ARPES data was taken for each sample. For two different states (or temperatures), electronic band maps and Fermi maps were measured for different incident photon energies, light polarization, and sample high-symmetry directions. In Figure 4.1, it is shown a survey of the electronic band structures, as a function of Mn content, in the tetragonal PM state ($T = 150$ K) of the MnBFA samples. Measurements were taken along the high-symmetry directions and adopting linear beam polarization as indicated in each panel, for incident energy ~ 80 eV for the three samples. It is possible to note how the spectral function depends on the polarization, which permits the association of the spectral features to a main orbital character, as explained in Section 3.1.4. This strong orbital character of the bands

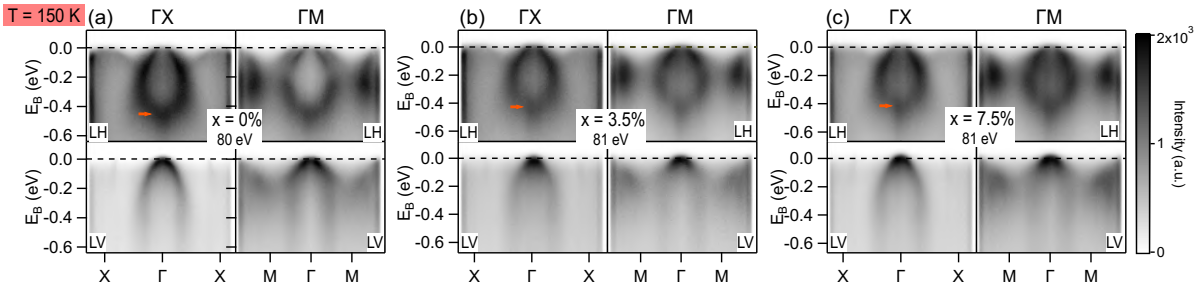

Figure 4.1: Overview of the measured electronic band maps of the (a) BFA, (b) Mn3.5% and (c) Mn7.5% samples for high temperature. Measurements were taken along the ΓX and ΓM directions and for σ and π polarizations, as indicated. Higher intensities are darker on the color map.

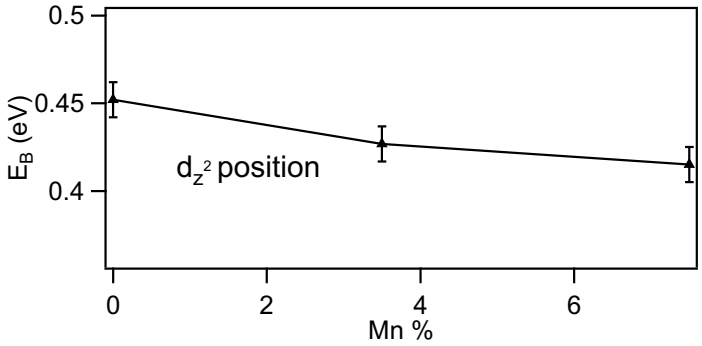

Figure 4.2: Maximum EDC position for the band associated with the d_{z^2} orbital as a function of Mn content, for the Γ point. The points correspond to the orange arrows marked in the panels of Figure 4.1.

is key in all theories of the FeSC materials [98–100, 40]. A feature that is easily distinguishable is the d_{z^2} derived band that appears only for π light polarization for energies close to $E_B = 0.5$ eV, in absolute values. This is marked as an orange arrow in the panels of Figure 4.1 for each sample.

To compare the evolution of the d_{z^2} band feature as a function of Mn content, the peak d_{z^2} position was obtained, as shown in Figure 4.2. It was determined by taking the energy distribution curve (EDC) for the π polarized data for $k_x = \Gamma = 0$, which means considering the intensity as a function of energy for a fixed value of momentum, and taking the energy value corresponding to the maximum intensity peak position. The peak is moving to higher binding energy (smaller in absolute value) as the Mn percentage increases. With this, it is expected that the energy bandwidth associated with this band is getting smaller, corresponding to a higher localization of this electronic band, associated with lower hybridization of the d_{z^2} band with other orbitals. This was shown already for MnBFA in a direction-dependent X-ray absorption spectroscopy study [101].

It is interesting to note that, despite being small, there is a k_z direction band dispersion in these materials, which can also be enhanced or hindered by the Mn introduction. To inspect this,

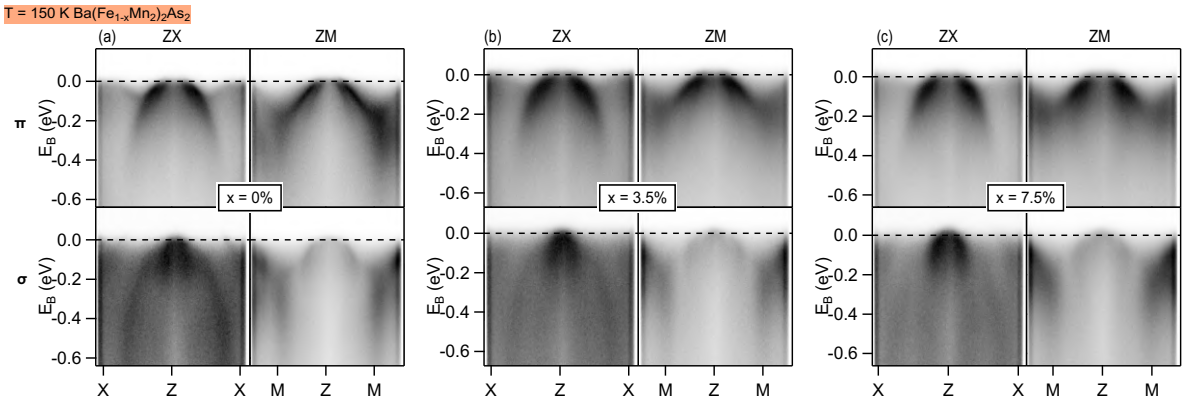

Figure 4.3: Overview of the measured electronic band maps of the (a) BFA, (b) Mn3.5% and (c) Mn7.5% samples for high temperature. Measurements were taken along the ZX and ZM directions and for σ and π polarizations, as indicated.

Figure 4.3 shows a similar survey of the electronic band structures than the one from Figure 4.1, but this time for incident energies ~ 61 eV for the three samples. It is noteworthy that the d_{z^2} derived band is missing for this k_z level, for the π polarized measurements. This contribution is expected to be pushed upwards with k_z dispersion until it vanishes above the Fermi energy [102]. Additionally, the hole pockets are larger for this energy, and the X electron pockets visible for the σ polarized measurements are more shallow in E_B.

The k_z =Z data will be further discussed for the low-temperature results. For now, the analysis will be focused in the $k_z = \Gamma$ data.

The band determination and orbital assignment can be difficult by direct observation of the raw data when there is an overlap of several bands. The FeSC materials are multi-orbital and the electronic substitution causes the broadening of the bands. To overcome these difficulties, the data analysis can be supported by the second derivative analysis, a widespread method in the ARPES community [103, 104]. This type of analysis takes the second derivative of the momentum or energy distribution curves (MDCs or EDCs) as a function of momentum and/or energy. The resulting intensity can be convoluted with a Gaussian function compatible with the energy and momentum resolution. Although there are some other advanced methods to perform the band characterization, such as the curvature method [105], or machine learning methods [106, 107], the second derivative is reliable to some extent and well implemented, and was used for the analysis here presented.

For the MnBFA samples, the second derivative data is presented in Figure 4.4. The band features are more distinguishable and clear, but it also depends on the type of derivative. For the ΓX σ polarization, for example, the band closer to the X point, related to the electron pocket, is only visible for momentum derivatives. With these new spectra, it is possible to fit the band point position and determine the band shape and changes with the Mn introduction. Since the spectral function is expected to have a Lorentzian shape (see equation 3.14), its second

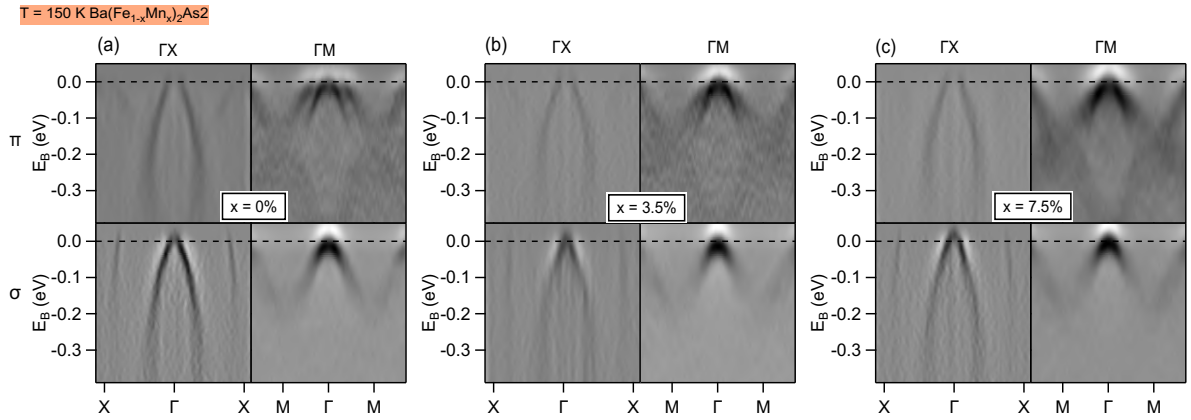

Figure 4.4: MnBFA high-temperature second derivative maps. The high-symmetry direction and polarization for each measurement is indicated. (a) BFA sample results, (b) Mn3.5% sample results, and (c) Mn7.5% sample results. The band points were fitted to the darker point.

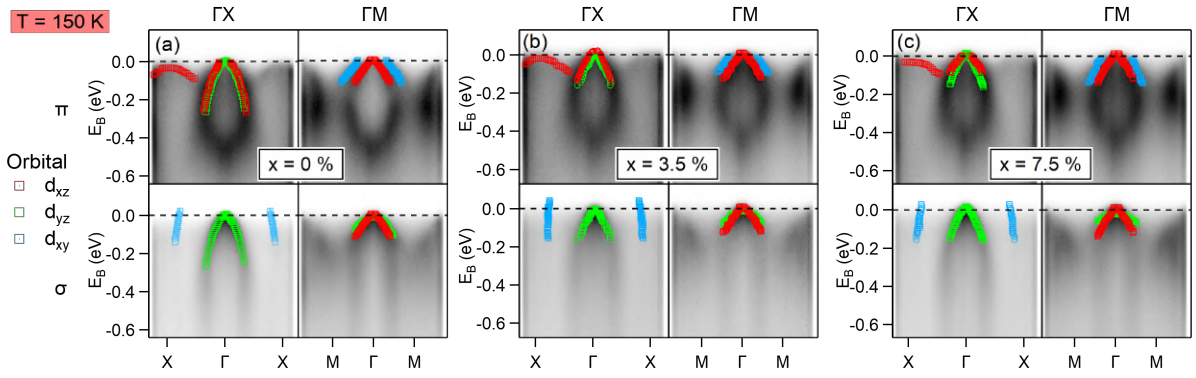

Figure 4.5: Overview of the fitted band points for the (a) BFA, (b) Mn3.5% and (c) Mn7.5% samples obtained from the second derivatives of Figure 4.4. The orbital character of each band is indicated by the legend color code and was assigned following Tables 3.1 and 3.2.

derivative will have a minimum point in the position of the Lorentzian peak. Therefore, the darker spots represent these Lorentzian maximum points, because for the second derivatives the color scale is reversed than the one for the raw bands.

The fitted points are presented in Figure 4.5, where the orbital character is represented in a color code in the legend. The Γ point has two inner, locally degenerated, bands with d_{xz} and d_{yz} characters and one outer band with d_{xy} characters. Visible in the ΓX direction, the electron pocket region presents two bands, one that does not cross the Fermi level and is almost flat, of d_{xz} character, for π polarization measurements, and other that forms a deep electron pocket band, of d_{xy} character, for σ polarization. These two bands in the electron pocket region will be termed "flat" and "deep" bands.

To further investigate the electron pockets, is possible to recur to the Fermi maps. These maps are measured either by joint band measurements with different tilt angles ϕ, or, if the analyzer has the deflecting lens, by a band map measurement taken without moving the sample.

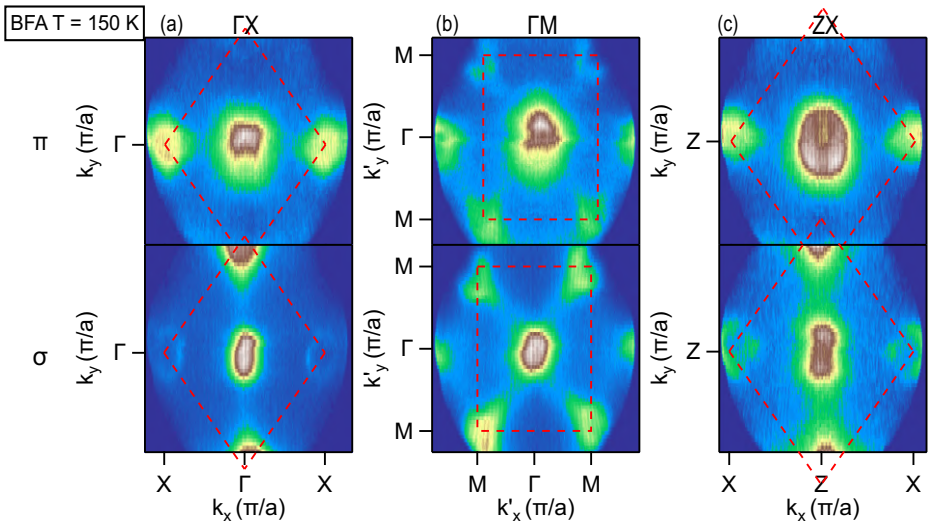

Figure 4.6: High-temperature Fermi Surface measured for the BFA sample. Measurements were taken along the ΓX, ΓM, and ZX directions and for σ and π polarizations, as indicated. The dashed red lines delimit the first BZ.

As explained in Section 3.2.2, the electron analyzer at Bloch beamline permits to do the second type of acquisition. These maps are three-dimensional matrices with axis related to k_x, k_y, and binding energy E_B.

Fixing the map binding energy to the Fermi level ($E_B = 0$), it is possible to plot the Fermi Surface (FS). In Figures 4.6, 4.7, and 4.8 there are presented the measured Fermi surfaces (FS) for the samples BFA, Mn3.5%, and Mn7.5%, respectively. Again, it is possible to observe the polarization selectivity for the spectral function. The dashed red lines delimit the first BZ, revealing the rotation of the sample high-symmetry direction being probed.

For the FS it is clear that the hole pockets at Γ are larger for the k_z =Z photon energy. Also, the electron pockets measured for the ΓX/ZX directions show different relative intensities for σ polarization. This is a consequence of the selection rules, since this direction is associated with the d_{xz} orbital that forms the X electron pocket, and its intensity is zero for σ polarization, leaving only the d_{xy} weak contribution.

For the Mn substituted samples Mn3.5% and Mn7.5%, the changes in the Fermi surface are mainly in the broadening of the spectral features. The pocket sizes are not notably different with Mn introduction. As we shall see, that will not be the case for the CrBFA samples.

To inspect the pocket size as a function of Mn closely the focus will be the X electron pocket for ΓX direction and σ light polarization. In Figure 4.9 there is a comparison of the FS maps taken in these conditions, for the three samples at high temperature. A planar cut of the Brillouin Zone (BZ) is plotted above the FS, with the high-symmetry points highlighted. It is possible to observe the d_{xy} contribution electron pockets at the X points, and the stronger intensity for the Y electron pockets. The green dashed line marks the YZ high-symmetry direction.

Furthermore, by fixing the map k_y to a high-energy point, it is possible to plot the electronic

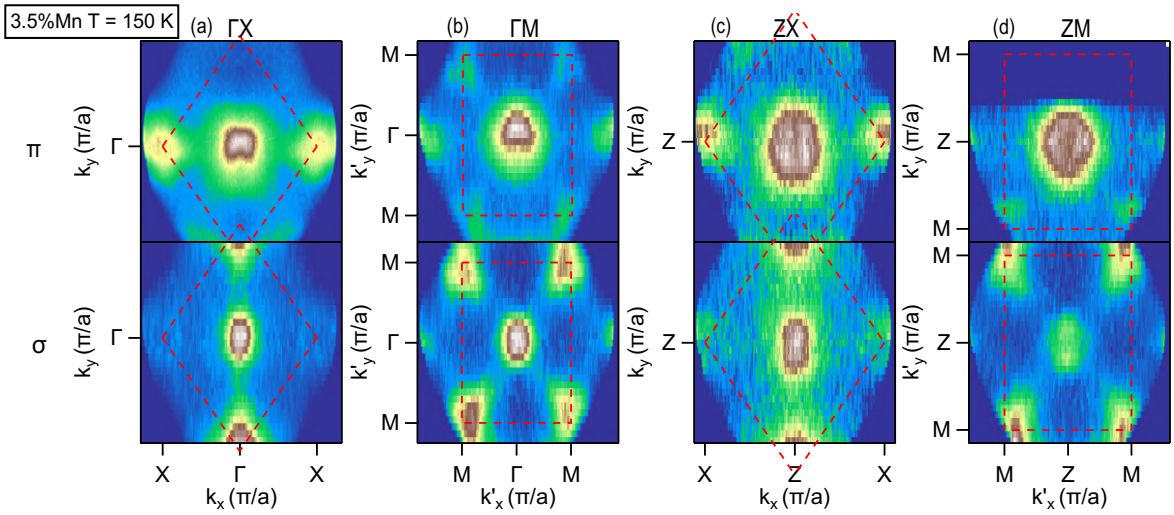

Figure 4.7: High-temperature Fermi Surface measured for the Mn3.5% sample. Measurements were taken along the ΓX, ΓM, ZX, and ZM directions and for σ and π polarizations, as indicated. The dashed red lines delimit the first BZ.

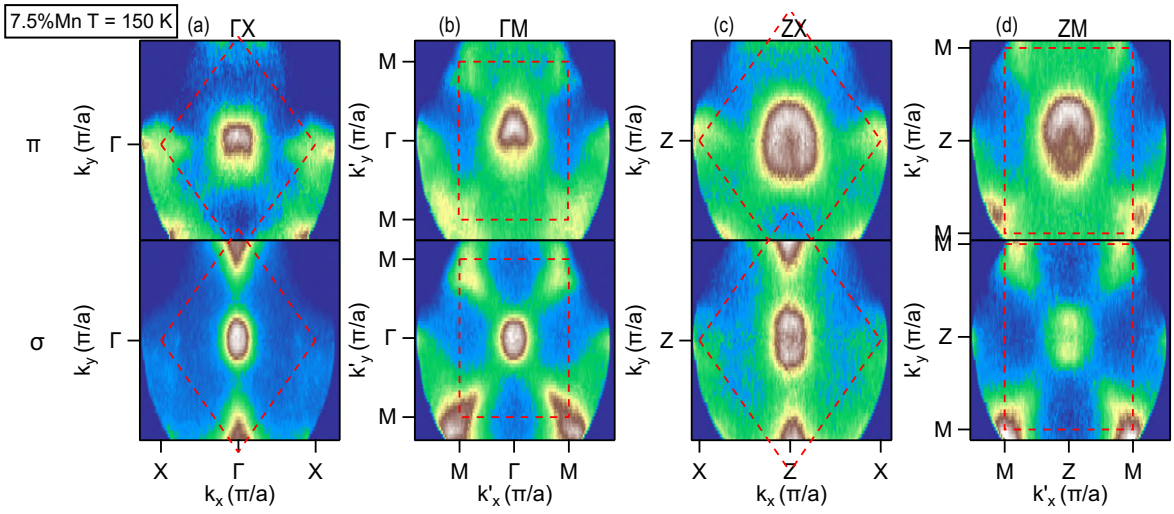

Figure 4.8: High-temperature Fermi Surface measured for the Mn7.5% sample. Measurements were taken along the ΓX, ΓM, ZX, and ZM directions and for σ and π polarizations, as indicated. The dashed red lines delimit the first BZ.

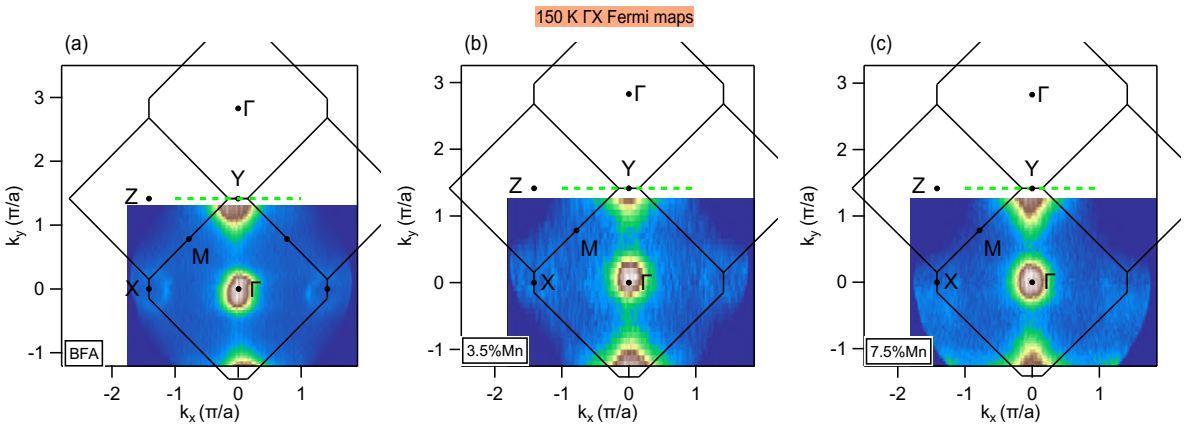

Figure 4.9: Fermi surface measured with σ polarization with the BZ drawn and its high-symmetry points indicated for samples (a) BFA, (b) Mn3.5% and (c) Mn7.5%. The green dashed lines indicate the cut based upon which the electron pockets of Figure 4.10 were reconstructed.

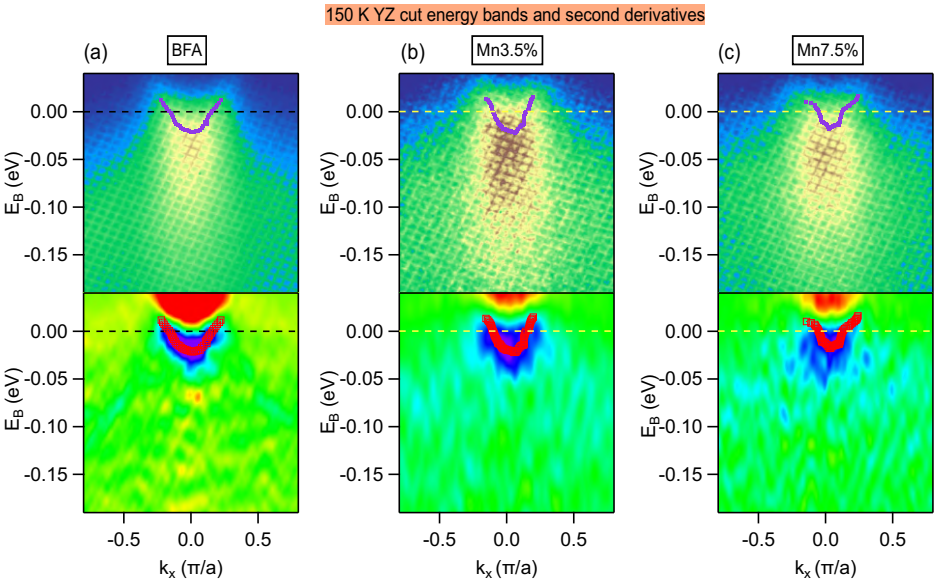

Figure 4.10: High-temperature energy maps for the YZ direction and its second derivatives for samples (a) BFA, (b) Mn3.5% and (c) Mn7.5%. The marked points represent the points forming the electron pocket band at Y.

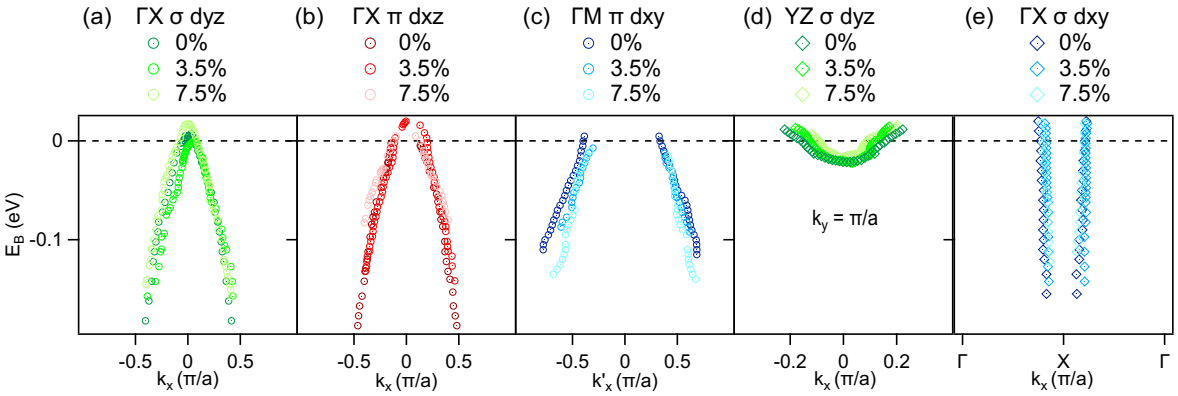

Figure 4.11: Comparison between the band points for the three samples. Lighter markers indicate more Mn content and the orbital color code follows the legend of Figure 4.5. (a)-(c) Γ centered hole-like bands. (d)-(e) X/Y centered electron-like bands.

band as a function of k_x and E_B for a different high-symmetry direction, parallel to the measured ΓX direction. This is shown in Figure 4.10, where is possible to see the electron pockets for the YZ high-symmetry direction. These spectra have lower resolution than the electronic bands of figure 4.1, since the Fermi map acquisition mode is different and for achieve the same resolution would take several hours. The spectral weight associated with the electron pocket, however, is still visible by choosing a more contrasting color scale. By taking the energy second derivatives of the spectra, it is possible to fit the electron band points, as shown in the lower panels of Figure 4.10. This electron band will be termed "shallow" electron pocket.

The electron pocket is composed of a minor and a major axis, forming an ellipse. This is possible due to the C_4 symmetry of the crystal structure, which makes the X and Y points equivalent, but the direction perpendicular to ΓX/Y does not need to be equivalent. Electronic states at the electron pockets around the X/Y points have, therefore, C_{2v} point symmetry which is reflected in the idealized elliptical shape of the pockets. The minor axis is determined by the shallow electron pocket, of d_{yz} orbital character, while the major axis is determined by the deep electron pocket, of d_{xy} orbital character.

After identifying three hole pocket bands and two electron pocket bands, it is possible to compare the effect of Mn substitution in these bands. This comparison is shown in Figure 4.11. The focus is on the states in the vicinity of E_F. The hole pockets change as a function of Mn content is summarized in Figures 4.11(a)-(c), while the electron pockets changes are in Figures 4.11(d)-(e).

Naively thinking in terms of band filling, increasing hole pockets and shrinking electron pockets would be the putative effects of the nominal hole doping caused by Mn. However, the experimentally determined scenario is more involved. Bands forming the hole pockets and the deep electron-like band are barely affected by Mn, whereas the intersection of the shallow electron-like band with E_F is systematically decreasing. In turn, it is only the minor semi-axis of the idealized elliptical electron pocket which shrinks with Mn content. Thus, a fraction

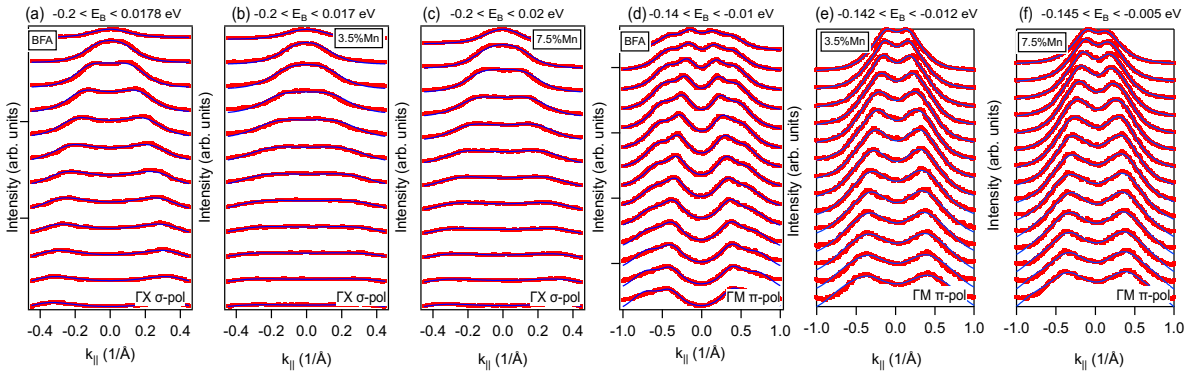

Figure 4.12: ARPES spectral function analysis. Fittings (blue lines) of several MDCs (red dots) for increasing binding energies. (a)-(c) data obtained for σ polarization, measured along ΓX for samples BFA, Mn3.5% and Mn7.5%, as indicated, with a single band fitting. (d)-(f) data obtained for π polarization, measured along ΓM for samples BFA, Mn3.5% and Mn7.5%, with a double band fitting.

of electron and hole states retain their original nesting condition. This distinct behavior of shallow and deep electron-like bands and the lack of change in the hole pockets are completely unanticipated and are evidence that Fe substitution by Mn atoms is changing the electronic band structure instead of simply changing its electronic filling.

4.1.1 Self-energy analysis

As demonstrated by the band analysis, the role played by Mn is more complicated than nominal hole doping, demanding a quantitative analysis of the ARPES spectral function $A(\mathbf{k}, E)$. To do so, it is usual to perform a spectral analysis by fitting the momentum distribution curves (MDCs) to the expression for the one-particle $A(\mathbf{k}, E)$ (equation 3.14). This one-particle spectral function can be used for a system of weakly correlated electrons [39]. The objective is to extract the electronic scattering rate $\Gamma(E)$ as a function of the binding energy E.

The analysis for the band in ΓX direction and σ light polarization, with d_{yz} main orbital character, is presented in Figures 4.12(a)-(c) for samples BFA, Mn3.5% and Mn7.5%, respectively. This analysis follows Refs [87, 86], where a method of fitting directly Γ for all MDCs at once following a given band dispersion is presented. The dispersion relation will determine the maximum position of the Lorentzian peaks. This method, termed as “all at once” fitting, takes into account the experimental resolution for energy and momentum and finite temperature effects and was shown to be reliable for different kinds of band dispersions, such as linear bands, Dirac cones, parabolic bands, and bands with a "kink" anomaly resulting from electron–phonon coupling [87]. It was particularly useful for single parabolic bands in the ΓX direction and σ light polarization for 122 FeSC [86], however, when the multiband character is in play, the method could not be implemented, due to the twice as large number of parameters necessary to minimize the square fitting of all MDCs simultaneously.

Therefore, for the analysis of the band with d_{yz} main orbital character, measured along the

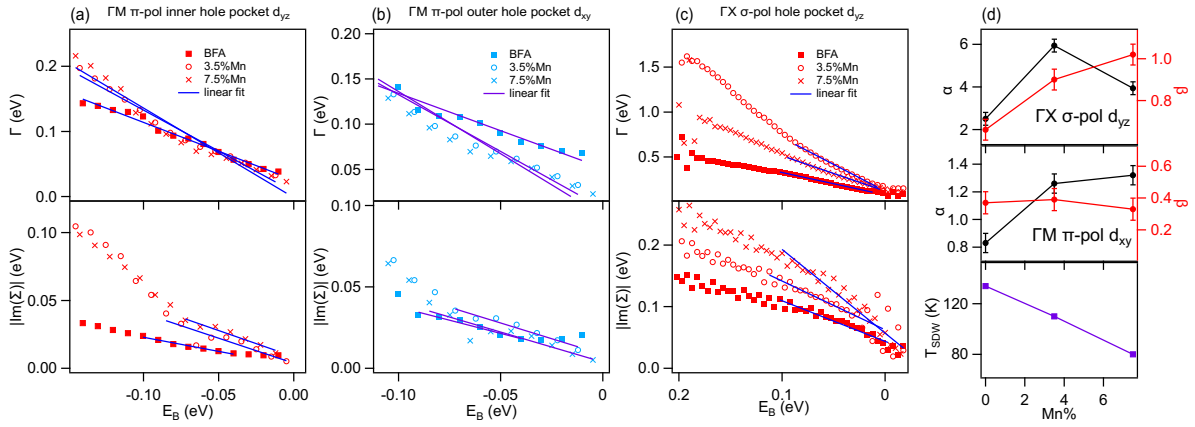

Figure 4.13: ARPES spectral function analysis resulting scattering rate $\Gamma(E)$ and imaginary part of self-energy $\mathrm{Im}\Sigma(E)$ for (a) ΓM inner hole pocket band, (b) ΓM outer hole pocket band and (c) ΓX single hole pocket band. The blue and purple lines indicate linear fittings close to the Fermi level. (d) resulting linear coefficients from panels (b) and (c) and the T_{SDW} behavior as a function of Mn content.

ΓM direction and π light polarization, a more commonly used method was employed. It consists of one-by-one fittings of the MDCs, where the spectrum is considered a linear combination of each band Lorentzian peaks and the dispersion relation does not need to be given in advance. The fitting is a usual multiple Lorentzian and the scattering rate is obtained by multiplying the peaks' full width at half maximum (fwhm) by the local band velocity [108]. To implement this method for these samples, a Python code was written, where the Lorentzian peak positions can have as the initial guess the bands obtained from the second derivative process, the points of Figure 4.5. The resulting fitting of two bands is presented in Figures 4.12(d)-(f). Energy and momentum finite resolution and finite temperature were not considered, but suitable fittings could be performed nevertheless.

Given the two methods used, the results cannot be reliably compared between bands fitted with these different methods, and only the trend as a function of Mn for each band is a trustworthy result. To analyze this trend it is possible to compare the scattering rates as a function of binding energy $\Gamma(E)$ for the three samples, as shown on the top panels of Figures 4.13(a)-(c), where the (a) and (b) panels are results from the two-band fitting of ΓM direction and the (c) panel have the results of one-band all-at-once fitting of ΓX direction.

As explained in Section 3.1.2, if the system is a Fermi liquid, a quadratic dependence of the scattering rate as a function of energy is expected, and the renormalization factor that relates the scattering rate $\Gamma(E)$ with the imaginary part of the self-energy Σ'' (or $\mathrm{Im}\Sigma(E)$) is expected to be constant. The scattering rate E dependence clearly distinct from $\mathrm{Im}\Sigma(E)$, a result suggesting that the renormalization function Z is not a simple constant as a function of E. In this case, a marginal Fermi liquid (MFL) behavior is needed to analyze the data. Therefore, the relation between $\Gamma(E)$ and Σ'' will follow the expression 3.17, from where Σ'' can be extracted, as shown on the bottom panels of Figures 4.13(a)-(c).

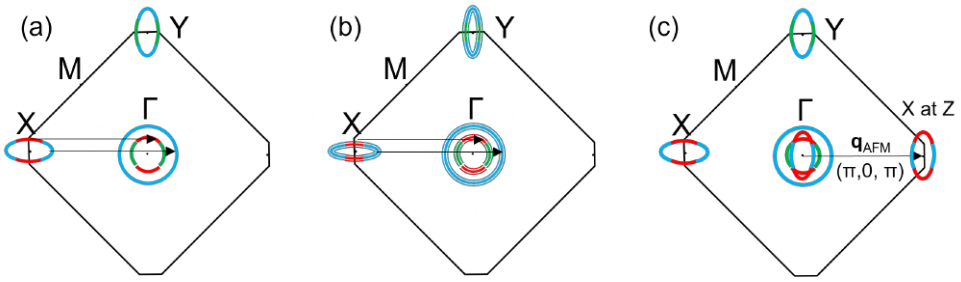

Figure 4.14: (a) Schematic FS for the parent compound $BaFe_2As_2$. (b) Mn substituted FS, the bands are enlarged and the electron pocket shrinks in the minor axis direction. (c) Low-temperature FS for BFA, with the SDW folding. The color code indicates the orbital character of the pockets.

In the vicinity of E_F, for all bands, $\Gamma(E)$ and $\mathrm{Im}\Sigma(E)$ are fairly well described as linear functions of E, within the paradigm of an MFL regime. The slopes, or angular coefficients, related to $\Gamma(E)$ and $\mathrm{Im}\Sigma(E)$ can be defined as α and β, respectively.

Physically, being $\Gamma(E)$ proportional to the inverse of the quasiparticle lifetime, α is a measurement of the electronic states' coherence. In this sense, an increase in α as a function of Mn content would correspond to a stronger response of $\Gamma(E)$ to the binding energy which translates into an increase in band incoherence and electron-electron interaction inelastic scattering [109]. Similarly, an increase in β is related to increasing electronic correlations, due to electron-electron interaction response. The α and β angular coefficients of the curves of Figures 4.13 (b) and (c) are obtained as a function of Mn content and are presented in Figure4.13(d) for bands with main d_{yz} (top panel) and d_{xy} (middle panel) orbital character. The lower panel shows the T_{SDW} as a function of Mn content.

A linkage between the $\alpha(d_{yz})$ dependence as a function of K and Co content and T_{SC} was found [86]. In the MnBFA case, it can be speculated about a connection between either $\alpha(d_{yz})$ or $\alpha(d_{xy})$, either $\beta(d_{yz})$ or $\beta(d_{xy})$ and T_{SDW}, which is the relevant energy scale of these samples. Overall, $\alpha(d_{yz})$ and $\alpha(d_{xy})$ increase when Mn is introduced whereas $\beta(d_{yz})$ increases and $\beta(d_{xy})$ is nearly constant as a function of Mn percentage.

The increase of the α parameters, observed for all bands, suggests that electronic disorder dominates and controls the T_{SDW} behavior, exemplifying the key role of substitution disorder [45, 59, 60, 86, 110–112] in the phase diagram of FeSC materials. Given the impurity scattering on Co substituted $BaFe_2As_2$ [113, 114], with Co being close to Fe, one would expect similar behavior in MnBFA. However, it behaves similarly to Zn which, in principle, is a much stronger impurity scatter. The increase of β, which is observed only for bands with d_{yz} character, is an effect of increasing electronic interactions and illustrates the orbital specificity of the chemical substitution effects in FeSC materials, which was largely reported and theorized about [96, 111, 101, 115–120].

To summarize the results in the high-temperature paramagnetic state for the MnBFA samples, Figure 4.14(a) illustrates the parent compound $BaFe_2As_2$ FS at the paramagnetic state with

two hole pockets and one electron pocket. Nested electron and hole states are connected by a $(\pi, 0)$ vector. Figure 4.14(b) shows the schematics for Mn substitution, where Mn causes the partial detuning of the nesting condition and a significant broadening of all electronic states.

Figure 4.14(c) illustrates the effect of the SDW folding, as explained in Section 2.3. The SDW vector $\mathbf{q}_{\mathrm{AFM}} = (\pi, 0, \pi)$ has a k_z component, causing the folding of the electron pocket at Z level into the hole pocket at Γ level. The low-temperature results and the folding effect as a function of Mn content are the topics of the following section.

4.2 Low-temperature results

The same measurements performed for all samples, incident light polarization, and high-symmetry directions for the paramagnetic stare were replicated in the magnetically ordered state. In Figure 4.15 there is a survey of the electronic band structures as a function of Mn content in the orthorhombic SDW state, measured at $T = 20$ K for photon energy ~ 80 for all three samples. Again, the polarization selectivity is notable for the band structure. However, the bands are more visible due to less thermal broadening and reduced effect of the Fermi-Dirac distribution close to the Fermi level. New band features are visible for the BFA sample in panel (a), firstly, the splitting of the "flat" band in the electron pocket region, for ΓX direction π polarized measurements, and secondly, a new electron-like band with $E_B = 100$ meV, at the Γ point. These two features originated from the nematic splitting and the expected SDW folding, respectively. This is in close agreement with the observations for BFA sample reported before [42]. The folded band is associated with a main d_{xy} orbital character, as a result of the deep electron band folding, as shown in Figure 4.14.

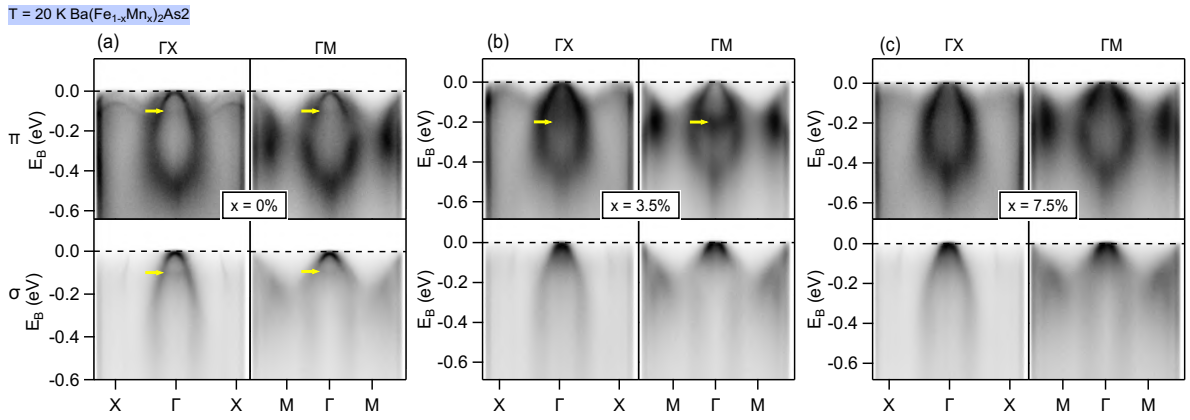

Figure 4.15: Overview of the measured electronic band maps of the (a) Mn3.5% and (b) Mn7.5% samples for low temperature. Measurements were taken along the ZX and ZM directions and for σ and π polarizations, as indicated. Yellow arrows indicate band features absent for high-temperature measurements.

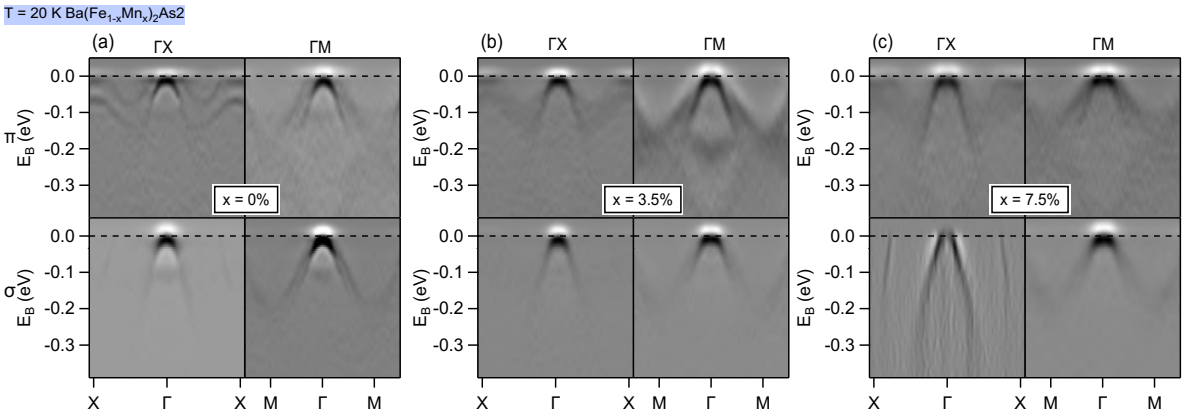

Figure 4.16: MnBFA low-temperature second derivative maps. The high-symmetry direction and polarization for each measurement are indicated. (a) BFA sample results, (b) Mn3.5% sample results, and (c) Mn7.5% sample results. The band points were fitted to the darker point.

To better visualize such bands, the second derivative can be employed again to gain contrast of the band maximum points. This is shown in Figure 4.16. The mentioned new features are clearer for the BFA sample in panel (a), where the bands resulting from the folding reconstruction are visible. However, for the Mn3.5% sample, the band resulting from the band folding has a bigger binding energy of $E_B = 200$ meV. This is visible for ΓM direction and π light polarization. The Mn7.5% sample, in its turn, does not show any sign of SDW folding.

The band folding absence can be confirmed by looking at measurements for incoming photon energy probing the k_z = Z plane of the reciprocal space, shown in Figure 4.17. taken with incident energies ~ 61 eV for the three samples. For the Mn3.5% sample, the new band is clear and marked by a yellow arrow for the π polarized data. For the Mn7.5% sample, it is again absent.

The low-temperature measurements for ZX and ZM directions also show the band splitting of the d_{xz}/d_{yz} orbitals for the almost flat electron band, visible for the ZX direction measurements using π light polarization. Also, the same k_z direction band dispersion is expected for the LT data. It is noteworthy that the d_{z^2} derived band is missing for this k_z level again.

The folded band absence for the Mn7.5% sample can be evidence that increasing Mn content has the effect of suppressing the band folding that is associated with the onset of the SDW state. Is possible to speculate that this occurs for two reasons: first, the d_{xy} derived bands become more incoherent with increasing Mn content; and second, the local character of Fe local moment is amplified by Mn [5]. It was argued before that band folding does not occur even for the parent compound, as explained in ref. [121], making the ordered state band structure a consequence of the orthorhombic crystal structure and AFM order (see Section 2.3).

The band splitting, by its turn, is currently understood as evidence of nematic ordering and consequence of the orthorhombic distortion. The predicted nematic band splitting is visible for all samples, but the spectral feature gets broader and weaker for the Mn-substituted samples. To

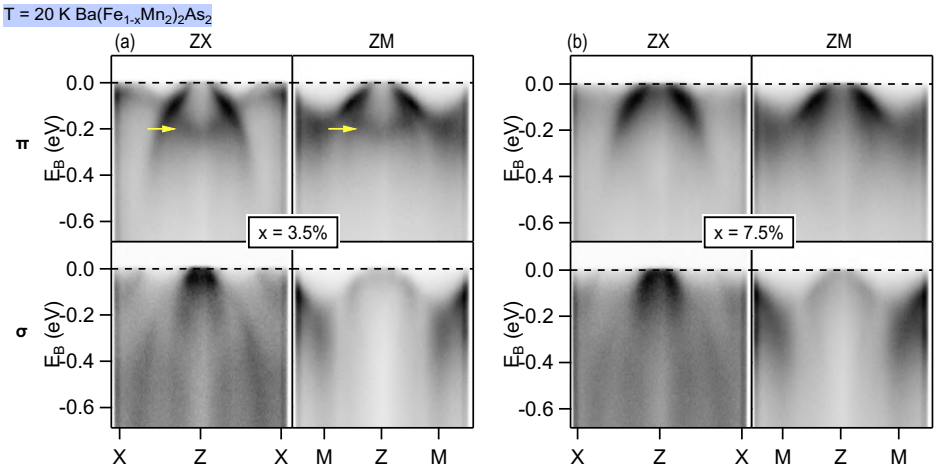

Figure 4.17: Overview of the measured electronic band maps of the (a) BFA, (b) Mn3.5% and (c) Mn7.5% samples for low temperature. Measurements were taken along the ZX and ZM directions and for σ and π polarizations, as indicated. Higher intensities are darker on the color map. Yellow arrows indicate band features absent for high-temperature measurements.

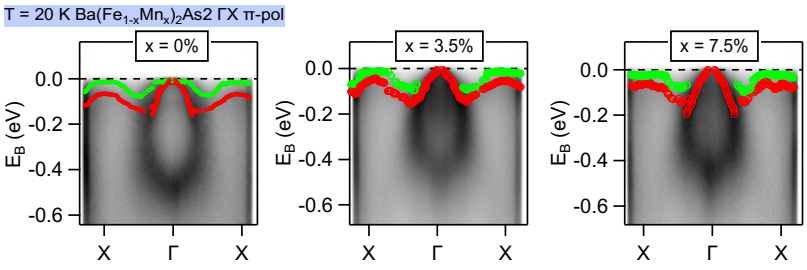

Figure 4.18: MnBFA low-T flat band fitted points, evidencing the nematic splitting.

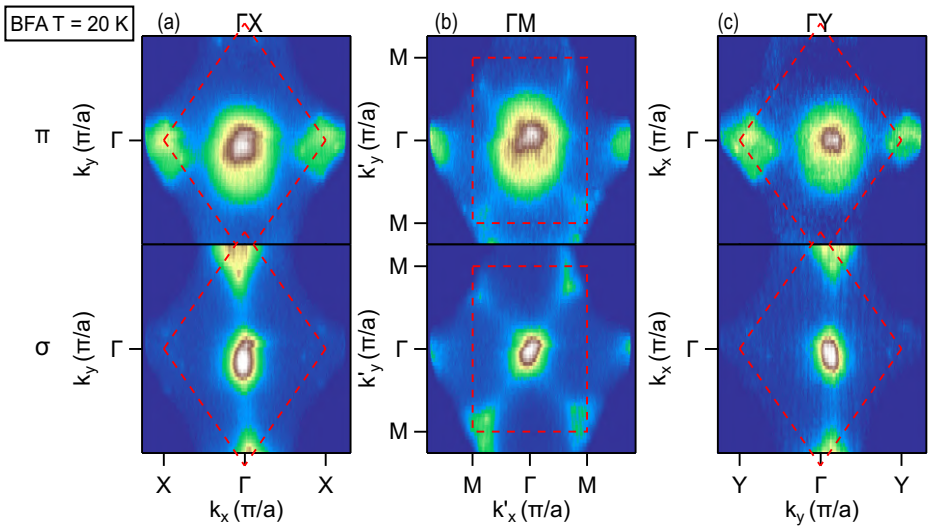

Figure 4.19: Low-temperature Fermi Surface measured for the BFA sample. Measurements were taken along the ΓX, ΓM, ZX, and ZM directions and for σ and π polarizations, as indicated. The dashed red lines delimit the first BZ.

better visualize it, EDCs can be used to fit the spectral minimum as a function of momentum. The resulting fitted points are shown in Figure 4.18. The nematic splitting is evidenced by the breaking of degeneracy between d_{xz} and d_{yz} bands, with a characteristic splitting size.

To gain a more detailed understanding of the splitting, it is important to closely examine the minor axis of the electron pocket, the shallow electronic band. Unlike the major axis, of d_{xy} character, which does not undergo any splitting, the shallow band has a d_{xz}/d_{yz} character. To analyze this, the FS maps will be inspected.

In Figures 4.19, 4.20, and 4.21 there are presented the measured Fermi surfaces (FS) for the samples BFA, Mn3.5%, and Mn7.5%, respectively, similarly for what was shown for HT. The dashed red lines delimit the first BZ, reveling the rotation of the sample high-symmetry direction being probed.

For the parent compound, the k_z = Z photon energy was not probed. Instead, the sample was rotated by 90° to probe the possibility of twin domains. As explained, in the orthorhombic direction the k_x and k_y directions become inequivalent. If the sample was detwinned, we would expect to see different bands and FS for the ΓX and ΓY direction, and the nematic splitting would never be visible for a single measurement. Therefore, we confirm with the ΓY direction measurements in the SDW state that the samples are indeed twinned.

Again, for the Mn substituted samples Mn3.5% and Mn7.5% it, is clear that the hole pockets at Γ are larger for the k_z = Z photon energy. Furthermore, the relative different intensities reveal the polarization selectivity for the spectral function. For these ordered state measurements, the pocket sizes are not notably different with Mn introduction.

For the three samples, it is possible to observe weak signatures of the 4-fold "petal"-like electron pocket formation, observed recently with nano-ARPES for the BFA sample [121].

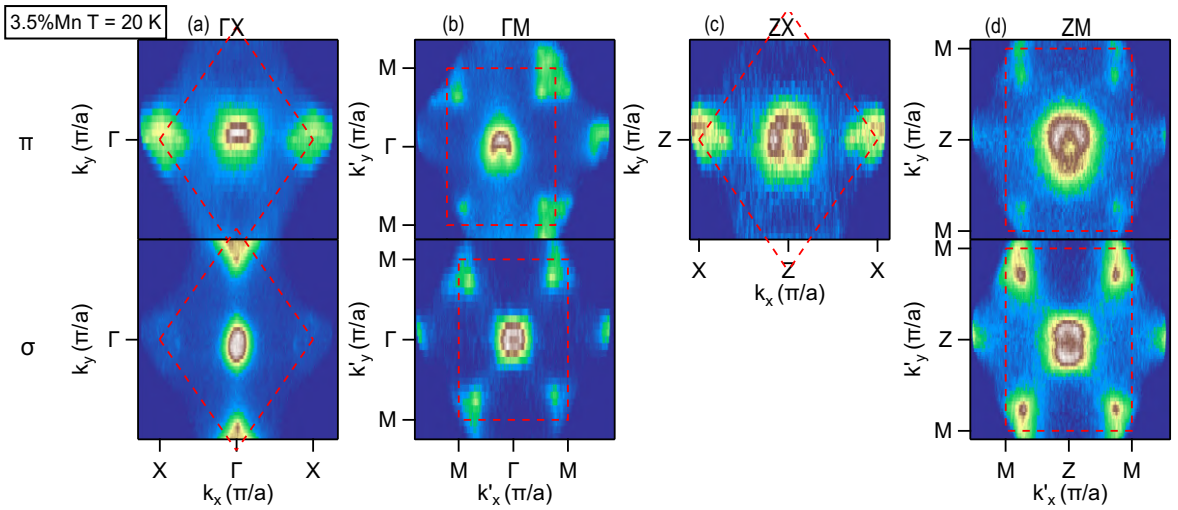

Figure 4.20: Low-temperature Fermi Surface measured for the Mn3.5% sample. Measurements were taken along the ΓX, ΓM, ZX, and ZM directions and for σ and π polarizations, as indicated. The dashed red lines delimit the first BZ.

This is clearer, for example, in the ΓM σ polarized FS, or for the ΓX π polarized band. The full electron pocket visualization, however, is impaired by the limited $\mathbf{k}$ reach of the Γ centered FS. Measurements centered at the electron pocket were not taken.

For the inspection of the electron pocket minor axis, it is possible to reconstruct the YZ cut of the low-temperature band maps, as illustrated in Figure 4.22. This provides valuable insights into the size and nature of the nematic splitting. To fit the band point positions, second derivatives can be employed. This is shown in the lower panels of figure 4.22.

To better understand the effect of Mn substitution for the nematic splitting, the comparison between the splitting size for both flat and shallow bands are shown in Figure 4.23 as a function of Mn content. The energy values were estimated by using EDCs to fit the band positions and superimposing the bands performing a rigid energy shift on the lower duplicated band.

For both electronic bands, there is no scaling between the nematic splitting size and T_{SDW}: indeed, the splitting decreases only about 20% from its value for BFA whereas T_{SDW} decreases by about 60%. Mn substitution, however, is believed to suppress the transition temperature [49, 12] but the splitting dependence on Mn content is not reflecting this phenomenology. It can be speculated if the SDW transition is indeed associated with nematic splitting and how the orthorhombic distortion is vital for this magnetic order.

There is still debate about the nematic splitting size for these materials [122], reported as 60 meV for FeSe thin film [123] and 70 meV for BFA [124], which is in good agreement with our findings. The nematic splitting for the shallow electron-like band was reported as 40 meV for BFA [94].

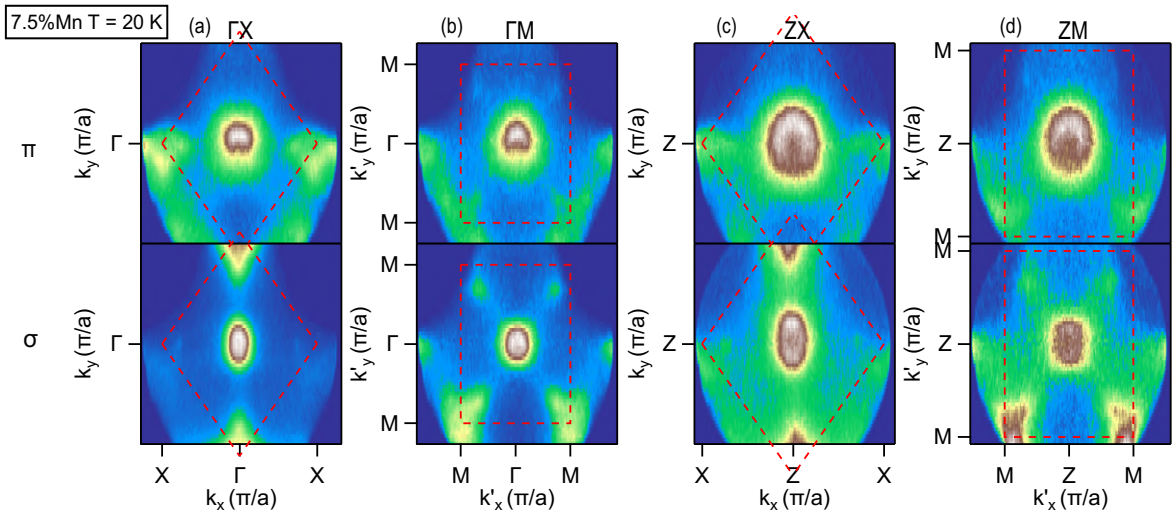

Figure 4.21: Low-temperature Fermi Surface measured for the Mn7.5% sample. Measurements were taken along the ΓX, ΓM, ZX, and ZM directions and for σ and π polarizations, as indicated. The dashed red lines delimit the first BZ.

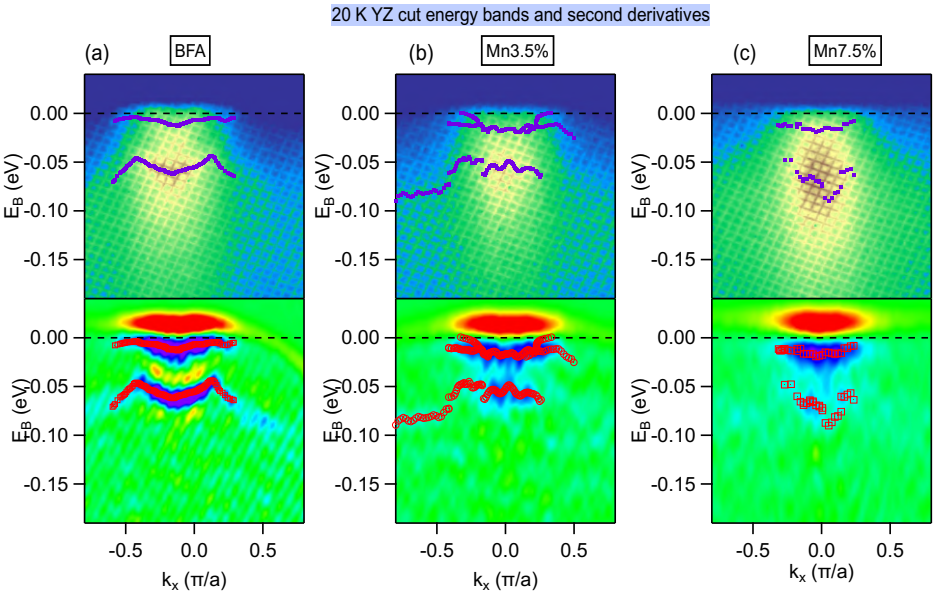

Figure 4.22: Low-temperature energy maps for the YZ direction and its second derivatives for samples (a) BFA, (b) Mn3.5% and (c) Mn7.5%. The marked points represent the points forming the electron pocket band at Y.

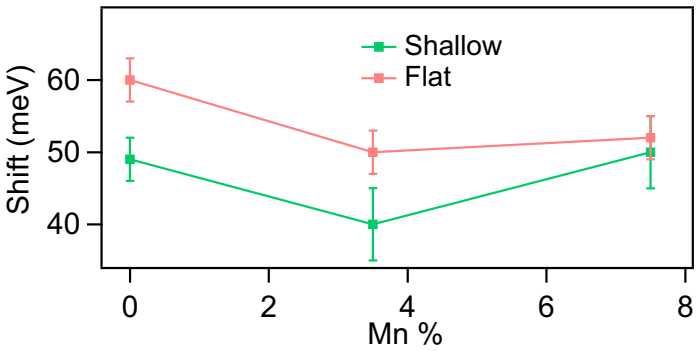

Figure 4.23: Nematic splitting size as a function of Mn content. The green line corresponds to the flat band of ΓX direction, visible for π light polarization in Figure 4.16. The pink line corresponds to the flat shallow electron pocket of YZ direction, visible in the cuts of Figure 4.22.

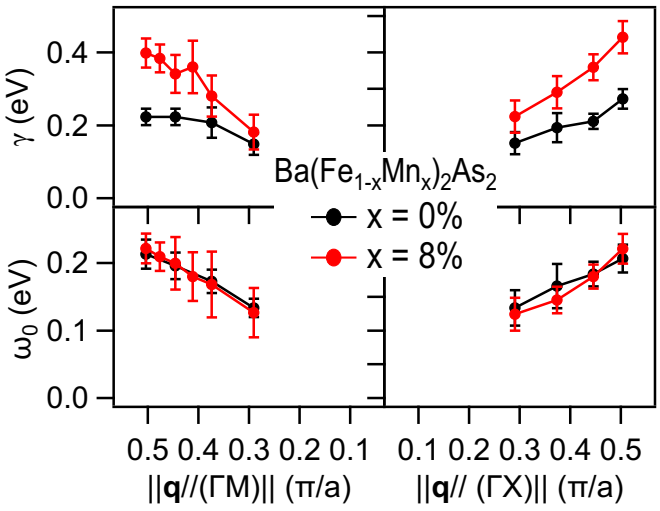

Figure 4.24: RIXS derived magnon damping coefficients (γ) and bare frequencies (ω_0) for 0% and 8% Mn samples as a function of momentum for two directions. Adapted from ref. [7].

4.3 Magnon dispersion results

The spectral function investigation of Section 4.1.1 can be employed for a deeper examination of previous Resonant Inelastic X-ray Scattering (RIXS) experiments of MnBFA samples [7], which characterized the magnon dispersions along ΓX and ΓM as a function of Mn. In Figure 4.24, RIXS extracted parameters, for measurements in the SDW state ($T = 20$ K) are shown. In this analysis, the magnon peak was fitted as a damped harmonic oscillator, for it is proportional to the complex part of the dynamic susceptibility [125, 126]. The oscillator frequency is defined as $\omega_{\mathbf{q}} = \sqrt{\omega_0^2 - (\gamma/2)^2}$, where γ is the magnon damping coefficient and ω_0 is the magnon bare frequencies.

These coefficients are shown in Figure 4.24 for BFA and Mn8.0% samples, as a function of the in-plane momentum, $||\mathbf{q}||$, along the main symmetry directions. As a function of Mn,

ω_0 remains unaffected, whereas γ increases, with the excitations becoming overdamped ($\omega_0 \lessapprox \gamma/2$) for almost all values of $||\boldsymbol{q}||$ in the case of the Mn8.0% sample. This abnormally large magnon damping is not observed in RIXS results for other FeSC materials [126–128].

The RIXS measured magnons in these materials were related to spin flips associated with the d_{xy} orbitals [129]. Therefore, the vanishing of the folded band with d_{xy} character provides a natural explanation for the large damping of the RIXS detected magnons and, in addition, makes a direct connection between the increasing band incoherence and the evolution of magnetic properties, here represented by the large scattering of the magnons.

Chapter 5

ARPES results of lightly Cr substituted $BaFe_2As_2$

In this chapter, the ARPES experimental results for the Cr-substituted samples (CrBFA) $Ba(Fe_{1-x}Cr_x)_2As_2$ are presented. The probed samples are $x = 0, 0.03, 0.085$, referred to as BFA, Cr3%, and Cr8.5%, respectively, as defined in Table 2.2.

To describe the experimental ARPES results and their analysis, the same notation and convention of the previous chapter were adopted. For the Cr3% sample, however, only the electronic structure of the paramagnetic (PM) phase was measured (at $T = 150$ K). Therefore, the low-temperature (LT) analysis presented for the low doping region of the CrBFa phase diagram is more limited.

The methods for the ARPES measurements are described in Section 3.3, and the results here presented will be discussed and put in context with the Mn results for the low doping region of the phase diagram described in the previous Chapter 4.

5.1 High-temperature results

Figure 5.1 shows a survey of the electronic band structures, as a function of Cr content, in the tetragonal PM state ($T = 150$ K) of the CrBFA samples. Measurements were taken along the high-symmetry directions and adopting linear beam polarization as indicated in each panel, for incident energy 80 eV for the BFA sample, 78 eV for the Cr3% sample, and 81 eV for the Cr8.5% sample. It is possible to note how the spectral function depends on the polarization, which again allows associating the spectral features to a main orbital character. Since the degree of substitution is small and the phases are the same, similar bands to the MnBFA case are expected. This time, however, an increase of the hole pockets for the Cr8.5% sample is visible, mainly for the ΓX direction measurements. This will be discussed for the band comparison and the Fermi Surface (FS) data later in this chapter.

Once more, the d_{z^2} derived band appears only for π light polarization for energies close to

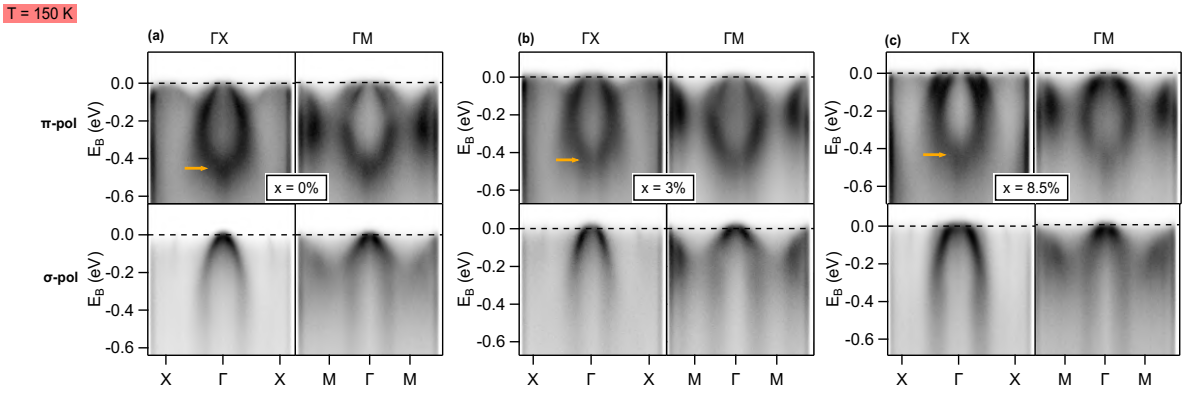

Figure 5.1: Overview of the measured electronic band maps of the (a) BFA, (b) Cr3%, and (c) Cr8.5% samples for high temperature. Measurements were taken along the ΓX and ΓM directions and for σ and π polarizations, as indicated. Higher intensities are darker on the color map.

$E_B = 0.5$ eV, in absolute values. This is marked as orange arrows in the panels of Figure 5.1 for each sample. To inspect the evolution of the d_{z^2} band feature as a function of Cr content, the peak d_{z^2} position was obtained, as shown in Figure 5.2. It was determined with the same method employed for the MnBFA samples. The peak moves to higher binding energy (smaller in absolute value) as the Cr percentage increases.

To compare these results with the one presented in the previous chapter, the Cr percentage was multiplied by two, since the amount of holes theoretically introduced by a Cr atom is twice the amount introduced by Mn. It is possible to observe that the changes in CrBFA are smaller even without considering the doubled amount of holes, with the d_{z^2} peak moving very little. It means that the electronic band derived from d_{z^2} retains a larger bandwidth in the case of CrBFA samples which, in turn, suggests that the hybridization of the d_{z^2} orbitals in CrBFA materials is larger than for the MnBFA samples. Here, again, it is exemplified a case wherein the change in orbital hybridization is a more relevant parameter to understand the evolution of the electronic bands than electronic doping.

To inspect the k_z direction band dispersion for the CrBFA samples, Figure 5.3 shows a similar survey of the electronic band structures to the one from Figure 5.1, but this time for incident energy 62 eV for the BFA sample, 60 eV for the Cr3% sample, and 67 eV for the Cr8.5% sample. It is noteworthy that the d_{z^2} derived band is missing for this k_z level, for the π polarized measurements. The hole pockets are larger for all samples in this energy, and the X electron pockets visible for the σ polarized measurements are more shallow in E_B. Furthermore, there is a considerable change for the Cr8.5% sample band structure compared with the other samples.

The second derivative data for the CrBFA samples at Γ BZ plane is presented in Figure 5.4. The darker spots represent the Lorentzian maximum points. The band features are more distinguishable and clear, but it also depends on the type of derivative. For the ΓX σ polarization,

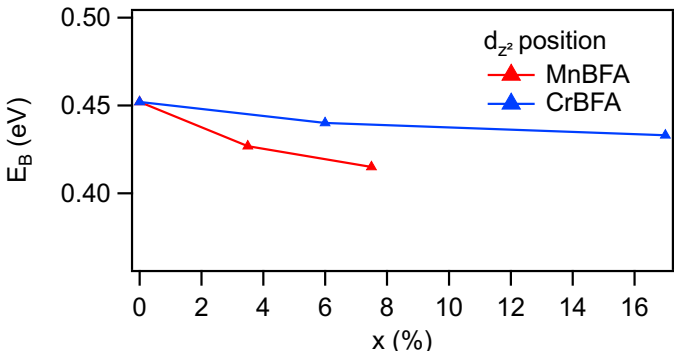

Figure 5.2: Maximum EDC position for the band associated with the d_{z^2} orbital as a function of Cr content (blue points), for the Γ point. The points correspond to the orange arrows marked in the panels of Figure 5.11. The Cr content was multiplied by two to be compared with the MnBFA result of Figure 4.2 (red points) since Cr introduces a double amount of holes when compared with Mn substitution.

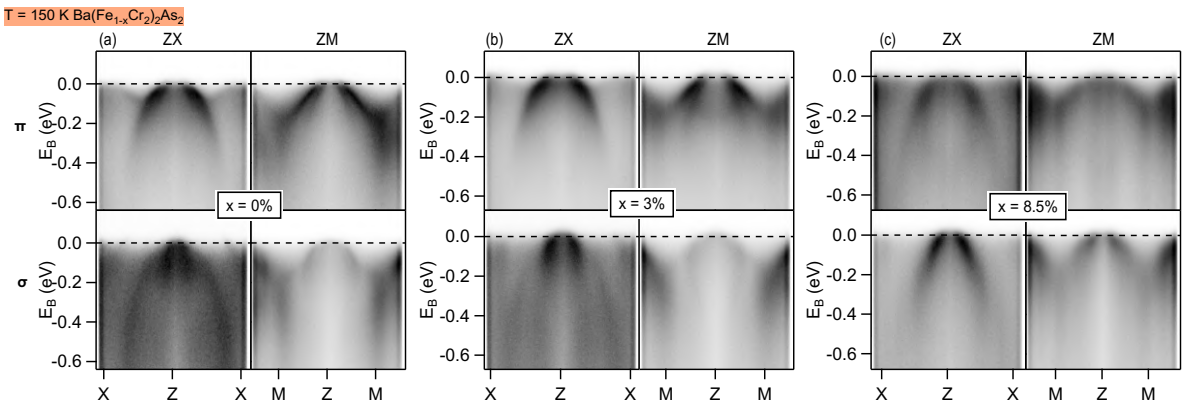

Figure 5.3: Overview of the measured electronic band maps of the (a) BFA, (b) Cr3% and (c) Cr8.5% samples for high temperature. Measurements were taken along the ZX and ZM directions and for σ and π polarization, as indicated.

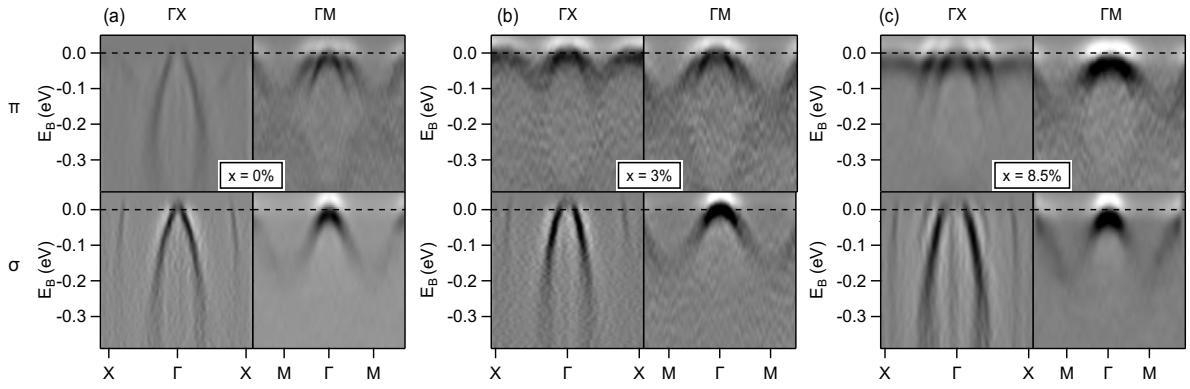

Figure 5.4: CrBFA high-temperature second derivative maps for $k_z = \Gamma$ energy. The high-symmetry direction and polarization for each measurement are indicated. (a) BFA sample results, (b) Cr3% sample results, and (c) Cr8.5% sample results. The band points were fitted to the darker point.

for example, the band closer to the X point, related to the electron pocket, is only visible for momentum derivatives. With these new spectra, it is possible to fit the band point position and determine the band shape and changes with the Cr introduction.

The fitted points are presented in Figure 5.5, where the orbital character is represented in a color code in the legend. The Γ point has two inner hole bands with d_{xz} and d_{yz} characters and one outer band with d_{xy} character. Visible in the ΓX direction, the electron pocket region presents two bands, one that does not cross the Fermi level and is almost flat, of d_{xz} character, for π polarization measurements, and another that forms a deep electron pocket band, of d_{xy} character, for σ polarization. These two bands in the electron pocket region will be termed "flat" and "deep" bands.

The results for the Cr3% sample are remarkably similar to the ones presented for the MnBFA samples in chapter 4. For the Cr8.5% sample, however, there are some changes. Firstly, the outer band with d_{xy} character is visible for σ light polarization for ΓX measurements. This is clear in the second derivative of Figure 5.4. This band is only visible in this experimental configuration for the Cr8.5% sample. Secondly, the flat electron band seems to be moved up and it is much flatter when compared with the BFA sample, which is visible in the ΓX π polarized measurements. Additionally, the $d_{xz/yz}$ hole pockets are bigger and there is a clear distinction between the two bands. It can be speculated that the degree of hybridization with As-derived orbitals is changing the band's main orbital character and symmetry. This can be further analyzed regarding changes in electronic correlations, as shall be discussed for the spectral analysis.

To further investigate these changes for the Cr8.5% sample and the electron pockets, it is possible to recur to the Fermi maps. Fixing the map binding energy to the Fermi level ($E_B = 0$), it is possible to plot the Fermi Surface (FS). In Figures 5.6, and 5.7 there are presented the measured Fermi surfaces (FS) for the samples Cr3%, and Cr8.5%, respectively. Again, it is possible to observe the polarization selectivity for the spectral function. The dashed red lines

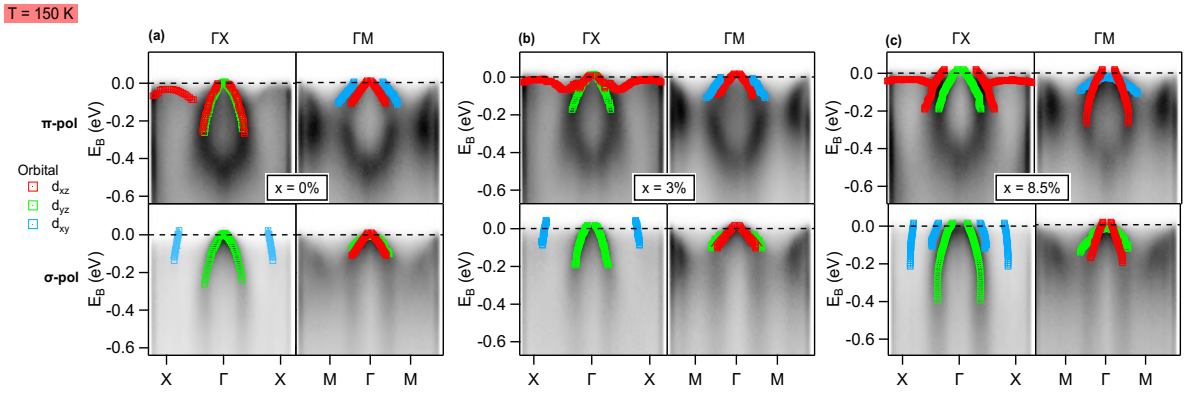

Figure 5.5: Overview of the fitted band points for the (a) BFA, (b) Cr3% and (c) Cr8.5% samples obtained from the second derivatives of Figure 5.4. The orbital character of each band is indicated by the legend color code and was assigned following Tables 3.1 and 3.2.

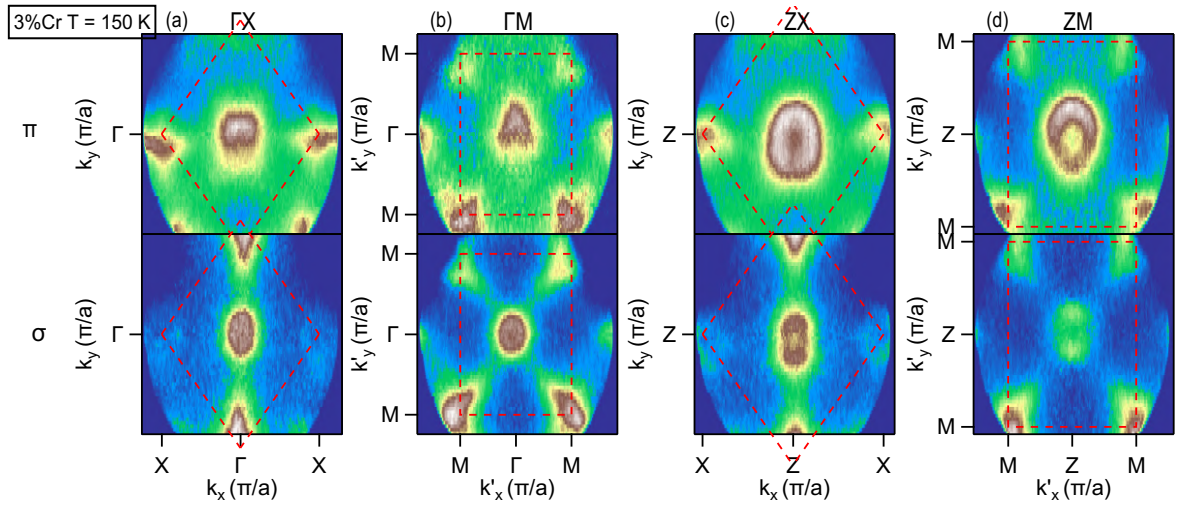

Figure 5.6: High-temperature Fermi Surface measured for the Cr3% sample. Measurements were taken along the ΓX, ΓM, ZX, and ZM directions and for σ and π polarization, as indicated. The dashed red lines delimit the first BZ.

delimit the first BZ, revealing the rotation of the sample high-symmetry direction being probed.

For the Cr3% sample, it is clear that the hole pockets at Γ are larger for the $k_z = \mathrm{Z}$ photon energy, as in the case of the MnBFA samples. Again, the electron pockets measured for the ΓX/ZX directions show different relative intensities for σ polarization. This is a consequence of the selection rules, since this direction is associated with the d_{xz} orbital that forms the X electron pocket, and its intensity is zero for σ polarization, leaving only the d_{xy} weak contribution.

For the ΓX π polarized measurements, it is even more evident the sizable increase of the hole pocket for the Cr8.5% sample. For the same sample, also, the electron pockets for ΓM σ polarized results seem to get more elongated in the ΓX direction, which can be further inspected with high-symmetry cuts reconstruction.

To inspect the electron pocket size as a function of Cr closely, we focus on the X-centered

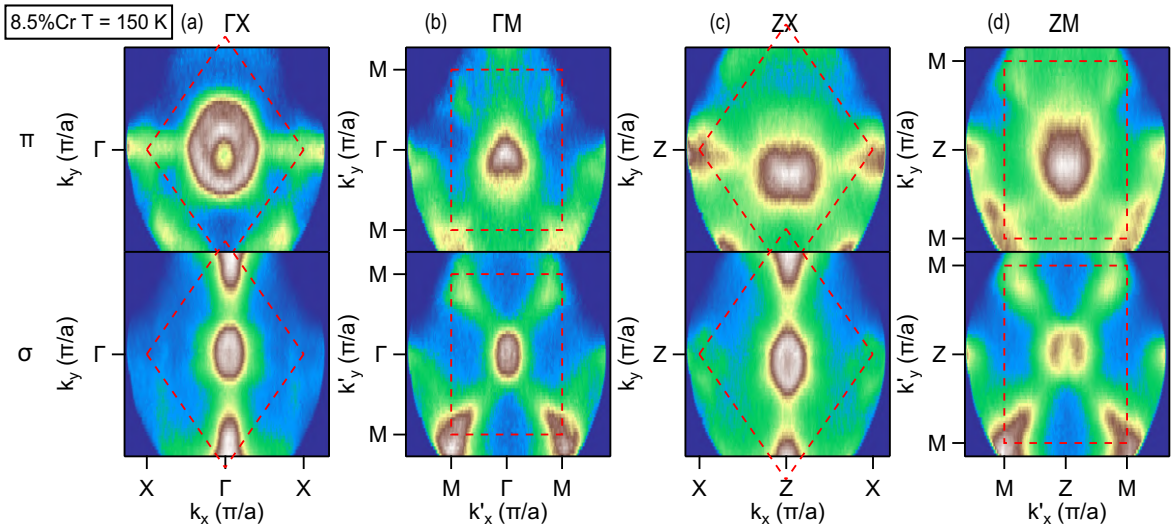

Figure 5.7: High-temperature Fermi Surface measured for the Cr8.5% sample. Measurements were taken along the ΓX, ΓM, ZX, and ZM directions and for σ and π polarization, as indicated. The dashed red lines delimit the first BZ.

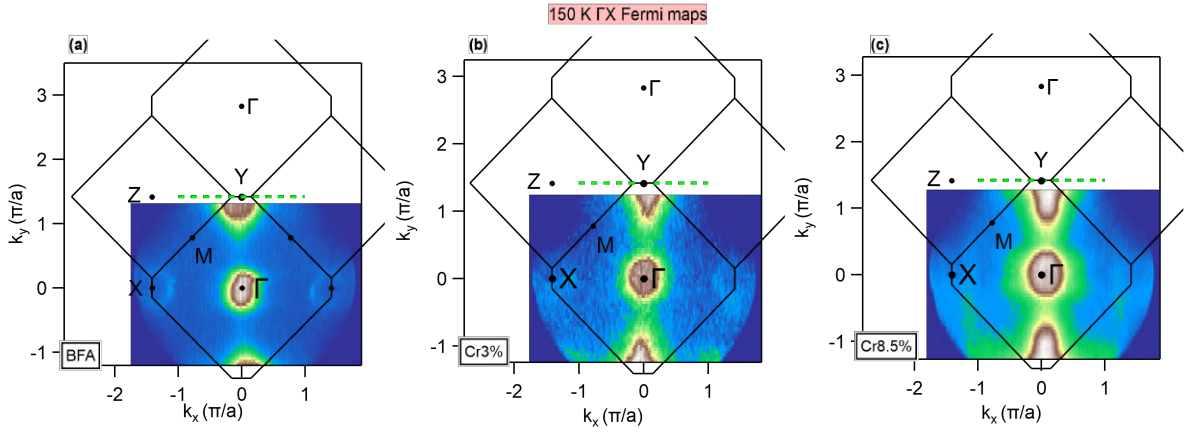

Figure 5.8: Fermi Surface measured for ΓX direction with σ polarization with the BZ drawn and its high-symmetry points indicated for samples (a) BFA, (b) Cr3% and (c) Cr8.5%. The green dashed lines indicate the cut based upon which the electron pockets of Figure 5.9 were reconstructed.

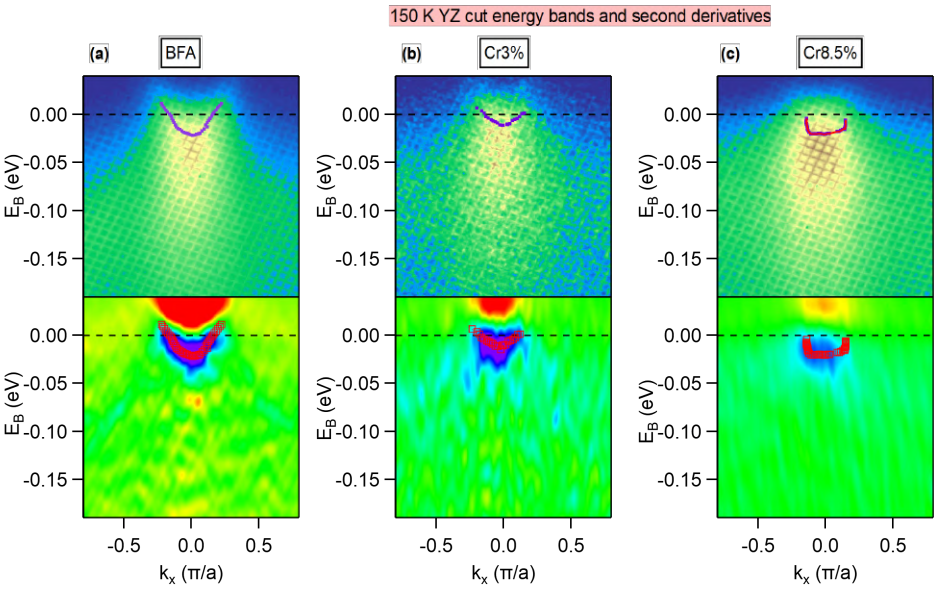

Figure 5.9: High-temperature energy maps for the YZ direction and its second derivatives for samples (a) BFA, (b) Cr3% and (c) Cr8.5%. The marked points represent the points forming the electron pocket band at Y.

electron pocket for ΓX directions and σ light polarization. In Figure 5.8, there is a comparison of the FS maps, for ΓX direction, for the three samples at high temperature. A planar cut of the Brillouin Zone (BZ) is plotted above the FS, with the high-symmetry points highlighted. It is possible to observe the d_{xy} contribution electron pockets at the X points, and the stronger intensity for the Y electron pockets. The green dashed line marks the YZ high-symmetry direction.

In analogy to what was done for the MnBFA samples, by fixing the map k_y to a high-energy point, it is possible to plot the electronic band as a function of k_x and E_B for a different high-symmetry direction, parallel to the measured ΓX direction. This is shown in Figure 5.9, where is possible to see the electron pockets for the YZ high-symmetry direction. These spectra have lower resolution than the electronic bands of figure 5.1, since the Fermi map acquisition mode is different and achieving the same resolution would take several hours. The spectral weight associated with the electron pocket, however, is still visible by choosing a more contrasting color scale. By taking the energy second derivatives of the spectra, it is possible to fit the electron band points, as shown in the lower panels of Figure 5.9. This electron band will be termed a "shallow" electron pocket.

As mentioned, the electron pocket $d_{xz/yz}$ contribution seems to get more elongated with the Cr introduction, but this is not visible in the shallow electron pocket, due to its d_{xy} character. Therefore, in Figure 5.10 there is a similar procedure performed to the ΓM direction XY high-symmetry cut, to obtain another direction to compare the electron pocket evolution. The orange dashed lines indicate the k'_x cut for which the XY direction maps of the lower panels were reconstructed. It is possible to fit, using second derivatives, the band points corresponding to the X pocket right half and Y pocket left half. This is shown as red dots in Figure 5.10. This

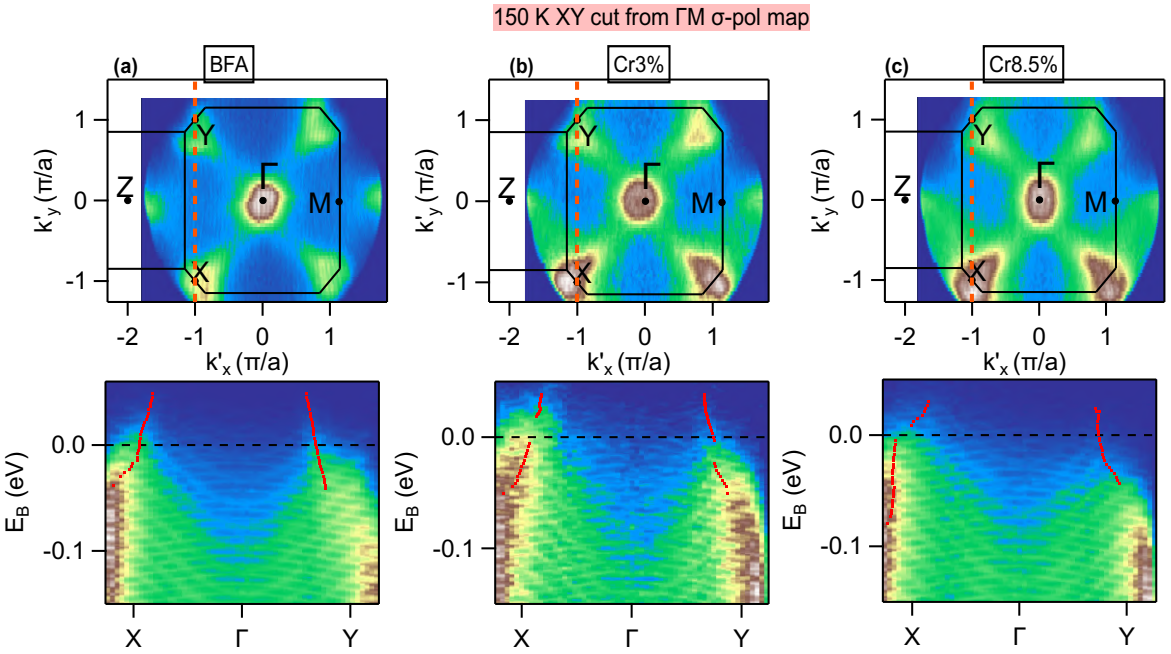

Figure 5.10: Fermi Surface measured for ΓM direction with σ polarization with the BZ drawn and its high-symmetry points indicated for samples (a) BFA, (b) Cr3% and (c) Cr8.5%. The orange dashed lines indicate the cut based upon which the electron pockets of the lower panels were reconstructed. The red dots are the fitted band points from the second derivatives.

band will be termed a "diagonal" electron pocket.

After identifying three hole pocket bands and three electron pocket cuts, it is possible to compare the effect of Cr substitution in these bands. This comparison is shown in Figure 5.11. The focus is on the states in the vicinity of E_F. The hole pockets change as a function of Mn content is summarized in Figures 5.11(a)-(c), while the electron pockets changes are in Figures 5.11(d)-(f).

Treating the evolution of the electronic band structure in terms of the BFA Fermi Surface, as illustrated in figure 4.14 for the MnBFA case, the electron pocket can be considered to consist of a minor and a major axis, forming an ellipse. The minor axis is determined by the shallow electron pocket, of d_{yz} orbital character, while the major axis is determined by the deep electron pocket, of d_{xy} orbital character. By performing a $\pm\sqrt{2}\pi/a$ shift in the ΓX deep electron pockets it is possible to have the parabola as shown in Figure 5.11(e). Similarly, a $\pm\pi/a$ shift in the XY diagonal electron pocket is possible to achieve the parabola of Figure 5.11(f).

This time, one can observe an increase in the hole pockets as a consequence of the hole doping caused by Cr, at least for the Cr8.5% sample. Bands forming the hole pockets seem to increase their Fermi energy crossing point positions in momentum k_F. This is particularly visible for the outer d_{xy} hole pocket. The bands forming the electron pocket, however, seem less affected by Cr. This represents a greater detuning of the nesting condition when compared with the MnBFA results. To better visualize these changes, Figure 5.12 shows the extracted

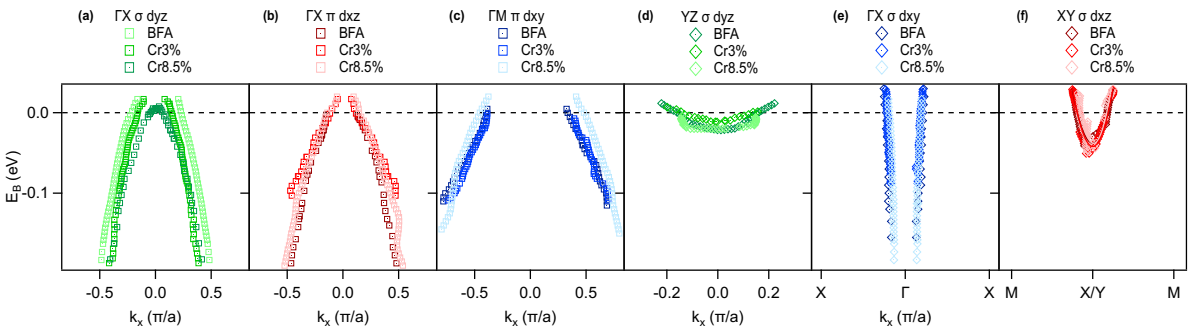

Figure 5.11: Comparison between the band points for the three samples. Lighter markers indicate more Cr content and the orbital color code follows the legend of Figure 5.5. (a)-(c) Γ centered hole-like bands. (d)-(f) X/Y centered electron-like bands.

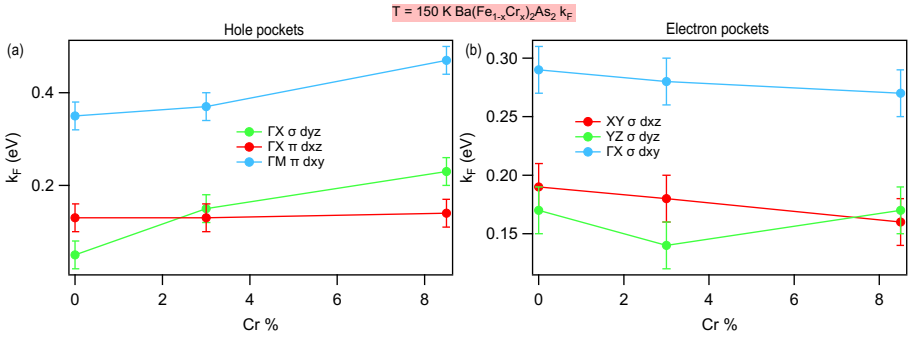

Figure 5.12: Comparison between the Fermi vectors k_F for the three samples based on the fitted band points of Figure 5.11. (a) Γ centered hole-like bands. (b) X/Y centered electron-like bands.

k_F from each band of Figure 5.11 and for the electron pocket high-symmetry cuts of Figures 5.9 and 5.10. As expected, the most striking change occurs for the outer hole pocket with d_{xy} character, which increases considerably as a signature of the hole doping. At the same time, electron pockets are getting systematically smaller with Cr, but the observed changes are within error bars.

With these results, it is clear that the same degree of transition metal substitution acts differently for the MnBFA and CrBFA systems. This will be further explored in the spectral analysis in the following section.

5.1.1 Self-energy analysis

It is interesting to perform a quantitative analysis of the ARPES spectral function $A(\mathbf{k}, E)$ to compare with what was previously found for the MnBFA samples. To do so, the spectral analysis was done by fitting the momentum distribution curves (MDCs) to the expression for the one-particle $A(\mathbf{k}, E)$ (equation 3.14). The objective is to extract the electronic scattering rate $\Gamma(E)$ as a function of the binding energy E.

The analysis for the band in ΓX direction and σ light polarization, with d_{yz} main orbital character, is presented in Figures 5.13(a)-(c) for samples BFA, Cr3% and Cr8.5%, respectively. This analysis again follows Refs. [87, 86], where the "all at once" fitting method is presented. When the multiband character is in play, however, the method could not be implemented, due to the twice as large number of parameters necessary to minimize the square fitting of all MDCs simultaneously.

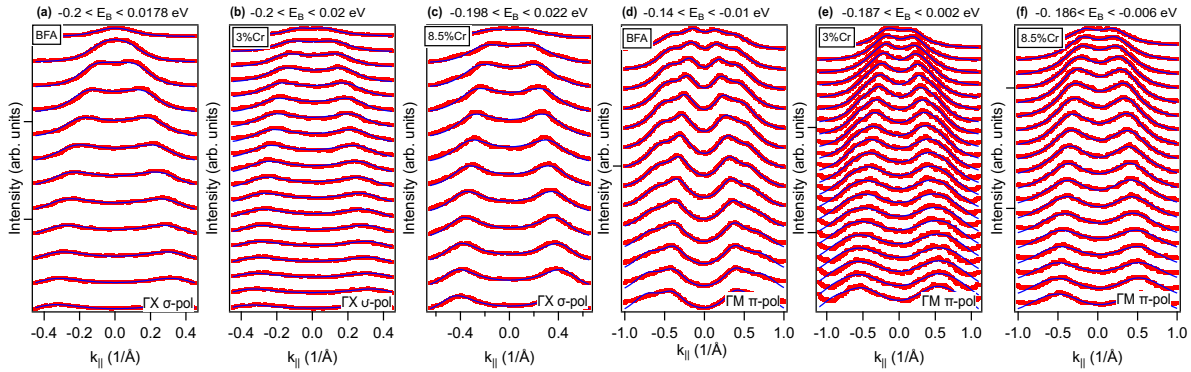

Figure 5.13: ARPES spectral function analysis. Fittings (blue lines) of several MDCs (red dots) for increasing binding energies. (a)-(c) data obtained for σ polarization, measured along ΓX for samples BFA, Cr3% and Cr8.5%, as indicated, with a single band fitting. (d)-(f) data obtained for π polarization, measured along ΓM for samples BFA, Cr3% and Cr8.5%, with a double band fitting.

Therefore, for the analysis of the band with d_{yz} main orbital character, measured along the ΓM direction and π light polarization, a one-by-one fitting of the MDCs was performed. These two methods are described in Section 4.1.1. The Lorentzian peak positions can have as the

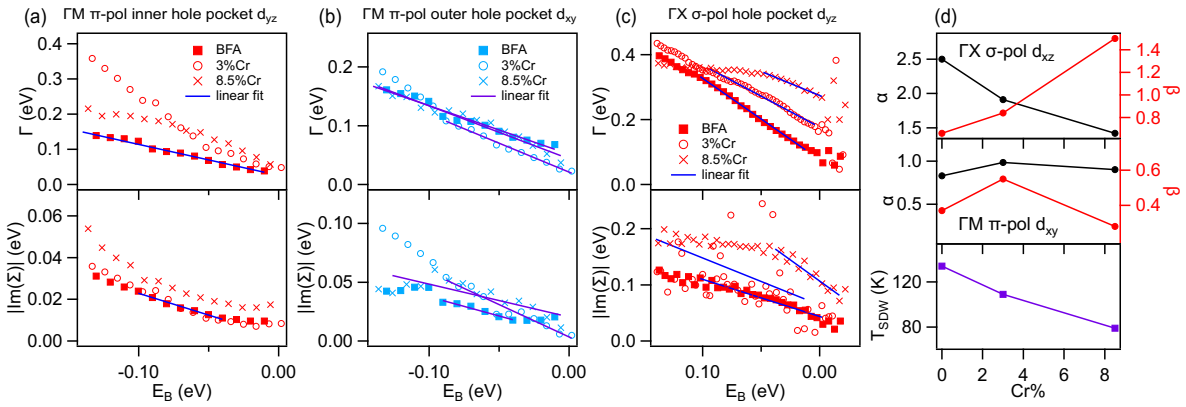

Figure 5.14: ARPES spectral function analysis resulting scattering rate $\Gamma(E)$ and imaginary part of self-energy $\mathrm{Im}\Sigma(E)$ for (a) ΓM inner hole pocket band, (b) ΓM outer hole pocket band and (c) ΓX single hole pocket band. The blue and purple lines indicate linear fittings close to the Fermi level. (d) resulting linear coefficients from panels (b) and (c) and the T_{SDW} behavior as a function of Cr content.

initial guess the bands obtained from the second derivative process, the points of Figure 5.5. The resulting fitting of two bands is presented in Figures 5.13(d)-(f). For the one-by-one fitting method the energy and momentum finite resolution and finite temperature were not considered, but suitable fittings could be performed nevertheless.

Given the two methods used, the results cannot be reliably compared between bands fitted with these different methods, and only the trend as a function of Cr for each band is a trustworthy result. To analyze this trend it is possible to compare the scattering rates as a function of binding energy $\Gamma(E)$ for the three samples, as shown on the top panels of Figures 5.14(a)-(c), where the (a) and (b) panels are results from the two-band fitting of ΓM direction and the (c) panel have the results of one-band all-at-once fitting of ΓX direction.

Again, a marginal Fermi liquid (MFL) behavior is employed to analyze the data, due to the linear behavior of $\Gamma(E)$. Therefore, the relation between $\Gamma(E)$ and Σ'' will follow the expression 3.17, from where Σ'' can be extracted, as shown on the bottom panels of Figures 5.14(a)-(c).

In the vicinity of E_F, for all bands, $\Gamma(E)$ and $\mathrm{Im}\Sigma(E)$ are fairly well described as linear functions of E, within the paradigm of an MFL regime. The slopes, or angular coefficients, related to $\Gamma(E)$ and $\mathrm{Im}\Sigma(E)$ can be defined as α and β, respectively.

Again, α is a measurement of the electronic states' coherence. In this sense, a decrease of α as a function of Cr content would correspond to a weaker response of $\Gamma(E)$ to the binding energy which translates into a decrease in band incoherence. On the other hand, an increase in β is related to increasing electronic correlations. The α and β angular coefficients of the curves of Figures 5.14 (b) and (c) are obtained as a function of Cr content and are presented in Figure5.14(d) for bands with main d_{yz} (top panel) and d_{xy} (middle panel) orbital character. The lower panel shows the T_{SDW} as a function of Cr content.

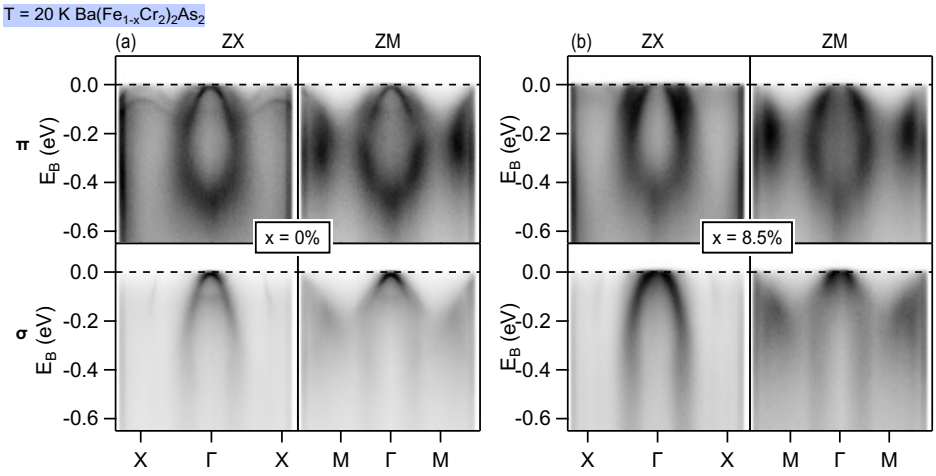

Figure 5.15: Overview of the measured electronic band maps of the (a) BFA and (b) Cr8.5% samples for low temperature. Measurements were taken along the ΓX and ΓM directions and for σ and π polarization, as indicated.

Overall, $\alpha(d_{yz})$ decreases with Cr introduction while $\alpha(d_{xy})$ is almost constant. $\beta(d_{yz})$ increases and $\beta(d_{xy})$ oscillates in function of Cr percentage. An increase of electronic correlations is expected on the CrBFA phase diagram [69], this is reflected on the d_{yz} derived orbital, but not on the d_{xy}. This can be rationalized in terms of effective hole doping. Since the d_{xy} is the higher orbital in energy [4, 101], it would form the hole pocket with the highest depleting of electrons, hindering the increase of electronic correlations associated with this orbital.

5.2 Low-temperature results

The same measurements performed for all samples, incident light polarization, and high-symmetry directions for the paramagnetic stare were replicated in the magnetically ordered state. In Figure 5.15 there is a survey of the electronic band structures as a function of Cr content in the orthorhombic SDW state, measured at $T = 20$ K for BFA and Cr8.5% samples. The bands are more visible due to less thermal broadening and reduced effect of the Fermi-Dirac distribution close to the Fermi level. The nematic splitting and the expected SDW folding features are visible for the BFA sample, as explained in the previous chapter.

Without the low-temperature data for the Cr3% sample is not possible to perform a low-temperature study as a function of Cr content, such as was done for the paramagnetic state. In this case, this brief section is focused on inspecting the properties of the Cr8.5% sample on the ordered state. In this regard, in Figure 5.15 it is visible that, as in the case of Mn7.5% sample, the Cr8.5% sample shows no sign of SDW band folding. The bands are the same as the paramagnetic ones, with the difference in the splitting of the d_{xz} flat electron band, visible for the ZX direction measurements using π light polarization, being very smeared out. The increase in the hole pockets is again clear, and the outer hole pocket spectral weight for the ΓX

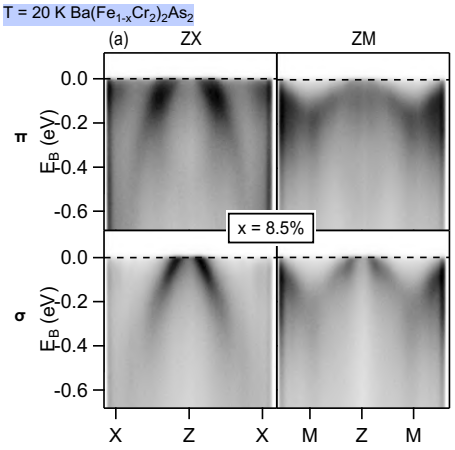

Figure 5.16: Overview of the measured electronic band maps of the Cr8.5% sample for low temperature. Measurements were taken along the ZX and ZM directions and for σ and π polarization, as indicated.

σ polarized measurement is present.

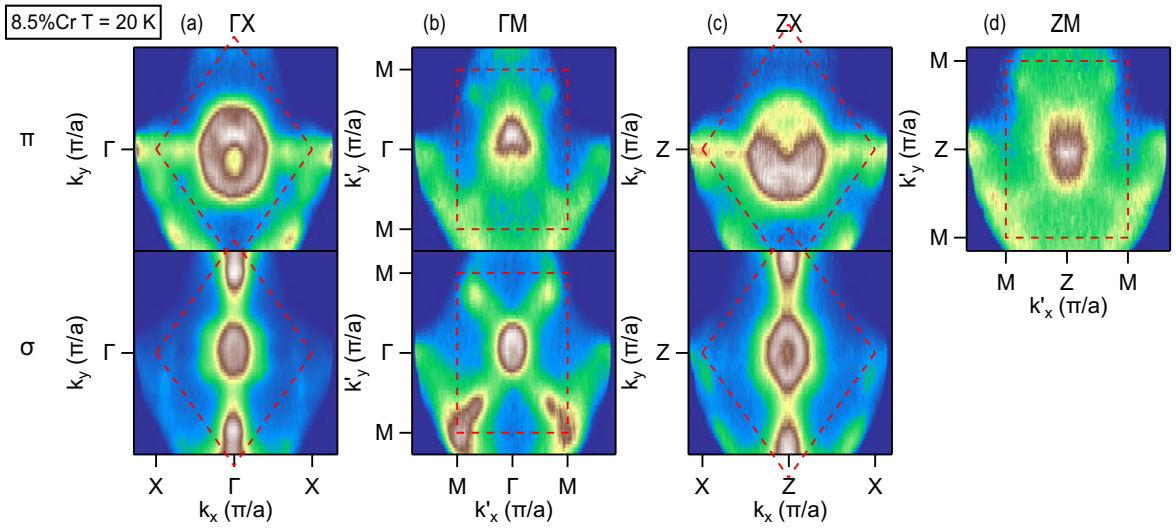

Figure 5.17: Low-temperature Fermi Surface measured for the Cr8.5% sample. Measurements were taken along the ΓX, ΓM, ZX, and ZM directions and for σ and π polarization, as indicated. The dashed red lines delimit the first BZ.

To investigate the absence of band folding, measurements for incoming photon energy probing the k_z = Z plane of the reciprocal space can be inspected. In Figure 5.16, for the π polarized data there is no sign of the d_{z^2} band, as expected, but there is also no sign of band folding.

For the case of Mn7.5%, this was rationalized in terms of increasing incoherence of the d_{xy} electron pocket that folds into the Γ point and increasing localization of the Fe moments. For the Cr8.5% sample, however, the α_{xy} parameter associated with this orbital incoherence is almost constant, leaving only the increasing localization as an explanation. This absence of folded bands in both cases calls for more investigation.

The overview of the Fermi Surfaces for the Cr8.5% sample is shown in Figure 5.17, where the dashed red lines delimit the first BZ. The hole band increased size is visible in all directions and polarization. By a close inspection of ΓX and ZX π polarized data, it is possible to see small dot-like pockets around the X point. This was observed before [121] for BFA and was interpreted in terms of a twinned AFM reconstruction, not derived from folding. If the ordered electronic band structure results from a different mechanism for the samples BFA and Cr8.5% it is still up for debate.

5.3 RIXS results

Resonant Inelastic X-ray Scattering (RIXS) is a powerful technique that allows the investigation of low-energy excitations in a material. These excitations must be charge-neutral and are limited in their energy scale by the experimental energy resolution. This technique is described in detail in Appendix A, where the fundamentals and experimental setups are explained and presented along with the optical study of the IPE beamline spectrometer.

For CrBFA, the magnetic ground state changes between an itinerant SDW state with stripe order symmetry to a localized AFM state with G-type order symmetry [46, 58]. Therefore, the substitution of Fe by Cr leads to the coexistence of magnetic fluctuations with different symmetries, which compete to form different ground states along the phase diagram. Besides, the SDW order is preceded by a structural orthorhombic transition related to the nematic phase. In the AFM state, a such transition does not occur, revealing a suppression of nematic transition as a function of Cr content [130].

With RIXS results for the Cr3% and Cr8.5% samples at the Fe edge, it is possible to investigate the magnetic excitations as a function of high-symmetry direction and momentum and compare it with previous BFA and MnBFA results [7].

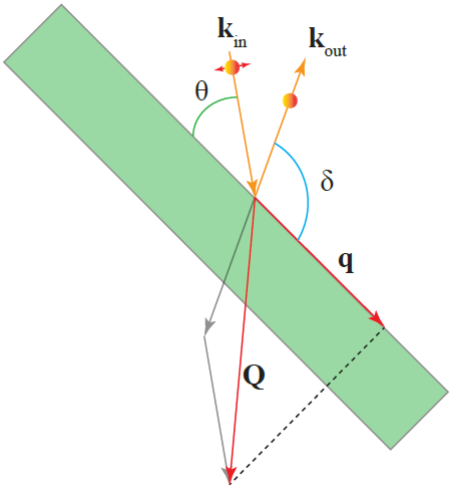

Figure 5.18: RIXS experimental geometry. The backscattering angle is defined as $\psi = \theta + \alpha$ and was kept as $\psi = 130°$

The RIXS results here presented were taken at the I21 beamline of the Diamond Light Source, in April 2023. All spectra were taken with incident photon energy at the maximum resonance of FeL_3 XAS spectrum with $h\nu = 709.5$ eV, using π polarized light and for a fixed temperature of $T = 15$ K. The total energy resolution of the experiment was about 30 meV, extracted from the full width at half maximum (FWHM) of the elastic scattering of a carbon-filled acrylic tape.

The measurements were taken with backscattering geometry, defined by an acute angle between the incidence direction and the detection direction. This geometry allows detecting photons with higher momentum transfer to the sample, following the equations 5.1 and 5.2, where λ is the incoming photon wavelength, ψ is the scattering angle, $\mathbf{Q}$ is the total transferred momentum and $\mathbf{q}_{\parallel}$ is the transferred momentum projection into the sample plane. Such configuration is illustrated in Figure 5.18.

$$|\mathbf{Q}| = \frac{4\pi}{\lambda} \sin\left(\frac{\psi}{2}\right) \tag{5.1}$$

$$|\mathbf{q}_{\parallel}| = |\mathbf{Q}| \sin\left(\frac{\psi}{2} - \theta\right) \tag{5.2}$$

During the experiments, the scattering angle was kept as $\psi = \alpha + \theta = 154°$, with the spectrometer arm fixed, and the sample was rotated inside the experimental chamber to vary the incident angle θ. As lower as θ is, the higher will be the transferred momentum projection $\mathbf{q}_{\parallel}$. The corresponding variation of the out-of-plane component $\mathbf{q}_{\perp}$ is not considered since the Fe order is expected to be almost 2D.

Considering mechanical limitations and the efficiency of sample surface reflection, the smallest angle to achieve is $\theta \approx 15°$, corresponding to the grazing incidence direction. The smaller possible $\mathbf{q}_{\parallel} = 0$ will be when $\theta = \alpha = \psi/2$, with no in-plane momentum transfer, which is called specular geometry.

The samples were glued to the sample holder using silver epoxy. A metal cylindrical pin was glued on top of the sample for the cleaving inside the load lock, with pressures close to 1×10^{-8} mbar. A pressure of 3×10^{-10} mbar or better was achieved in the sample chamber. All results here described are adopting a 1-Fe 2D unit cell, as shown in Table 2.1, with a lattice parameter of $a = 2.80$ Å. In this notation, the $[100]$ direction corresponds to the diagonal of the 1-Fe lattice, along (π,π), while the $[110]$ direction corresponds to the Fe-Fe first neighbor distance along (π,0). To keep parallel with the ARPES results, these directions will also be referred to as ΓM for (π,π) and ΓX for (π,0).

For each high-symmetry direction, some different points of θ were used to probe a RIXS spectrum with different $\mathbf{q}_{\parallel}$ values. This results in several RIXS spectra to be analyzed for their magnetic excitation contribution.

Figure 5.19 shows the RIXS spectrum and fittings for the BFA sample along the Fe second neighbor, or $[100]$, direction and momentum transfer of $Q = 0.63$ Å^{-1}. In the left panel, the

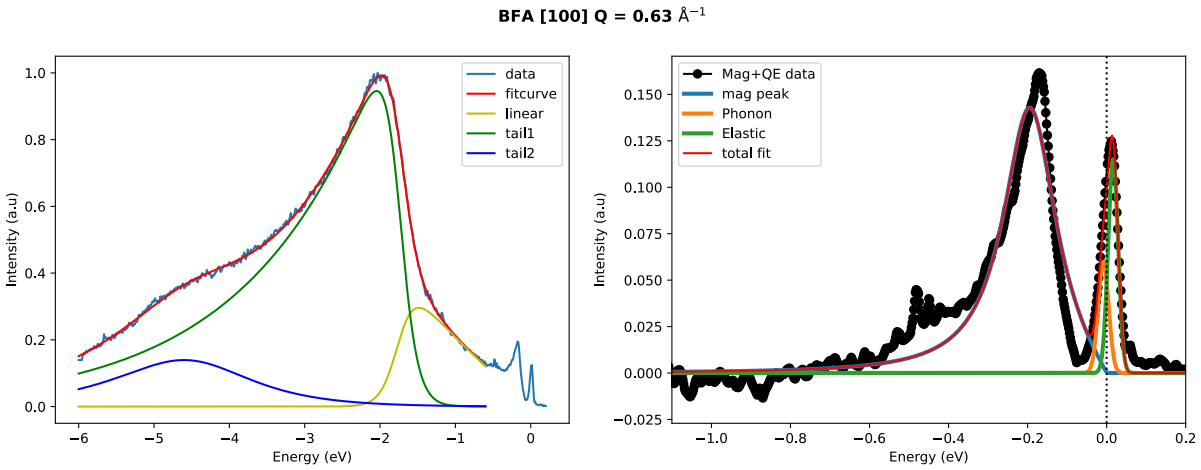

Figure 5.19: Left: RIXS spectrum for the BFA sample along the crystallographic $[100]$ direction and momentum transfer of $Q = 0.63$ Å^{-1}. The red line represents the curve fitted to extract the fluorescence background contribution. Right: the black points represent the resultant spectrum after the subtraction, which is fitted to the red curve. The fitting contributions are discussed in the text.

fluorescence background related to charge excitations is fitted to a model, shown as a red line and described below, and it is then subtracted, resulting in the black points of the right panel.

After this subtraction, the resulting spectrum is then fitted to a function, shown as a red line in the right panel, consisting of the sum of a magnon peak (blue line) and a quasi-elastic (QE) part, which is composed of the elastic line contribution (green line) and a phonon peak (orange line), both fitted using energy resolution limited Gaussian peaks.

The fluorescence background was fitted to a phenomenological model introduced by Yang et al. [131] as implemented already for the 11 and BFA compounds [132, 126]. The model separates the background into three regions with two crossover functions between them. The regions correspond to a linear behavior close to energy transfer $E \approx -1$ eV, shown as a yellow line, one exponential curve in the region to $-4.5 \lessapprox E \lessapprox -2$ eV, shown as a green line, and another exponential curve in the region $-6 \lessapprox E \lessapprox -4.5$ eV, represented by a navy blue line. The complete model is depicted with the red line, which is a sum of the other three lines.

This model is described in equation 5.3, where the three curves are weighted by coefficients α, β, and γ. In this model, the frequency ω corresponds to the transferred energy, which is defined as negative by $E = E_d - E_i$, where E_d is the detected photon energy and $E_i = \mu h$ is the incident photon energy. The parameter a, b, and c determine the exponential shape.

$$I_{fluo} = \alpha \exp(-a\omega)\omega(1 - g_{\Gamma_1}) + \beta \exp(b\omega)g_{\Gamma_1} + \gamma \exp(c\omega) - g_{\Gamma_2} \tag{5.3}$$

The function that is responsible for the crossover between the curves is described in equation 5.4, where $\omega_{1,2}$ is the crossover position in transferred energy E and $\Gamma_{1,2}$ determines the width of the crossover region.

$$g_{\Gamma_{1,2}} = (\exp(-(\omega - \omega_{1.2})/\Gamma_{1,2}) + 1)^{-1} \tag{5.4}$$

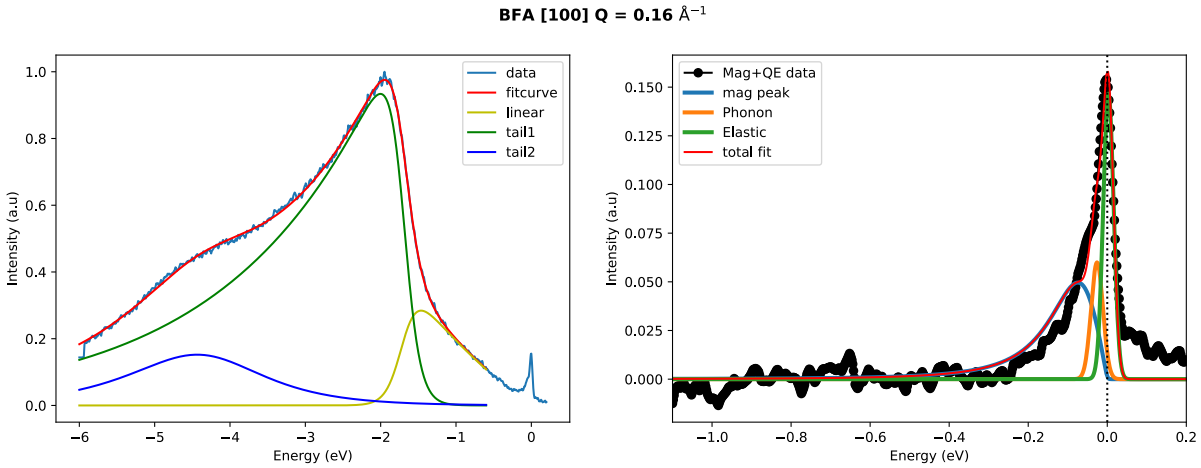

Figure 5.20: RIXS spectrum and fittings for the BFA sample along the crystallographic [100] direction and momentum transfer of $Q = 0.16$ Å^{-1}. The curves and fitting contributions are discussed in the text.

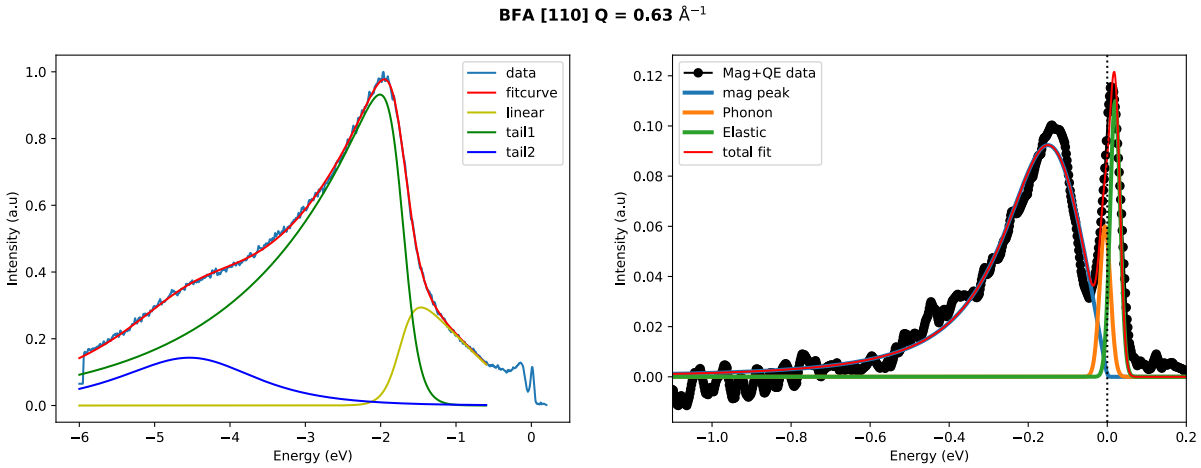

Figure 5.21: RIXS spectrum and fittings for the BFA sample along the crystallographic [110] direction and momentum transfer of $Q = 0.63$ Å^{-1}. The curves and fitting contributions are discussed in the text.

Examples of fittings for the highest and lowest momentum points of each direction for each sample are shown in Figures 5.19 to 5.30. The sample, direction, and transferred momentum are described in each figure. The data were normalized by the maximum fluorescence intensity, allowing a proper comparison of the quasi-elastic and magnon peaks intensity as a function of momentum and Cr concentration.

As we can observe, the quasi-elastic peak gets bigger as a function of Cr content, getting more intense than the fluorescence background for the Cr8.5% sample. The magnon peak, by its turn, is clearly visible for the maximum transferred momentum point for every sample, but

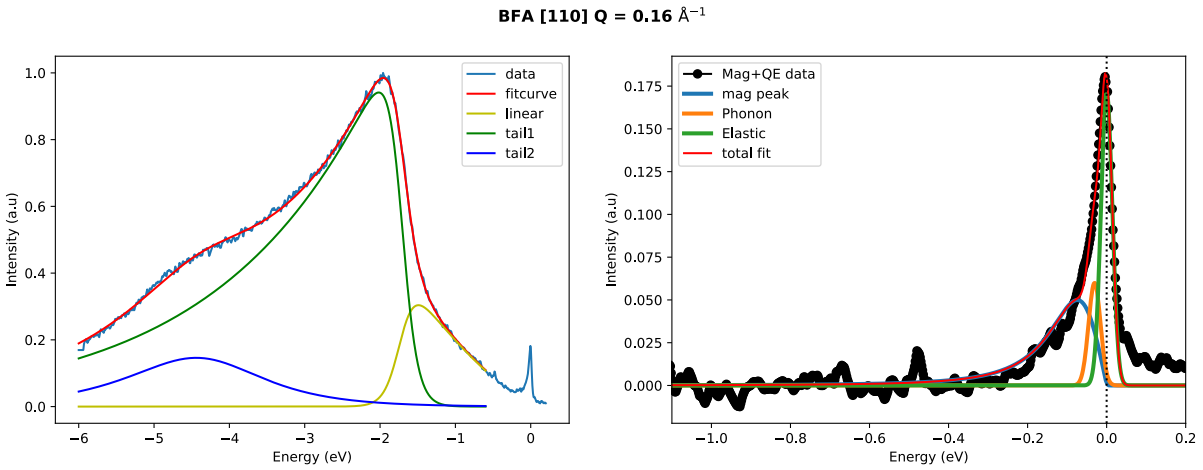

Figure 5.22: RIXS spectrum and fittings for the BFA sample along the crystallographic [110] direction and momentum transfer of $Q = 0.16$ Å^{-1}. The curves and fitting contributions are discussed in the text.

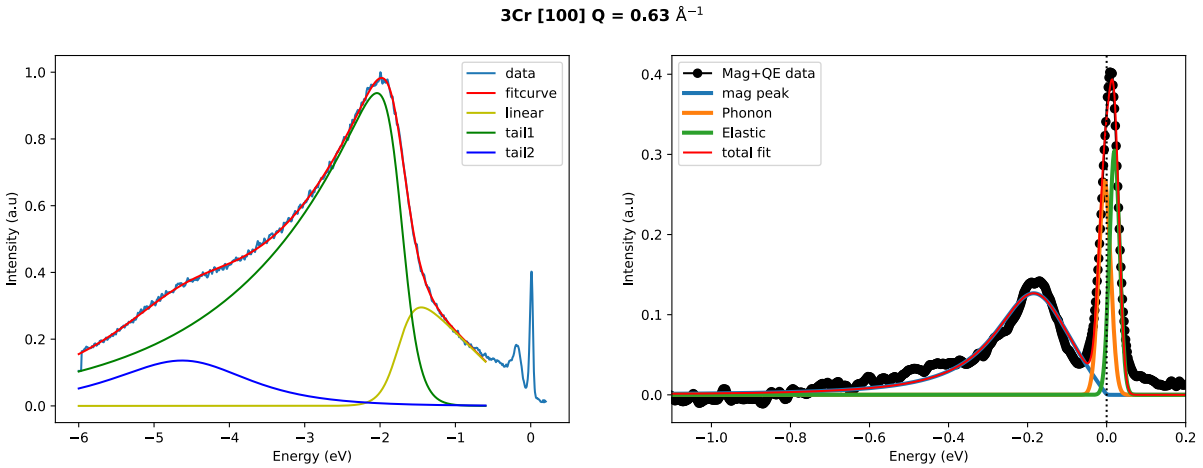

Figure 5.23: RIXS spectrum and fittings for the Cr3% sample along the crystallographic [100] direction and momentum transfer of $Q = 0.63$ Å^{-1}. The curves and fitting contributions are discussed in the text.

when the transferred moment gets smaller, it resembles a shoulder of the quasi-elastic peak, revealing the magnon dispersive behavior.

To gain a more quantitative insight into the magnon behavior, it can be fitted to the complex part of the dynamic susceptibility $\chi''(\omega)$, as shown in Equation 5.5 [126, 125], where the $\mathbf{q}$ dependency reveals the magnon dispersion. This equation has the form of an antisymmetric Lorentzian peak. To avoid redundant notation, the peak FWHM will be called γ in the RIXS results.

$$\chi''(\omega) = \frac{\chi_0''}{2\omega_q}\left(\frac{\gamma/2}{(\omega-\omega_q)^2+(\gamma/2)^2} - \frac{\Gamma/2}{(\omega+\omega_q)^2+(\gamma/2)^2}\right) \tag{5.5}$$

Within this approach, the peak can be interpreted like a damped harmonic oscillator [7], where χ_0'' is an intensity constant, γ is the excitation lifetime, and ω_q is the propagation fre-

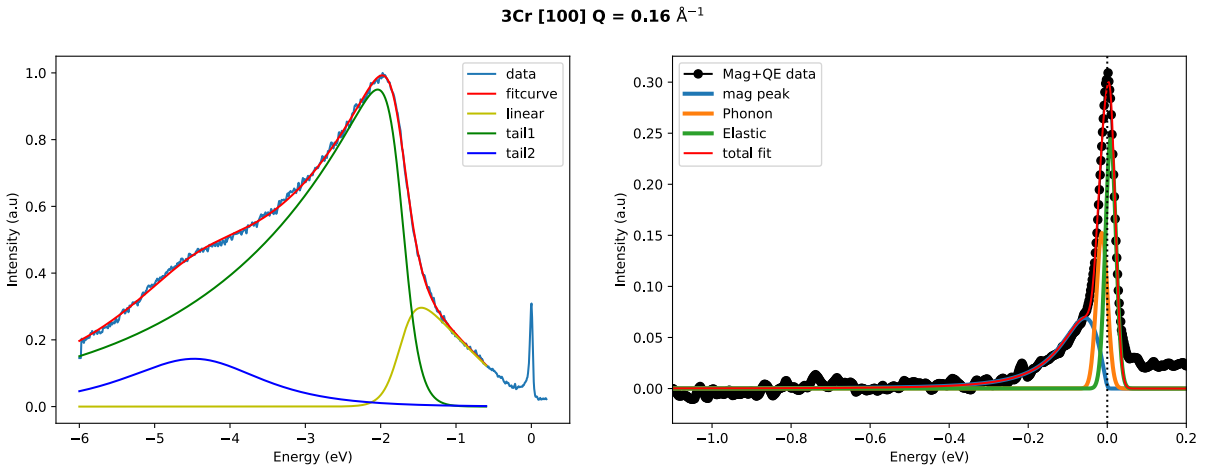

Figure 5.24: RIXS spectrum and fittings for the Cr3% sample along the crystallographic [100] direction and momentum transfer of $Q = 0.16$ Å^{-1}. The curves and fitting contributions are discussed in the text.

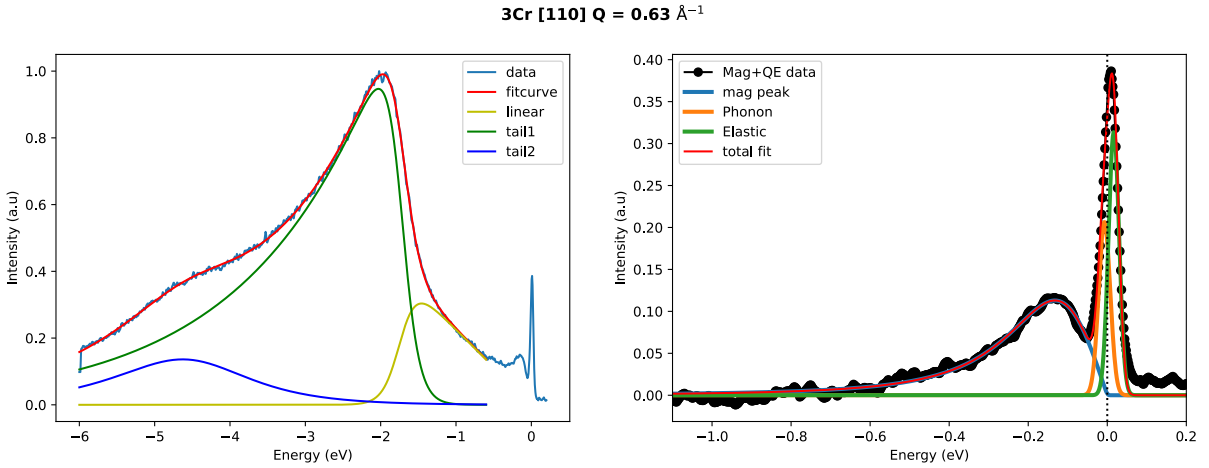

Figure 5.25: RIXS spectrum and fittings for the Cr3% sample along the crystallographic [110] direction and momentum transfer of $Q = 0.63$ Å^{-1}. The curves and fitting contributions are discussed in the text.

quency of the excitation along the $\mathbf{q}$ direction. The excitation bare frequency without the damping effect can be defined as $\omega_0 = \sqrt{\omega_q^2 + (\gamma/2)^2}$.

By inspecting the $\Delta E(\mathbf{q})$ in Figure 5.31, which is the maximum position of the fitted magnetic peak as a function of momentum, it is possible to observe the energy dispersion of the magnon peak as a function of direction and transferred momentum. For the (π, π) direction, the Cr3% sample dispersion is almost the same as the one for the parent compound measured in the same experimental conditions. The Cr8.5% sample dispersion is not dispersing as much, showing the suppression of the Fe second neighbors spin excitation with Cr introduction.

For the $(\pi, 0)$ direction, the Cr3% sample dispersion is suppressed when compared with the BFA samples, revealing an anisotropic magnon hindering in this substitution level. The Cr8.5% is equally suppressed in both directions, which is in contrast with the Mn8% sample, as we saw

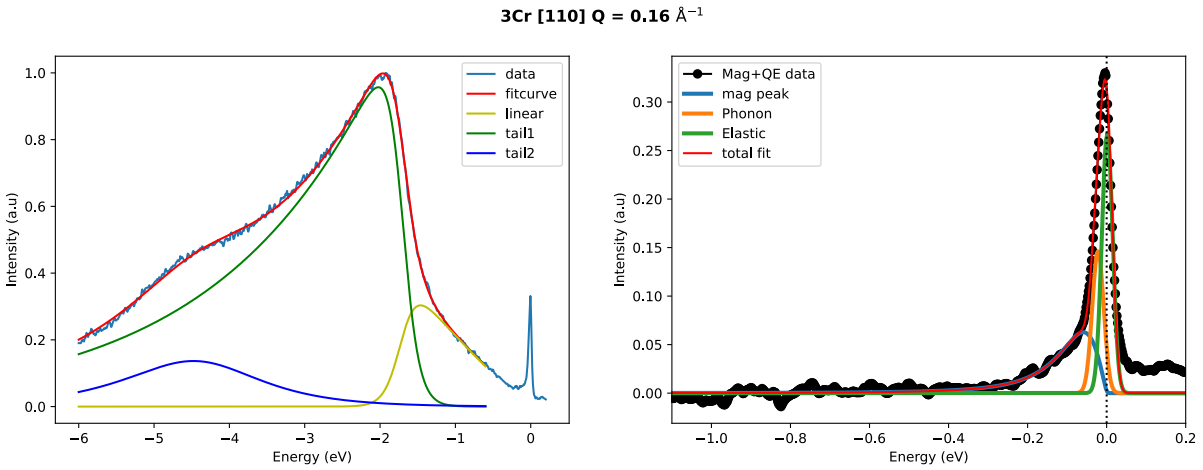

Figure 5.26: RIXS spectrum and fittings for the Cr3% sample along the crystallographic [110] direction and momentum transfer of $Q = 0.16$ Å^{-1}. The curves and fitting contributions are discussed in the text.

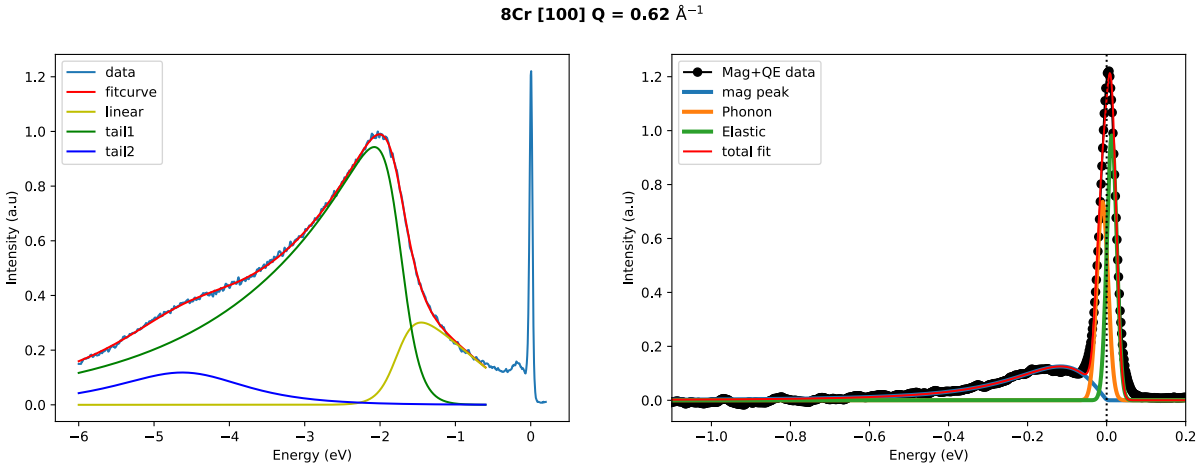

Figure 5.27: RIXS spectrum and fittings for the Cr8.5% sample along the crystallographic [100] direction and momentum transfer of $Q = 0.62$ Å^{-1}. The curves and fitting contributions are discussed in the text.

in the previous chapter. In this regard, it seems like 3% Cr acts similarly to 8% Mn substitution when it comes to magnon dispersion anisotropic damping, suppressing the Fe-Fe direction spin excitation.

To further investigate this effect, we can analyze also the trend of the bare frequency ω and the damping coefficient γ, as shown in Figures 5.32 and 5.33.

The bare frequency is almost sample independent, showing a $\mathbf{q}$ dispersion very similar for both $(\pi, 0)$ and (π, π) directions for all samples. On the other hand, analyzing the corresponding damping, it is possible to conclude that, for the Cr8.5% sample, the oscillator is overdamped in both directions, which represents the hindering of the magnon excitations in a more isotropic fashion. For the Cr3% sample, the magnon peak is overdamped for the (π, π) direction, meaning an isotropic hindering of spin excitations, which is stronger for Fe-Fe direction.

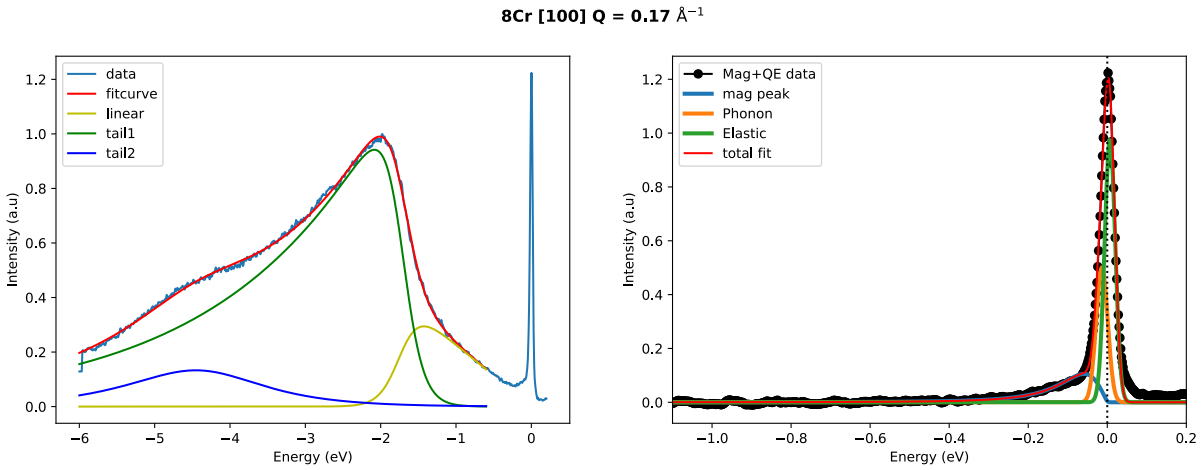

Figure 5.28: RIXS spectrum and fittings for the Cr8.5% sample along the crystallographic $[100]$ direction and momentum transfer of $Q = 0.17$ Å^{-1}. The curves and fitting contributions are discussed in the text.

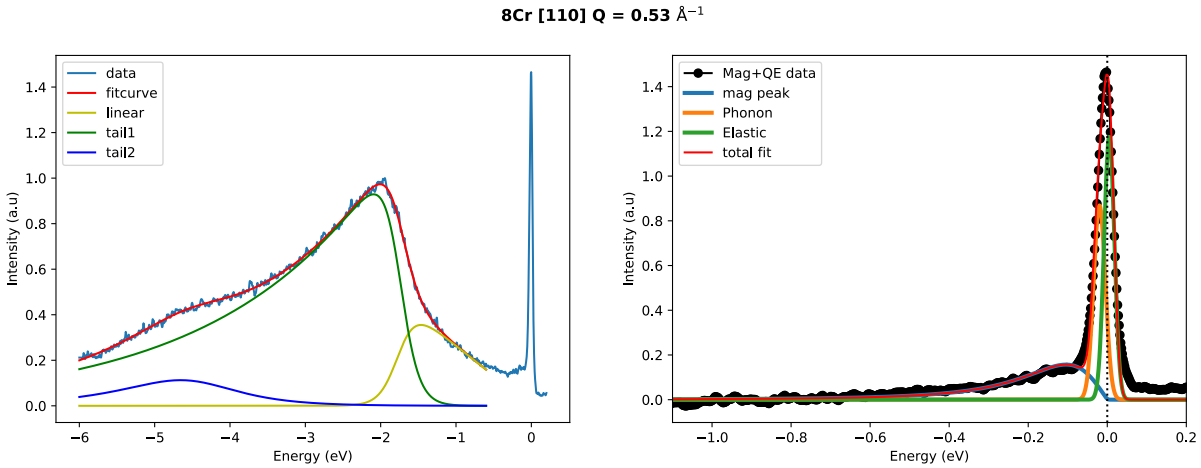

Figure 5.29: RIXS spectrum and fittings for the Cr8.5% sample along the crystallographic $[110]$ direction and momentum transfer of $Q = 0.53$ Å^{-1}. The curves and fitting contributions are discussed in the text.

Overall, the CrBFA samples Fe-derived magnon dispersion behavior is the same as BFA for the (π, π) direction, while for the $(\pi, 0)$ direction the excitation is overdamped, but is still dispersive. This is an indication of the strong magnetic interaction anisotropy that appears for the CrBFA phase diagram, with the $(\pi, 0)$ Fe-Fe direction excitation being strongly suppressed.

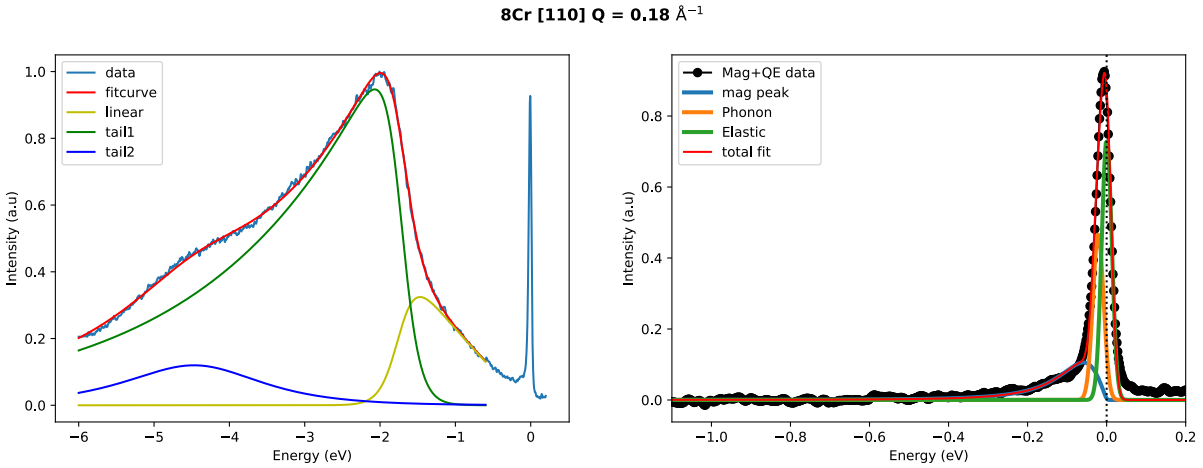

Figure 5.30: RIXS spectrum and fittings for the Cr8.5% sample along the crystallographic $[110]$ direction and momentum transfer of $Q = 0.18$ Å^{-1}. The curves and fitting contributions are discussed in the text.

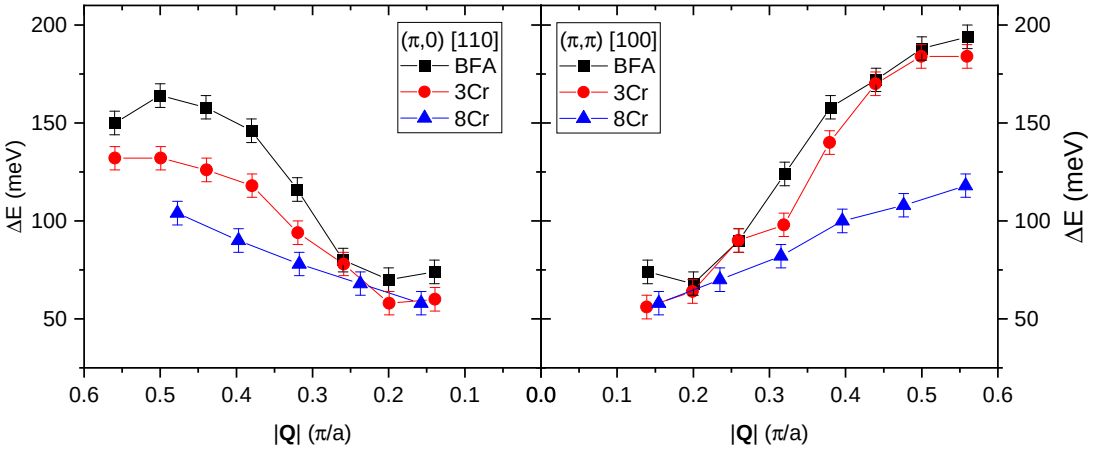

Figure 5.31: RIXS fitted magnetic peak position ΔE for all momentum points for samples BFA, Cr3% and Cr8.5% at $(\pi, 0)$ direction and (π, π) direction.

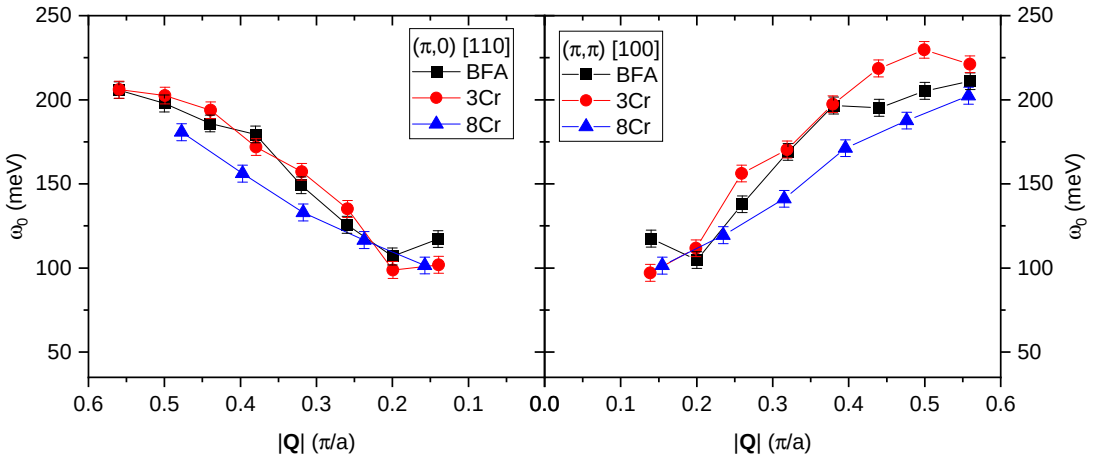

Figure 5.32: RIXS fitted peak bare frequency ω_0 for all momentum points for samples BFA, Cr3% and Cr8.5% at $(\pi, 0)$ direction and (π, π) direction.

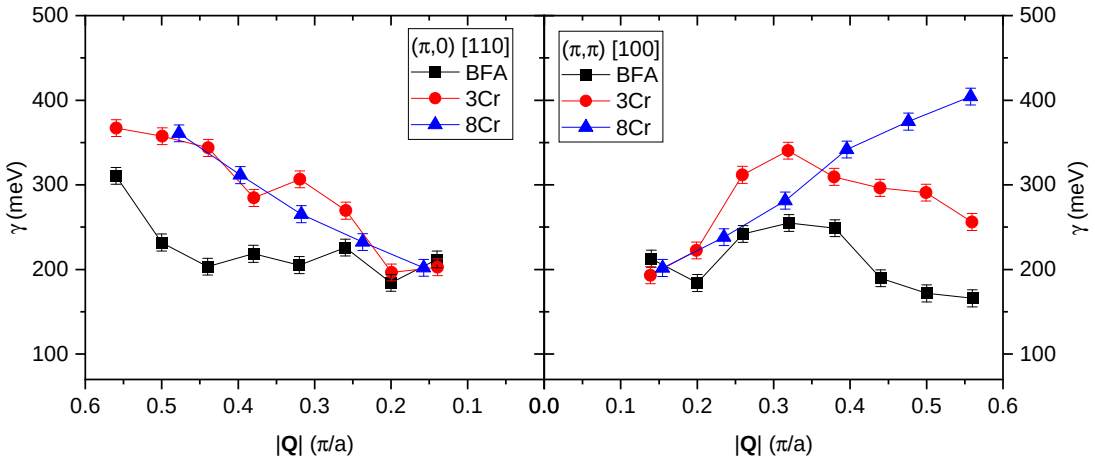

Figure 5.33: RIXS fitted peak damping γ for all momentum points for samples BFA, Cr3% and Cr8.5% at $(\pi, 0)$ direction and (π, π) direction.

Chapter 6

ARPES and RIXS results of $BaCr_2As_2$ and $Ba(Fe_{0.515}Cr_{0.485})_2As_2$

In this chapter, the ARPES experimental results for the samples $Ba(Fe_{0.515}Cr_{0.485})_2As_2$ and $BaCr_2As_2$ are presented. The samples will be referred to as BFCA and BCA, respectively, as defined in Table 2.2.

To describe the experimental ARPES results and their analysis the same notation and convention as the previous chapters were adopted. The methods for the ARPES measurements are described in Section 3.3, and the results here presented will be discussed and put in context with some preliminary RIXS results taken at the ADRESS beamline of the Swiss Light Source [133, 134].

6.1 ARPES results

Figure 6.1 shows a survey of the electronic band structures in the ordered state of the BCA sample, measured at $T = 20$ K. Measurements were taken along the high-symmetry directions and adopting linear beam polarization as indicated in each panel, for incident energy 74 eV for the $k_z = \Gamma$ energy level and 89 eV for the $k_z =$ Z energy level.

It is possible to note how the spectral function depends on the polarization, and this time the selection rules are not as clear as in $BaFe_2As_2$. This is a consequence that in $BaCr_2As_2$ the Cr-derived bands are more hybridized with the As-derived orbitals than in $BaFe_2As_2$ [57].

By inspecting the band measurements, it is visible that the bands are much sharper when compared with the ones found in previous chapters. This is an indication of the coherent electronic properties at the ordered state of BCA. There are three hole pockets, visible in almost all directions and polarizations, and no electron pockets. The hole pockets will be termed inner, middle, and outer, accordingly to previous ARPES results for this sample [60, 59].

In previous ARPES studies, the BCA electronic bands' orbital character was discussed. P. Richard et al. [60] identified the inner and the middle hole pockets as having a predominant

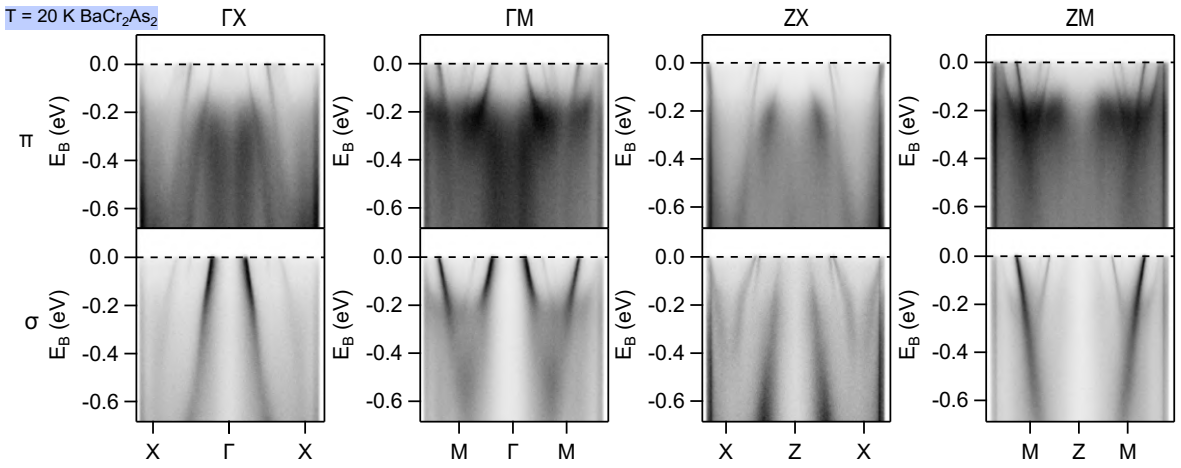

Figure 6.1: $BaCr_2As_2$ electronic band maps measure for $k_z = \Gamma$ and $k_z = \mathrm{Z}$ energies. Measurements were taken along the ΓX, ΓM, ZX, and ZM directions and for σ and π polarization, as indicated. Higher intensities are darker on the color map.

Cr-derived $d_{xz/yz}$ character, with even and odd main symmetries, respectively. The outer hole pocket was identified as having a main Cr-derived d_{xy} character. These findings were supported by local density approximation (LDA) calculations. J. Nayak et al. [59], on the other hand, had identified that the inner hole pocket has a Cr3d_{xy} character mixed with As4p_z contribution, while the middle and outer hole pockets have a combination of Cr3$d_{xz/yz}$, Cr3d_{z^2} and As4$p_{x/y}$ contributions. This was also supported by LDA contribution, even though resulting in different orbital characters.

For our results, the intense hybridization is evident, as mentioned. The main orbital dependencies are: the vanishing of the middle band for ΓX direction σ polarization; weak contributions of the outer band for ΓX π results and its vanishing for ΓM σ polarized data; the stronger intensity of the inner band for σ polarized band maps. Inspecting the Table 3.1, the main orbital character associated with these three bands consists of the inner band being of main d_{yz} character, the middle band with predominant d_{xz} character, and the outer band of main d_{xy} character. This is aligned with what was previously reported by P. Richard et al. Additionally, there is a broad spectral weight close to $E_B = -0.2$ eV only present for π polarized data, from which the d_{z^2} orbital character can be attributed. The polarization dependency will be further discussed for the Fermi Surface (FS) data later in this chapter, where the full direction dependency can be explored at the Fermi level.

Since the bands are not overlapping as much as in the case of $BaFe_2As_2$ and they are sharper, the full spectral analysis can be performed for this sample, as will be discussed in Section 6.1.1.

ARPES measurements for the BFCA sample, close to the putative d^5 configuration at the center of the phase diagram can be compared with the BCA sample results to elucidate the evolution upon Cr substitution. Figure 6.2 shows a survey of the electronic band structures in the ordered state of the BFCA sample, measured for $T = 20$ K. Measurements were taken along

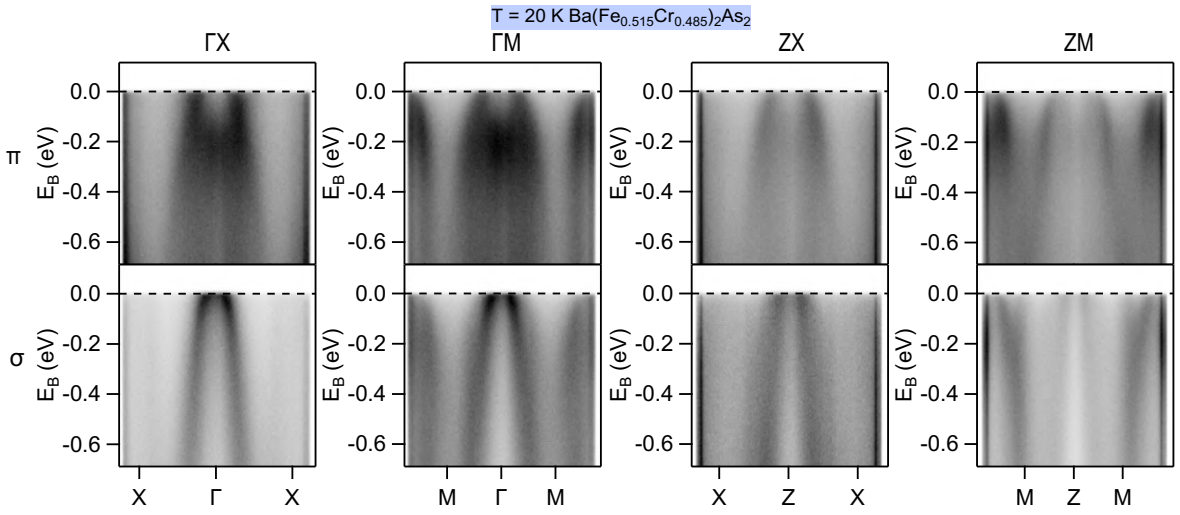

Figure 6.2: $Ba(Fe_{0.515}Cr_{0.485})_2As_2$ low-temperaure electronic band maps measure for $k_z = \Gamma$ and $k_z = Z$ energies. Measurements were taken along the ΓX, ΓM, ZX, and ZM directions and for σ and π polarization, as indicated. Higher intensities are darker on the color map.

the high-symmetry directions and adopting linear beam polarization as indicated in each panel, for incident energy 77 eV for the $k_z = \Gamma$ energy level and 93 eV for the $k_z = Z$ energy level.

As we can see, the overall aspect is kept, but the bands are much broader and less defined. It is not possible to distinguish the three hole pockets for any of the directions or polarizations. The only band that can be clearly identified without overlap is the inner hole pocket, but only in the ΓX direction with σ polarized light. Again, there is a broad contribution close to $E_B = -0.2$ eV only present for π polarized data, that can be attributed to a d_{z^2} orbital character.

The spectral analysis for the BFCA sample, as shown in Section 6.1.1, cannot be as complete as the one for the BCA sample. But the broadness of the electronic bands can give information about the electronic coherence and disorder effects.

The electronic band structure was also measured for higher temperatures of $T = 150$ K, but still within the ordered state. The survey of these bands is shown in Figure 6.3. There is no remarkable difference between these results and the $T = 20$ K results. The same bands are present, but less defined and with some thermal broadening close to the Fermi level for the $T = 150$ K case. Therefore, only the $T = 20$ K data will be analyzed further in this work.

To further investigate the electronic band changes and properties for these two samples, it is possible to recur to the Fermi maps. Fixing the map binding energy to the Fermi level ($E_B = 0$), it is possible to plot the Fermi Surface (FS). In Figures 6.4, and 6.5 there are presented the measured Fermi surfaces (FS) for the samples BFA, and BFCA, respectively. The dashed red lines delimit the first BZ, revealing the rotation of the sample high-symmetry direction being probed.

By inspecting the Fermi maps of Figure 6.4 it is possible to see how sharp the bands are, where the three hole pockets are distinguishable and their shape and k_z dispersion are visible.

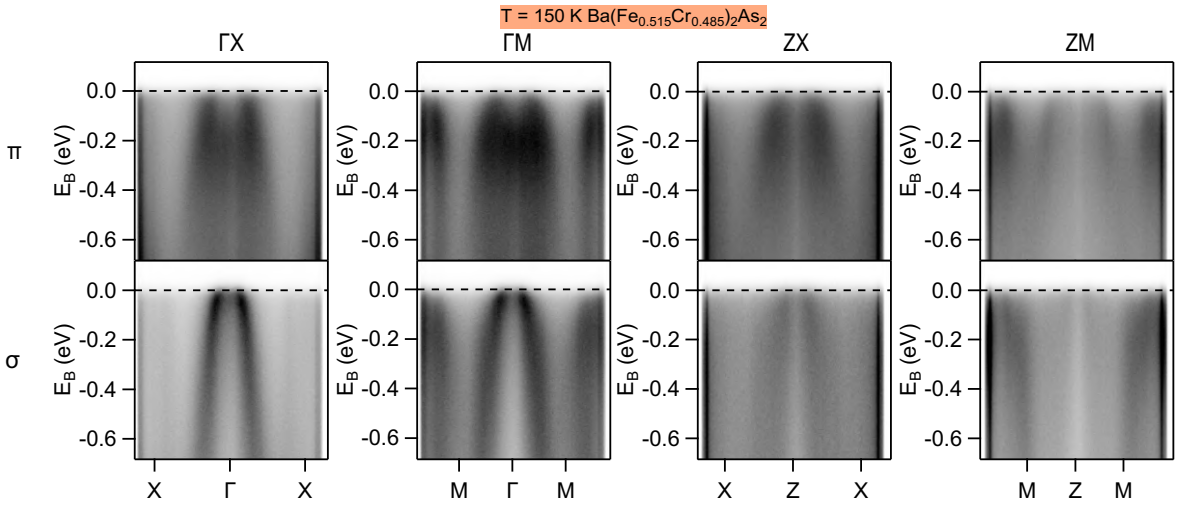

Figure 6.3: $Ba(Fe_{0.515}Cr_{0.485})_2As_2$ high-temperature electronic band maps measure for $k_z = \Gamma$ and $k_z = Z$ energies. Measurements were taken along the ΓX, ΓM, ZX, and ZM directions and for σ and π polarization, as indicated. Higher intensities are darker on the color map.

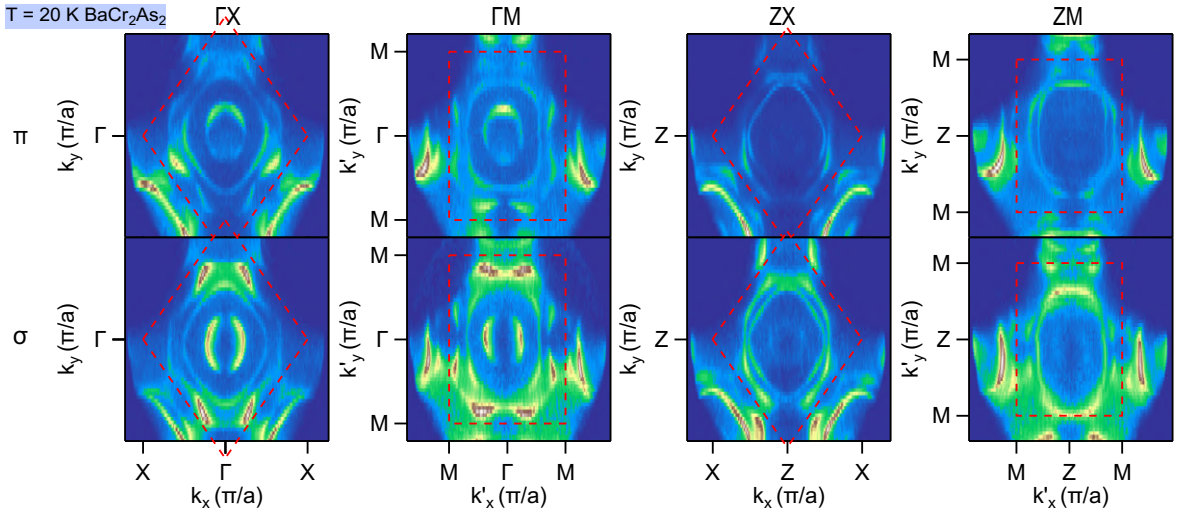

Figure 6.4: $BaCr_2As_2$ Fermi Surfaces measured for $k_z = \Gamma$ and $k_z = Z$ energies. Measurements were taken along the ΓX, ΓM, ZX, and ZM directions and for σ and π polarization, as indicated. The dashed red lines delimit the first BZ

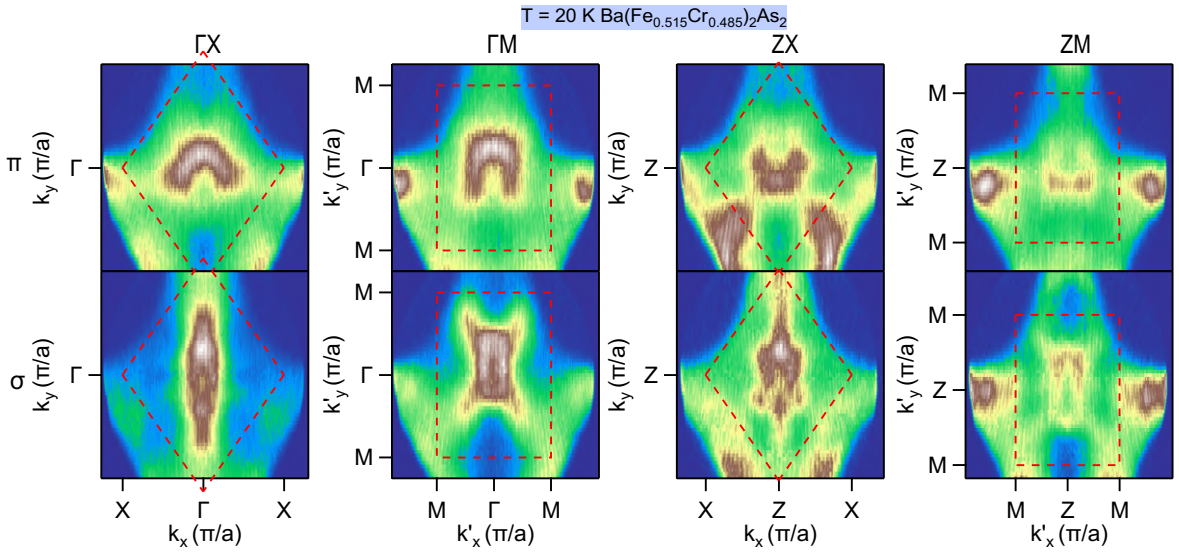

Figure 6.5: $Ba(Fe_{0.515}Cr_{0.485})_2As_2$ Fermi Surfaces measured for $k_z = \Gamma$ and $k_z = Z$ energies. Measurements were taken along the ΓX, ΓM, ZX, and ZM directions and for σ and π polarization, as indicated. The dashed red lines delimit the first BZ

The inner hole pocket is the most circular and is not visible or very weak for the k_z = Z level, but the size does not seem to change a lot, indicating a weak k_z dispersion but strong intensity dependency. The middle hole pocket is the most squarish, looking like a diamond shape for the ΓX direction. Its size, therefore, is changing with direction but not as much with k_z. The outer hole pocket is the most affected with k_z, changing its shape and size. For $k_z = \Gamma$ it looks more "flower" like, or with a clover shape, while for $k_z = Z$ it seems like a circle in which the middle pocket square is circumscribed inside. All these changes will be quantified in the spectral analysis.

On the other hand, the Fermi maps of Figure 4.19, with broader less defined bands, limit the possibility of analyzing in such details the shapes and anisotropies. It seems like the squarish contribution is present, but overlapped with the inner pocket, except for the ΓX direction and σ polarization. Contributions from the putative third hole pocket are very weak and can seem like elongations of the pocket's shape. Therefore, some resemblance with the BCA Fermi Surface is present but the contributions can not be separately analyzed.

With these results, a systematic quantitative analysis as a function of Cr content is very difficult and will not be performed in analogy with previous chapters. The inner hole pocket self-energy analysis is presented for both samples in the following Section, but a more detailed spectral study is present only for the BCA sample.

6.1.1 Self-energy analysis

A quantitative analysis of the ARPES spectral function $A(\mathbf{k}, E)$ can be made to compare with what was previously found for the BFA sample. To do so, the spectral analysis was done by

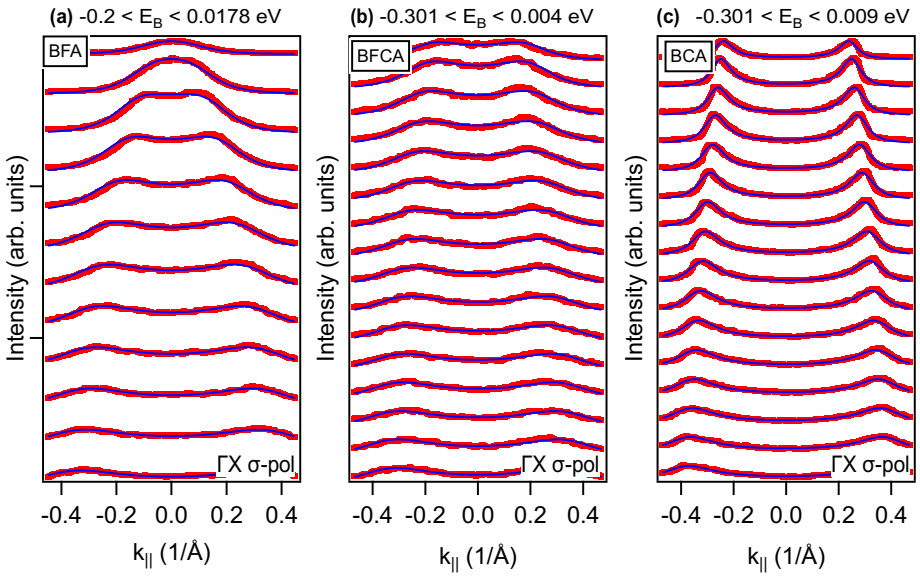

Figure 6.6: ARPES spectral function analysis. Fittings (blue lines) of several MDCs (red dots) for increasing binding energies. (a)-(c) data obtained for σ polarization, measured along ΓX for samples BFA, BFCA, and BCA, as indicated, with a single band fitting.

fitting the momentum distribution curves (MDCs) to the expression for the one-particle $A(\mathbf{k}, E)$ (equation 3.14). The objective is to extract the electronic scattering rate $\Gamma(E)$ as a function of the binding energy E.

The analysis for the band in ΓX direction and σ light polarization, with d_{yz} main orbital character, is presented in Figure 6.6(a)-(c) for samples BFA, BFCA and BCA, respectively. This analysis again follows Refs. [87, 86], where the "all at once" fitting method is presented. This method where the energy and momentum finite resolution and finite temperature were considered is described in Section 4.1.1. It is possible to observe how the Lorentzian peaks are getting more separated and sharp with Cr introduction. It reflects in increasing hole pocket size and band coherence as a function of Cr content.

To further analyze the trend of the spectral features as a function of Cr content, it is possible to compare the scattering rates as a function of binding energy $\Gamma(E)$ for the three samples, as shown in Figure 6.7(a). Again, a marginal Fermi liquid (MFL) behavior is employed to analyze the data, due to the linear behavior of $\Gamma(E)$ close to the Fermi level. Therefore, the relation between $\Gamma(E)$ and Σ'' will follow the expression 3.17, from where Σ'' can be extracted, as shown in Figure 6.7(b).

In the vicinity of E_F, for all bands, $\Gamma(E)$ and $\mathrm{Im}\Sigma(E)$ are fairly well described as linear functions of E, within the paradigm of an MFL regime. The slopes, or angular coefficients, related to $\Gamma(E)$ and $\mathrm{Im}\Sigma(E)$ can be defined as α and β, respectively, in analogy to what was done for the MnBFA and slightly doped CrBFA.

Again, α is a measurement of the electronic states' coherence. In this sense, a decrease of α as a function of Cr content would correspond to a weaker response of $\Gamma(E)$ to the binding

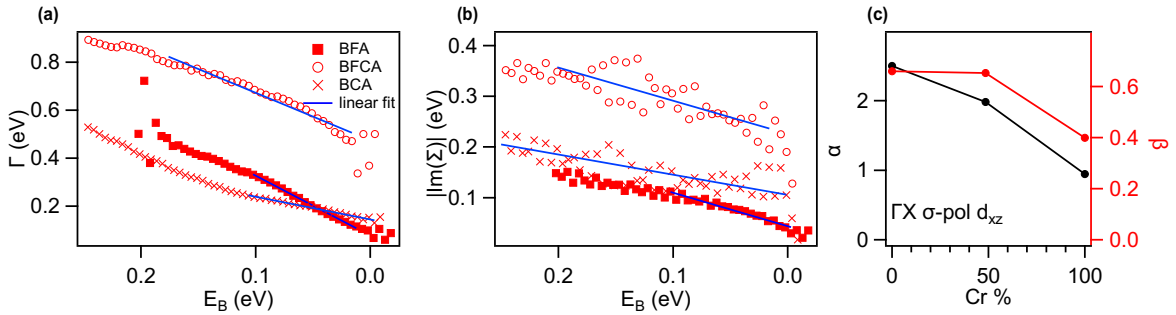

Figure 6.7: ARPES spectral function analysis resulting (a) scattering rate $\Gamma(E)$ and (b) imaginary part of self-energy $\mathrm{Im}\Sigma(E)$ for ΓX single hole pocket band as a function of Cr content. The blue lines indicate linear fittings close to the Fermi level. (c) resulting linear coefficients from panels (a) and (b).

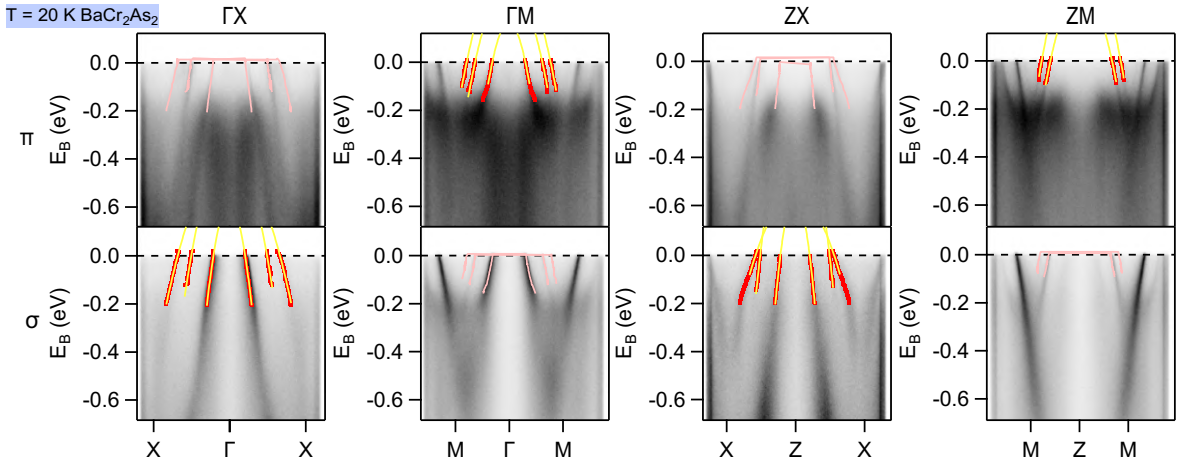

Figure 6.8: $BaCr_2As_2$ fitted band points for the electronic band maps of Figure 6.1. Red dots represent the fitted band points, while yellow solid lines are the fitted parabolic dispersion. Pale pink solid lines show the fitted band points for the complementary polarization from which they were fitted, for comparison.

energy which translates into a decrease in band incoherence. On the other hand, a decrease in β is related to decreasing electronic correlations. The α and β angular coefficients of the curves of Figures 6.7 (a) and (b) are obtained as a function of Cr content and are presented in Figure 6.7(c) for the inner hole pocket band with main d_{yz} orbital character.

For the $BaCr_2As_2$ spectra, it is possible to perform a detailed spectral analysis for the three hole pockets with MDC fitting. Each MDC can be individually fitted to six Lorentzians, following again the expression 3.14, and a constant background. The spectrum is considered a linear combination of each band Lorentzian peaks and the dispersion relation does not need to be given in advance.

The resulting fitted point obtained by this process is shown as red dots in Figure 6.8. This analysis was performed for directions ΓX and ZX with σ light polarization and directions ΓM and ZM with π light polarization, for which the three bands were most visible. The points

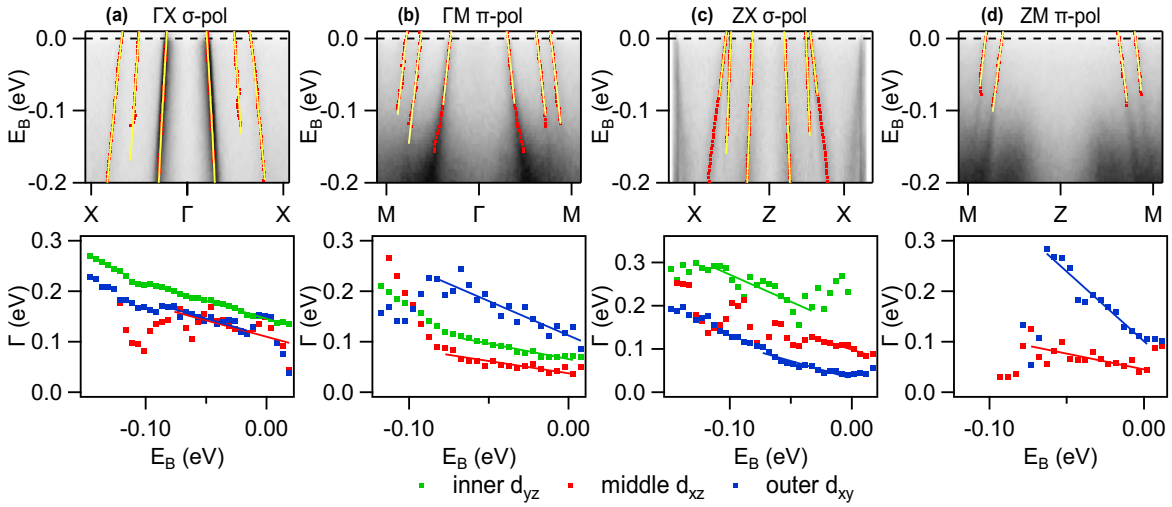

Figure 6.9: $BaCr_2As_2$ fitted bands' scattering rates for (a) ΓX (b) ΓM, (c) ZX and (d) ZM directions. The polarization used to measure the band maps is indicated. The top panels show the bands of Figure 6.8 used to perform these fittings, with a zoom on the E_F region. The bottom panels show the extracted scattering rates with their respective linear fittings for each of the bands. The color code follows the legend at the bottom.

were then fitted to a parabolic dispersion, represented by yellow lines. The pale pink lines are intended to compare the fitted points to the bands in the complementary polarization from which they were fitted.

The Fermi wave vectors k_F in units of π/a were obtained from the band points E_B dependency and the Fermi velocities v_F in units of eVa/π were calculated using the parabolic dispersion derivative for k_F. The scattering rate is obtained by multiplying the peaks' full width at half maximum (fwhm) by the local band velocity [108] for each E_B cut or each MDC. In Figure 6.9 it is possible to observe, on top panels, a closer zoom for the fitted bands in the region of E_F. Again, the red dots are the fitted Lorentzian maximum positions and the solid yellow lines show the fitted parabolic dispersion. On the lower panels the extracted scattering rates $\Gamma(E)$ for the fitted bands are shown along with linear fittings. The colors represent the main orbital character of each band, as already discussed, with green, red, and blue points being the results for the inner, middle, and outer bands respectively.

To calculate the effective mass m^* from the band parabolic dispersion, the expression 6.1 can be employed, where a is the parabolic quadratic coefficient. To convert this formula from SI units for the units of $[a] = \text{eV Å}^2$, and to display the resulting mass in terms of electron mass m_e, the transformation of equation 6.2 can be made, where e is the electron charge, converting the energy from J to eV and the 10^{-20} term converts the distance to Å units.

$$m^* = \frac{\hbar^2}{d^2E(k)/dk^2} = \frac{\hbar^2}{2a} \tag{6.1}$$

$$\frac{m^*}{m_e} = \frac{\hbar^2}{2a} \times \frac{10^{-20}}{em_e} = \frac{3.80998}{a} \tag{6.2}$$

Hole pocket		Inner	Middle	Outer
k_F (π/a)	ΓM	0.31 ± 0.05	0.63 ± 0.05	0.78 ± 0.05
	ZM	-	0.63 ± 0.05	0.81 ± 0.05
	ΓX	0.30 ± 0.05	0.71 ± 0.05	0.95 ± 0.05
	ZX	0.31 ± 0.05	0.71 ± 0.05	0.81 ± 0.05
v_F (eVa/π)	ΓM	1.08 ± 0.10	1.04 ± 0.10	1.08 ± 0.10
	ZM	-	0.95 ± 0.10	1.12 ± 0.10
	ΓX	1.49 ± 0.10	1.31 ± 0.10	0.86 ± 0.10
	ZX	1.74 ± 0.10	1.81 ± 0.10	0.63 ± 0.10
m^*/m_e	ΓM	1.39 ± 0.10	2.91 ± 0.10	3.49 ± 0.10
	ZM	-	3.21 ± 0.10	3.48 ± 0.10
	ΓX	0.98 ± 0.10	2.64 ± 0.10	5.38 ± 0.10
	ZX	0.88 ± 0.10	1.93 ± 0.10	6.32 ± 0.10
α	ΓM	0.61 ± 0.10	0.48 ± 0.10	1.36 ± 0.20
	ZM	-	0.62 ± 0.20	2.76 ± 0.30
	ΓX	0.71 ± 0.10	0.65 ± 0.20	0.70 ± 0.20
	ZX	1.25 ± 0.10	0.90 ± 0.10	0.81 ± 0.10

Table 6.1: Quantitative results from spectral analysis of $BaCr_2As_2$, showing the Fermi wave vectors k_F (π/a), Fermi velocities v_F (eVa/π), mass renormalizations m^*/m_e, and slopes α of the scattering rate $\Gamma(E)$ for the three hole pockets for different directions.

Table 6.1 shows all the quantitative results from this analysis with the Fermi wave vectors k_F (π/a), Fermi velocities v_F (eVa/π), mass renormalizations m^*/m_e, and slopes α of the scattering rate $\Gamma(E)$ for the three hole pockets for four different directions.

As expected from the Fermi Surfaces of Figure 6.4, the inner hole pocket does not change its size with direction and k_z, evidencing its circular shape and 2D character, without significant k_z dispersion. The middle hole pocket, by its turn, also shows no k_z dependency, but is larger along ΓX/ZX direction than along ΓM/ZM, illustrating its squarish shape, with vertices on the X direction. Finally, the outer hole pocket shows the most significant dependency with k_z along the ΓM direction, while the ΓX direction is unaffected. This means a significant shape distortion for this particular hole pocket, as observed in Figure 6.4, with the smaller radius of the clover-like shape increasing to a more round shape.

The Fermi velocity and mass renormalization change significantly with pocket and direction. Systematically, the outer role pocket, of mainly d_{xy} character, shows the smallest velocities and strong renormalizations, both as a consequence of smaller parabolic quadratic coefficients. The inner hole pockets, on the contrary, have larger Fermi velocities and weaker renormalization, closer to 1. These findings are in agreement with what was found by J. Nayak et al. [59], but their work only inspected the ΓM/ZM direction.

The α coefficient, extracted from the slope of the scattering rates of Figure 6.9, does not show a clear trend as a function of the hole pocket. However, it seems to achieve the greatest values for the outer pocket, as was observed by J. Nayak [59].

In summary, the self-energy analysis depicts a scenario where the correlations are stronger

for the BFCA sample, and that Cr introduction enhances the band coherence for these materials. Furthermore, the Fermi Surface three hole pockets were inspected, resulting in a trend in which the inner pocket is less renormalized and the outer hole pocket is more renormalized. The outer hole pocket also has a stronger k_z dependency, changing drastically its shape.

6.2 RIXS results

For CrBFA, as mentioned in the previous chapter, the substitution of Fe by Cr leads to the coexistence of magnetic fluctuations with different symmetries, which compete to form different ground states along the phase diagram. These magnetic, electronic, and structural degrees of freedom can be related to the putative Mott localization associated with the proximity to a half-filling d^5 state for these materials when $x \approx 0.5$, in an analogy to the $BaMn_2As_2$ case.

The ARPES results give no evidence of an orbital-selective Mottness that would occur for these materials. In this case, an orbital-dependent gap should appear in the ordered state for the BFCA sample. This points out that the most likely scenario is for the localization being of a Hund's metal, characterized by spin-orbital energy scale separation [135]. In this scenario, the localization would be a consequence of Hund's coupling in the multiorbital system.

With RIXS results for the $x = 0.485$ (BFCA) sample at the Fe edge, it is possible to investigate the magnetic excitations as a function of high-symmetry direction and momentum and compare it with previous BFA and MnBFA results [7]. This can bring a more complete scenario of the evolution of magnetic degrees of freedom along the phase diagram.

The RIXS results here presented were taken at the ADRESS beamline of the Swiss Light Source, in June 2021, while I was in a research internship abroad at the University of Fribourg, Switzerland. The only probed sample was BFCA, from the same batch as the ARPES measurements (PGJ762, see Table 2.2).

All spectra were taken with incident photon energy at the maximum resonance of FeL_3 XAS spectrum with $h\nu = 707.7$ eV, using π polarized light and for a fixed temperature of $T = 20$ K, the same as ARPES results of Figure 6.2. The total energy resolution of the experiment was about 93 meV, extracted from the full width at half maximum (FWHM) of the elastic scattering of a carbon-filled acrylic tape.

The measurements were taken with backscattering geometry, defined by an acute angle between the incidence direction and the detection direction. This geometry allows detecting photons with higher momentum transfer to the sample, following the equations 6.3 and 6.4, where λ is the incoming photon wavelength, ψ is the scattering angle, $\mathbf{Q}$ is the total transferred momentum and $\mathbf{q}_{\parallel}$ is the transferred momentum projection into the sample plane. Such configuration is illustrated in Figure 6.10.

$$|\mathbf{Q}| = \frac{4\pi}{\lambda} \sin\left(\frac{\psi}{2}\right) \tag{6.3}$$

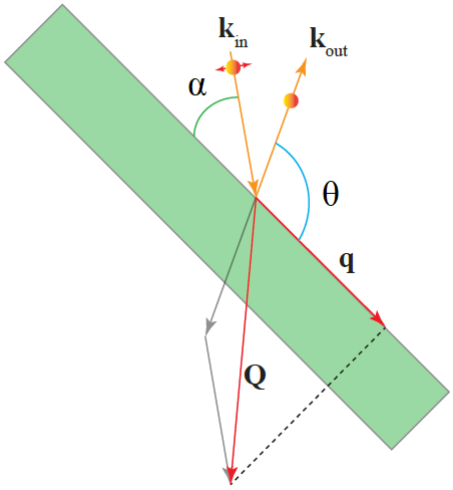

Figure 6.10: RIXS experimental geometry. The backscattering angle is defined as $\psi = \theta + \alpha$ and was kept as $\psi = 130°$

$$|\mathbf{q}_{\parallel}| = |\mathbf{Q}| \sin(\theta - \frac{\psi}{2}) \tag{6.4}$$

During the experiments, the scattering angle was kept as $\psi = \alpha + \theta = 130°$, with the spectrometer arm fixed, and the sample was rotated inside the experimental chamber to vary the detection angle θ. As higher as θ is, the higher will be the transferred momentum projection $\mathbf{q}_{\parallel}$. The corresponding variation of the out-of-plane component $\mathbf{q}_{\perp}$ is not considered since the Fe order is expected to be almost 2D.

Considering mechanical limitations and the efficiency of sample surface reflection, the larger angle to achieve is $\theta \approx 110°$, to leave $\approx 20°$ for the grazing incidence direction. The smaller possible $\mathbf{q}_{\parallel} = 0$ will be when $\theta = \alpha = \psi/2$, with no in-plane momentum transfer.

The sample was aligned using Laue diffraction, to identify the [100] and [110] directions in the ab plane, and glued to the sample holder using silver epoxy. A metal cylindrical pin was glued on top of the sample for in situ cleaving. A pressure of 2×10^{-10} mbar or better was achieved in the sample chamber. All results here described are adopting a 1-Fe 2D unit cell, as shown in Table 2.1, with a lattice parameter of $a = 2.84$ Å. In this notation, the [100] direction corresponds to the diagonal of the 1-Fe lattice, along (π,π), while the [110] direction corresponds to the Fe-Fe first neighbor distance along (π,0). To keep parallel with the ARPES results, these directions will also be referred to as ΓM for (π,π) and ΓX for (π,0).

For each high-symmetry direction, four points of θ were used to probe a RIXS spectrum, probing different $\mathbf{q}_{\parallel}$ points in that direction. This results in 8 RIXS spectra to be analyzed for their magnetic excitation contribution.

In Figure 6.11(a) the XAS spectrum measured for the BFCA sample is shown. The maximum resonance energy of 707.7 eV was chosen for the RIXs measurements. It is a typical L_3 edge with a single Fe 2+ valency, showing that Cr introduction is not disturbing the Fe valency.

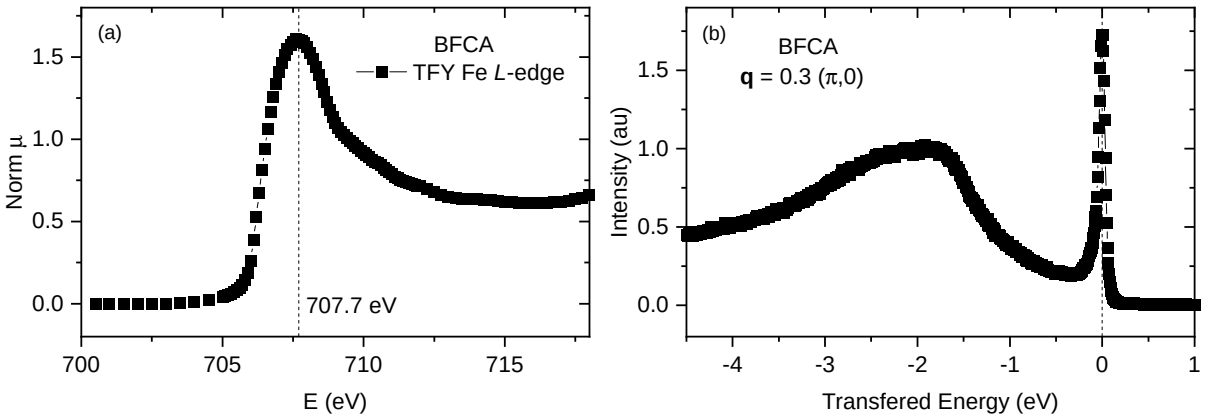

Figure 6.11: (a) Total Fluorescence Yield XAS spectra for the BFCA sample. (b) A representative RIXS spectrum for the BFCA sample evidences the intense elastic line and fluorescence peak.

Figure 6.11(b) shows a representative RIXS spectrum for the $(\pi, 0)$ direction with momentum transfer of $\mathbf{q}_{\parallel} = 0.3$ in units of π/a.

It is possible to observe that the elastic line contribution is very intense. This is due to the substitution disorder introduced by Cr and agrees with ARPES scattering rate results for the BFCA sample. Nevertheless, this intense contribution disturbs the determination of the magnetic excitation peak, which should appear in an energy range of ≈ 100 meV. To perform the magnetic peak analysis, an elastic subtraction procedure should be employed. This procedure consists of some steps: i) normalize the RIXS intensity by the maximum of the interpolated fluorescence signal at around 2 eV transferred energy; ii) define the elastic peak central position by its maximum interpolated point, and shift the data, if necessary, so that this point corresponds to zero transferred energy; iii) define the elastic line by taking the positive half and symmetrizing around $E = 0$ [136]; iv) Subtract the defined elastic peak from the shifted data.

The data of Figure 6.11(b) is already normalized and shifted. By performing this procedure for all spectra, we can observe the extracted elastic line and compare it with the carbon tape elastic line. This is shown in Figure 6.12. For this comparison, the carbon tape spectrum was normalized to the peak with the higher momentum of the same graph. As can be observed, the shape and width of the peaks compare well with the carbon tape reference, which is expected to result in a pure elastic line with no inelastic excitations. In this sense, the elastic contribution subtraction can be considered reliable enough for the magnetic analysis quantitative results.

After subtracting the elastic contribution of Figure 6.12, the resulting spectrum includes the magnetic peak and the fluorescence contribution. The latter can be treated as a background in the magnon region and fitted to a parabolic background. Figure 6.13 shows the resulting inelastic intensities after the elastic peak subtraction. The fluorescence background is almost linear in the region of the magnon peak. To gain insight into the magnon behavior, this inelastic signal can be fitted to a combination of a complex part of the dynamic susceptibility $\chi''(\omega)$, representing the magnon peak, and a quadratic background. The former is shown in Equation

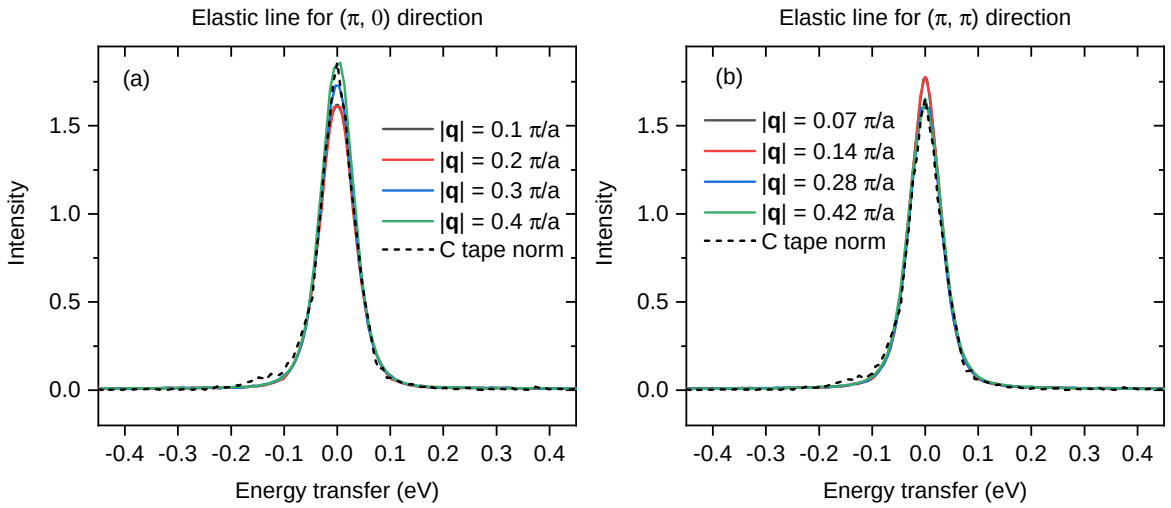

Figure 6.12: RIXS extracted elastic lines for all momentum points for (a) $(\pi, 0)$ direction and (b) (π, π) direction. The dashed line is the Carbon tape spectrum normalized to have the same maximum intensity as the maximum $\mathbf{q}$ point of each graph (the green peaks).

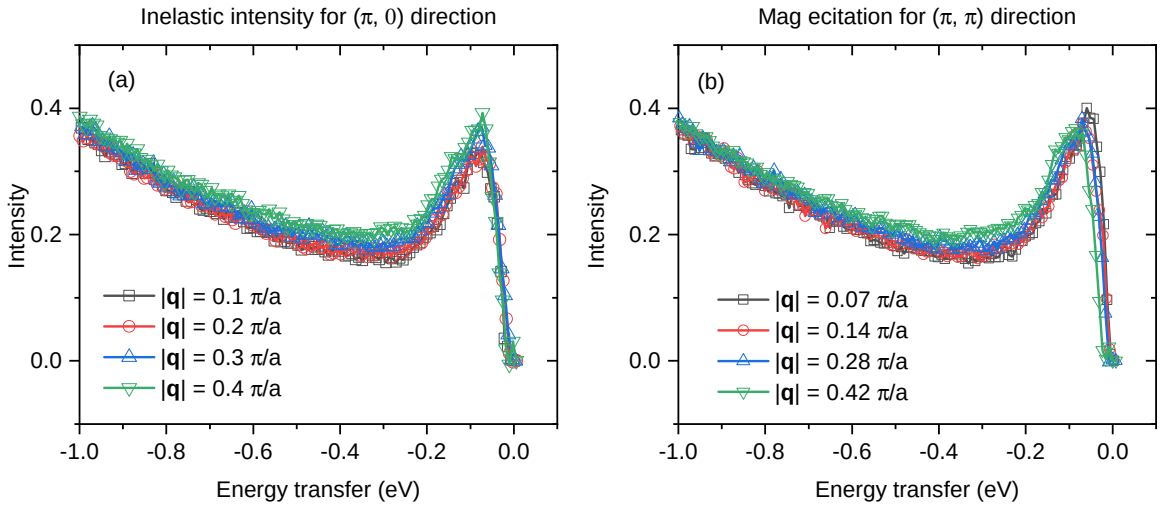

Figure 6.13: RIXS inelastic intensities for all momentum points for (a) $(\pi, 0)$ direction and (b) (π, π) direction.

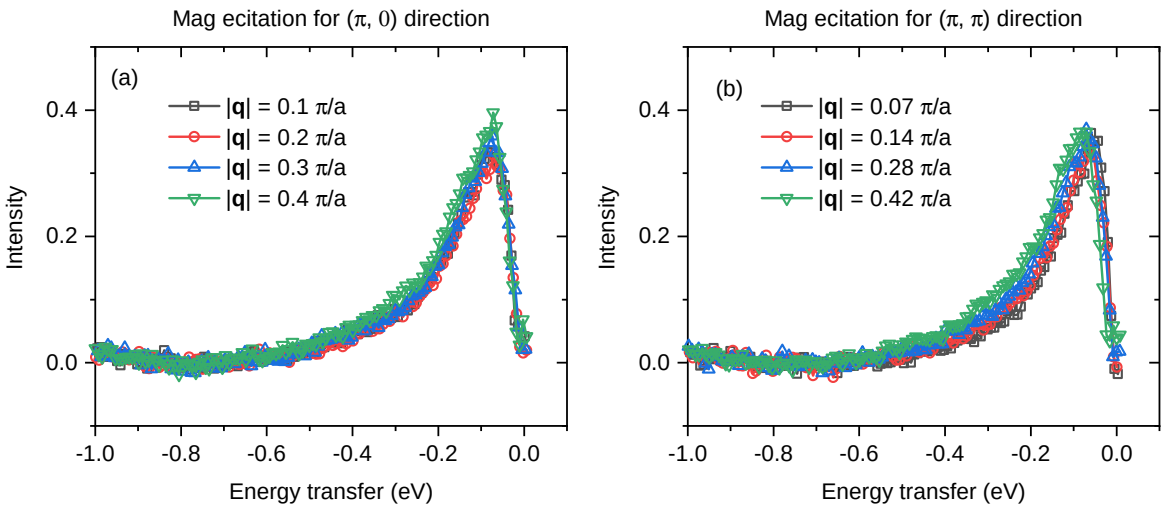

Figure 6.14: RIXS extracted magnetic peaks for all momentum points for (a) $(\pi, 0)$ direction and (b) (π, π) direction.

6.5 [126, 125] and has the form of an antisymmetric Lorentzian peak. To avoid redundant notation, the peak FWHM will be called γ in the RIXS results.

$$\chi''(\omega) = \frac{\chi''_0}{2\omega_q}\left(\frac{\gamma/2}{(\omega-\omega_q)^2+(\gamma/2)^2} - \frac{\Gamma/2}{(\omega+\omega_q)^2+(\gamma/2)^2}\right) \tag{6.5}$$

Within this approach, the peak can be interpreted like a damped harmonic oscillator [7], where χ''_0 is an intensity constant, γ is the excitation lifetime, and ω_q is the propagation frequency of the excitation along the $\mathbf{q}$ direction. The excitation bare frequency without the damping effect can be defined as $\omega_0 = \sqrt{\omega_q^2 + (\gamma/2)^2}$.

With the fitting result, it is possible to subtract the quadratic fluorescence background to obtain a signal that should be of the pure magnon excitation. This is shown in Figure 6.14. A subtle change in energy, intensity, and width can be observed in the peaks as a function of $\mathbf{q}$, especially for the (π, π) direction. To further inspect it, the fitting coefficients are shown as a function of direction and momentum $\mathbf{q}$ in Figures 6.15, 6.16, and 6.17. Alongside these coefficients for the BFCA sample, there are the results for the BFA and Mn8% samples as discussed in Section 4.3, for comparison.

By inspecting the $\Delta E(\mathbf{q})$ in Figure 6.15, which is the fitted magnetic peak maximum position as a function of momentum, it is possible to observe the energy dispersion of the magnon peak as a function of direction and transferred momentum. For the (π, π) direction the excitation energy dispersion seems compatible with what was found for BFA and Mn8%, with almost the same behavior as a function of $\mathbf{q}$. For the $(\pi, 0)$ direction, however, the dispersion is getting suppressed for the BFCA sample, with almost no $\mathbf{q}$ dependency within error bars. The Mn8% result still has some dispersion but is hindered when compared with the BFA sample. Therefore, the effect of Mn substitution of suppressing Fe-Fe direction magnon excitation dispersion is even more strong for Cr close to $x = 0.5$.

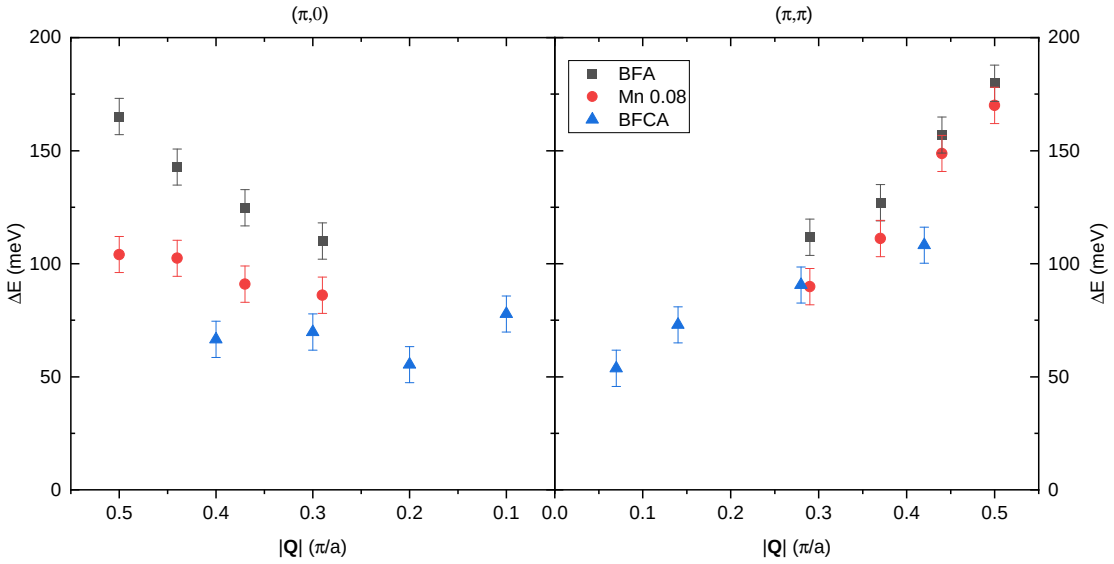

Figure 6.15: RIXS fitted magnetic peak position ΔE for all momentum points and compared with results BFA and Mn8% samples for $(\pi, 0)$ direction and (π, π) direction.

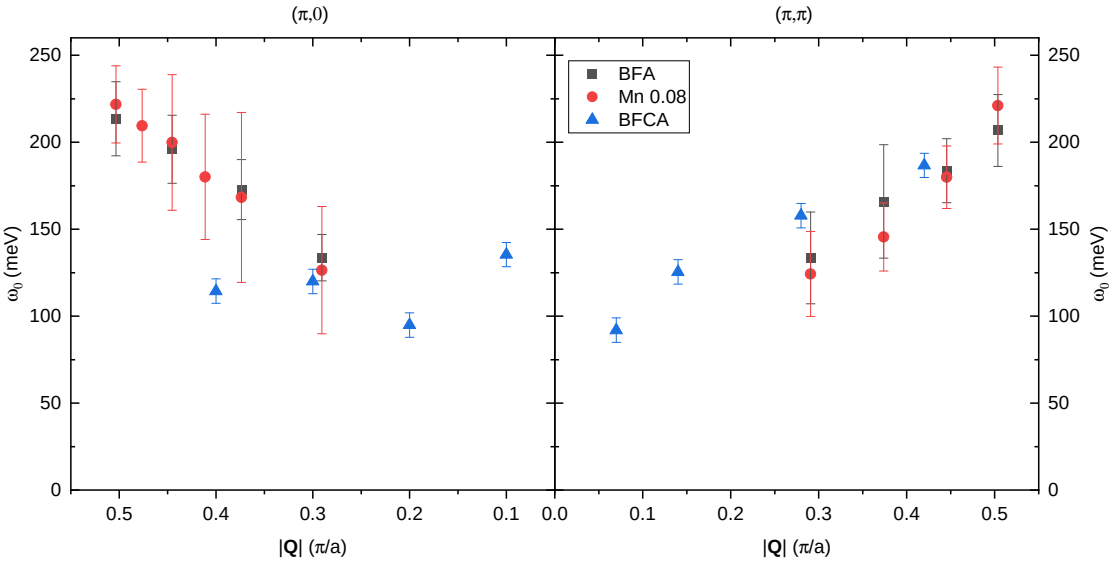

Figure 6.16: RIXS fitted peak bare frequency ω_0 for all momentum points and compared with results BFA and Mn8% samples for $(\pi, 0)$ direction and (π, π) direction.

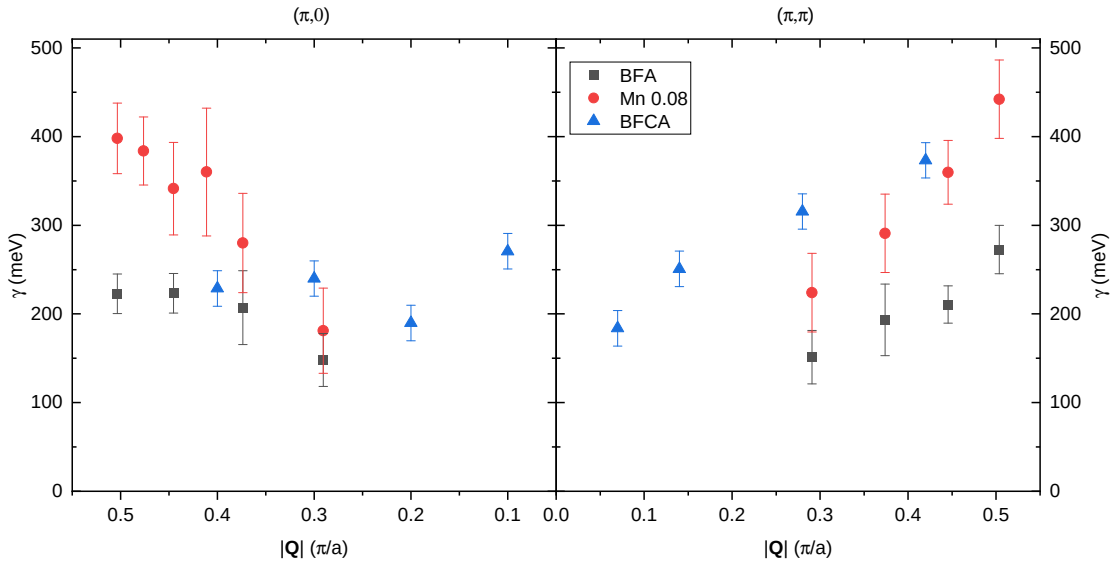

Figure 6.17: RIXS fitted peak damping γ for all momentum points and compared with results BFA and Mn8% samples for $(\pi, 0)$ direction and (π, π) direction.

In Figure 6.16 is possible to observe the magnon bare frequency $\omega_0(\mathbf{q})$ as a function of momentum. Again, for (π, π) direction, a very similar result to what was previously found for BFA and Mn8% appears, with similar values and $\mathbf{q}$ dependency. For the $(\pi, 0)$ direction, on the other hand, the frequency is almost constant as a function of $\mathbf{q}$. This is in contrast with BFA and Mn8% results, where the bare frequency was increasing in both directions.

To better understand the relation of these coefficients for the BFCA sample, the damping γ can be analyzed, as shown in Figure 6.17. When compared with BFA and Mn8% samples, the (π, π) direction damping seems larger for the BFCA sample, but in the $(\pi, 0)$ case, the damping is almost constant as a function of $\mathbf{q}$ for BFCA, on a similar damping level as BFA, and smaller than the damping of Mn8%.

Overall, the BFCA samples Fe-derived magnon dispersion behavior is the same as BFA for the (π, π) direction, while for the $(\pi, 0)$ direction the excitation is overdamped like Mn8% but almost non-dispersive. This is an indication of the strong magnetic interaction anisotropy that appears for the middle point of the CrBFA phase diagram, with the $(\pi, 0)$ Fe-Fe direction excitation being suppressed, probably due to the average suppression of Fe-Fe first neighbors bonding with this substitution level of Cr.

Chapter 7

Conclusion and outlook

This thesis presents a comprehensive ARPES/RIXS study of Mn and Cr substituted $BaFe_2As_2$ samples. The aim of exploring these phase diagrams is to study the absence of superconductivity in these materials, their ground state properties, the mechanisms behind transition metal substitution, and how it affects Fe-Fe correlations and interactions.

For the MnBFA samples, Fermi surface analysis revealed that a fraction of electron and hole states remain nested as in the parent compound for Mn introduction up to 7.5%, meaning that nominal hole doping does not take place. Mn introduction increases electronic correlations and the incoherence of the d_{xy}-derived bands. The disorder associated with the Mn introduction reflects the increasing electronic incoherence.

Overall, the absence of superconductivity for MnBFA can be interpreted as a combination of disorder, magnetic impurities, and electronic correlations. This is aligned with the picture described by Gastiasoro et al. [11], where the cooperative behavior of the magnetic impurities in the presence of magnetic interactions results in strong suppression of electron-phonon coupling and superconductivity. This reveals the importance of impurity effects and their interaction with conduction electrons, more than just their role as magnetic scatterers.

When compared with previous RIXS results for the MnBFA samples [7], a direct connection between the increasing band incoherence and the evolution of the magnon dispersion can be made. Additionally, the observed vanishing of the folded band with d_{xy} character for Mn7.5% sample in ARPES provides a natural explanation for the large damping of the RIXS detected magnons, once the magnetic excitation is mainly related to d_{xy} derived electrons.

For the CrBFA sample, the ARPES results show that Cr indeed introduces hole doping into the system while Mn does not. The hole doping is observed as an increase of hole pockets Fermi vectors $\mathbf{k}_F$, mainly for the d_{xy}-derived outer hole pocket, and with a decrease of $\mathbf{k}_F$ for the electron pockets. The electronic correlations increase with Cr content, as expected, but the Cr8.5% d_{xy}-derived orbital escapes this trend. This behavior is attributed to the effective hole doping, depleting the highest energy orbital d_{xy} from electrons and preventing the increase of correlation in this specific orbital. In terms of electronic disorder, CrBFA compares to Mn substituted samples, but no sign of cluster order was ever reported. These findings point to

the importance of Hund interactions and orbital-specific correlation and localization effects. It is possible to infer that SC is absent in CrBFA mainly because of magnetic pair breaking and suppression of the itinerant spin fluctuations which promote the SC.

Looking for the BFCA sample RIXS results, it is suggested that the trend in the magnons dispersion is the same as for Mn8%, but with stronger damping and almost no dispersion in the $(\pi, 0)$ direction. This indicates that the Fe-Fe magnetic interaction that could promote the electron phonon-coupling is hindered for these two non-superconductor materials.

Comparing MnBFA and CrBFA systems, which seem analogous at first glance, is not a novel idea. It was previously reported [5], in an optical conductivity study as a function of Mn and Cr concentration, some different responses of these two systems to the transition metal concentration. It was found that a new impurity-induced peak appears in the optical conductivity spectrum. This peak showed a larger increasing energy rate for Mn when compared with Cr. This suggests different impurities' interaction strengths. Additionally, using a Drude-Lorentz to fit the optical conductivity, it was found that coherent spectral weight is drastically reduced with Mn/Cr introduction, while it increases for Co substitution. The incoherent spectral weight, by its turn, is kept constant for Co and slightly decreases for Mn while it increases a little for Cr. These differences evidence the possible mechanisms to hinder the emergence of superconductivity in Mn/Cr substituted samples while showing the differences between the two systems. It can be speculated from this that Mn impurities are more likely to show collective behavior and cluster order, which is in agreement with ARPES results.

The electron/hole-doping asymmetry was also evidenced in an ARPES study [110], where a stronger incoherence of the charge carries, associated with the scattering rate, was found for hole-doped K-BFA when compared with electron-doped Co-BFA. This incoherence is associated with strong electronic correlations. This is because the scattering rate is proportional to the effective on-site Coulomb interaction U_{eff} and/or the Hund's exchange interaction J_H [109]. The scattering rate can also be enhanced by the nesting between electron and hole pockets of the Fermi surface, causing electron-hole interaction scattering [137].

Several results previously reported the enhancement of correlations in FeSC upon hole-doping [138, 69, 59], which is interpreted in terms of proximity to a Mott insulator [139, 100]. However, the experimental evidence points to the existence of an electronic metal-like ground state even when the magnetism seems localized. This can be understood in terms of an orbital-selective Mott physics [100]. However, this scenario demands the opening of an orbital selective gap induced by Coulomb interactions. Our results, clearly present Orbital Selective Physics, but the role of Mott-like interactions is not observed. Indeed, the similarities between the electronic state of $BaCr_2As_2$ and $BaFeCrAs_2$ presented in this work, with no visible gap opening, supports that Hund's Physics should dominate.

Keeping in mind a Mott-like scenario, Pizarro et al. [140] have found, using density functional theory (DFT) theoretical calculations, that for the Fe d^6 electronic configuration, the t_{2g} orbitals are closer to half filling than the e_g, whereas, for the Cr d^4 configuration, the e_g

orbitals are closer to half filling. Since the Fermi Surface mainly consists of t_{2g} orbitals for $BaFe_2As_2$ and $BaCr_2As_2$, the latter is the more correlated material. This scenario also explains why $BaFeCrAs_2$ is not equivalent to $BaMn_2As_2$ in terms of correlation and localization.

On the other hand, a dynamical mean-field theory (DMFT) study [141] has shown that the energy scales of the charge and orbital degrees of freedom of a three-band Hund's metal are different from the spin degrees of freedom. This implies that for intermediate temperatures the spins can be localized while the charges are itinerant. This is the hallmark that separates the Hund's metal from a Mott insulator and seems to describe the physics of the $BaCr_2As_2$ and $BaMn_2As_2$ materials, and their substitution phase diagram with $BaFe_2As_2$.

The theoretical approach to treat the impurities effects and different interaction energy scales must combine perturbative methods, such as random phase approximation, with DMFT to capture the effects of local interactions between electrons. In this regard, the results of Chapters 5 and 6 will be published in collaboration with DMFT results to back up the conclusions here presented.

In summary, this work highlights the ongoing importance of experimental and theoretical research on FeSC. The techniques and theory developed to treat this family of materials are examples of this relevance, such as multiple orbital orders and nematicity studies, strain-based techniques, ARPES analysis tools, refinement of RIXS energy resolution and simulation, etc. These findings not only advance the understanding of FeSC but also enrich the field of quantum materials, paving the way for investigating novel materials and proposing interesting material properties.

Bibliography

[1] H.-H. Wen, Journal of Physics: Conference Series **2323**, 012001 (2022).

[2] R. M. Fernandes, A. I. Coldea, H. Ding, I. R. Fisher, P. J. Hirschfeld, and G. Kotliar, Nature **601**, 35 (2022).

[3] H. Hosono and K. Kuroki, Physica C: Superconductivity and its Applications **514**, 399 (2015).

[4] K. Haule and G. Kotliar, New Journal of Physics **11**, 025021 (2009).

[5] T. Kobayashi, M. Nakajima, S. Miyasaka, and S. Tajima, Physical Review B **94**, 224516 (2016).

[6] H. Suzuki, T. Yoshida, S. Ideta, G. Shibata, K. Ishigami, T. Kadono, A. Fujimori, M. Hashimoto, D. H. Lu, Z.-X. Shen, K. Ono, E. Sakai, H. Kumigashira, M. Matsuo, and T. Sasagawa, Physical Review B **88**, 100501 (2013).

[7] F. A. Garcia, O. Ivashko, D. E. McNally, L. Das, M. M. Piva, C. Adriano, P. G. Pagliuso, J. Chang, T. Schmitt, and C. Monney, Physical Review B **99**, 115118 (2019).

[8] R. M. Fernandes and A. J. Millis, Physical Review Letters **110**, 117004 (2013).

[9] R. M. Fernandes and A. V. Chubukov, Reports on Progress in Physics **80**, 014503 (2016).

[10] M. N. Gastiasoro and B. M. Andersen, Physical Review Letters **113**, 067002 (2014).

[11] M. N. Gastiasoro, F. Bernardini, and B. M. Andersen, Physical Review Letters **117**, 257002 (2016).

[12] D. S. Inosov, G. Friemel, J. T. Park, A. C. Walters, Y. Texier, Y. Laplace, J. Bobroff, V. Hinkov, D. L. Sun, Y. Liu, R. Khasanov, K. Sedlak, P. Bourges, Y. Sidis, A. Ivanov, C. T. Lin, T. Keller, and B. Keimer, Physical Review B **87**, 224425 (2013).

[13] J. G. Bednorz and K. A. Müller, Zeitschrift für Physik B Condensed Matter **64**, 189 (1986).

[14] B. Keimer, S. A. Kivelson, M. R. Norman, S. Uchida, and J. Zaanen, Nature **518**, 179 (2015).

[15] E. Fradkin, S. A. Kivelson, and J. M. Tranquada, Rev. Mod. Phys. **87**, 457 (2015).

[16] S. D. Edkins, A. Kostin, K. Fujita, A. P. Mackenzie, H. Eisaki, S. Uchida, S. Sachdev, M. J. Lawler, E.-A. Kim, J. C. S. Davis, and M. H. Hamidian, Science **364**, 976 (2019).

[17] H.-H. Kim, S. M. Souliou, M. E. Barber, E. Lefrançois, M. Minola, M. Tortora, R. Heid, N. Nandi, R. A. Borzi, G. Garbarino, A. Bosak, J. Porras, T. Loew, M. König, P. J. W. Moll, A. P. Mackenzie, B. Keimer, C. W. Hicks, and M. L. Tacon, Science **362**, 1040 (2018).

[18] E. H. da Silva Neto, B. Yu, M. Minola, R. Sutarto, E. Schierle, F. Boschini, M. Zonno, M. Bluschke, J. Higgins, Y. Li, G. Yu, E. Weschke, F. He, M. L. Tacon, R. L. Greene, M. Greven, G. A. Sawatzky, B. Keimer, and A. Damascelli, Science Advances **2**, e1600782 (2016).

[19] L. Gao, Y. Y. Xue, F. Chen, Q. Xiong, R. L. Meng, D. Ramirez, C. W. Chu, J. H. Eggert, and H. K. Mao, Phys. Rev. B **50**, 4260(R) (1994).

[20] Y. Kamihara, T. Watanabe, M. Hirano, and H. Hosono, Journal of the American Chemical Society **130**, 3296 (2008).

[21] A. Chubukov and P. J. Hirschfeld, Physics today **68**, 46 (2015).

[22] J. Paglione and R. L. Greene, Nature physics **6**, 645 (2010).

[23] M. Rotter, M. Tegel, D. Johrendt, I. Schellenberg, W. Hermes, and R. Pöttgen, Physical Review B **78**, 020503 (2008).

[24] S. Avci, O. Chmaissem, D. Y. Chung, S. Rosenkranz, E. A. Goremychkin, J. P. Castellan, I. S. Todorov, J. A. Schlueter, H. Claus, A. Daoud-Aladine, D. D. Khalyavin, M. G. Kanatzidis, and R. Osborn, Phys. Rev. B **85**, 184507 (2012).

[25] A. S. Sefat, R. Jin, M. A. McGuire, B. C. Sales, D. J. Singh, and D. Mandrus, Physical Review Letters **101**, 117004 (2008).

[26] J.-H. Chu, J. G. Analytis, C. Kucharczyk, and I. R. Fisher, Physical Review B **79**, 014506 (2009).

[27] M. A. Tanatar, N. Ni, C. Martin, R. T. Gordon, H. Kim, V. G. Kogan, G. D. Samolyuk, S. L. Bud'ko, P. C. Canfield, and R. Prozorov, Phys. Rev. B **79**, 094507 (2009).

[28] L. J. Li, Y. K. Luo, Q. B. Wang, H. Chen, Z. Ren, Q. Tao, Y. K. Li, X. Lin, M. He, Z. W. Zhu, G. H. Cao, and Z. A. Xu, New Journal of Physics **11**, 025008 (2009).

[29] N. Ni, A. Thaler, A. Kracher, J. Q. Yan, S. L. Bud'ko, and P. C. Canfield, Phys. Rev. B **80**, 024511 (2009).

[30] S. Jiang, H. Xing, G. Xuan, C. Wang, Z. Ren, C. Feng, J. Dai, Z. Xu, and G. Cao, Journal of Physics: Condensed Matter **21**, 382203 (2009).

[31] P. C. Canfield and S. L. Bud'ko, Annual Review of Condensed Matter Physics **1**, 27 (2010).

[32] S. Nandi, M. G. Kim, A. Kreyssig, R. M. Fernandes, D. K. Pratt, A. Thaler, N. Ni, S. L. Bud'ko, P. C. Canfield, J. Schmalian, R. J. McQueeney, and A. I. Goldman, Phys. Rev. Lett. **104**, 057006 (2010).

[33] S. R. Saha, T. Drye, K. Kirshenbaum, N. P. Butch, P. Y. Zavalij, and J. Paglione, Journal of Physics: Condensed Matter **22**, 072204 (2010).

[34] M. G. Kim, D. K. Pratt, G. E. Rustan, W. Tian, J. L. Zarestky, A. Thaler, S. L. Bud'ko, P. C. Canfield, R. J. McQueeney, A. Kreyssig, and A. I. Goldman, Phys. Rev. B **83**, 054514 (2011).

[35] M. G. Kim, J. Lamsal, T. W. Heitmann, G. S. Tucker, D. K. Pratt, S. N. Khan, Y. B. Lee, A. Alam, A. Thaler, N. Ni, S. Ran, S. L. Bud'ko, K. J. Marty, M. D. Lumsden, P. C. Canfield, B. N. Harmon, D. D. Johnson, A. Kreyssig, R. J. McQueeney, and A. I. Goldman, Physical Review Letters **109**, 167003 (2012).

[36] P. F. S. Rosa, C. Adriano, T. M. Garitezi, M. M. Piva, K. Mydeen, T. Grant, Z. Fisk, M. Nicklas, R. R. Urbano, R. M. Fernandes, and P. G. Pagliuso, Scientific Reports **4**, 6252 (2014).

[37] A. A. Kordyuk, Low Temperature Physics **38**, 888 (2012).

[38] I. I. Mazin, D. J. Singh, M. D. Johannes, and M. H. Du, Phys. Rev. Lett. **101**, 057003 (2008).

[39] J. A. Sobota, Y. He, and Z.-X. Shen, Reviews of Modern Physics **93**, 025006 (2021).

[40] M. Yi, Y. Zhang, Z.-X. Shen, and D. Lu, npj Quantum Materials **2**, 1 (2017).

[41] R. M. Fernandes, A. V. Chubukov, and J. Schmalian, Nature Physics **10**, 97 (2014).

[42] H. Pfau, C. R. Rotundu, J. C. Palmstrom, S. D. Chen, M. Hashimoto, D. Lu, A. F. Kemper, I. R. Fisher, and Z.-X. Shen, Physical Review B **99**, 035118 (2019).

[43] W. Lv, F. Krüger, and P. Phillips, Phys. Rev. B **82**, 045125 (2010).

[44] C. Fang, H. Yao, W.-F. Tsai, J. Hu, and S. A. Kivelson, Phys. Rev. B **77**, 224509 (2008).

[45] H. Wadati, I. Elfimov, and G. A. Sawatzky, Phys. Rev. Lett. **105**, 157004 (2010).

[46] K. Marty, A. D. Christianson, C. H. Wang, M. Matsuda, H. Cao, L. H. VanBebber, J. L. Zarestky, D. J. Singh, A. S. Sefat, and M. D. Lumsden, Physical Review B **83**, 060509(R) (2011).

[47] J. P. Clancy, B. D. Gaulin, and A. S. Sefat, Physical Review B **85**, 054115 (2012).

[48] M. G. Kim, A. Kreyssig, A. Thaler, D. K. Pratt, W. Tian, J. L. Zarestky, M. A. Green, S. L. Bud'ko, P. C. Canfield, R. J. McQueeney, and A. I. Goldman, Physical Review B **82**, 220503 (2010).

[49] A. Thaler, H. Hodovanets, M. S. Torikachvili, S. Ran, A. Kracher, W. Straszheim, J. Q. Yan, E. Mun, and P. C. Canfield, Physical Review B **84**, 144528 (2011).

[50] A. Pandey, V. K. Anand, and D. C. Johnston, Physical Review B **84**, 014405 (2011).

[51] Y. Texier, Y. Laplace, P. Mendels, J. T. Park, G. Friemel, D. L. Sun, D. S. Inosov, C. T. Lin, and J. Bobroff, EPL (Europhysics Letters) **99**, 17002 (2012).

[52] X.-G. Li, J.-M. Sheng, C.-K. Tian, Y.-Y. Wang, T.-L. Xia, L. Wang, F. Ye, W. Tian, J.-C. Wang, J.-J. Liu, H.-X. Zhang, W. Bao, and P. Cheng, Europhysics Letters **122**, 67006 (2018).

[53] M. Rotter, M. Tegel, and D. Johrendt, Physical Review Letters **101**, 107006 (2008).

[54] Z. Bukowski, S. Weyeneth, R. Puzniak, P. Moll, S. Katrych, N. D. Zhigadlo, J. Karpinski, H. Keller, and B. Batlogg, Phys. Rev. B **79**, 104521 (2009).

[55] G. Mu, H. Luo, Z. Wang, L. Shan, C. Ren, and H.-H. Wen, Phys. Rev. B **79**, 174501 (2009).

[56] P. Popovich, A. V. Boris, O. V. Dolgov, A. A. Golubov, D. L. Sun, C. T. Lin, R. K. Kremer, and B. Keimer, Phys. Rev. Lett. **105**, 027003 (2010).

[57] D. J. Singh, A. S. Sefat, M. A. McGuire, B. C. Sales, D. Mandrus, L. H. VanBebber, and V. Keppens, Physical Review B **79**, 094429 (2009).

[58] K. A. Filsinger, W. Schnelle, P. Adler, G. H. Fecher, M. Reehuis, A. Hoser, J.-U. Hoffmann, P. Werner, M. Greenblatt, and C. Felser, Physical Review B **95**, 184414 (2017).

[59] J. Nayak, K. Filsinger, G. H. Fecher, S. Chadov, J. Minár, E. D. L. Rienks, B. Büchner, S. P. Parkin, J. Fink, and C. Felser, Proceedings of the National Academy of Sciences **114**, 12425 (2017).

[60] P. Richard, A. van Roekeghem, B. Q. Lv, T. Qian, T. K. Kim, M. Hoesch, J.-P. Hu, A. S. Sefat, S. Biermann, and H. Ding, Physical Review B **95**, 184516 (2017).

[61] S. Nandi, Y. Xiao, N. Qureshi, U. B. Paramanik, W. T. Jin, Y. Su, B. Ouladdiaf, Z. Hossain, and T. Brückel, Phys. Rev. B **94**, 094411 (2016).

[62] R. A. Ewings, T. G. Perring, R. I. Bewley, T. Guidi, M. J. Pitcher, D. R. Parker, S. J. Clarke, and A. T. Boothroyd, Phys. Rev. B **78**, 220501 (2008).

[63] Y. Singh, M. A. Green, Q. Huang, A. Kreyssig, R. J. McQueeney, D. C. Johnston, and A. I. Goldman, Physical Review B **80**, 100403 (2009).

[64] Y. Singh, A. Ellern, and D. C. Johnston, Physical Review B **79**, 094519 (2009).

[65] W.-L. Zhang, P. Richard, A. van Roekeghem, S.-M. Nie, N. Xu, P. Zhang, H. Miao, S.-F. Wu, J.-X. Yin, B. B. Fu, L.-Y. Kong, T. Qian, Z.-J. Wang, Z. Fang, A. S. Sefat, S. Biermann, and H. Ding, Physical Review B **94**, 155155 (2016).

[66] Y. X. Yao, J. Schmalian, C. Z. Wang, K. M. Ho, and G. Kotliar, Phys. Rev. B **84**, 245112 (2011).

[67] A. Antal, T. Knoblauch, Y. Singh, P. Gegenwart, D. Wu, and M. Dressel, Phys. Rev. B **86**, 014506 (2012).

[68] D. E. McNally, S. Zellman, Z. P. Yin, K. W. Post, H. He, K. Hao, G. Kotliar, D. Basov, C. C. Homes, and M. C. Aronson, Phys. Rev. B **92**, 115142 (2015).

[69] S. Lafuerza, H. Gretarsson, F. Hardy, T. Wolf, C. Meingast, G. Giovannetti, M. Capone, A. S. Sefat, Y.-J. Kim, P. Glatzel, and L. de' Medici, Physical Review B **96**, 045133 (2017).

[70] X. Wang and R. M. Fernandes, Physical Review B **89**, 144502 (2014).

[71] T. Kobayashi, K. Tanaka, S. Miyasaka, and S. Tajima, Journal of the Physical Society of Japan **84**, 094707 (2015).

[72] D. C. Johnston, Advances in Physics **59**, 803–1061 (2010).

[73] M. Tomić, H. O. Jeschke, and R. Valentí, Physical Review B **90**, 195121 (2014).

[74] T. M. Garitezi, C. Adriano, P. F. S. Rosa, E. M. Bittar, L. Bufaiçal, R. L. de Almeida, E. Granado, T. Grant, Z. Fisk, M. A. Avila, R. A. Ribeiro, P. L. Kuhns, A. P. Reyes, R. R. Urbano, and P. G. Pagliuso, Brazilian Journal of Physics **43**, 223 (2013).

[75] A. Chubukov, Annual Review of Condensed Matter Physics **3**, 57 (2012).

[76] M. D. Johannes and I. I. Mazin, Phys. Rev. B **79**, 220510(R) (2009).

[77] M. J. Calderón, G. León, B. Valenzuela, and E. Bascones, Phys. Rev. B **86**, 104514 (2012).

[78] H. Ding, P. Richard, K. Nakayama, K. Sugawara, T. Arakane, Y. Sekiba, A. Takayama, S. Souma, T. Sato, T. Takahashi, Z. Wang, X. Dai, Z. Fang, G. F. Chen, J. L. Luo, and N. L. Wang, EPL (Europhysics Letters) **83**, 47001 (2008).

[79] Y. Zhang, L. X. Yang, F. Chen, B. Zhou, X. F. Wang, X. H. Chen, M. Arita, K. Shimada, H. Namatame, M. Taniguchi, J. P. Hu, B. P. Xie, and D. L. Feng, Physical Review Letters **105**, 117003 (2010).

[80] Y. Xu, Y. Huang, X. Cui, E. Razzoli, M. Radovic, M. Shi, G. Chen, P. Zheng, N. Wang, C. Zhang, *et al.*, Nature Physics **7**, 198 (2011).

[81] P. Richard, T. Sato, K. Nakayama, T. Takahashi, and H. Ding, Reports on Progress in Physics **74**, 124512 (2011).

[82] A. Damascelli, Z. Hussain, and Z.-X. Shen, Reviews of Modern Physics **75**, 473 (2003).

[83] C. N. Berglund and W. E. Spicer, Physical Review **136**, A1030 (1964).

[84] S. Hüfner, *Photoelectron spectroscopy: principles and applications* (Springer Science & Business Media, 2013).

[85] F. Reinert and S. Hüfner, New Journal of Physics **7**, 97 (2005).

[86] J. Fink, E. D. L. Rienks, M. Yao, R. Kurleto, J. Bannies, S. Aswartham, I. Morozov, S. Wurmehl, T. Wolf, F. Hardy, C. Meingast, H. S. Jeevan, J. Maiwald, P. Gegenwart, C. Felser, and B. Büchner, Physical Review B **103**, 155119 (2021).

[87] R. Kurleto and J. Fink, Journal of Electron Spectroscopy and Related Phenomena **253**, 147127 (2021).

[88] T. Valla, A. V. Fedorov, P. D. Johnson, and S. L. Hulbert, Phys. Rev. Lett. **83**, 2085 (1999).

[89] C. M. Varma, Reviews of Modern Physics **92**, 031001 (2020).

[90] T. Shibauchi, A. Carrington, and Y. Matsuda, Annual Review of Condensed Matter Physics **5**, 113 (2014).

[91] J. Zaanen, Nature **430**, 512 (2004).

[92] D. Haberer, *Electronic Properties of Functionalized Graphene Studied With Photoemission Spectroscopy*, Ph.D. thesis, Technische Universität Dresden (2012).

[93] Y. Zhang, F. Chen, C. He, B. Zhou, B. P. Xie, C. Fang, W. F. Tsai, X. H. Chen, H. Hayashi, J. Jiang, H. Iwasawa, K. Shimada, H. Namatame, M. Taniguchi, J. P. Hu, and D. L. Feng, Physical Review B **83**, 054510 (2011).

[94] M. Fuglsang Jensen, V. Brouet, E. Papalazarou, A. Nicolaou, A. Taleb-Ibrahimi, P. Le Fèvre, F. Bertran, A. Forget, and D. Colson, Phys. Rev. B **84**, 014509 (2011).

[95] V. Brouet, M. F. Jensen, P.-H. Lin, A. Taleb-Ibrahimi, P. Le Fèvre, F. Bertran, C.-H. Lin, W. Ku, A. Forget, and D. Colson, Phys. Rev. B **86**, 075123 (2012).

[96] S. Thirupathaiah, S. de Jong, R. Ovsyannikov, H. A. Dürr, A. Varykhalov, R. Follath, Y. Huang, R. Huisman, M. S. Golden, Y.-Z. Zhang, H. O. Jeschke, R. Valentí, A. Erb, A. Gloskovskii, and J. Fink, Phys. Rev. B **81**, 104512 (2010).

[97] V. Brouet, M. Marsi, B. Mansart, A. Nicolaou, A. Taleb-Ibrahimi, P. Le Fèvre, F. Bertran, F. Rullier-Albenque, A. Forget, and D. Colson, Physical Review B **80**, 165115 (2009).

[98] Z. P. Yin, K. Haule, and G. Kotliar, Nature Physics **7**, 294 (2011).

[99] R. Yu and Q. Si, Phys. Rev. Lett. **110**, 146402 (2013).

[100] L. de' Medici, G. Giovannetti, and M. Capone, Physical Review Letters **112**, 177001 (2014).

[101] A. G. de Figueiredo, M. R. Cantarino, W. R. da Silva Neto, K. R. Pakuszewski, R. Grossi, D. S. Christovam, J. C. Souza, M. M. Piva, G. S. Freitas, P. G. Pagliuso, C. Adriano, and F. A. Garcia, Physical Review B **105**, 045130 (2022).

[102] A. van Roekeghem, P. Richard, H. Ding, and S. Biermann, Comptes Rendus Physique Iron-based superconductors / Supraconducteurs à base de fer, **17**, 140 (2016).

[103] H. Liu, G. F. Chen, W. Zhang, L. Zhao, G. Liu, T.-L. Xia, X. Jia, D. Mu, S. Liu, S. He, Y. Peng, J. He, Z. Chen, X. Dong, J. Zhang, G. Wang, Y. Zhu, Z. Xu, C. Chen, and X. J. Zhou, Phys. Rev. Lett. **105**, 027001 (2010).

[104] P. Richard, K. Nakayama, T. Sato, M. Neupane, Y.-M. Xu, J. H. Bowen, G. F. Chen, J. L. Luo, N. L. Wang, X. Dai, Z. Fang, H. Ding, and T. Takahashi, Phys. Rev. Lett. **104**, 137001 (2010).

[105] P. Zhang, P. Richard, T. Qian, Y.-M. Xu, X. Dai, and H. Ding, Review of Scientific Instruments **82**, 043712 (2011).

[106] Y. Yamaji, T. Yoshida, A. Fujimori, and M. Imada, Physical Review Research **3**, 043099 (2021).

[107] R. P. Xian, V. Stimper, M. Zacharias, M. Dendzik, S. Dong, S. Beaulieu, B. Schölkopf, M. Wolf, L. Rettig, C. Carbogno, S. Bauer, and R. Ernstorfer, Nature Computational Science , 1 (2022).

[108] A. A. Kordyuk, S. V. Borisenko, A. Koitzsch, J. Fink, M. Knupfer, and H. Berger, Phys. Rev. B **71**, 214513 (2005).

[109] J. Fink, A. Charnukha, E. D. L. Rienks, Z. H. Liu, S. Thirupathaiah, I. Avigo, F. Roth, H. S. Jeevan, P. Gegenwart, M. Roslova, I. Morozov, S. Wurmehl, U. Bovensiepen, S. Borisenko, M. Vojta, and B. Büchner, Phys. Rev. B **92**, 201106(R) (2015).

[110] J. Fink, E. D. L. Rienks, S. Thirupathaiah, J. Nayak, A. van Roekeghem, S. Biermann, T. Wolf, P. Adelmann, H. S. Jeevan, P. Gegenwart, S. Wurmehl, C. Felser, and B. Büchner, Physical Review B **95**, 144513 (2017).

[111] Z. R. Ye, Y. Zhang, F. Chen, M. Xu, J. Jiang, X. H. Niu, C. H. P. Wen, L. Y. Xing, X. C. Wang, C. Q. Jin, B. P. Xie, and D. L. Feng, Physical Review X **4**, 031041 (2014).

[112] T. Berlijn, C.-H. Lin, W. Garber, and W. Ku, Physical Review Letters **108**, 207003 (2012).

[113] G. Levy, R. Sutarto, D. Chevrier, T. Regier, R. Blyth, J. Geck, S. Wurmehl, L. Harnagea, H. Wadati, T. Mizokawa, I. S. Elfimov, A. Damascelli, and G. A. Sawatzky, Physical Review Letters **109**, 077001 (2012).

[114] S. Ideta, T. Yoshida, I. Nishi, A. Fujimori, Y. Kotani, K. Ono, Y. Nakashima, S. Yamaichi, T. Sasagawa, M. Nakajima, K. Kihou, Y. Tomioka, C. H. Lee, A. Iyo, H. Eisaki, T. Ito, S. Uchida, and R. Arita, Physical Review Letters **110**, 107007 (2013).

[115] L. Fanfarillo and E. Bascones, Physical Review B **92**, 075136 (2015).

[116] E. Bascones, B. Valenzuela, and M. J. Calderón, Comptes Rendus Physique **17**, 36 (2016), iron-based superconductors / Supraconducteurs à base de fer.

[117] T. Kawashima, S. Miyasaka, H. Tsuji, T. Yamamoto, M. Uekubo, A. Takemori, K. T. Lai, and S. Tajima, Scientific Reports **11**, 10006 (2021).

[118] M. Yi, Z.-K. Liu, Y. Zhang, R. Yu, J.-X. Zhu, J. J. Lee, R. G. Moore, F. T. Schmitt, W. Li, S. C. Riggs, J.-H. Chu, B. Lv, J. Hu, M. Hashimoto, S.-K. Mo, Z. Hussain, Z. Q. Mao, C. W. Chu, I. R. Fisher, Q. Si, Z.-X. Shen, and D. H. Lu, Nature Communications **6**, 7777 (2015).

[119] M. Yi, Y. Zhang, Z.-K. Liu, X. Ding, J.-H. Chu, A. F. Kemper, N. Plonka, B. Moritz, M. Hashimoto, S.-K. Mo, Z. Hussain, T. P. Devereaux, I. R. Fisher, H. H. Wen, Z.-X. Shen, and D. H. Lu, Nature Communications **5**, 3711 (2014).

[120] M. Merz, P. Schweiss, P. Nagel, M.-J. Huang, R. Eder, T. Wolf, H. von Loehneysen, and S. Schuppler, Journal of the Physical Society of Japan **85**, 044707 (2016).

[121] M. D. Watson, P. Dudin, L. C. Rhodes, D. V. Evtushinsky, H. Iwasawa, S. Aswartham, S. Wurmehl, B. Büchner, M. Hoesch, and T. K. Kim, npj Quantum Materials **4**, 1 (2019).

[122] A. Fedorov, A. Yaresko, E. Haubold, Y. Kushnirenko, T. Kim, B. Büchner, S. Aswartham, S. Wurmehl, and S. Borisenko, Phys. Rev. B **100**, 024517 (2019).

[123] Y. Zhang, M. Yi, Z.-K. Liu, W. Li, J. J. Lee, R. G. Moore, M. Hashimoto, M. Nakajima, H. Eisaki, S.-K. Mo, Z. Hussain, T. P. Devereaux, Z.-X. Shen, and D. H. Lu, Physical Review B **94**, 115153 (2016).

[124] M. Yi, D. Lu, J.-H. Chu, J. G. Analytis, A. P. Sorini, A. F. Kemper, B. Moritz, S.-K. Mo, R. G. Moore, M. Hashimoto, W.-S. Lee, Z. Hussain, T. P. Devereaux, I. R. Fisher, and Z.-X. Shen, Proceedings of the National Academy of Sciences **108**, 6878 (2011).

[125] M. Le Tacon, G. Ghiringhelli, J. Chaloupka, M. M. Sala, V. Hinkov, M. W. Haverkort, M. Minola, M. Bakr, K. J. Zhou, S. Blanco-Canosa, C. Monney, Y. T. Song, G. L. Sun, C. T. Lin, G. M. De Luca, M. Salluzzo, G. Khaliullin, T. Schmitt, L. Braicovich, and B. Keimer, Nature Physics **7**, 725 (2011).

[126] K.-J. Zhou, Y.-B. Huang, C. Monney, X. Dai, V. N. Strocov, N.-L. Wang, Z.-G. Chen, C. Zhang, P. Dai, L. Patthey, J. van den Brink, H. Ding, and T. Schmitt, Nature Communications **4**, 1470 (2013).

[127] J. Pelliciari, K. Ishii, Y. Huang, M. Dantz, X. Lu, P. Olalde-Velasco, V. N. Strocov, S. Kasahara, L. Xing, X. Wang, *et al.*, Communications Physics **2**, 1 (2019).

[128] J. Pelliciari, K. Ishii, M. Dantz, X. Lu, D. E. McNally, V. N. Strocov, L. Xing, X. Wang, C. Jin, H. S. Jeevan, P. Gegenwart, and T. Schmitt, Phys. Rev. B **95**, 115152 (2017).

[129] E. Kaneshita, K. Tsutsui, and T. Tohyama, Physical Review B **84**, 020511 (2011).

[130] A. S. Sefat, D. J. Singh, L. H. VanBebber, Y. Mozharivskyj, M. A. McGuire, R. Jin, B. C. Sales, V. Keppens, and D. Mandrus, Physical Review B **79**, 224524 (2009).

[131] W. L. Yang, A. P. Sorini, C.-C. Chen, B. Moritz, W.-S. Lee, F. Vernay, P. Olalde-Velasco, J. D. Denlinger, B. Delley, J.-H. Chu, J. G. Analytis, I. R. Fisher, Z. A. Ren, J. Yang, W. Lu, Z. X. Zhao, J. van den Brink, Z. Hussain, Z.-X. Shen, and T. P. Devereaux, Phys. Rev. B **80**, 014508 (2009).

[132] J. N. Hancock, R. Viennois, D. van der Marel, H. M. Rønnow, M. Guarise, P.-H. Lin, M. Grioni, M. Moretti Sala, G. Ghiringhelli, V. N. Strocov, J. Schlappa, and T. Schmitt, Phys. Rev. B **82**, 020513 (2010).

[133] G. Ghiringhelli, A. Piazzalunga, C. Dallera, G. Trezzi, L. Braicovich, T. Schmitt, V. N. Strocov, R. Betemps, L. Patthey, X. Wang, and M. Grioni, Review of Scientific Instruments **77**, 113108 (2006).

[134] V. N. Strocov, T. Schmitt, U. Flechsig, T. Schmidt, A. Imhof, Q. Chen, J. Raabe, R. Betemps, D. Zimoch, J. Krempasky, X. Wang, M. Grioni, A. Piazzalunga, and L. Patthey, Journal of Synchrotron Radiation **17**, 631 (2010).

[135] K. M. Stadler, G. Kotliar, S.-S. B. Lee, A. Weichselbaum, and J. von Delft, Phys. Rev. B **104**, 115107 (2021).

[136] H. Suzuki, M. Minola, Y. Lu, Y. Peng, R. Fumagalli, E. Lefrançois, T. Loew, J. Porras, K. Kummer, D. Betto, S. Ishida, H. Eisaki, C. Hu, X. Zhou, M. W. Haverkort, N. B. Brookes, L. Braicovich, G. Ghiringhelli, M. Le Tacon, and B. Keimer, npj Quantum Materials **3**, 1 (2018).

[137] I. Avigo, S. Thirupathaiah, E. D. L. Rienks, L. Rettig, A. Charnukha, M. Ligges, R. Cortes, J. Nayak, H. S. Jeevan, T. Wolf, Y. Huang, S. Wurmehl, M. I. Sturza, P. Gegenwart, M. S. Golden, L. X. Yang, K. Rossnagel, M. Bauer, B. Büchner, M. Vojta, M. Wolf, C. Felser, J. Fink, and U. Bovensiepen, physica status solidi (b) **254**, 1600382 (2017).

[138] F. Hardy, A. E. Böhmer, D. Aoki, P. Burger, T. Wolf, P. Schweiss, R. Heid, P. Adelmann, Y. X. Yao, G. Kotliar, J. Schmalian, and C. Meingast, Phys. Rev. Lett. **111**, 027002 (2013).

[139] T. Misawa, K. Nakamura, and M. Imada, Phys. Rev. Lett. **108**, 177007 (2012).

[140] J. M. Pizarro, M. J. Calderón, J. Liu, M. C. Muñoz, and E. Bascones, Phys. Rev. B **95**, 075115 (2017).

[141] K. M. Stadler, Z. P. Yin, J. von Delft, G. Kotliar, and A. Weichselbaum, Phys. Rev. Lett. **115**, 136401 (2015).

[142] L. J. P. Ament, M. van Veenendaal, T. P. Devereaux, J. P. Hill, and J. van den Brink, Reviews of Modern Physics **83**, 705 (2011).

[143] A. Kotani and S. Shin, Reviews of Modern Physics **73**, 203 (2001).

[144] L. J. P. Ament, G. Ghiringhelli, M. M. Sala, L. Braicovich, and J. van den Brink, Phys. Rev. Lett. **103**, 117003 (2009).

[145] J. van den Brink and M. van Veenendaal, Journal of Physics and Chemistry of Solids 5th International Conference on Inelastic X-ray Scattering (IXS 2004), **66**, 2145 (2005).

[146] P. Willmott, *An introduction to synchrotron radiation: techniques and applications* (Wiley, 2019).

[147] "Ipê beamline," `https://lnls.cnpem.br/facilities/ipe/` (2023), [Accessed: 22-February-2023].

[148] A. C. Thompson, D. Vaughan, *et al.*, *X-ray data booklet*, Vol. 8 (Lawrence Berkeley National Laboratory, University of California Berkeley, CA, 2001).

[149] C. A. Palmer and E. G. Loewen, *Diffraction grating handbook* (Newport Corporation New York, 2005).

[150] S. G. Chiuzbăian, C. F. Hague, and J. Lüning, Applied Optics **51**, 4684 (2012).

[151] V. Strocov, T. Schmitt, U. Flechsig, L. Patthey, and G. Chiuzbăian, Journal of synchrotron radiation **18**, 134 (2011).

[152] B. C. Meyer, T. C. Rocha, S. A. Luiz, A. C. Pinto, and H. Westfahl Jr, in *Advances in Computational Methods for X-Ray Optics IV*, Vol. 10388 (International Society for Optics and Photonics, 2017) p. 103880D.

[153] G. L. M. P. Rodrigues, M. Guarise, A. Rocha, B. Meyer, and T. C. R. Rocha, AIP Conference Proceedings **2054**, 040007 (2019).

[154] W. B. Peatman, *Gratings, mirrors and slits: beamline design for soft X-ray synchrotron radiation sources* (Routledge, 2018).

[155] M. Sanchez del Rio, N. Canestrari, F. Jiang, and F. Cerrina, Journal of synchrotron radiation **18**, 708 (2011).

[156] M. S. d. Rio and L. Rebuffi, AIP Conference Proceedings **2054**, 060081 (2019).

[157] V. Martynov, B. Vidal, P. Vincent, M. Brunel, D. V. Roschupkin, Y. Agafonov, A. Erko, and A. Yuakshin, Nuclear Instruments and Methods in Physics Research Section A: Accelerators, Spectrometers, Detectors and Associated Equipment **339**, 617 (1994).

[158] M. Bagieu and D. Maystre, J. Opt. Soc. Am. A **15**, 1566 (1998).

[159] L. Li, J. Chandezon, G. Granet, and J.-P. Plumey, Applied Optics **38**, 304 (1999).

[160] T. Vallius, J. Opt. Soc. Am. A **19**, 1555 (2002).

[161] M. Boots, D. Muir, and A. Moewes, Journal of Synchrotron Radiation **20**, 272 (2013).

[162] F. Schäfers, in *Modern Developments in X-Ray and Neutron Optics* (Springer, 2008) pp. 9–41.

[163] T. pandas development team, "pandas-dev/pandas: Pandas," (2020), software, Version 1.3.4.

Appendix A

Resonant Inelastic X-ray Scattering (RIXS)

Resonant Inelastic X-ray Scattering (RIXS) is a spectroscopic technique that uses x-rays to probe the electronic and structural properties of materials. In RIXS, x-ray photons are absorbed by an atom, which undergoes a transition to an excited state before emitting a secondary photon. The energy and polarization of the emitted photon provide information about the electronic and structural properties of the sample.

RIXS is particularly useful for studying materials with strongly correlated electrons, such as high-temperature superconductors and transition metal oxides, for example. These materials can present several interesting phenomena, such as magnetism, charge density waves, and orbital ordering, which can be probed using RIXS. RIXS can also be used to study the dynamics of electronic excitations, including phonons, plasmons, and magnons, and to investigate the local environment around specific atoms in a material.

RIXS is increasingly standing out for applications in fields such as materials science, catalysis, and energy storage. For example, RIXS can be used to study catalysis materials under reaction conditions or to investigate the electronic properties of battery materials. Overall, RIXS is a powerful spectroscopic tool that allows researchers to study a wide range of materials and phenomena at the atomic scale.

The concepts behind RIXS are known for some decades: it is a photon-in photon-out second-order process in which inelastic intensities are measured. RIXS is, therefore, an inelastic technique, where the energy and momentum that are incident in the sample can be different from the detected energy and momentum emitted by the sample. With it, it is possible to measure the characteristic energy and momentum transfer to the sample, related to different excitations present in a material.

It is an X-ray technique basically because, for the relevant wavelength (momentum) range for solids, X-rays have the greatest energy when compared to neutrons or electrons, as shown in Figure A.1 [142]. Consequently, it can fully probe a larger scattering phase space and reaches the dispersion of characteristic low-energy excitations that appears on solids, with the energy of the order $10^{-2} \sim 10^{1}$ eV as shown in Figure A.2. Since the photon is charge neutral, the possible excitations to be measured must also be charge-neutral.

Lastly, RIXS is a resonant technique: it is element-specific. Upon choosing a characteristic absorption edge of an atom in the material, it is possible to tune the energy for that specific atom only, with the possibility of differentiating between different valencies, bonds, and orbitals. To achieve this tunability of energy, it is needed to use an X-ray source of continuous energy range. That is why RIXS requires the use of synchrotron light sources.

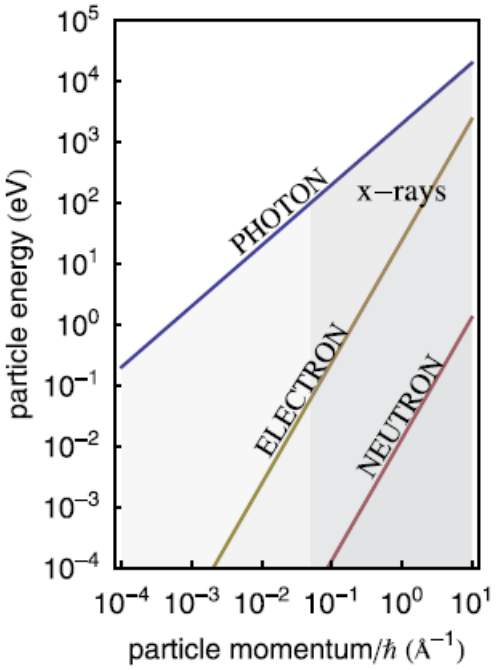

Figure A.1: Energy of X-rays, neutrons, and electrons with different wavelengths. Figure from [142].

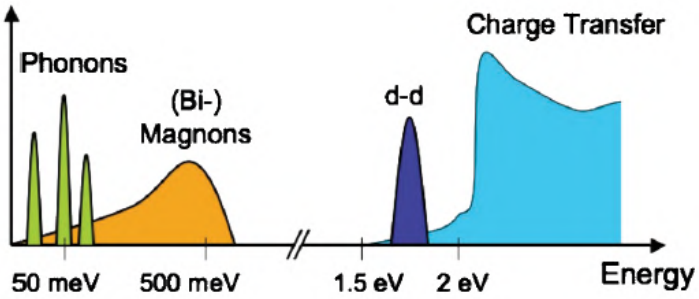

Figure A.2: Excitations and their scale for strongly correlated electron materials such as transition-metal oxides, which can be probed using RIXS. Figure from [142].

The RIXS spectrum, which is a plot of the intensity of the scattered photons as a function of energy and polarization, provides detailed information about the electronic and structural properties of the material. In particular, the RIXS spectrum can reveal information about the valence electronic structure, the charge and spin excitations, and the local atomic environment around specific atoms in the material. Additionally, only a small volume of sample is necessary to have a good RIXS intensity, making it advantageous when compared to neutron scattering to probe magnetic properties of materials, since the light-matter interaction is stronger when compared to neutron-matter interaction [142].

Thinking about these definitions, one can wonder why the use of RIXS is so recent in the experimental study of materials. Even though the concepts are not new, the RIXS process has a great loss of photons, which demands a high flux of photons. Also, it needs a very high energy resolution to separate the different characteristic features in the measured spectra. Only with the improvement of the synchrotron light sources around the world, it was possible to achieve the technology necessary to perform a good RIXS experiment with a variety of

materials. This technique began to spread with third-generation synchrotron sources, but with the next generation of sources, such as Sirius in Brazil, the potential of RIXS to several different areas of study will be further explored.

Considering all these features, we can now address the basic concepts of this technique, the theory, instrumentation, and more specifically, the analytical and numerical methods used to model the spectrometer performance. This work was part of the IPE beamline commission for the Sirius synchrotron facility in Campinas, Brazil.

A.1 Fundamentals

The theory behind Resonant Inelastic X-ray Scattering (RIXS) involves light-matter interaction, more specifically the interaction of x-ray photons with electrons in a material. In RIXS, the incident x-ray photon energy is tuned to be resonant with a particular core level transition in the material, enhancing the probability of the electron absorbing the photon and transitioning to the excited state [143]. This occurs due to anomalous scattering cross-sections associated with the x-ray absorption spectroscopy (XAS) resonance peak.

When the photons are incident on a material, they can be absorbed by electrons in the core level, which causes the electron to transition to an excited state in the valence band. As a result, there is an intermediate state that is very unstable, with a core hole with a lifetime typically of a few fs [142]. After the electron is excited, an electron from the valence band can decay, filling the core hole and emitting a secondary photon. This process is called *direct RIXS* and is illustrated in Fig. A.3(a).

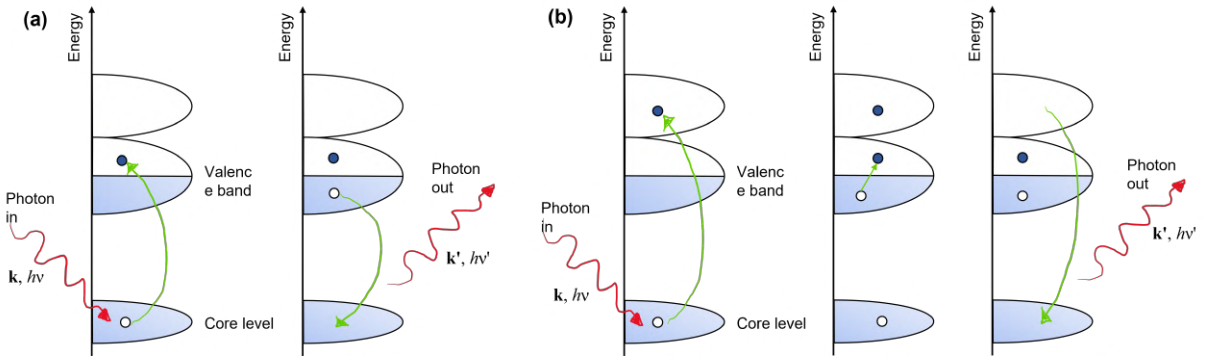

Figure A.3: (a) Illustration of a direct RIXS process. (b) Illustration of an indirect RIXS process.

The final product of this RIXS process is an electron-hole excitation, which can propagate into the material with energy $h\nu_{\mathbf{q}}$ and momentum $\mathbf{q}$, where $\nu_{\mathbf{q}} = \nu - \nu'$ and $\mathbf{q} = \mathbf{k} - \mathbf{k}'$. Here $\mathbf{k}$ and $h\nu$ are the initial photon momentum and energy and $\mathbf{k}'$ and $h\nu'$ are for the final photon.

The main characteristic of the direct RIXS process is that it is dominated by transitions permitted by selection rules, among which the strongest should be dipolar $1s \rightarrow 2p$ (XAS K-edge energies) and $2p \rightarrow 3d$ (XAS L-edge energies) transitions. Since the inelastic process requires a different p or d orbital to decay into the core hole, this permits us to probe the energy difference between different occupied and unoccupied p and d levels, which is particularly interesting for cuprate materials and other insulating transition-metal-based materials.

The polarization of this secondary photon depends on the polarization of the incident photon, and its energy is equal to the energy difference between the core level and the excited state. If they have the same energy, no net energy was transferred to the material, and we have a resonant process. The electronic and structural properties of the material will have a direct influence

on this process, with particular energy scales. Spin-flip excitations can occur associated with magnon for cuprate materials [144], for example.

The *indirect RIXS* process, by its turn, can only occur when the probability of transition between the core hole and the valence band is weak [145]. In this case, it is more likely that the incoming photon will promote a core electron to an empty state well above the Fermi energy, as illustrated in Fig. A.3(b). In a simple picture, this would not result in an inelastic emission, since we would not expect discrete energies for the possible decaying states close to the promoted electron. However, the interaction between the valence states and the core hole tends to screen the core hole in the intermediate state. As a result an electron-hole excitation, similar to the final product of direct RIXS, is created in the valence state, permitting that, indirectly, the excited electron can decay into the core hole.

At first, the resulting state of a direct and an indirect RIXS process seems very similar. Nevertheless, This classification is useful in the sense that the physical properties, mechanisms, and scattering cross-section that lead to each type of RIXS are quite different. In most transition metal materials, the direct RIXS process dominates the detected intensities.

A.2 Instrumentation

The instrumentation for performing RIXS includes the light source beamline and the spectrometer. The light source, as mentioned, must be a synchrotron, due to the energy tunability required to perform RIXS. Several beamlines have different optics to deliver at the sample a well-collimated, highly monochromatic, and focused beam, which is essential to perform a good RIXS experiment [142].

In this section, I will introduce the basic idea of a synchrotron light source and beamline, and focus on the RIXS terminal of the IPE beamline at Sirius, especially the design of the monochromator grating at the spectrometer. The details of optics and all types of considered errors are explained, to present the optimization of the grating done by ray-tracing simulations and analytical calculations.

A.2.1 Synchrotron Source

A synchrotron is a type of circular particle accelerator. It can accelerate charged particles by using bending magnets. These magnets generate a field that bends the particle trajectory, accelerating the electrons, which causes electromagnetic radiation emission. The light emitted by this process is called synchrotron light.

The higher the velocity of electrons, the higher the emitted energy radiation. Larger rings or stronger magnets, however, are needed to accelerate such electrons.

To generate the light, the synchrotron light source includes the storage ring, responsible for maintaining the velocity of the accelerated electron, the linear accelerator (linac), which injects the electron beam in the ring, and usually a booster ring that accelerates the electrons before they are injected in the storage ring. This is illustrated in Figure A.4.

The radiation emitted is always tangent to the electron trajectory, and consequently tangent to the storage ring. It is distributed to different experimental stations, called beamlines. The beamlines are based upon straight lines coming out of the storage ring, as shown in Figure A.4. The instrumentation in the beamline changes accordingly to the technique used at the experimental station.

A wiggler or an undulator is used as an insertion device to deviate the radiation to the beamlines. The storage ring radiation is white, or polychromatic, so a monochromator is required at

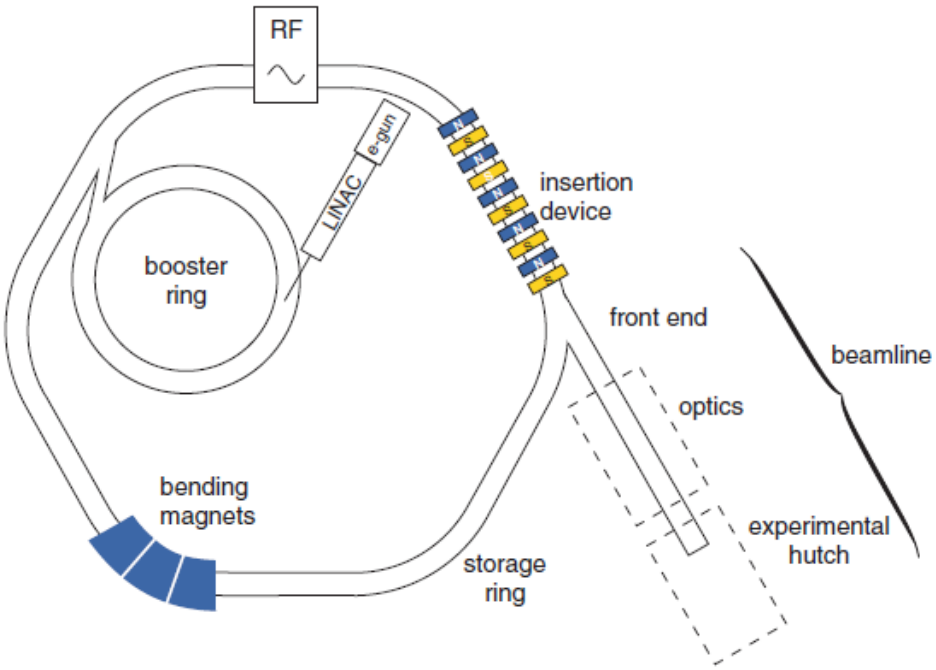

Figure A.4: Representative scheme of a synchrotron light source and beamline from [146].

the optical hutch to filter the desired incident energy. The optical hutch also includes focusing and collimating elements to deliver a small beam of light to the experimental hutch.

Apart from energy tunability, the main properties of synchrotron radiation are their high flux and high stability. When compared to the free-electron laser source, it is not that coherent, even though some small fraction of the synchrotron x-ray can be made to be phase coherent (in this case, it can allow better tomography and imaging techniques with high-flux sources). Also, it permits the choice of the beam to be polarized linearly and circularly, which is interesting for several investigations, such as magnetic and anisotropic properties in materials.

A.2.2 Beamline Optics

The main optical elements of a beamline are the monochromator, the collimator, and the focusing elements.

The collimator is responsible for narrowing down the light beam, which reaches this optical element with a larger dispersion. When collimated, the emergent photons diverge less in their angles and additionally, the beam can become smaller. The ultimate effect is an improvement in flux and mainly in resolution. Since the photon energies are separated by their angle in the monochromator, any deviation in the initial beam will propagate to a worse resolution.

The monochromator "filters" the energy of interest, since the storage ring beam has photons with different energies. For soft x-rays, diffraction gratings must be used to disperse the energy.

Finally, the focusing mirror will focus the monochromatic beam to the exit slit to the experimental hutch.

The beamline optical elements are almost the same for every technique. The main difference usually lies in the experimental hutch, where the sample is placed and hit by synchrotron radiation.

However, the beamline differs fundamentally for soft X-ray and hard x-ray regimes. While the hard X-ray regime in general uses crystal monochromators, such as Si or Ge single crystals,

for separating specific energy, it cannot be used for soft X-rays due to the high absorption of the crystal atoms in this energy range.

Additionally, for soft X-rays, all optical elements should be in ultra-high vacuum (UHV), since the presence of air would absorb and scatter the photons with low energy. This implies another layer of technical considerations and difficulties.

Given that, for soft X-rays, the monochromator will be a blazed mirrored grating, which uses the diffraction of a small periodic pattern that reflects the photons in different directions depending on their wavelength. To obtain good reflectivity, low incident angles (grazing incidence) must be used.

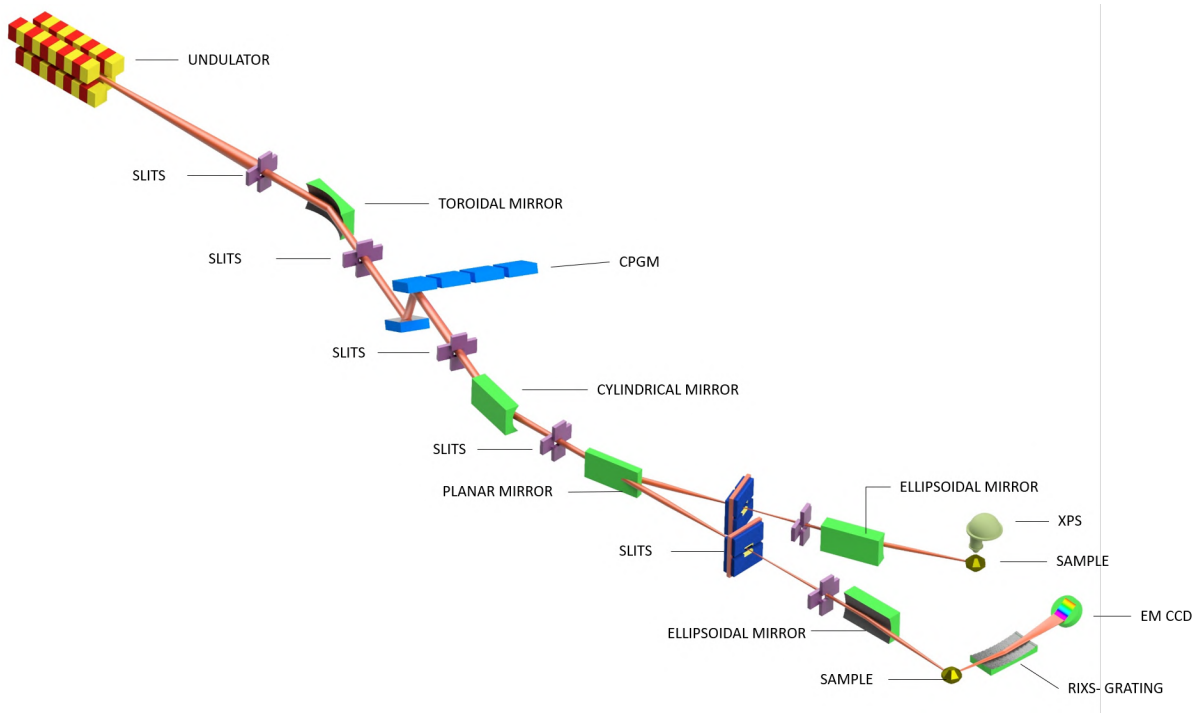

Figure A.5: Optical layout of IPE beamline at Sirius, from [147].

In the experimental hutch, by its turn, the X-rays hit the sample. Depending on the desired experiment, the detection can be of ejected electrons, making it a photon-in/electron-out technique. In the case of RIXS, we want to detect photons, so it is a photon-in/photon-out technique.

Since RIXS is an inelastic technique, the emitted radiation should also be resolved in energy. Therefore, the RIXS detection device, called spectrometer, includes a grating and a photon area detector, for which each photon energy will land in a different position of the detector.

Nowadays, there are no manufacturers in the industry that sells high-resolution RIXS spectrometers. Each synchrotron beamline that wishes to pursue this technique has to project and build its instruments. Therefore, it becomes necessary to study deeply the optics and theory to determine which optical elements will be used for the spectrometer and their operating parameters.

The concept and theory behind the grating will be explained further in the next section, where the optimization of the spectrometer grating will be explained.

Figure A.5 shows the beamline for both XPS (X-ray Photoelectron Spectroscopy) and RIXS branches of the IPE beamline at Sirius. The main optical components are presented from the front end to the optical hutch, and for the two experimental endstations. The plane deflecting mirror is an element to choose between the two end stations, which can not receive radiation

simultaneously. The RIXS spectrometer consists of everything after the sample: the grating and the EM-CCD (Electron Multiplying Charge-Coupled Device) detector.

A.3 RIXS Spectrometer Optics

Depending on the energy regime the spectrometer is different: for hard X-rays, the radiation emitted by the sample can be deflected by a monochromator and collected using a single crystal, typically of Ge or Si. However, for soft X-rays, the use of such crystals is prohibited by the longer wavelengths. Instead, a diffraction grating is used with grazing incident angle, which gives origin to limitations in the collected angle and energy resolution.

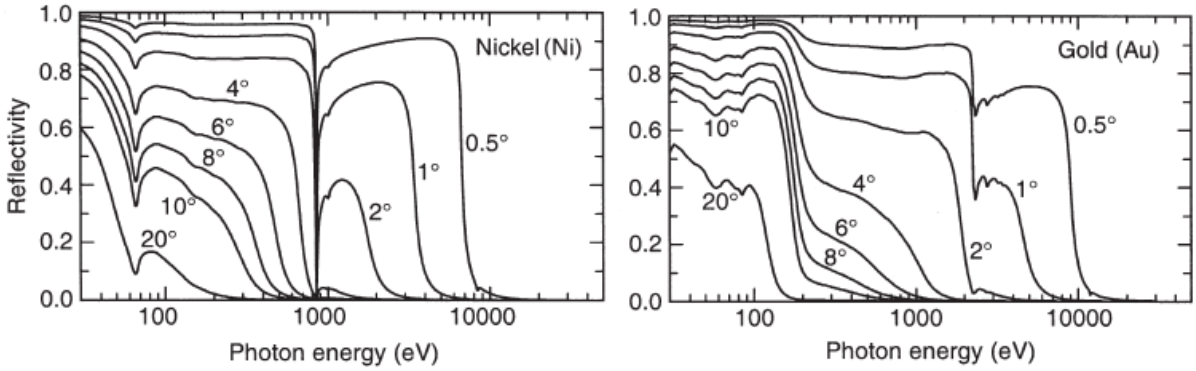

Figure A.6: Specular reflectivity curves for Ni and Au at incident angles of 0.5, 1, 2, 4, 6, 8, 10, and 20 degrees. From ref [148].

Grazing incidence is an optical geometry where the X-ray incidence angle is very small. This is necessary due to the angle dependency in the reflectivity of a mirror at soft X-rays energy: as shown in Figure A.6 for nickel and gold surfaces, the higher the angle, the fewer photons are reflected. So, it is necessary to have a spectrometer based on low-angle incidence.

To do so, a mirror with a surface shape following a certain pattern is used to separate the different wavelengths, reflecting each energy in a slightly different direction: it is called a grating. The idea is very simple and it is illustrated in Figure A.7. The optical path difference between photons hitting different steps of the pattern is $d(\sin\alpha - \sin\beta)$, where d_0 is the distance between the grooves in the surface, α is the incoming angle defined positively between the normal and

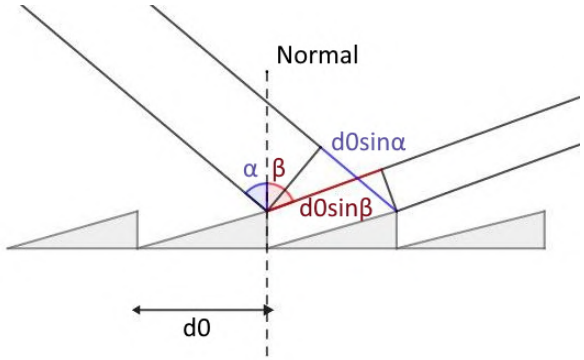

Figure A.7: The optical path difference resulting from the periodic shape of the surface gives origin to the grating equation. Both α and β are defined as being positive.

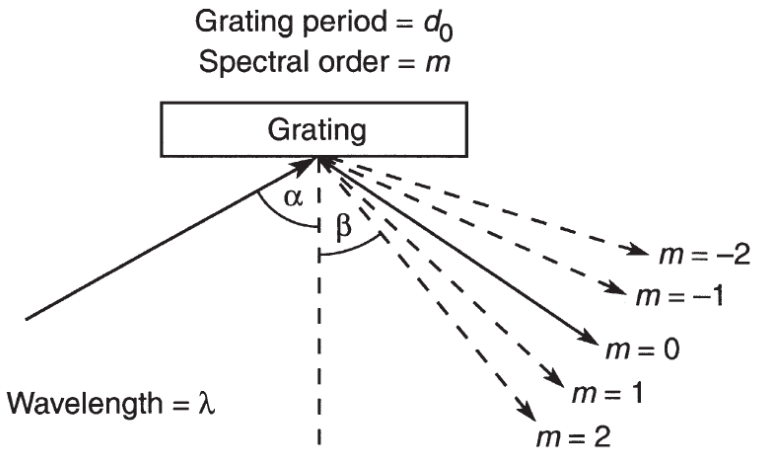

Figure A.8: Different orders of diffraction for a single incident energy. Extracted from ref [148].

the incoming ray and β is the outgoing angle defined positively between the normal to the surface and the outgoing ray. Considering constructive interference between those rays, the optical path difference must be equal to an integer number of wavelengths. This gives origin to the **grating equation**:

$$\sin\alpha - \sin\beta = \frac{m\lambda}{d_0} = a_0 m\lambda, \tag{A.1}$$

where a_0 is defined as the grating line density, usually in units of lines/mm. However, for a certain pair of α and β, multiple wavelengths satisfy the equation. This is illustrated in figure A.8. The same wavelength λ is reflected in several directions, being the $m = 0$ direction equal for all wavelengths, as seen in the equation A.1. Therefore, this order is not of interest to monochromator purposes.

Some different configurations or geometries can be chosen to solve this multiplicity of solutions for λ and m. One such configuration is to set $m = 1$, which will have more photon counting. Anyway, since the angles α and β are very large, there is better separation between orders, and therefore better resolution, using the internal orders with $m > 1$. $m = 2$ could be used, but it has a much lower intensity than $m = 1$ since the intensity of the reflections decreases as m increases.

Another way to fix the relation between α and β for given energy is to choose a constant focal distance c_{ff}, where

$$\frac{\cos\beta}{\cos\alpha} = c_{\mathrm{ff}}, \tag{A.2}$$

making the grating equation A.1 turns to

$$1 - \left(\frac{m\lambda}{d_0} + \sin\beta\right)^2 = \frac{\cos^2\beta}{c_{ff}^2} \tag{A.3}$$

Besides the diffraction properties, there are the focusing properties that we should be concerned about. When the RIXS sample is hit with the incoming beam of photons, the scattering process will emit in an isotropic manner. It demands a collecting mirror after the sample along with the monochromator grating. However, the grating can be manufactured with a curved surface, combining the effects of collecting and focusing the scattered photons and separating their kinetic energies in a single optical element.

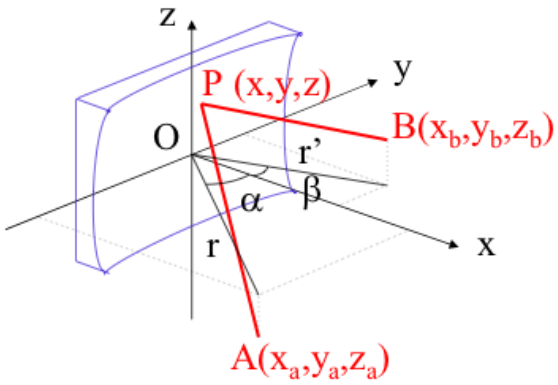

Figure A.9: Illustration of an optical path from point A to B, passing through point P into the mirror surface.

Additionally, we should remember that the source, the RIXS sample, is not punctual. It emits not only with a finite size but also in all directions. In this regard, let us first think about the focus of a punctual source. A perfect focusing mirror (or lens) would take all rays from point A, through the mirror, at the same point B, independent of the wavelength of those rays, this is illustrated in figure A.9. Following Fermat's principle (or principle of least time), since the light did not change its media of propagation, its velocity is constant, which means that the path traveled to any light beam from point A to point B would have the same length. That is the definition of an ellipse. From this, one can conclude that a perfect mirror to focus a punctual and divergent source would be an ellipse.

On the other hand, one can wish to focus a pencil of parallel rays on the same point. In this case, the source is approximate to have a finite size, but no divergence (or be already well collimated), and, following similar arguments, the best mirror would be a parabolic one. However, it is still very challenging and impracticable to fabricate an ellipsoidal mirror, and is very hard to fabricate a parabolic mirror that is not huge.

So, in practice, beamline design is mostly based on using toroidal (spherical and cylindrical are sub-cases here) and plane mirrors. The chosen grating for the IPE beamline RIXS spectrometer, called BRIXS, is cylindrical, with its curvature focusing in the meridional (vertical) direction.

A.3.1 Variable Line Spacing gratings

Manufacture imperfections and optical aberrations due to the grating shape result in distortion and deterioration of the focal and energy resolution qualities of the grating. One bright solution to this problem is to project a grating that, instead of having constant line density a_0, would have a line density that is variable along the grating length. This is called a Variable Line Spacing (VLS) grating and follows a polynomial line density following the expression [149]:

$$a(x) = a_0 + a_1 x + a_2 x^2 + a_3 x^3 + ... \tag{A.4}$$

It is possible to expand the grating surface in Taylor's series and write the optical path in terms of this expansion. After applying the least action principle (Fermat) to the optical paths, each a_n coefficient will be attributed to different orders. Annulling the derivative of such terms

will be the good conditions for the x-ray path. The zero-order expression obtained by this method is the grating equation A.1, already presented here by geometrical arguments. A first-order expression obtained is the **meridional focus equation**, presented as equation A.5. By its turn, a second-order expression is the aberration coma equation, presented as equation A.6. The coma aberration is related to an asymmetric line shape on the intensity peak of detected photons, causing an enlargement of the line width.

$$\frac{\cos^2\alpha}{r_1} + \frac{\cos^2\beta}{r_2} = \frac{\cos\alpha + \cos\beta}{R} + a_1 k\lambda \tag{A.5}$$

$$\frac{\sin\alpha}{2r_1}\left(\frac{\cos^2\alpha}{r_1} - \frac{\cos\alpha}{R}\right) - \frac{\sin\beta}{2r_2}\left(\frac{\cos^2\beta}{r_2} - \frac{\cos\beta}{R}\right) + \frac{1}{3}a_2 k\lambda = 0 \tag{A.6}$$

Each equation depends on the angles α and β, grating curvature R, A and B points distance r_1 and r_2, respectively, and on the line density polynomial coefficient term a_n related to that expansion order. Therefore, it is possible to choose the terms a_n that minimize each of these expressions, taking them as close as possible to zero, which means: perfect focus, no coma aberration, etc.

A.3.2 Analytical optimization of the spectrometer

The spectrometer resolution depends on the parameters that define the diffraction geometry and VLS terms. Additionally, some important error parameters can be taken into account analytically to estimate the energy separation capacity of the diffraction grating. These errors include the source error Δ_S, the slope error Δ_{SE}, and the detection error Δ_D. This is shown in figure A.10. Another important term is the detector inclination γ, since it is possible to reduce the *effective* detector pixel size by inclining the detector concerning the focal plane, defined by equation A.7. This is, however, limited by the low penetration depth of the photons once the inclination gets too small. The optimal inclination is around 20°.

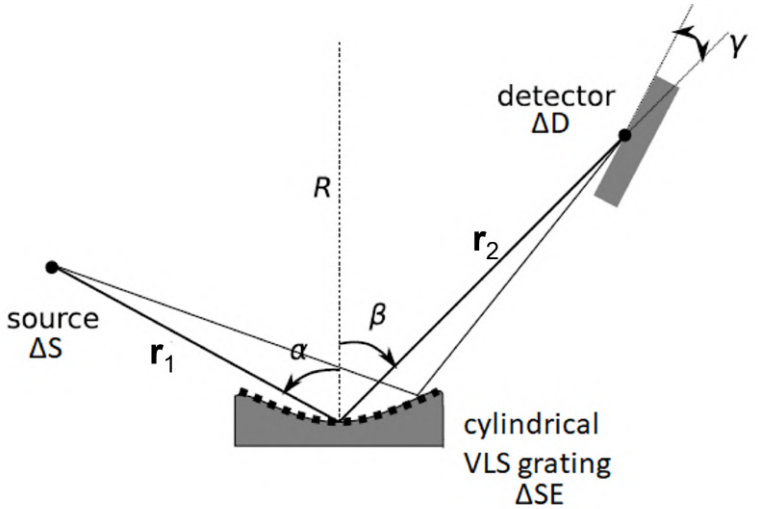

Figure A.10: Optical layout for the cylindrical VLS RIXS spectrometer of IPE beamline where α and β are the incidence and diffraction angles, r_1 and r_2 are the input and output arm length, γ is the focal plane inclination, Δ_{SE} is the grating meridional slope error, Δ_D is the detector pixel size and Δ_S incident beam size. Adapted from Ref [150].

$$\tan\gamma = \frac{\cos\beta}{2\sin\beta - r_2[(\tan\beta])/R + a_1/a_0} \tag{A.7}$$

The source error Δ_S is related to the finite illuminated size of the sample emitting the scattered radiation. This is directly connected to the spot size of the incoming beam at the sample chamber position, therefore is an external parameter to the spectrometer itself, depending on the previous optical elements.

The slope error Δ_{SE} relates to the imperfections on the grating surface, which can be experimentally characterized by metrology techniques by average deviations of the ideal grating surface angles. This is measured in angle units.

Finally, the detection error Δ_D is the detector pixel size in mm. As the detector pixel gets smaller, it can separate better the final position of the separated light by its final angle, which is energy dependent. As a consequence, this affects the final energy resolution.

We can estimate the final energy resolution as a line width ΔE, which is a function of all these parameters [151], following equation A.8. The final resolution will be a quadratic sum of the different sources of error or line widths.

$$\Delta E = \sqrt{\left(\Delta_S \frac{\cos\alpha}{r_1 a_0 k\lambda} E\right)^2 + \left(\Delta_{SE} \frac{E}{\tan[(\alpha-\beta)/2]}\right)^2 + \left(\Delta_D \sin\gamma \frac{\cos\beta}{r_2 a_0 k\lambda} E\right)^2} \tag{A.8}$$

For the optimization process, as we saw, there are a lot of parameters to consider. The important parameters can be divided into three groups: fabrication parameters (a_0, a_1, a_2, a_3, R), operation or geometrical parameters (α, β, r_1, r_2, γ), and error parameters (Δ_S, Δ_{SE}, Δ_D). Therefore, to optimize the fabrication parameters necessary to order a grating, we should fix some of the other parameters, or at least give them some constraint. On the other hand, once the grating is ready to use, we can use the same set of equations to optimize the operation parameters while keeping the grating parameters fixed.

In my work on the IPE spectrometer commissioning, I took both approaches. The first is to learn how to use the optimization tools and benchmark the ordered grating. The second is to simulate the operational parameters to choose how to best use the spectrometer.

For the analytical optimization of the VLS grating parameters, I fixed the parameters: total size of the spectrometer $r_1 + r_2 = L$, incidence angle α, detector inclination γ, and a_0 line density term. It leaves us with five parameters to optimize: β, r_1, R, a_1, and a_2 using five equations.

The fixed parameter values were chosen based on manufacture restrictions, better efficiency, and previous studies and simulations [152, 153]. They are: reference energy $E = 930$ eV, corresponding to the Cu L_3-edge, $a_0 = 2000$ lines/mm, diffraction order $k = 1$, $\alpha = 87.6$ deg, total spectrometer length $L = 5000$ mm, $\gamma = 20$ deg, source error $\Delta_S = 1 \times 10^{-3}$ mm, slope error $\Delta_{SE} = 0.217 \times 10^{-6}$ rad, and pixel detector size $\Delta_D = 5 \times 10^{-3}$ mm. The choice of α and a_0 will also be justified by the grating efficiency simulation, as we shall see in section A.3.4.

From the grating equation A.1, we can determine β. By minimizing the energy resolution equation A.8, with the condition $r_1 + r_2 = L$, we can get the best r_1 value. Solving the system of meridional focus A.5 and focal plane inclination A.7 equations it is possible to solve for the best a_1 and R. Finally, the coma aberration equation A.6 gives us the best a_2 value to minimize the coma error.

The results of this method are listed in the table A.1. With these parameters, we estimate an

analytical energy resolution of 20 meV for the reference photon energy of 930 eV.

r_1 (mm)	r_2 (mm)	β	R (mm)	a_1 (mm^{-2})	a_2 (mm^{-3})
1525.78	3474.22	85.1736	51484.5	0.55411	-0.00011724

Table A.1: Grating and geometry parameters obtained by the analytical optimization method.

A.3.3 Optimization of IPE spectrometer by ray-tracing simulation

The analytical model described previously is very useful for the initial choice of the grating manufacturing parameters. However, it has its limitations, the main being the paraxial approximation which does not describe well the grating for grazing incidence. Additionally, the methods do not determine the a_3 VLS parameter, which is related to the control and reduction of the photon line width distribution at the detection plane.

To overcome these limitations still within the limits of geometrical optics, we can rely on ray-tracing calculations [154]. In this paradigm, each beam is treated as a vector and each optical element is treated as a matrix that transforms such vectors. It is possible to use a statistical distribution of incoming beams with a finite size and angular divergence which propagates through the optical system. With it, it is possible to count where the losses in photon count occur, which helps design a system with the minimum loss possible.

There is some software for performing ray-tracing calculations. In this work, I employed the SHADOW package, which was developed to use Monte Carlo simulation for X-ray optical elements to simulate its propagation to describe all the main optical elements, such as gratings, mirrors, monochromator crystals, slits, etc [155]. This code was recently implemented in the OASYS platform (OrAnge SYnchrotron Suite) [156]. The OASYS interface and workflow engine are based on the software Orange, which is a framework based in python designed for data treatment and analysis and machine learning applications. With the SHADOW it is possible to perform ray tracing calculations using a graphical interface to build the optical system and it is possible to export the whole optical system as a python code, which can be edited and implemented with other functions.

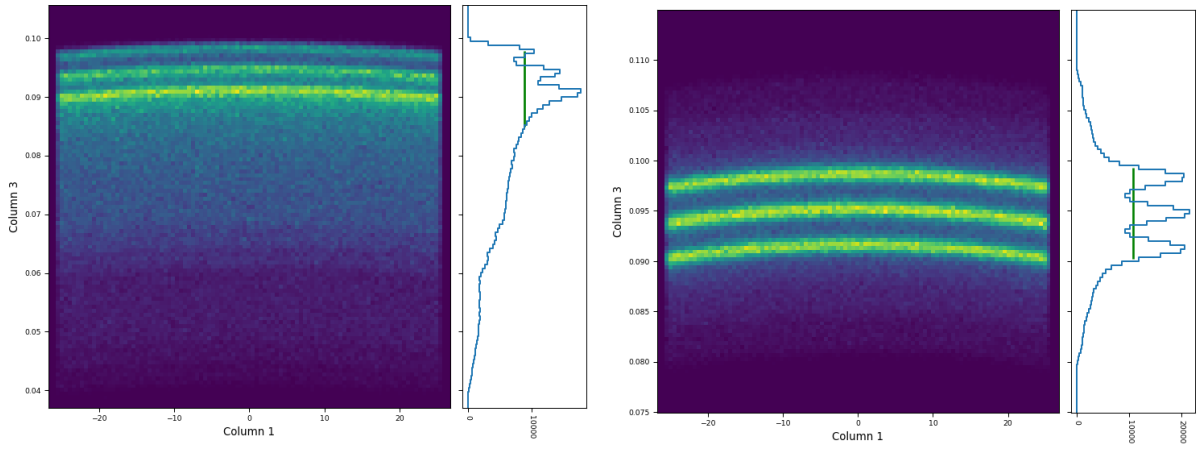

Figure A.11: Detected images for the SHADOW calculations using three incident energies, separated by 30 meV around 930 eV. The left image has $a_2 = 0$ and $a_3 = 0$ and the right one has $a_2 = -0.00011724$ mm^{-3} and $a_3 = 0$.

In figure A.11 we can inspect the use of the shadow package to simulate the effect of the a_2 VLS parameter to reduce the coma aberration for the detected photons. For this, I prepare a source beam with three different energies, separated by 30 meV around the reference energy of 930 eV. The source has a finite size with a Gaussian distribution of photons' initial positions and uniform horizontal and vertical angular divergence. After interacting with the grating, the image is formed on a plane element that doubles as a detector. Since the grating has a vertical ruling to separate the energies, we can integrate the horizontal image intensity. This is illustrated in the right inset.

Both simulations show the calculated grating, but on the left one, we have $a_2 = 0$ and $a_3 = 0$, while in the right one $a_2 = -0.00011724$ mm^{-3} and $a_3 = 0$. From this, we can see in practice that the right choice of a_2 can reduce the noise caused by asymmetric peaks. However, there is still a symmetric noisy tail at the base of the peaks. This is what we expect to remove by fine-tuning the a_3 parameter.

To achieve this, the method used to optimize the a_3 parameter consists of choosing a range of a_3 values, running the shadow code for a beam with 930 eV photon energy, and calculating the standard deviation of the distribution at the detector plane after integrated on the horizontal. The a_3 value which results in the smaller standard deviation corresponds to a sharper peak with less noise.

However, in practice, there is a small correlation between a_2 and a_3, since the optical path expansion works better in the vicinity of the central beam, once the optical geometry takes a punctual source for the expansion. Therefore, the optimization of a_3 will be improved if we optimize a_2 on each run to ensure peak symmetry. The peak symmetry, by its turn, can be related to the distribution skewness, which we want to be as close as possible to zero.

Grating	R (m)	a_1 (mm^{-2})	a_2 (mm^{-3})	a_3 (mm^{-4})
Final calculation	51.5	0.554	-0.000119	3.6×10^{-7}
Manufactured	52.9 ± 0.2	0.532 ± 0.009	-0.000123 ± 0.000005	$3.7 \pm 0.3 \times 10^{-7}$

Table A.2: Final grating parameters obtained with the described method and compared to the manufactured grating.

The final grating obtained by this calculation method is described in table A.2. Every value was rounded to correspond to the fabrication precision parameters. When compared with the grating ordered, based on previous studies, we see that the main difference lies in the grating curvature radius R and in the a_1 parameter. From the meridional focus equation A.5, we see that their difference cancel out. This is a consequence of the fact that the analytical results are sensitive to the initial set of fixed parameters. However, both gratings have the same energy resolution capacity.

In Figure A.12 we can observe the SHADOW detected intensity profile for the final grating, using the same source beam as in figure A.11. We can see that peaks are more Gaussian and that the symmetrical noise was considerably reduced. This is a result that points to the SHADOW tools and the methods here presented as good resources to simulate the grating operation.

A.3.4 Optimization of throughput using the REFLEC code

As explained, to perform RIXS experiments, not only the energy resolution should achieve a threshold related to the interesting scales in the materials, but also there is an intense loss of photons in the process. Therefore, we would like to have the spectrometer manufactured and operating in conditions where the photon loss would be minimized. In this sense, we can

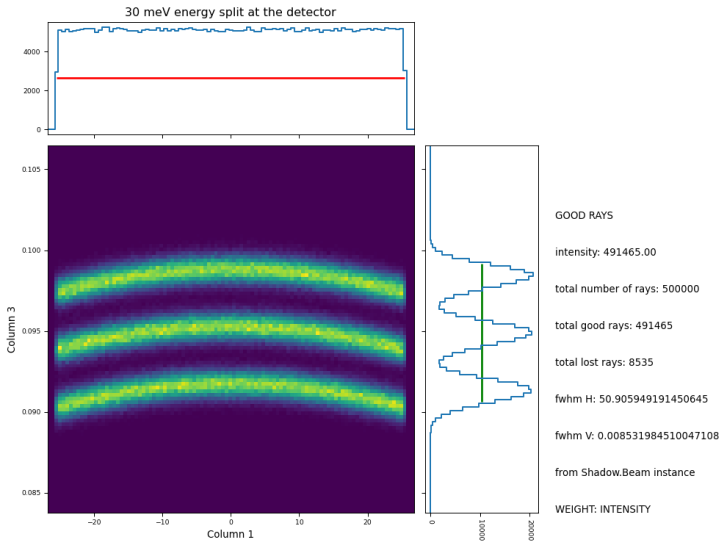

Figure A.12: Imagem formada no detector com 3 energias incidentes separadas por 30 meV em torno da energia central 930 eV para a grade final.

define the grating *efficiency* as the ratio between the diffracted light through reflection and the collected light.

However, since the diffraction results from the light wave nature, it can not be simulated by ray-tracing and geometric optical tools. To estimate the efficiency we should calculate the electromagnetic fields in the proximity of a periodic medium, with a determined incidence angle. Several numerical methods were developed to solve such a problem: the modal method, the integral method, and the differential method [157–160]. The latter applies the Maxwell equation in a differential form employing a Fourier expansion of the fields and the material's permissivity along the grating periodicity [161]. In this work, I rely on the implementation of the differential method in a Fortran code called REFLEC, developed by the German synchrotron Bessy II to perform simulations of the beamlines optics [162].

Using REFLEC it is possible to calculate the efficiency curve as a function of energy for several fixed parameters. Among these parameters, the main ones are the grating surface, such as coating material, the density of the coating, line density a_0, and the roughness of the surface. The geometrical parameters are also important, such as α or c_{ff}, as well as two parameters that configure the groove shape in the ruling pattern: the *aspect angle* (apex) and the *blaze angle*, corresponding respectively to the bigger angle at the top of the groove and the smaller angle at the base of the groove.

For the REFLEC calculations, I fixed the parameters based on the manufactured grating, with the coating material being Au, with density 19.3 g/cm^3, and surface roughness of 0.01, a_0 line density of 2000 lines/mm, and diffraction order $k = 1$. A study for the dependency of the grating efficiency as a function of aspect and blaze angles is illustrated in the left panel of figure A.13, where the grating optimization energy and α angle of 930 eV and $87.6°$ were used.

As we can observe, the best value for the aspect angle and the blaze angle are, respectively, $90°$ and $1.4°$. Using these values, we can see the effect of changing energy and α on the grating efficiency in the right panel of figure A.13. To build this map, I run the REFLEC code for $80 < \alpha < 89.5°$, with steps of $0.5°$ and using energies between 100 and 2000 eV with steps of 20 eV. The grating optimization energy and α are marked as dashed lines and we observe that for lower photon energies the efficiency peak as a function of α shifts for lower values of α. We see that, for line density 2000 lines/mm, the grating has a good efficiency performance for

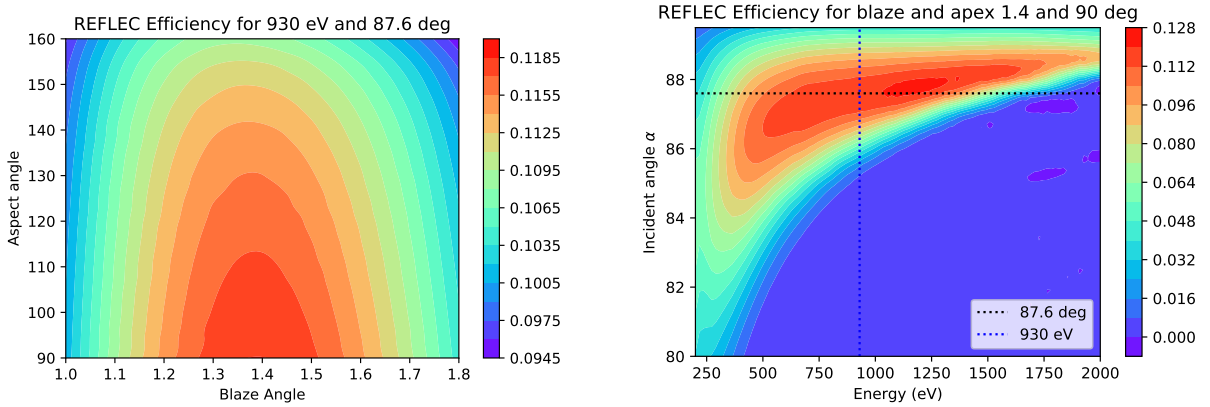

Figure A.13: Efficiency maps obtained using the REFLEC code as a function of the aspect and blaze angles and as a function of the incident angle α and photon energy.

energies between 500 and 1600 eV.

However, to estimate the photon loss in the whole RIXS process and detection, one should also think in terms of the collected fraction of photons, which can be resumed in two angular factors [1]: meridional and sagittal acceptance angles. These angles translate the fraction of photons emitted by the sample that hits the grating. The meridional dispersion, in this case, is equal to vertical dispersion, since the meridional plane is the plane defined by the source, detector, and optical element center. The sagittal, then, is equal to the horizontal direction.

In a preliminary analysis, we can consider only the vertical acceptance, since this is the one that changes with the change of geometrical operation parameters. Using trigonometry, it is straightforward to calculate the vertical angular acceptance as a function of α and r_1:

$$\sigma_v = \frac{l\cos(\alpha)}{r_1}, \tag{A.9}$$

where l is the grating length, fixed in 160 mm. In the left panel of figure A.14 we can observe the vertical acceptance as a function of α and photon energy. Since the r_1 parameter depends on our optimization choice, the value obtained by the method described in the section A.3.2 can be used for the analytical optimization. The result is that lower α values imply a larger fraction of photons being collected by the grating, a different effect from the efficiency trend. To take both calculations into account simultaneously, we can multiply the vertical acceptance by the grating efficiency for each α and energy value, and the result will be the vertical transmittance or vertical throughput. This is shown in the right panel of figure A.14.

Finally, it was possible to establish a method employing analytical and simulation tools for the best design of the spectrometer grating. This method can support the design of other VLS gratings, by aiming the choice of VLS parameters to cancel aberrations for geometries that benefit the throughput.

A.3.5 Optimization of operation parameters

In the previous sections, the choice of α and its implication on the other geometry parameters was not uniquely defined. It was chosen for the analytical calculations to obtain r_1 by minimizing the energy resolution equation A.8, while α was fixed. Additionally, all optimiza-

[1] It can also be considered as a solid angle. However, the effects of focusing are different in the meridional and sagittal directions, so both effects are counted separately.

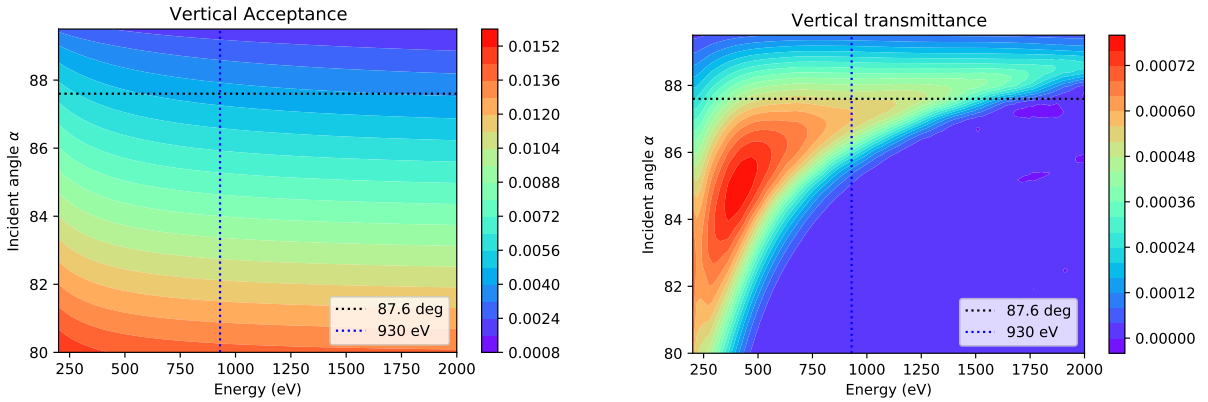

Figure A.14: Maps of vertical acceptance and total throughput as a function of the incident angle α and photon energy.

tion was made for single photon energy, so when we have different energies the geometrical parameters will change. These parameters will have an impact on the focal quality at the detector plane, in the energy resolution, and in the throughput.

Now that we have all the grating parameters defined, we can be flexible with the previous constraints and explore a range of possible α, and instead of getting the best energy resolution, it is possible to prioritize minimal coma aberrations, maximum throughput, or even considering second-order diffraction, for instance. Therefore, the next step is to optimize the geometrical operation parameters considering these different modes. After running several tests, it was clear that the most important condition to keep the detection quality was to keep the coma aberration as low as possible, and this could be done for any value of α. So we can use α as a main geometrical variable, for which all other parameters can depend on.

For this purpose, the same equations used to optimize the grating can be used. Naturally, the β parameter can be calculated again from the grating equation A.1 as a function of α and energy E:

$$\beta(\alpha, E) = \arcsin(\sin\alpha - a_0 k\lambda). \tag{A.10}$$

The r_2 paramter can also be obtained as a function of α and E by replacing $\beta(\alpha, E)$ on the meridional focal equation A.5:

$$r_2(\alpha, E) = \frac{\cos^2\beta}{(\cos\alpha + \cos\beta)/R - \cos^2\alpha/r_1 + a_1 k\lambda}. \tag{A.11}$$

However, r_2 stills depends on r_1, which can be obtained by replacing $\beta(\alpha, E)$ and $r_2(\alpha, E)$ into the coma equation A.6. The functional dependency is quite complicated because it is implicit, but the final form of the coma equation depends only on α, E, and r_1. So we can solve it numerically to obtain the r_1, which is the root of this equation for each value of α and E. With this value of r_1, we can get the r_2, and some other interesting values, such as the vertical acceptance (equation A.9) and analytical energy resolution (equation A.8).

One thing that must be considered is that the geometrical parameter range is restricted by the mechanical constraints of the spectrometer design. There is a maximum and a minimum value for the distances between the sample and the grating and the grating and the detector, r_1 and r_2, respectively, as well as the total spectrometer length and its height, $r_1 + r_2$ and h. The incidence angle α should also be within an interval, considering the surface efficiency properties already explained. These limits are listed below:

- $4000 < r_1 + r_2 < 5898$ mm
- $1814 < r_2 < 5148$ mm
- $750 < r_1 < 2288$ mm
- $0 < h < 1000$ mm
- $81° < \alpha < 90°$

With the described optimization method, I generated a table with all parameter configurations to operate the spectrometer grating. This table can be used to interpolate and plot the main graphical results as a function of incident energy and α. When imposing the mechanical constraints, the main limitation turns out to be the spectrometer length $r_1 + r_2$, as shown in figure A.15, where the black lines mark the mechanical limits. The region of allowed $r_1 + r_2$ is mainly contained inside the range of $87 < \alpha < 88.5°$. The allowed parameter range outside of this interval is not interesting, because it is forcing higher α angles for the lowest photon energies, which is not favorable for the throughput.

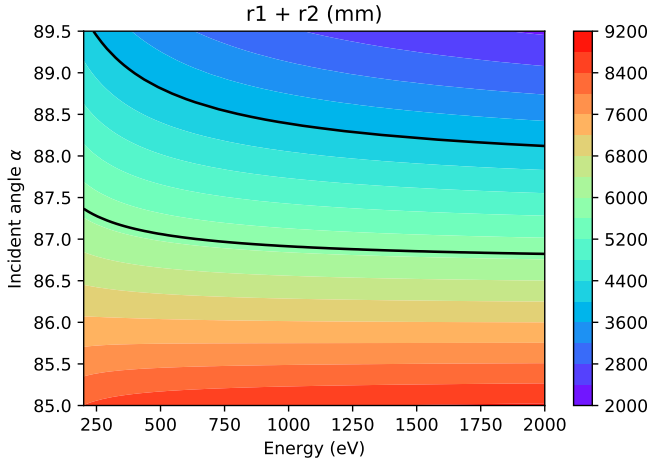

Figure A.15: Spectrometer length, $r_1 + r_2$, as a function of energy and α. The black lines mark the mechanical limits.

Therefore, I can recalculate, with more details, the geometrical parameters and other interesting properties for a restricted α region and smaller steps. Choosing $87 < \alpha < 88.5°$, with steps of $0.1°$ and using energies between 100 and 2000 eV with steps of 10 eV, a new table, denser in points, is calculated. The head of this table is shown in figure A.16, displayed by the use of the pandas, a data analysis package for python language [163].

In this table, for every energy and α combination, the geometrical parameters r_1, r_2, $r1 + r2$, γ, height h were calculated, along with vertical acceptance, horizontal acceptance, and analytical energy resolution. However, restrained values are still included, with the mechanical constraints being violated for some set of parameters. We can see, for example, that the solution of γ following the focal plane inclination equation A.7 has a divergence and negative solutions, which is unrealistic and interferes with the calculated analytical resolution.

To overcome this, we can use the pandas' tools to filter out of the dataframe every line where some constrain are not respected. This results in a new table, for which the calculated γ is shown in figure A.17. The dashed line represents $\gamma = 20°$, the value for which the grating

	alpha	energy (eV)	beta	r1 (mm)	r2 (mm)	r1+r2	gamma	height	accv (mrad)	acch (mrad)	DeltaE (meV)
0	87.0	100.0	76.864	980.080	5682.253	6662.333	-83.864	1579.218	8.010	7.805	0.7
1	87.0	110.0	77.445	1017.404	5621.783	6639.187	-84.545	1507.577	7.716	7.832	0.7
2	87.0	120.0	77.950	1052.303	5564.653	6616.955	-85.237	1444.936	7.460	7.859	0.8
3	87.0	130.0	78.394	1085.084	5510.557	6595.641	-85.941	1389.578	7.235	7.884	0.9
4	87.0	140.0	78.789	1115.997	5459.225	6575.222	-86.659	1340.213	7.034	7.908	1.0

Figure A.16: Numerically calculated table for the zero coma condition optimization, as a function of energy and α using the theoretical equations. Generated by pandas.

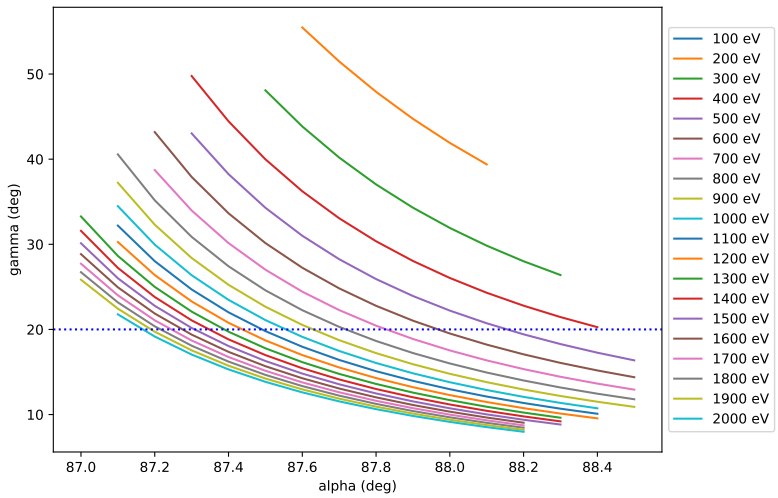

Figure A.17: Allowed values of γ calculated numerically using the theory as a function of α for a list of photon energies.

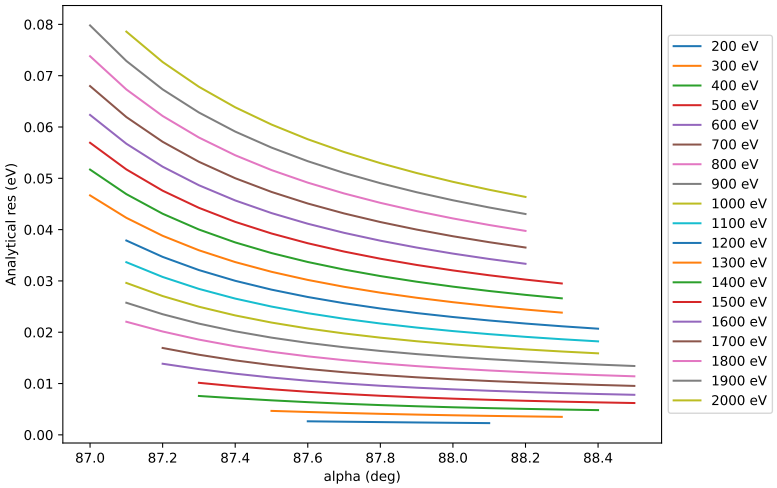

Figure A.18: Theoretically expected energy resolution as a function of α for a list of photon energies, for the allowed set of parameters.

parameters were optimized. This value presents less loss in the detector dead layer and reduces the effective pixel size $\Delta_D \sin\gamma$.

The analytically expected energy resolution is shown in figure A.18 for the allowed α and for different photon energies. Even with throughput constraints, this grating is expected to perform well in resolution for low energies.

To benchmark the process of choosing the zero coma condition as the best way to improve the grating energy resolution, ray-tracing tools can be used again. This time, I simulate the grating for a range of possible α and r_1 values, for a fixed photon energy. Therefore, I can fix β and r_2 calculated by following the grating A.10 and meridional focus A.11 equations, respectively, without forcing the zero coma condition. With this result, I inspect the detected photon peak full width at half-maximum (fwhm) that is related in the ray-tracing simulation to the energy resolution capacity of the grating, without the detector error considered.

An example is shown in figure A.19. The left panel shows the ray-tracing resulting fwhm as a function of α and r_1, for photon energy $E = 530$ eV (O K-edge). The lowest fwhm valley represents the best energy resolution region. Fitting the minimum fhwm as a function of α for fixed r_1 is possible to get the blue points. Taking these points for different intervals of α and comparing them to the analytical resolution points out that the best r_1 as a function of α are approximately the same for the ray-tracing and analytical zero coma results. This is shown in the right panel of figure A.19 for photon energy $E = 1530$ eV (Yb M_5-edge). It was tested for different photon energies and α intervals and the minimum fwhm consistently coincides with the zero coma condition.

However, there is still a degree of freedom to explore for the grating operation. Therefore, the zero-coma analytical table can be used as our standard for the best energy resolution and to access, along with REFLEC results, the grating throughput. In the next section, I will explain and illustrate the methods and results for operating the grating with a fixed γ angle and a mode to maximize the throughput for higher photon energies.

A.4 Operation modes

As mentioned, it is interesting to keep γ fixed, to avoid moving the detector too much. This is the Fixed Inclination (FI) operation mode (figure A.20) and it is very advantageous in terms of

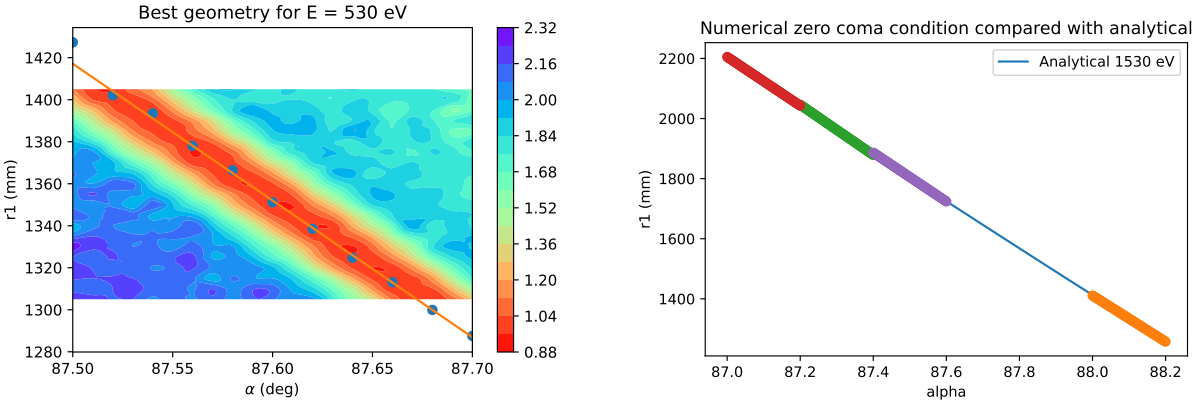

Figure A.19: Ray-tracing simulated detected beam fwhm, as a function of α and r_1.

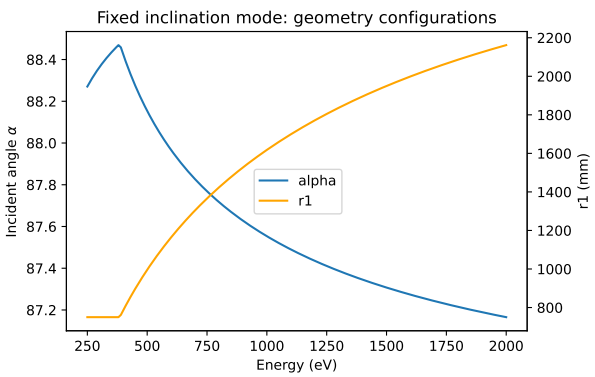

(a) Geometry configuration for the FI mode.

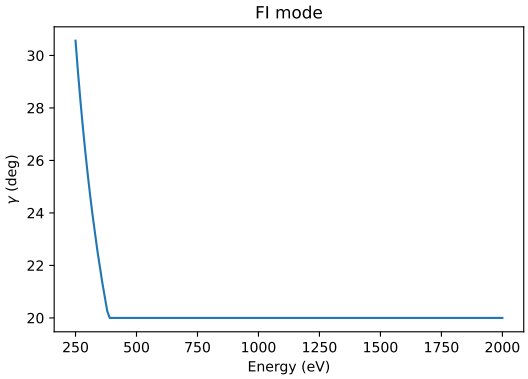

(b) γ values for the FI mode.

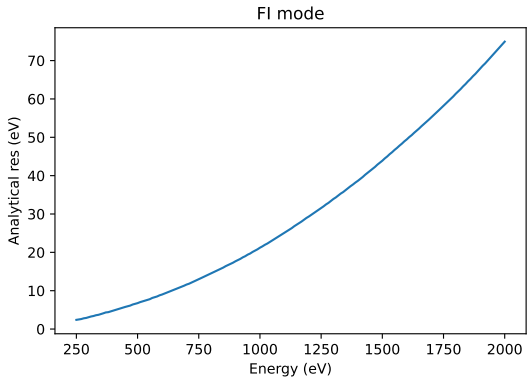

(c) Analytical resolution for the FI mode.

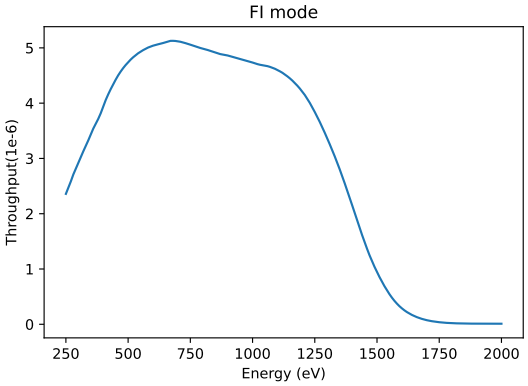

(d) Final throughput for the FI mode.

Figure A.20: Interpolated grating geometry and properties for the fixed inclination mode, as a function of photon energy.

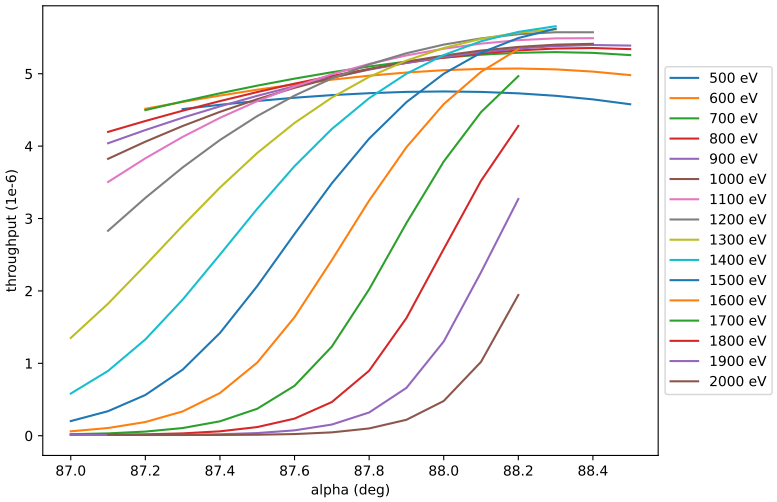

Figure A.21: Expected throughput as a function of α for a list of photon energies, for the allowed set of parameters.

mechanical maintenance and stability, with less necessity for calibration. It is also advantageous for the energy resolution since the effective detector pixel size can be reduced with lower angles. This is, however, limited for lower angles due to the absorption and reflectivity effect of the detector coating surface.

It is possible to use the zero-coma analytical solution table to interpolate, for each energy listed in the table, exactly the incident angle α that gives $\gamma = 20°$. With the resulting geometry, we can interpolate again the results as a function of energy to get the FI geometry for any energies we want within the interpolated range. This is shown in figure A.20(a), where the blue (orange) line represents the best α (r_1) that results from the condition $\gamma = 20°$, when it can be fulfilled.

For all energies above 400 eV, there is a geometrical solution for which $\gamma = 20°$. For lower energies, the lowest allowed γ can be chosen, which always corresponds to having the minimal $r_1 = 750$ mm value. For example, for the C K-edge at 285 eV, γ can be $26.8°$. This is shown in figure A.20(b).

The analytical resolution and throughput obtained by analytical calculations and REFLEC results are shown in figure A.20(c)-(d). A good plateau for the spectrometer throughput exists up to ≈ 1200 eV. After this energy, the detected number of photons drops drastically. Therefore, it is interesting to try to maximize the phonon counting for higher photon energies, even at the expense of lowering the resolution.

For this purpose, we can inspect the throughput evolution as a function of α, as in figure A.21, for a list of photon energies and only for allowed geometries. This is our motivation to calculate the spectrometer operation in the maximum throughput (MT) mode.

The maximum throughput can be achieved for higher α angles. Therefore, we can use the zero coma table to interpolate, for each energy listed in the table in the range between 1000 and 2000 eV, the configurations for the highest allowed α. This condition is equivalent to choosing the minimum spectrometer length of $r_1 + r_2 = 4000$ mm.

With all conditions listed, we can interpolate the dependence of resulting parameters as a function of energy, and use such functions to calculate the maximum throughput mode for any energy we want, as was made for the FI mode.

This is illustrated in figures A.22 (a)-(b). In the (a) panel the blue (orange) line represents the best α (r_1) that results from the MT condition. On panel (b), we can see the calculated γ for

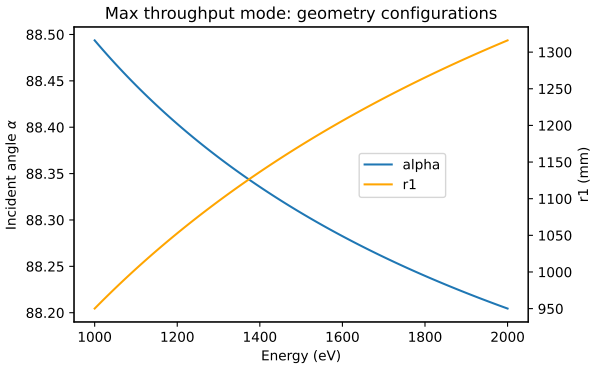

(a) Geometry configuration for the MT mode.

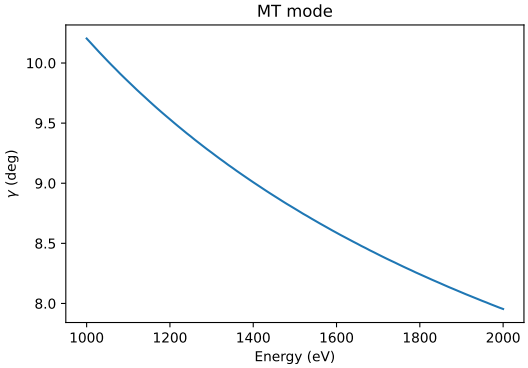

(b) γ values for the MT mode.

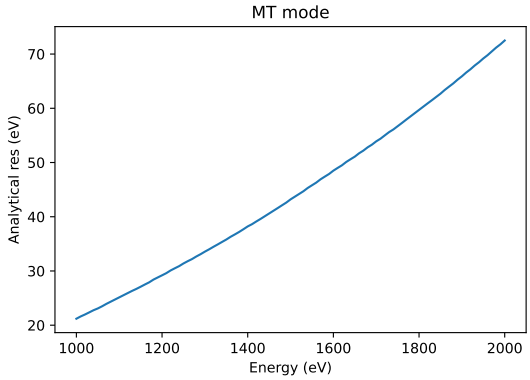

(c) Analytical resolution for the MT mode.

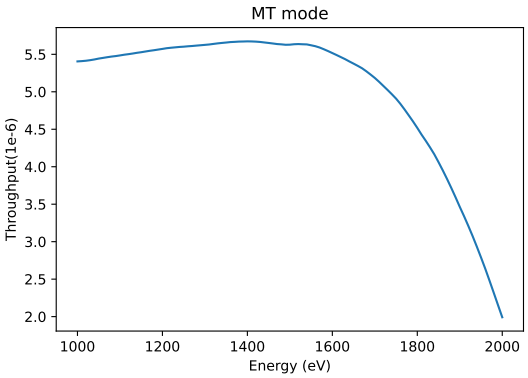

(d) Final throughput for the MT mode.

Figure A.22: Interpolated grating geometry and properties for the maximum throughput mode, as a function of photon energy.

the maximum allowed value of α, as we can see, the detector plane is pushed to very low angles, which can be harmful to the photon count in the end. This is a sign that a trade-off between the geometric and reflectivity properties and the detector coating surface penetration depth. It is expected that the second effect will be less important for this range of higher photon energies.

In figures A.22 (c)-(d) the analytical resolution and throughput obtained by analytical and REFLEC calculations are shown. There is no considerable difference in energy resolution for both modes, while the throughput is enhanced by a significant factor.

A.4.1 Conclusion

The analytical expressions for a VLS grating are a reliable tool to optimize the spectrometer design and operation. However, some of the phenomena, such as errors, efficiency, etc are only described by ray-tracing simulated grating and numerical calculations.

With a given VLS grating, optimized for Cu L_3-edge energy, it is possible to reach the best operating conditions to maximize the energy resolution by keeping the detector inclination plane at a fixed angle of 20°. This condition, however, reduces the photon counting at least by half for energies above 1300 eV, so, by avoiding this condition and maximizing the photon counting, we can choose the operation parameters that keep the photon counting up to 2000 eV by a marginal cost of energy resolution.

The tools here presented were shown to be a reliable and reproducible way to study, design, optimize, and commissioning a RIXS spectrometer. The final interpolation algorithm based on the calculated table is implemented to the alignment of the spectrometer in the commissioning state of the IPE beamline and hopefully, it will be useful for the user's beamtime preparation.